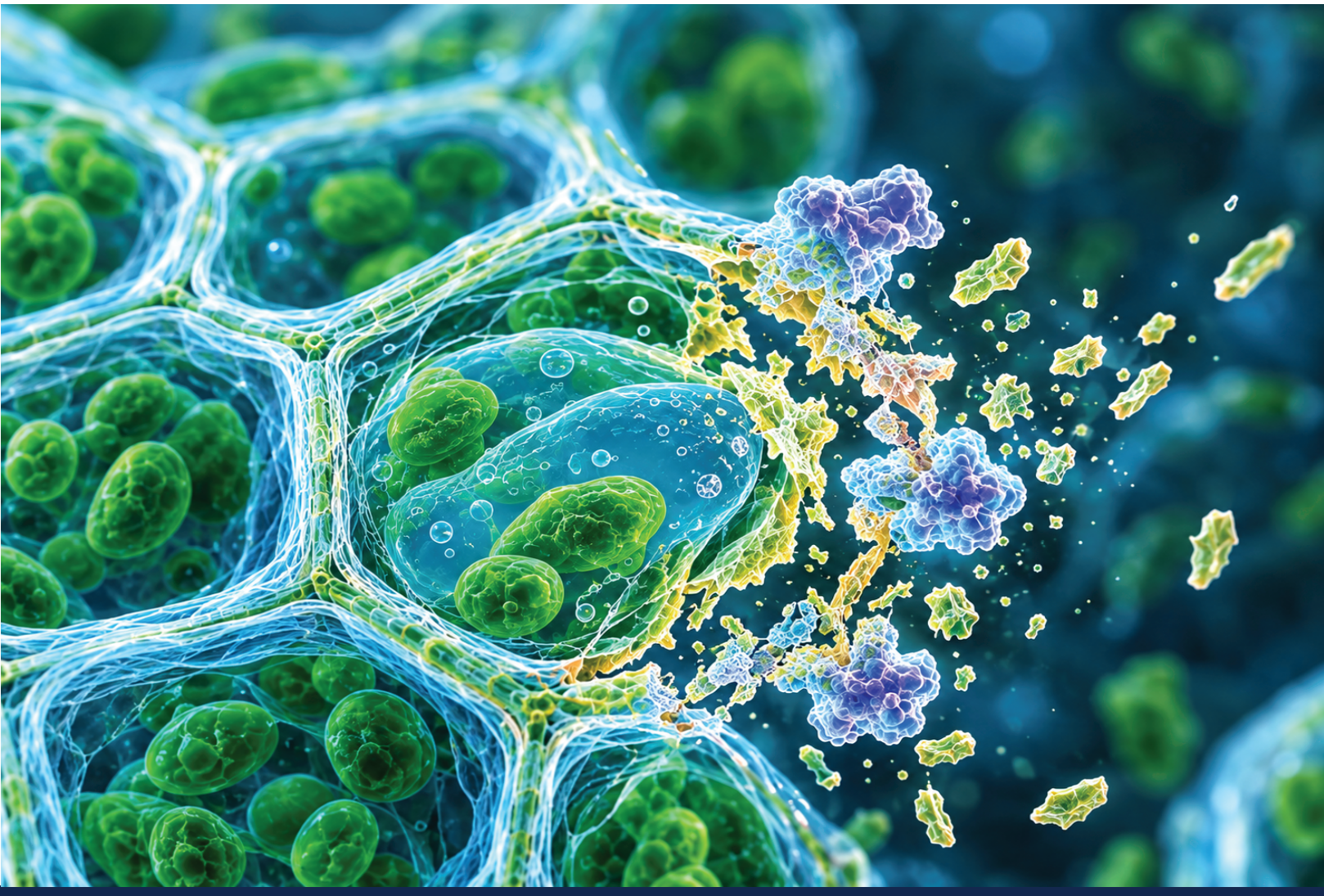
RST
RECENT SCIENCE AND TECHNOLOGY

Recent Science and Technology

ISSN 3057-0786 (Online)



Volume 18
Issue 3
(September - December 2026)

Published by
Rajamangala University of Technology Srivijaya

TABLE OF CONTENTS

VOC Emissions from Natural Latex Pillows: HS-SPME-GC/MS Characterization and Health Implications **e268926**

Roosanee Kulvijitra, Waraporn Ratsameephakai and Ekwipoo Kalkornsurapranee

Room-Temperature Vulcanization Time Controls Self-Crosslinking-Driven Self-Healing Behavior in Natural Rubber Sheets **e270555**

Nasruldin Masae and Korn Taksapattanakul

Evaluation of a Commercial β-Mannanase for Konjac Glucomannan Hydrolysis: Activity and Molecular Weight Analysis **e267961**

Chompoonuch Phuenpipob, Chaleeda Borompichaichartkul, Kittipong Rattanaporn, Putthapong Phumsombat, Supuksorn Masavang and Duangkamol Tungsatitporn

Organic Chinese Radish (Raphanus sativus L.) Cultivation in Raised Beds with Organic Amendments in Thailand **e269280**

Pattana Somniyam and Vimolchat Somniyam

Physical and Combustion Properties of Charcoal Briquettes Produced from Mangrove Wood and Coconut Shell Waste **e270270**

Wasu Suksuwan, Prateep Tippracha, Sopida Jornden, Pacharakron Chantaramanee, Suwat Rattanapan and Suchart Chantaramanee

Development of Biodegradable Plant Pots from Chitosan Reinforced with Natural Fibers for Agricultural Applications **e271479**

Thanchanok Kanlaoong, Sopida Jornden and Uraiwan Sookyung

Enrichment of Bioactive Compounds from Lotus (*Nelumbo nucifera* 'Roseum Plenum') Tea through Fermentation **e271665**

Udomrat Chueasuwanachai, Nuntaporn Pungsungvorn and Nipaporn Kanthong

Calcium Ion Adsorption-Desorption Behavior on Maize Residue-Derived Biochar for Soil Nutrient Retention **e268061**

Patcharee Intanoo and Sakkarin Khaedaeng

Design and Development of a Microcontroller-Based Control System for a Semi-Automatic Bean Sprout Cultivation Machine **e271208**

Panot Sripakarach

Dual-Heat-Zone Biomass-Assisted Pyrolysis of Polyethylene Waste for Community-Scale Fuel Recovery in Nakhon Phanom, Thailand **e272461**

Harid Klongdee and Narongrit Auppapong

Shelf-Life Assessment and Prediction of Gymnema inodorum (Lour.) Decne. Jelly under Accelerated Storage Conditions **e271280**

Natthanicha Banpacha, Hiran Janpeng and Rajnibhas Sukeaw Samakradhamrongthai

Integrated Earthquake-Induced Stability Assessment of Lam Chae Earth Dam Using Sentinel-1 DInSAR and Field Instrumentation **e269582**

Yanisa Klongchang, Soravis Supavetch and Anuphao Aobpaet

Natural Rubber Foam for Modular Acoustic Pods: Comparative Acoustic Performance and Full-Scale Prototype Performance Assessment **e272651**

Natdanai Pratoom and Nattapon Uthaipan

Plant Community Structure and Carbon Sequestration of the Forest Restoration Areas at Kamnoetvidya Science Academy **e270817**

Worawut Ngampiboonwet, Karun Chaivanich, Praphaiphan Kewkasem, Amnuayvit Thitibordin and Yutthana Thoenglom

Detection of Chronic Load Imbalance and Hot-Spot Risk in Building Electrical Systems using Long-Term Three-Phase Current Analysis and Mechanism-Informed Artificial Intelligence **e271202**

Sittisak Rojchaya and Santi Karisan

Recent Science and Technology 2026, Vol. 18(3): e268926

Recent Science and Technology

Journal homepage: https:// www.tci-thaijo.org/index.php/rmutsvrj/index

ISSN: 3057-0786 (Online)

Research Article

VOC Emissions from Natural Latex Pillows: HS-SPME-GC/MS Characterization and Health Implications

Roosanee Kulvijitra [a*], Waraporn Ratsameephakai [a] and Ekwipoo Kalkornsurapranee [b]

[a] *Office of Scientific Instrument and Testing, Prince of Songkla University, Hat Yai, Songkhla 90110, Thailand.*

[b] *Department of Material Science and Technology, Faculty of Sciences, Prince of Songkla University, Hat Yai, Songkhla 90110, Thailand.*

Article history:

Received: 2025-08-25
Revised: 2026-04-10
Accepted: 2026-04-25

Keywords:

Natural latex pillow;
GC-MS;
VOCs

ABSTRACT

Natural rubber pillows are widely used household products; however, their production process may release volatile organic compounds (VOCs) that can affect indoor air quality and human health. This study aimed to identify and characterize VOCs in commercial rubber pillows and evaluate their potential health implications based on toxicological references. Ten pillow samples (P01–P10) were analyzed using headspace solid-phase microextraction coupled with gas chromatography–mass spectrometry (HS-SPME–GC–MS). VOC identification was performed by comparison with NIST 14 and Wiley 10 mass spectral libraries, using a match score acceptance criterion of ≥ 90%. Semi-quantification was conducted based on relative peak area normalization. A total of 44 VOCs were identified and classified into nine chemical categories. Frequently detected compounds in all samples included sulfur compounds (e.g., carbon disulfide and benzothiazole); aromatic hydrocarbons (e.g., toluene and styrene); alcohols (e.g., 2-ethyl-1-hexanol and linalool); aromatic compounds (e.g., benzenemethanol, α,α-dimethyl-, and diethyl phthalate); and cyclic alkenes (e.g., α-copaene and δ-cadinene). Benzothiazole and phenol, 2-(1,1-dimethylethyl)-6-methyl-, both considered toxicologically relevant compounds, were consistently detected in all samples. The presence of benzothiazole was attributed to its role in the vulcanization process, whereas amines were observed only in selected samples (P04, P06, P08). Several detected VOCs have been identified as causing potential health risks, including neurotoxicity (carbon disulfide), mucosal irritation (amines), and endocrine disruption (phthalates). These findings indicate that natural rubber pillows may act as sources of diverse VOC emissions, predominantly sulfur- and aromatic-derived compounds. Notably, this is the first study on finished pillows to provide comprehensive evaluations of VOC emissions from them rather than raw materials. Although absolute concentrations were not determined, the results highlight the need for further exposure and risk assessment studies. These findings indicate that natural rubber pillows may act as sources of diverse VOC emissions, predominantly sulfur- and aromatic-derived compounds, particularly under prolonged exposure conditions during sleep. From a practical perspective, these results suggest that manufacturers should consider emission-reduction strategies, including process optimization and the use of low-emission additives, and support the development of eco-labeled, low-VOC products in line with international indoor air quality guidelines in order to enhance consumer safety.

© 2026 Kulvijitra, R., Ratsameephakai, W. and Kalkornsurapranee, E. Recent Science and Technology published by Rajamangala University of Technology Srivijaya

1. Introduction

More people are increasingly concerned about environmental sensitivities arising from a wide range of consumer products, including cosmetics, household items, food, and pharmaceuticals (Ramírez *et al*., 2010; Khalid and Abdollahi, 2021). In particular, indoor air quality has become a significant public health issue, as highlighted by international organizations such as the World Health Organization (WHO, 2010) and the U.S. Environmental Protection Agency (U.S. EPA, 2023), which emphasize the impact of VOCs on indoor air quality and human health in indoor environments. Natural rubber-based products, such as latex pillows and mattresses,

* **Corresponding author.**

E-mail address: *roosanee.l@psu.ac.th*

Cite this article as:

Kulvijitra, R., Ratsameephakai, W. and Kalkornsurapranee, E. 2026. VOC Emissions from Natural Latex Pillows: HS-SPME-GC/MS Characterization and Health Implications. **Recent Science and Technology** 18(3): e268926.

https://doi.org/10.65411/rst.2026.268926

are widely used personal and household items and are significant exports from Thailand. However, their manufacturing and processing stages can generate odorous compounds. VOCs in natural rubber are primarily formed through microbial degradation of non-rubber components, including carbohydrates and proteins, as well as through chemical additives used during production (Nor-Hidayaty *et al*., 2012; Pajarito *et al*., 2018). In particular, sulfur-containing compounds are commonly associated with vulcanization processes, where sulfur and accelerators are used to improve elasticity and durability. Additional VOCs may originate from antioxidants (e.g., butylated hydroxytoluene, BHT), plasticizers, foaming agents, and residual solvents. These compounds can contribute not only to unpleasant odors but also to potential health risks. VOCs are organic chemicals with high vapor pressure at ambient temperature, enabling their release into indoor air. Prolonged exposure to VOCs may cause irritation, respiratory effects, and other adverse health outcomes depending on their chemical properties (Capíková *et al*., 2019). Consequently, reducing VOC emissions has become a priority for manufacturers, and regulatory frameworks such as the European Union (EU) Ecolabel for bed mattresses have established criteria to limit total VOC emissions in consumer products (European Commission, 2014).

Much research focused on the identification of the malodors of natural products in various stages reported in the main technique was gas chromatography coupled with mass spectrometry (GC-MS) and various sampling processes. The components of obnoxious odor derived from various solid rubbers by headspace sampling. Various components were found in them. Standard Thai Rubber (STR XL) were mainly comprised of hydrocarbons, and STR 5L was found to contain small amounts of volatile fatty acids. In the case of skim crumb rubber was detected the sulfur-containing compounds (Sakdapipanich and Insom, 2006). Kamarulzaman *et al*. (2012) studied the malodorous vapors from the natural rubber drying process with the thermal desorption-gas chromatography technique and found mainly consisted of volatile fatty acids (VFA), acetic acid, and propionic acid were present with the highest concentrations. The odorous compounds of cup lamp natural rubber were collected using solid-phase micro extraction (SPME) to analyze the odor on a day-to-day basis for six days. It was found that samples were analyzed at early incubation period were mainly hydrocarbons, and other volatile compounds produced throughout the incubation were low-molecular-weight compounds such as volatile fatty acids, sulfurous compounds, amino compounds, esters and alcohols (Nornanysya *et al*., 2013). Kamarulzaman *et al*. (2019) studied four headspace sampling techniques of raw rubber materials such as Static headspace sampling (SHS), Dynamic headspace sampling (DHS), Headspace SPME (HS) and Micro-chamber/thermal Extractor (μ-CTE) and found that the highest extraction efficiency corresponded to aromatics and acids, and the lowest compound extraction was aldehyde and hydrocarbon. The various VOCs signature based on the extraction procedures and the experimental conditions employed.

This study was conducted to evaluate the VOCs and the malodors of rubber mattresses by HS-SPME in combination with GC-MS. It is the most common technique for headspace analysis, although it is limited by fiber discrimination (Kamarulzaman *et al*., 2019) and combines the advantages of both SHS and DHS (Jeleń, 2006). The advantages of this technique are highly sensitive, reliable and a beneficial alternative to classical methods for VOCs determination without sample preparation (Jeleń, 2006). An attractive alternative for the determination of VOCs in various samples (Caroprese *et al*., 2009; Shinoda *et al*., 2020; Chen *et al*., 2022; Agatonovic-Kustrin *et al*., 2023). Despite multiple studies on VOCs from rubber during processing, limited data is available on emissions from finished consumer products such as latex pillows. However, no studies have comprehensively reported the VOC emission profiles of finished natural latex pillows intended for indoor consumer use, despite their widespread market presence. This represents a critical gap in understanding the potential health implications of VOC emissions from final consumer products. Although several studies have investigated VOC emissions during rubber processing, there is limited scientific data regarding emissions from finished latex bedding products, which are directly relevant to public exposure.

Therefore, this study aimed to identify and semi-quantify volatile organic compounds (VOCs) emitted from commercially available natural rubber latex pillows using HS-SPME–GC–MS. The identified VOCs were further evaluated based on using Safety Data Sheets (SDS) to assess their potential health risks.

2. Materials and Methods

2.1 Chemicals and materials

A tripolar-phase divinylbenzene/carbozen/polydimethyl siloxane (DVB/CAR/PDMS) StableFlex autosampler fibre (1 cm, 50/30 μm, 24 gauge; Agilent Technologies Inc., USA) was used for headspace solid-phase microextraction (HS-SPME). Twenty-millilitre headspace screw-top vials fitted with PTFE/silicone septa and magnetic screw caps (Agilent Technologies Inc., USA) were also used. No solvents or additional chemical reagents were employed in this work because HS-SPME is a solvent-free extraction technique.

2.2 Natural latex pillow samples

The natural latex pillow samples were supplied by Natural Rubber Innovation Research Institute, Prince of Songkla University. The natural latex pillow samples were cut into small cubes (approx. 0.5 cm × 0.5 cm × 0.5 cm). 4 g of each sample was weighed and placed in the 20 mL headspace vial with screw cap. The cap was tightened, and the vial placed in the PAL system sample rack for analysis. As the objective of this

study was qualitative VOC profiling, each sample was analyzed in a single run without replicate measurements.

2.3 Analytical instrumentations

2.3.1 Headspace-SPME

For the HS-SPME method, the natural latex pillow samples were pre-incubated at 60 °C for 60 min with the agitation speed of 250 rpm to release the volatile compounds prior to extraction, and then the fiber was exposed in the headspace of the vial at 60 °C for 60 min for extraction. After the extraction of volatiles from the natural latex pillow samples onto the fiber, the analytes were thermally desorbed from the fiber in the injector port of the GC-MS for 15 min and transferred to the GC-MS column where volatile compounds were separated. After extraction and desorption, the SPME fiber was conditioned at 270 °C for 30 min the SPME conditioning module (PAL3RTC Auto Sampler Systems).

2.3.2 GC-MS condition

The characterization and identification of VOCs were performed using a 7890B gas chromatograph coupled with a 7000D tandem mass spectrometer (Agilent Technologies Inc., USA), equipped with a VF-WAXms capillary column (J&W Scientific, Berkshire, USA; 30 m × 0.25 mm i.d., 0.25 µm film thickness). Helium (UHP grade) was used as the carrier gas at a constant flow rate of 1.0 mL/min. Samples were introduced via a splitless injector maintained at 270 °C. The oven temperature program was set at 35 °C for 1 min, ramped at 5 °C/min to 250 °C, and held at the final temperature for 1 min. Mass spectra were acquired over the range of m/z 29–500 at a scan rate of 2 scans/s. MassHunter version 7 was used for GC–MS control and data acquisition.

Each VOC was tentatively identified by comparison of its EI mass spectrum with the National Institute of Standards and Technology (NIST) Mass Spectral Library, version 14, and Wiley version 10, using an acceptance criterion of match score ≥ 90%. The relative abundance of each detected compound was expressed as % of total peak area, calculated by dividing the peak area of an individual compound by the sum of all detected peak areas in the chromatogram and multiplying by 100. These values were used only to indicate the relative abundance of compounds within each sample and do not represent absolute concentrations.

As the present work was designed as a qualitative VOC screening study, no calibration curves, spiked standards, blank correction, or quantitative recovery experiments were performed. Likewise, repeatability parameters were not determined in this work.

3. Results and Discussion

A total of ten natural latex pillow samples were analysed for volatile organic compounds (VOCs) using headspace solid-phase microextraction coupled with gas chromatography–mass spectrometry (HS-SPME–GC/MS). This analytical technique enables solvent-free pre-concentration of VOCs directly from the sample headspace, followed by efficient chromatographic separation and mass spectral identification. Compound identification was performed by comparing the acquired mass spectra with the Wiley 10 and NIST 14 mass spectral libraries, with an acceptance criterion of match score ≥ 90%. The total ion chromatogram (TIC) obtained from sample P01 is presented in Figure 1 as a representative profile. The chromatogram shows a complex distribution of peaks with varying retention times and intensities, reflecting the diverse chemical nature and relative abundance of VOCs emitted from the sample. The major chemical classes identified included sulfur-containing compounds, aromatic compounds, aldehydes, ketones, terpenes, and hydrocarbons.

To better position the present work within the existing literature, a comparison with previous studies on VOC emissions from bedding, latex, and rubber-based materials is presented in Table 1. As shown, earlier studies have mainly focused on bedding products in general, raw rubber materials, or latex product development, whereas the present study specifically examines natural rubber latex pillows.

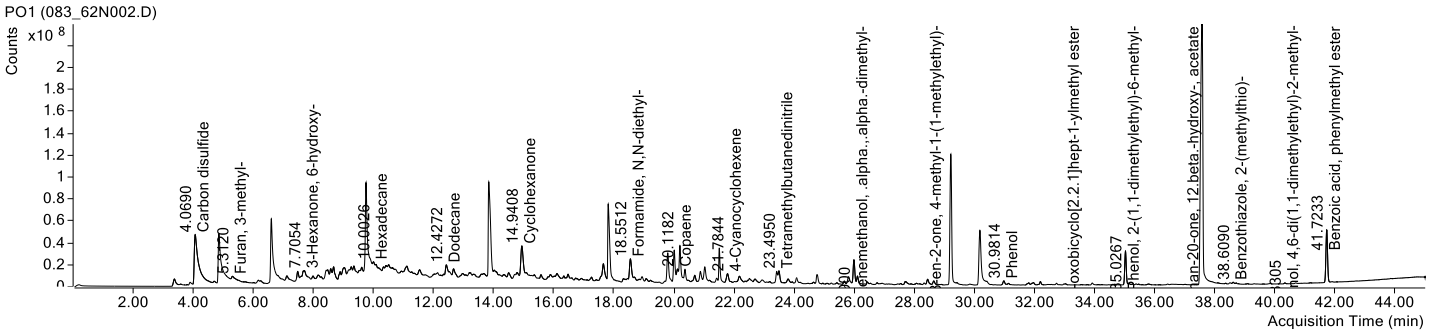


Figure 1 Representative total ion chromatogram (TIC) of volatile organic compounds (VOCs) from natural latex pillow sample P01 obtained using HS-SPME–GC/MS.

In addition to the within-sample VOC distribution, comparison with conventional pillow products reported in the literature provides further context for interpreting the VOC profile observed in the present study. Polyethylene-based pillows have

been shown to emit higher levels of aliphatic hydrocarbons, including tetradecane, toluene, and xylene, whereas the natural rubber latex pillows analysed in this study exhibited a distinct VOC profile dominated by sulfur-containing compounds, phenolic derivatives, and alcohols. This difference may reflect variations in raw materials, additives, and manufacturing processes between natural rubber latex and conventional synthetic pillow products. However, this comparison should be interpreted cautiously because it is literature-based and the products were evaluated under different analytical conditions.

Following these comparisons, the VOC profiles obtained from all samples were compiled and summarised in Table 2 for comparative evaluation and toxicological assessment. Table 2 presents the volatile organic compounds (VOCs) detected in natural rubber latex pillow samples, categorised by chemical group. For each compound, the molecular structure and formula, Globally Harmonized System (GHS) hazard pictograms, sample codes (with relative abundances expressed as % of total peak area), and potential health risks are presented. A more comprehensive summary of the detected VOCs, including chemical grouping, occurrence across samples, and relative abundance, is therefore provided to facilitate comparative interpretation.

Nitrogen-containing compounds were identified in several samples. Diethylamine, detected in P04, P06, and P08 (0.17–8.77%), is associated with severe skin and eye irritation or burns and respiratory damage. Triethylamine, present in P06 and P08 at trace levels (0.01–0.02%), is known to cause irritation to the eyes, skin, and respiratory tract.

Sulfur-containing compounds such as carbon disulfide and benzothiazole derivatives were among the most abundant VOCs detected, with documented neurotoxic, reproductive, and skin-sensitisation risks. These compounds are also likely associated with vulcanization chemistry and the degradation of sulfur-based accelerators and additives commonly used in rubber processing. In addition, several ketones, namely α-isomethylionone, 1-(4-tert-butylphenyl)propan-2-one, and 2(3H)-furanone, 5-heptyldihydro-, were primarily detected in P02 (≤ 1.81% of total VOCs). Although present at lower relative abundances, these compounds are classified as irritants and may intensify skin and respiratory irritation when present alongside sulfur-containing compounds. Moreover, the aldehyde 2-(4-tert-butylbenzyl)propionaldehyde detected in P02 presents further concern because of its potential to cause skin irritation, allergy, and reproductive toxicity. The co-occurrence of these chemical groups in specific samples suggests the possibility of additive or synergistic effects, particularly in sensitive individuals. In this context, the detected sulfur-containing compounds may reflect not only manufacturing residues but also progressive chemical changes occurring during material ageing and degradation.

Acidic compounds were detected across multiple samples, encompassing both aliphatic and aromatic acids. The most abundant, benzoic acid, phenylmethyl ester (P01, 2.54%), is a serious eye and respiratory irritant and poses long-term aquatic toxicity. Other acids, such as decanoic and dodecanoic acids, were linked to mild skin or respiratory irritation. Propanoic acid, 2-methyl-, 3-hydroxy-2,2,4-trimethylpentyl ester, while generally of low toxicity, may cause eye irritation. Acetic acid in P08 (1.12%) carries inhalation toxicity and can severely irritate the eyes, nose, and throat at higher concentrations, while nonanoic acid may also cause irritation at high exposure levels. Although each acid was detected at relatively low relative abundance, their combined presence could contribute to the cumulative sensory profile of the pillows and to overall inhalation risks.

Notably, the occurrence of acidic compounds, although generally less volatile than aromatic hydrocarbons, can significantly influence the toxicological profile of the samples. For example, acetic acid is a simple but corrosive carboxylic acid capable of irritating skin, eyes, and respiratory tract, with prolonged exposure causing discomfort and inflammation. Higher molecular weight acids such as hexanoic and octanoic acids, despite their natural occurrence, can produce strong odours and cause irritation upon contact. Some of these acids may also arise as degradation products, suggesting oxidative or hydrolytic processes within the material.

Alcohol compounds were also detected, adding to the complexity of the VOC profile. The predominant alcohol, 1-hexanol, 2-ethyl-, occurred in multiple samples at relatively high abundances. Although of low acute oral and dermal toxicity, it poses moderate inhalation risks. Linalool, a terpene alcohol found in fragrances, was also detected. While safe at low levels, linalool can act as a skin irritant and sensitiser, especially after oxidation. Polyfunctional alcohols such as 2-propanol, 1,1'-oxybis- and 2,2,4-trimethyl-1,3-pentanediol diisobutyrate were identified; both exhibit mild irritation potential, with the latter serving as a plasticiser in consumer products. The co-occurrence of alcohols with acidic and aromatic compounds suggests possible additive or synergistic irritant effects.

Alkanes were present at varying relative abundances. Heptane, while generally of low toxicity, can cause central nervous system (CNS) depression and mucous membrane irritation with repeated exposure. Higher molecular weight alkanes, such as tetradecane, showed low acute toxicity but mild irritation potential, and aspiration can lead to respiratory harm. Decane, although of low toxicity, may cause CNS depression at elevated levels. Halogenated alkanes such as methane, dichloro-, pose higher hazards, including respiratory irritation and cardiac effects. Branched-chain alkanes, such as octane, 3,6-dimethyl-, can cause skin and eye irritation and anaesthetic-like effects. Cyclic alkenes included both monocyclic and bicyclic structures. Furan, 3-methyl-, shares toxicological features with furan and is considered possibly carcinogenic to humans (IARC), as well as being an acute toxicant and irritant. 3-Cyclohexene-1-methanol, α,α,4-trimethyl-, (S)- is a GHS Category 2 irritant to skin and eyes. Bicyclic sesquiterpenes such as α-copaene

Table 1 Comparison of the present study with previous studies on VOC emissions from bedding, latex, and rubber-based materials.

Study	Material/Product	Analytical method	Main objective	Key findings	Distinction from the present study
Oshima et al. (2021)	Bedding products (pillows and mattresses)	VOC analysis of commercial products	Survey VOCs from household bedding items	Showed that bedding products can emit VOCs relevant to indoor exposure	Did not focus specifically on natural rubber latex pillows or provide compound-level hazard profiling
Kamarulzaman et al. (2019)	Natural rubber materials	SHS, DHS, HS-SPME, and μ-CTE coupled with GC-MS	Compare headspace techniques for VOC detection from natural rubber	Demonstrated suitability of HS-based methods for VOC recovery from rubber materials	Focused on extraction techniques and raw rubber, not finished pillow products or health-risk interpretation (PubMed) DOI: 10.1016/j.talanta.2018.09.019
Ramli et al. (latex pillow development)	Latex foam pillows	Product testing / materials characterisation	Develop and evaluate latex foam pillow properties	Addressed product development and physical properties of latex foam pillows	Did not provide detailed VOC profiling with GHS and potential health risks (ResearchGate) https://doi.org/10.1007/s42464-021-00130-7
Liu et al. (2025)	Latex pillows	GC-Orbitrap HRMS	Nontargeted screening of chemicals in latex pillows	Identified a broad range of volatile/semi-volatile compounds in multiple latex pillows	Broader nontargeted screening; the present study provides HS-SPME-GC/MS-based qualitative profiling with grouped occurrence and hazard-focused discussion (ScienceDirect) https://doi.org/10.1016/j.microc.2025.115275
Present study	Natural rubber latex pillows	HS-SPME-GC/MS	Qualitative profiling of VOCs and hazard interpretation	Identified key VOC groups, occurrence frequency, relative abundance, GHS pictograms, and potential health risks	Provides pillow-specific VOC profiling with integrated chemical and toxicological interpretation

Table 2 Summary of volatile organic compound (VOC) groups detected in natural rubber latex pillow samples, including molecular structures, GHS hazard classifications, sample occurrence with relative abundance (% of total peak area), and associated potential health risks.

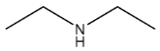
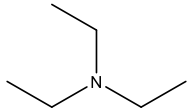
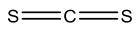
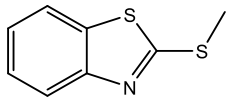
Compound group	Chemical structure and molecular formula	GHS pictograms	Sample codes (% of total peak area)	Potential Health Risks
1. Nitrogen-containing compounds				
Diethylamine	 $C_4H_{11}N$	 Flammable Corrosive Irritant	P04 (0.17%) P06 (0.50%) P08 (8.77%)	Severe skin and eye irritation/burns; respiratory damage
Triethylamine	 $C_6H_{15}N$	 Flammable Corrosive Acute Toxic	P06 (0.02%) P08 (0.01%)	Eye, skin, and respiratory tract irritation
2. Sulfur-containing compounds				
Carbon disulfide	 CS_2	 Flammable Irritant Health Hazard	P01 (6.30%) P02 (5.43%) P03 (10.83%) P04 (9.67%) P05 (5.73%) P06 (5.00%) P07 (9.14%) P08 (10.13%) P09 (7.00%) P10 (7.87%)	Neurotoxic; reproductive/skin sensitisation risks; high prevalence
2-(Methylmercapto)benzothiazole	 $C_8H_7NS_2$	 Irritant	P08 (1.37%) P10 (0.19%)	Skin/respiratory irritation; sensitisation; potential carcinogenicity/genotoxicity

Table 2 Summary of volatile organic compound (VOC) groups detected in natural rubber latex pillow samples, including molecular structures, GHS hazard classifications, sample occurrence with relative abundance (% of total peak area), and associated potential health risks (Continuous).

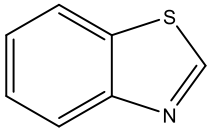
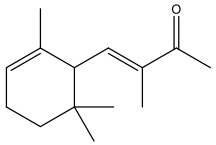
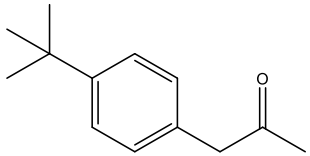
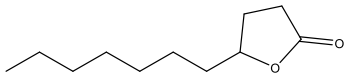
Compound group	Chemical structure and molecular formula	GHS pictograms	Sample codes (% of total peak area)	Potential Health Risks
Benzothiazole	 C_7H_5NS	 Acute Toxic Irritant	P01 (3.81%) P02 (8.34%) P03 (5.60%) P04 (7.14%) P05 (6.32%) P06 (3.62%) P07 (5.09%) P08 (2.70%) P09 (7.54%) P10 (5.36%)	Respiratory and dermal irritation
3. Ketones				
alpha-isomethylionone	 $C_{14}H_{22}O$	 Irritant Environmental Hazard	P02 (1.81%)	skin irritation and sensitization
1-(4-tert-Butylphenyl)propan-2-one	 $C_{13}H_{18}O$	 Irritant	P02 (0.14%)	Irritant; endocrine disruption potential; possible long-term effects
2(3H)-Furanone, 5-heptyldihydro-	 $C_{11}H_{20}O_2$	 Irritant	P02 (0.22%)	May cause mild skin and respiratory irritation

Table 2 Summary of volatile organic compound (VOC) groups detected in natural rubber latex pillow samples, including molecular structures, GHS hazard classifications, sample occurrence with relative abundance (% of total peak area), and associated potential health risks (Continuous).

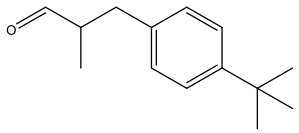
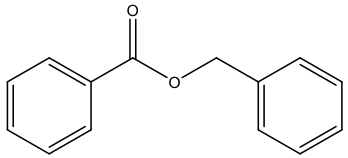
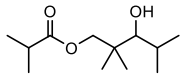
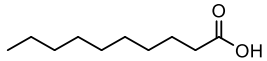
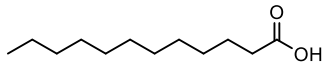
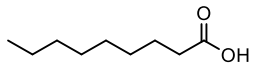
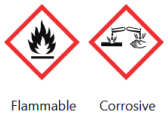
Compound group	Chemical structure and molecular formula	GHS pictograms	Sample codes (% of total peak area)	Potential Health Risks
4. Aldehydes compounds				
2-(4-tert-butylbenzyl)propionaldehyde (Lily aldehyde)	 $C_{14}H_{20}O$	 Health Hazard	P02 (1.29%)	Skin irritation; allergy; reproductive toxicity
5. Acids compounds				
Benzoic acid, phenylmethyl ester	 $C_{14}H_{12}O_2$	 Irritant Environmental Hazard	P01 (2.54%)	Serious eye irritation; respiratory irritation; toxic to aquatic life (long-term)
Propanoic acid, 2-methyl-, 3-hydroxy-2,2,4-trimethylpentyl ester	 $C_{12}H_{24}O_3$	Not classified under GHS	P03 (0.53%) P04 (0.35%) P09 (0.44%)	Low toxicity; possible eye irritation
Decanoic acid	 $C_{10}H_{20}O_2$	 Irritant	P04 (0.33%) P06 (0.44%)	May cause skin irritation
Dodecanoic acid	 $C_{12}H_{24}O_2$	 Corrosive Irritant	P04 (0.19%) P06 (0.13%)	Skin/respiratory irritation; may cause redness and discomfort
Nonanoic acid	 $C_9H_{18}O_2$	 Irritant	P07 (0.27%)	Low toxicity; possible irritant at high concentrations
Acetic acid	 $C_2H_4O_2$	 Flammable Corrosive	P08 (1.12%)	Slightly toxic by inhalation; 50 ppm causes severe eye/nose/throat irritation

Table 2 Summary of volatile organic compound (VOC) groups detected in natural rubber latex pillow samples, including molecular structures, GHS hazard classifications, sample occurrence with relative abundance (% of total peak area), and associated potential health risks (Continuous).

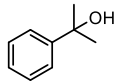
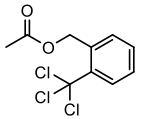
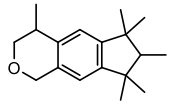
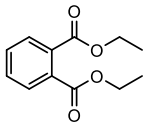
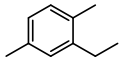
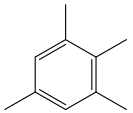
Compound group	Chemical structure and molecular formula	GHS pictograms	Sample codes (% of total peak area)	Potential Health Risks
6. Aromatics compounds				
Benzenemethanol, .alpha.,.alpha.-dimethyl-	 $C_9H_{12}O$	 Corrosive Irritant	P01 (1.20%) P02 (0.46%) P05 (0.74%) P07 (0.92%) P09 (0.69%) P10 (0.53%)	Harmful if swallowed; eye/respiratory/skin irritation; repeated contact may cause dryness/cracking
Benzenemethanol, .alpha.-(trichloromethyl)-, acetate	 $C_{10}H_9Cl_3O_2$	 Irritant	P02 (0.58%)	Skin/respiratory irritant; mild oral toxicity; may cause eye damage
Cyclopenta[g]-2-benzopyran, 1,3,4,6,7,8-hexahydro-4,6,6,7,8,8-hexamethyl (Galaxolide)	 $C_{18}H_{26}O$	 Environmental Hazard	P02 (0.09%)	Potential reproductive effects; environmentally persistent
Diethyl phthalate	 $C_{12}H_{14}O_4$	 Irritant	P01 (17.79%) P04 (0.12%) P06 (0.79%) P08 (0.35%)	Toxic if inhaled; may cause organ damage
Benzene, 2-ethyl-1,4-dimethyl-	 $C_{10}H_{14}$	 Flammable Corrosive Irritant	P10 (0.20%)	Low acute toxicity; irritant (eyes, skin, respiratory); chronic exposure risks
Benzene, 1,2,3,5-tetramethyl-	 $C_{10}H_{14}$	 Irritant	P10 (0.47%)	Irritant (skin, eyes, respiratory); prolonged exposure may cause dermatitis, nausea, dizziness, headaches; combustible

Table 2 Summary of volatile organic compound (VOC) groups detected in natural rubber latex pillow samples, including molecular structures, GHS hazard classifications, sample occurrence with relative abundance (% of total peak area), and associated potential health risks (Continuous).

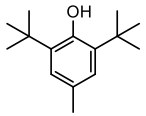
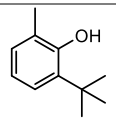
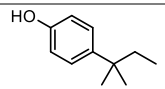
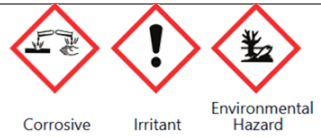
Compound group	Chemical structure and molecular formula	GHS pictograms	Sample codes (% of total peak area)	Potential Health Risks
2,6-bis (1,1-dimethylethyl)-4-methyl-phenol	 $C_{15}H_{24}O$	 Environmental Hazard	P01 (6.43%) P02 (4.87%) P03 (8.93%) P04 (4.78%) P05 (7.34%) P06 (5.44%) P07 (0.82%) P09 (2.60%) P10 (8.03%)	Low acute oral toxicity; skin/eye irritant; harmful if swallowed
Phenol, 2-(1,1-dimethylethyl)-6-methyl-	 $C_{11}H_{16}O$	 Corrosive Acute Toxic	P01 (1.50%) P02 (1.64%) P03 (3.00%) P04 (0.94%) P05 (2.12%) P06 (0.23%) P07 (0.61%) P08 (0.09%) P09 (0.51%) P10 (2.19 %)	Low general toxicity; corrosive/irritant (skin, eyes, respiratory); aquatic toxicity
Phenol, 4-(1,1-dimethylpropyl)-	 $C_{11}H_{16}O$	 Corrosive Irritant Environmental Hazard	P02 (0.22%) P04 (0.23%) P05 (0.31%) P06 (0.82%) P07 (1.20%) P08 (0.67%) P09 (0.12%) P10 (0.10%)	Low acute oral/dermal toxicity; causes severe skin burns and eye damage; toxic if inhaled

Table 2 Summary of volatile organic compound (VOC) groups detected in natural rubber latex pillow samples, including molecular structures, GHS hazard classifications, sample occurrence with relative abundance (% of total peak area), and associated potential health risks (Continuous).

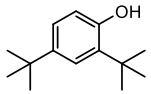
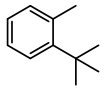
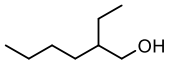
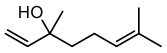
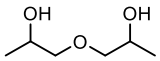
Compound group	Chemical structure and molecular formula	GHS pictograms	Sample codes (% of total peak area)	Potential Health Risks
Phenol, 2,4-bis(1,1-dimethylethyl)-	 $C_{14}H_{22}O$	 Irritant	P06 (0.10%) P07 (0.23%) P10 (0.29%)	Toxic natural secondary metabolite; also used as antioxidant
2-tert-Butyltoluene	 $C_{11}H_{16}$	 Flammable Irritant Environmental Hazard	P02 (0.40%) P03 (1.06%)	Harmful; skin/eye/respiratory irritant; harmful if swallowed or inhaled
7.Alcohols				
1-Hexanol, 2-ethyl-	 $C_8H_{18}O$	 Irritant	P01 (1.61 %) P02 (1.21%) P03 (1.99%) P04 (1.15%) P05 (1.74%) P06 (1.55%) P07 (1.58%) P08 (1.53%) P09 (1.95%) P10 (1.30%)	Low acute oral/dermal toxicity; moderate inhalation toxicity
Linalool	 $C_{10}H_{18}O$	 Irritant	P04 (0.92%)	Skin irritant; potential sensitisation upon oxidation
2-Propanol, 1,1'-oxybis-	 $C_6H_{14}O_3$	 Irritant	P04 (1.01%)	Low toxicity; used in cosmetics/fragrances/solvent; mild skin/eye irritant

Table 2 Summary of volatile organic compound (VOC) groups detected in natural rubber latex pillow samples, including molecular structures, GHS hazard classifications, sample occurrence with relative abundance (% of total peak area), and associated potential health risks (Continuous).

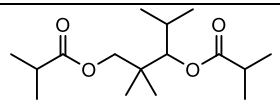
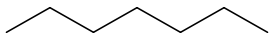
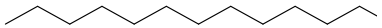
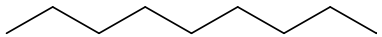
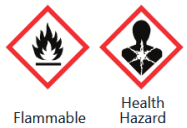
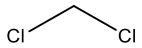
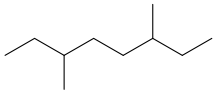
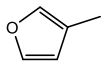
Compound group	Chemical structure and molecular formula	GHS pictograms	Sample codes (% of total peak area)	Potential Health Risks
2,2,4-Trimethyl-1,3-pentanediol diisobutyrate	 $C_{16}H_{30}O_4$	 Health Hazard	P08 (0.75%)	Low acute toxicity; not classified as acutely toxic
8.Alkanes				
Heptane	 C_7H_{16}	 Flammable Irritant Health Hazard Environmental Hazard	P03 (0.39%)	Low overall toxicity; acute/chronic exposure may cause CNS depression, mucous membrane irritation, neurobehavioral effects
Tetradecane	 $C_{14}H_{30}$	 Health Hazard	P04 (2.17%)	Low toxicity; skin/eye irritant; may be fatal if swallowed and aspirated
Decane	 $C_{10}H_{22}$	 Flammable Health Hazard	P05 (0.46%) P10 (0.91%)	Low toxicity; high levels may cause irritation, CNS depression, narcotic effects; harmful if aspirated
Methane, dichloro-	 CH_2Cl_2	 Health Hazard	P07 (0.57%)	Eye irritant; respiratory tract irritation; high levels may cause arrhythmia or cardiac arrest
Octane, 3,6-dimethyl-	 $C_{10}H_{22}$	 Flammable	P09 (0.08%)	Toxic; skin/eye irritant; may cause anaesthetic effects (drowsiness, dizziness)
9.Cyclic alkenes				
Furan, 3-methyl-	 C_5H_6O	 Acute Toxic Irritant	P01 (0.22%) P05 (0.35%)	Similar toxicity to furan (IARC: possibly carcinogenic to humans)

Table 2 Summary of volatile organic compound (VOC) groups detected in natural rubber latex pillow samples, including molecular structures, GHS hazard classifications, sample occurrence with relative abundance (% of total peak area), and associated potential health risks (Continuous).

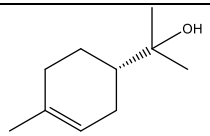
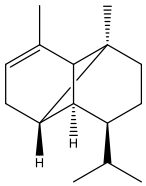
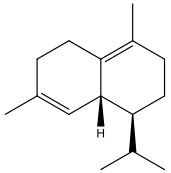
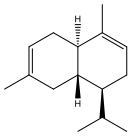
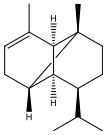
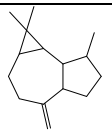
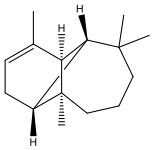
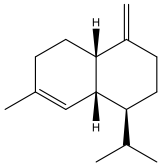
Compound group	Chemical structure and molecular formula	GHS pictograms	Sample codes (% of total peak area)	Potential Health Risks
3-Cyclohexene-1-methanol, .alpha.,.alpha.,4-trimethyl-, (S)-	 $C_{10}H_{18}O$	 Irritant	P02 (0.39%)	Causes skin irritation (GHS Category 2) and eye irritation (GHS Category 2)
.alfa.-Copaene	 $C_{15}H_{24}$	 Irritant Health Hazard Flammable	P02 (0.93%) P04 (0.36% P05 (1.68%) P07 (0.81%) P10 (1.30%)	Mixed antioxidant/cytotoxic profile; inhibits cell proliferation at high concentrations
.delta.-Cadinene	 $C_{15}H_{24}$	 Irritant Health Hazard	P01 (0.34%) P03 (0.26%) P04 (0.39%) P05 (0.51%) P07 (0.33%) P09 (0.31%) P10 (0.54%)	Low toxicity; some derivatives cause liver toxicity; skin/eye irritant; potential anticancer, antimicrobial, insecticidal
.beta.-Cadinene	 $C_{15}H_{24}$	Not classified under GHS	P02 (0.63%)	Irritant; allergy risk; hepatotoxic at high doses; antimicrobial potential
Copaene	 $C_{15}H_{24}$	 Flammable Irritant Health Hazard	P03 (0.56%)	Potential cytotoxicity (high concentrations)

Table 2 Summary of volatile organic compound (VOC) groups detected in natural rubber latex pillow samples, including molecular structures, GHS hazard classifications, sample occurrence with relative abundance (% of total peak area), and associated potential health risks (Continuous).

Compound group	**Chemical structure and molecular formula**	**GHS pictograms**	**Sample codes (% of total peak area)**	**Potential Health Risks**
Aromadendrene	 $C_{15}H_{24}$		P08 (0.83%)	Generally safe at typical levels; concentrated forms may be irritant/toxic
Tricyclo[5.4.0.0(2,8)]undec-9-ene, 2,6,6,9-tetramethyl-, (1R,2S,7R,8R)-	 $C_{15}H_{24}$	Not classified under GHS	P08 (0.83%)	Possible skin/eye irritation; avoid contact
gamma.-Muurolene	 $C_{15}H_{24}$	Not classified under GHS	P10 (0.15%)	Potential risks remain unclear; further toxicological studies required.

and δ-cadinene were also detected. α-Copaene has both antioxidant and cytotoxic effects, potentially inhibiting cell proliferation at high concentrations. δ-cadinene is of low acute toxicity, though some derivatives are hepatotoxic; it is also a mild irritant with potential anticancer, antimicrobial, and insecticidal properties.

Overall, the coexistence of diverse VOC groups including nitrogen-, sulfur-, oxygen-, and hydrocarbon-based compounds indicated a chemically complex environment within natural rubber pillow products. Such mixtures may present additive or synergistic toxicological effects, underscoring the need for comprehensive hazard assessments, particularly for products intended for prolonged human contact.

Building upon the compositional insights presented in Table 2, the frequency distribution of VOC occurrences across samples (Figure 2) further illustrates the chemical profile of natural rubber latex pillows. By integrating both concentration and occurrence data, it becomes evident that sulfur-containing compounds, phenolic derivatives, and alcohols are not only dominant in abundance but also highly prevalent across products, making them key chemical markers for VOC characterisation in these materials.

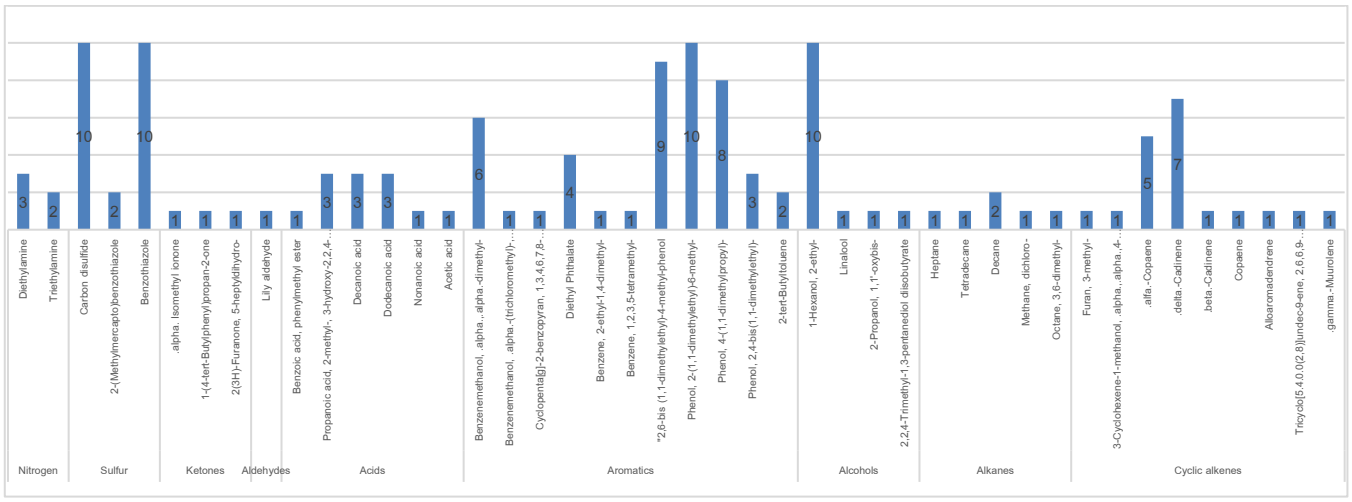


Figure 2 Distribution of volatile organic compounds (VOCs) detected in natural rubber latex pillow samples, classified by chemical groups. The y-axis represents the number of samples in which each compound was detected, while the x-axis lists individual compounds grouped under their respective chemical classes.

From a health perspective, inhalation during sleep is likely to be the most relevant exposure pathway, since pillows are used for prolonged periods in close proximity to the breathing zone. Temperature and duration of use may also influence VOC emissions through enhanced volatilisation, off-gassing, and material ageing or degradation. However, these factors were not specifically evaluated in the present study and should be investigated in future work.

The present findings are also relevant in the context of product safety and regulatory assessment. Frameworks such as the EU Ecolabel criteria for bed mattresses and latex foam, together with ISO 16000-based emission testing approaches, provide useful benchmarks for future studies on VOC emissions from bedding materials. Under the EU Ecolabel criteria for latex foam, total VOC emissions are limited to 0.5 mg/m³, and carbon disulfide is specifically limited to 0.02 mg/m³ under standardised chamber-based testing conditions (European Commission, 2014). Since the present work was designed as a qualitative VOC profiling study using HS-SPME–GC/MS, the reported VOC data should be interpreted as preliminary qualitative to semi-quantitative information rather than chamber-based quantitative emission concentrations.

In addition to compound identification, the occurrence frequency of VOCs across the ten samples is illustrated in Figure 2, highlighting the most recurrent VOC markers and inter-sample variability. Sulfur-containing compounds, phenolic derivatives, and alcohols were among the most prevalent groups detected across the analysed products. This distribution pattern also helps distinguish compounds that were consistently detected from those that appeared only in selected samples, suggesting differences in raw materials, additives, or manufacturing conditions.

4. Conclusion

Multiple volatile organic compounds (VOCs) were detected in natural rubber pillow samples, including sulfur-containing compounds, phthalates, amines, alcohols, and aromatic antioxidants. Notably, substances such as carbon disulfide, diethyl phthalate, and butylated hydroxytoluene (BHT) are associated with potential health risks, including neurotoxicity, endocrine disruption, and respiratory irritation. In addition, naturally occurring terpenes may undergo indoor chemical reactions, leading to the formation of secondary pollutants.

Given that latex pillows are used in proximity to the human respiratory zone for extended periods during sleep, these VOC

emissions may contribute to continuous indoor exposure, particularly in poorly ventilated environments. The co-occurrence of multiple VOCs highlights the importance of comprehensive safety evaluations for latex-based consumer products intended for prolonged human contact.

From a manufacturing perspective, the findings suggest that VOC emissions could be reduced through process optimization, such as improving washing and post-curing steps to remove residual chemicals, selecting low-emission additives (e.g., alternative antioxidants and plasticizers), and optimizing vulcanization conditions to minimize sulfur-related byproducts. The adoption of eco-design principles and compliance with VOC emission standards, such as eco-label criteria, may further enhance product safety and environmental performance. This study provides essential baseline data for VOC profiles in commercially available natural latex pillows, which can be used to inform manufacturers, consumers, and policymakers.

This study provides essential baseline data on VOC profiles in commercially available natural latex pillows, which can support manufacturers, regulators, and consumers in decision-making. However, the study was limited to semi-quantitative analysis using a single sampling technique. Future research should focus on quantitative emission measurements, long-term exposure assessment under real indoor conditions, and the evaluation of alternative raw materials or green manufacturing technologies to reduce VOC emissions.

5. Acknowledgments

The authors gratefully acknowledge the Office of Scientific Instrument and Testing, Prince of Songkla University, for providing laboratory facilities and technical support. Appreciation was also extended to the Natural Rubber Innovation Research Institute, Prince of Songkla University, for supplying the rubber pillow samples used in this study.

6. References

Agatonovic-Kustrin, S., Gegechkori, V., Kobakhidze, T. and Morton, D. 2023. Solid-phase microextraction techniques and application in food and horticultural crops. **Molecules** 28(19): 1-14.

Capíková, A., Tesařová, D., Hlavaty, J., Ekielski, A. and Mishra, P.K. 2019. Estimation of volatile organic compounds (VOCs) and human health risk assessment of simulated indoor environment consisting of upholstered furniture made of commercially available foams. **Advances in Polymer Technology** 2019(1): 1-10.

Caroprese, A., Gabbanini, S., Beltramini, C., Lucchi, E. and Valgimigli, L. 2009. HS‐SPME‐GC‐MS analysis of body odor to test the efficacy of foot deodorant formulations. **Skin Research and Technology** 15(4): 503-510.

Chen, X., Zhang, B., Wang, D., Chen, L., Du, Z. and Wu, Y. 2022. Traceability of VOCs in tire inner liner by chromatography-mass spectrometry. **Environmental Science and Pollution Research** 29(7): 9685-9692.

European Commission. 2014. **Commission Decision 2014/391/EU of 23 June 2014 establishing the ecological criteria for the award of the EU Ecolabel for bed mattresses**. Official Journal of the European Union. Available Source: https://www.eur-lex.europa.eu/legalcontent/EN/TXT/?uri=CELEX:02014D0391-20220718, August 24, 2025.

European Commission. 2014. **EU Ecolabel bed mattresses: User manual**. Official Journal of the European Union. Available Source: https://api.eublomsten.dk/api/docs/CriteriaDocumentFiles/1008, March 20, 2026.

Idris, N.F., Le-Minh, N., Hayes, J.E. and Stuetz, R.M. 2022. Performance of wet scrubbers to remove VOCs from rubber emissions. **Journal of Environmental Management** 305: 1-13.

Jeleń, H.H. 2006. Solid-phase microextraction in the analysis of food taints and off-flavors. **Journal of chromatographic science** 44(7): 399-415.

Kamarulzaman, N.H., Idris, N.F. and Nor, Z.M. 2012. Characteristics of odour concentration from rubber processing factories via olfactometry technique. **Chemical Engineering Transactions** 30: 121-126.

Kamarulzaman, N.H., Le-Minh, N. and Stuetz, R.M. 2019. Identification of VOCs from natural rubber by different headspace techniques coupled using GC-MS. **Talanta** 191: 535-544.

Khalid, M. and Abdollahi, M. 2021. Environmental distribution of personal care products and their effects on human health. **Iranian journal of pharmaceutical research** 20(1): 216-253.

Liu, J.-Q., Han, H.-L., Zhang, Q., Ding, S.-N., Wang, Z.-J. and Lv, Q. 2025. Nontargeted analysis of potential chemicals in latex pillows using gas chromatography–Orbitrap high resolution mass spectrometry. **Microchemical Journal** 218: 115275.

Nornanysya, F.K., Aminah, S.M. and Samsuri, A. 2013. Odourless natural rubber (ONR). **Journal of Rubber Research** 16(1): 15-35.

Oshima, N., Tahara, M., Sakai, S. and Ikarashi, Y. 2021. Analysis of volatile organic compounds emitted from bedding products. **BPB Reports** 4(6): 182-192.

Pajarito, B.B., Castañeda, K.C., Jeresano, S.D.M. and Repoquit, D.A.N. 2018. Reduction of offensive odor from natural rubber using zinc‐modified bentonite. **Advances in Materials Science and Engineering** 2018(1): 1-8.

Ramírez, N., Marcé, R.M. and Borrull, F. 2010. Development of a thermal desorption-gas chromatography–mass spectrometry method for determining personal care products in air. **Journal of Chromatography A** 1217(26): 4430-4438.

Ramli, R., Chai, A.B., Kamaruddin, S., Ho, J.H., Mohd. Rasdi, F.R. and De Focatiis, D.S.A. 2021. Development of latex foam pillows from deproteinized natural rubber latex. **Journal of Rubber Research** 24(4): 615-630.

Sakdapipanich, J. and Insom, K. 2006. High-resolution gas chromatography-mass spectrometry - Characterization and mechanism to generate the obnoxious odor in natural rubber. **Kautschuk Gummi Kunststoffe rubberpoint** 59(7-8): 382-387.

Shinoda, R., Takahashi, K., Ichikawa, S., Wakayama, M., Kobayashi, A., Miyagawa, S. and Uchimura, T. 2020. Using SPME-GC/REMPI-TOFMS to measure the volatile odor-active compounds in freshly cooked rice. **American Chemical Society Omega** 5(32): 20638-20642.

Unites Stated. Environmental Protection Agency. 2023. **Volatile organic compounds' impact on indoor air quality**. Available Source: https://www.epa.gov/indoor-air-quality-iaq/volatile-organic-compounds-impact-indoor-air-quality, March 23, 2026.

World Health Organization. 2010. **WHO guidelines for indoor air quality: Selected pollutants**. WHO Regional Office for Europe. Available Source:https://www.who.int/publications/i/item/9789289002134, March 23, 2026.

Recent Science and Technology 2026, Vol. 18(3): e270555

Recent Science and Technology

Journal homepage: https:// www.tci-thaijo.org/index.php/rmutsvrj/index

ISSN: 3057-0786 (Online)

Research Article

Room-Temperature Vulcanization Time Controls Self-Crosslinking-Driven Self-Healing Behavior in Natural Rubber Sheets

Nasruldin Masae [a] and Korn Taksapattanakul [b *]

[a] *Faculty of Science and Technology, PNU Wittayanusorn School, Princess of Naradhiwas University, Narathiwat 96000, Thailand.*

[b] *Faculty of Science and Technology, Princess of Naradhiwas University, Narathiwat 96000, Thailand.*

Article history:

Received: 2026-01-18
Revised: 2026-05-10
Accepted: 2026-05-13

Keywords:

Self-healing rubber sheets;
Sulfur curing system;
Controlled crosslinking reaction;
Natural rubber;
Fourier transform infrared spectroscopy

ABSTRACT

This study investigated the preparation of natural rubber sheets with self-crosslinking-driven self-healing behavior under controlled curing conditions at room temperature. The work aimed to develop a simpler and more practical approach for producing recoverable rubber materials without complex chemical modification or external heating. Natural rubber sheets were prepared using a sulfur vulcanization casting process under different curing temperatures and curing times. The effects of curing conditions on network formation, swelling behavior, crosslink density, and mechanical recovery were evaluated. Fourier transform infrared spectroscopy was used to monitor changes in the chemical structure during vulcanization. The results showed that increasing curing temperature and curing time promoted sulfur crosslink formation within the rubber network. However, curing at 30 ± 5 °C preserved a greater amount of remaining unsaturated bonds and maintained lower crosslink density, which favored polymer-chain mobility during the healing process. The swelling analysis confirmed the gradual development of a denser network structure with increasing curing severity. Mechanical testing demonstrated progressive recovery of tensile properties after the damaged samples were rejoined and healed under room-temperature conditions. Healing efficiency increased continuously with healing time, indicating gradual interfacial recovery through continued network rearrangement and self-crosslinking reactions. The findings suggested that controlled room-temperature curing provided a suitable balance between crosslink formation and chain mobility, allowing recovery behavior to occur without additional external stimuli. This study demonstrated a simple and low-temperature strategy for preparing natural rubber sheets with recoverable mechanical performance and provided useful information for the future development of functional and sustainable rubber materials.

© 2026 Masae, N. and Taksapattanakul, K. Recent Science and Technology published by Rajamangala University of Technology Srivijaya

1. Introduction

Natural rubber had played an important role in human technological development long before the formal establishment of polymer science. Prior to the development of synthetic rubber in petrochemical laboratories, plants naturally produced a complex polymer known as cis-1,4-polyisoprene. This material, commonly referred to as natural rubber (NR), remained an essential raw material in modern industry. It had been widely utilized in more than 40,000 products, including over 400 critical medical devices. Despite extensive efforts to develop synthetic alternatives, commercial natural rubber production continued to rely predominantly on a single plant species, the Brazilian rubber tree, *Hevea brasiliensis* (Mooibroek and Cornish, 2000).

Natural rubber remained widely used because of its unique molecular structure. Its regular cis-1,4 configuration and very high molecular weight, often exceeding one million daltons, provided a combination of elasticity, strength, and durability that was difficult for synthetic rubbers to achieve. These molecular characteristics contributed to several important properties, including high green strength, excellent resistance to deformation, strong crack-growth resistance, and low heat build-up after vulcanization. As a result, natural rubber was extensively applied in demanding products such as tires, seals,

* **Corresponding author.**

E-mail address: *korn.t@pnu.ac.th*

Cite this article as: Masae, N. and Taksapattanakul, K. 2026. Room-Temperature Vulcanization Time Controls Self-Crosslinking-Driven Self-Healing Behavior in Natural Rubber Sheets. **Recent Science and Technology** 18(3): e270555

https://doi.org/10.65411/rst.2026.270555

vibration isolators, and medical gloves (Nimpaiboon and Sakdapipanich, 2013). These superior properties were also associated with the efficient biological structure of *Hevea brasiliensis*. The plant possessed a thick and smooth bark together with a highly developed latex transport system. This structure enabled the continuous production, transport, and storage of rubber particles within a water-based latex medium. The organized latex system not only supported high productivity but also contributed to the high purity and favorable processing characteristics of natural rubber, making it more advantageous than many other rubber-producing plants (Omar *et al*., 2025).

This biological efficiency explained why natural rubber continued to play an essential role even after the widespread development of synthetic polymers. Despite these advantages, the molecular structure of natural rubber also introduced several limitations. The large number of unsaturated double bonds along the polymer backbone made the material sensitive to heat, oxygen, oils, and ozone, which restricted its application under severe environmental conditions. To address these issues, many studies investigated chemical modification methods, particularly epoxidation and hydrogenation. These modifications improved the resistance of natural rubber to heat, oil, and oxidative aging while preserving its mechanical performance, resulting in materials with enhanced durability and longer service life (Ngudsuntear *et al*., 2022).

Over time, research on natural rubber evolved from improving conventional performance toward developing advanced and sustainable functions. Inspired by biological systems capable of self-repair, researchers began to design natural rubber as a self-healing material. Various reversible interactions, including dynamic sulfur bonds, ionic interactions, coordination bonds, and vitrimer-type networks, were incorporated into rubber structures (Trinh *et al*., 2023). These reversible systems enabled damaged rubber materials to recover their properties either autonomously or under external stimulation such as heat. Consequently, self-healing rubber materials showed improved durability, extended service life, and reduced material waste (Hernández *et al*., 2016; Boden *et al*., 2022; Olejnik and Mašek, 2023).

Previous studies demonstrated a progressive development in self-healing strategies for natural rubber (NR) and epoxidized natural rubber (ENR). Rather than relying on a single mechanism, researchers explored a wide range of reversible network designs based on sulfur chemistry, cross-link density control, supramolecular interactions, sacrificial networks, vitrimer chemistry, and hybrid filler systems. Each approach provided distinct advantages and limitations in terms of healing performance, mechanical strength, processing complexity, and industrial applicability. Early investigations showed that self-healing behavior could be introduced into vulcanized rubber without major changes to conventional processing methods. Hernández *et al*. (2016) reported that sulfur-crosslinked networks containing disulfide and polysulfide bonds were capable of bond dissociation and recombination under thermal or mechanical stimulation. This approach preserved acceptable mechanical strength and remained compatible with existing industrial vulcanization processes, although high healing temperatures were generally required and recyclability remained limited.

Subsequent studies highlighted the important role of cross-link density in determining healing efficiency. Boden *et al*. (2022) demonstrated that an optimum cross-link density was necessary to achieve a balance between mechanical performance and chain mobility. Excessive cross-linking restricted polymer-chain movement and significantly reduced healing ability, emphasizing the need for precise structural control. Simpler self-healing systems were also investigated. Rahman *et al*. (2013) found that lightly vulcanized NR and ENR could exhibit healing through chain diffusion and surface adhesion without the addition of specific healing agents. Although healing could occur at room temperature, the resulting mechanical properties were relatively low, which limited their practical application. Chemical modification further broadened the range of self-healing designs. Olejnik and Mašek (2023) reviewed several reversible chemistries, including disulfide exchange, Diels–Alder reactions, imine bonds, ester exchange reactions, and vitrimer networks. These systems improved recyclability and sustainability; however, they often required more complex synthesis routes and elevated healing temperatures. Supramolecular strategies enabled faster healing under mild conditions. Gong *et al*. (2022) developed ENR systems containing ionic and coordination interactions, which provided efficient healing together with balanced mechanical performance. Nevertheless, these systems remained sensitive to environmental factors such as humidity.

Hybrid systems combining fillers with dynamic polymer networks showed strong potential for practical applications. Supramaniam *et al*. (2022) incorporated zinc oxide–cellulose nanofibers into ENR matrices, improving mechanical reinforcement while maintaining heat-responsive healing capability. This concept was successfully demonstrated in self-healing rubber gloves, although uniform filler dispersion remained challenging. Self-healing concepts were also extended beyond conventional rubber products. Zhao *et al*. (2022) developed starch–NR latex hydrogels with high stretchability and toughness for wearable electronic devices. However, their limited thermal resistance and load-bearing capability restricted broader applications.

For high-strength applications, sacrificial network structures were introduced. Mandal *et al*. (2023) designed ENR systems containing ionic sacrificial bonds that effectively dissipated energy and promoted healing, resulting in very high tensile strength. Despite these advantages, the synthesis process remained relatively complex and the materials were sensitive to

environmental conditions. More advanced multifunctional systems were later reported. Yan *et al*. (2024) developed self-healing NR-based strain sensors using reversible bonding and conductive components, achieving stable sensing performance even after repeated damage. However, high production cost and complicated fabrication procedures limited their large-scale application. Other studies focused on improving healing speed and recyclability. Kong *et al*. (2022) incorporated dynamic disulfide and ester bonds into ENR systems and achieved nearly complete healing efficiency. Nevertheless, the systems still required heating and involved relatively high material costs. Additional reinforcement using fillers such as halloysite nanotubes further enhanced both mechanical and healing properties when the filler concentration was carefully optimized (Rehman *et al*., 2024). Sustainability-oriented approaches also gained increasing attention. Han *et al*. (2023) combined ENR with bio-based chitosan to produce recyclable and self-healing rubber materials. Although these materials offered environmental advantages, they exhibited moderate mechanical strength and sensitivity to moisture.

Overall, previous studies demonstrated that effective self-healing behavior in NR and ENR could be achieved through the integration of reversible bonding mechanisms with carefully controlled network structures. Sulfur-based and supramolecular systems provided good industrial compatibility and room-temperature healing capability, whereas vitrimer and sacrificial network systems offered improved strength and recyclability. Among the reported approaches, hybrid systems integrating dynamic reversible chemistry with nano-scale reinforcement appeared to provide the most promising balance between mechanical performance, healing efficiency, and sustainability for future self-healing rubber materials.

Although many previous studies investigated self-healing behavior in natural rubber and epoxidized natural rubber, most reported systems still required high healing temperatures or complex chemical modification processes. Moreover, several preparation methods involved complicated procedures that limited their suitability for large-scale industrial applications. Based on earlier findings, existing self-healing rubber systems were often associated with high production cost, limited scalability, and difficult processing conditions. To overcome these limitations, the present study investigated a simpler and more cost-effective approach for preparing self-healing natural rubber materials. The rubber sheets were prepared at room temperature through a casting process that allowed self-crosslinking vulcanization to occur under ambient conditions. The vulcanization behavior was controlled by curing temperature and curing time, which influenced the formation of the crosslinked rubber network. In addition, the effect of curing temperature and curing time on crosslink development and self-healing performance at room temperature was systematically evaluated. This approach was proposed as a practical and scalable alternative for the future development of self-healing natural rubber materials.

2. Materials and Methods

2.1 Preparation of pre-vulcanized natural rubber latex samples

In this study, pre-vulcanized natural rubber latex samples were prepared. The latex, commonly used in rubber product manufacturing, contained several chemical components (Table 1). Each chemical was added step by step and mixed for 2 minutes at a stirring speed of 50 rpm. This process produced pre-vulcanized natural rubber latex.

Table 1 Chemical formulation that was used to prepare pre-vulcanized natural rubber latex.

Materials	Parts per hundred rubber (phr)
Natural rubber latex	100
50% Zinc oxide dispersion	3.0 ± 0.2
50% Sulfur dispersion	1.5 ± 0.2
50% ZMBT, Zinc 2-Mercaptobenzo-thiazole dispersion	1.0 ± 0.2
50% ZDEC, Zinc Diethyldithiocarbamate dispersion	1.0 ± 0.2

2.2 Preparation of natural rubber sheets via controlled crosslinking through a casting process

Pre-vulcanized natural rubber latex was prepared by mixing natural rubber latex with chemical additives at 30 ± 5°C (room temperature). The mixture was poured into molds to form sheets with a thickness of 3 mm. Drying and vulcanization through controlled crosslinking were carried out using two different methods. In the first method, the samples were cured step by step in a hot air oven at 30°C, 40°C, 50°C, and 60°C, with each temperature maintained for 7 days. This approach was used to study how temperature influenced the development of crosslinking in the rubber structure. In the second method, the filled molds were kept at 30 ± 5°C (room temperature) for 7 days under UV light (fluorescent light irradiation, 480-570 nm visible light range) and allowed to dry, followed by an additional resting period of 49 days. This approach was used to study how curing time affected network formation and the self-healing behavior of the vulcanization system.

2.3 Fourier transforms infrared spectroscopy (FT-IR) analysis of crosslinking reactions

The rubber samples were cut into 1 cm x 1 cm pieces and analyzed using the attenuated total reflection (ATR) mode on a Bruker Tensor spectrometer. The spectra were recorded across a wavenumber range of 550-4200 cm^{-1} with a resolution of 2 cm^{-1}. The data were processed using OPUS software, and absorbance was reported in arbitrary units (a.u.) as a function

of wavenumber (cm^{-1}). For FT-IR analysis, the spectra were first aligned using linear interpolation at a resolution of 16 cm^{-1}. Baseline correction was performed with a first-order polynomial for 10 iterations, followed by min-max normalization. Finally, peak positions and their corresponding areas were identified and analyzed using OriginPro software.

The conversion of rubber measured by FT-IR was usually calculated by comparing the area of a reactive peak with that of a stable reference peak, using the following formulas (Gunasekaran *et al*., 2007; Chakraborty *et al*., 2007):

$$Area\ peak\ ratio = \frac{A_t}{A_0} \quad (1)$$

where A_t is the area peak at curing time and temperature

A_0 is the initial area peak of reference band

The peak area in the range of 1495-1729 cm^{-1}, corresponding to C=C bonds (Coran, 1965; Lu and Hsu, 1987), was analyzed together with the peak areas at 942-1175 cm^{-1} and 698-786 cm^{-1}, which were attributed to C-S bonds (Coran, 1965; Lu and Hsu, 1987).

2.4 Evaluation of swelling behavior and crosslink density properties

A controlled crosslinking process was applied to develop a model for self-healing behavior. The effects of different curing time and temperatures on the sulfur crosslinking ability of the material were examined. Crosslink density was calculated using the Flory-Rehner equation and rubber elasticity theory, while swelling behavior was measured following ASTM D3616-95.

2.4.1 Swelling behavior analysis

The samples were cut into small pieces and weighed, with masses ranging from 0.35 to 0.45 g. Each piece was placed in a sealed container with 25 mL of toluene at 30 ± 5 °C for 24 hours. The mass of each sample was recorded before soaking (dry state) and after absorbing the solvent (swollen state). After the swelling period, the samples were removed, gently wiped with tissue paper to remove excess solvent, and weighed again. The swelling percentage at time (Q_t) was then calculated using the standard formula, following ASTM D3616-95 and the method described by Kumnuantip and Sombatsompop (2003).

$$Q_t = \frac{(W_t - W_o)/W_o}{M_W} \times 100 \quad (2)$$

where W_o is the weight of the dry sample, W_t is the weight of the swollen sample, and M_W is the molar mass of toluene (92.14 g mol^{-1}).

2.4.2 Determination of crosslink density using the swelling index

Swelling index, the crosslink density of the samples was calculated using the Flory-Rehner equation (Xu *et al*., 2016; Kumnuantip and Sombatsompop, 2003; Flory and Rehner, 1943) as shown below:

$$-In(1-V_r) - V_r - \chi V_r^2 = 2V_s\eta_{swell}\left(V_r^{1/3} - \frac{2V_r}{f}\right) \quad (3)$$

where V_r is the volume fraction of rubber in the swollen gel, χ is the rubber-toluene solvent interaction parameter (0.3795), V_s is the molar volume of the toluene (106.2 $cm^3 \cdot mol^{-1}$), η_{swell} is the cross-link density of the rubber ($mol \cdot cm^{-3}$), and f is the functionality of the crosslinks (being 4 for the sulfur curing system).

$$V_r = \frac{(W_d - W_f)/\rho_r}{(W_d - W_f)/\rho_r + (W_s - W_d)/\rho_s} \quad (4)$$

where W_d is the weight of the de-swollen sample, W_f is the weight of the filler in the compound (0, non-filled system (Xu *et al*., 2016)), W_s is the weight of the swollen sample, and ρ_s is the density of the toluene solvent (0.87 g/cm^3), and ρ_r is the density of the rubber (0.91 g/cm^3).

2.5 Tensile properties characterization

Stress-strain behavior of a natural rubber sheet: tensile tests were carried out using a tensile testing machine (model H10KS, Hounsfield Test Equipment, Tinius Olsen Ltd., UK). Test specimens were prepared using die D in accordance with ASTM D412. The tests were performed on rubber sheets with a thickness of 3 mm at a crosshead speed of 50 ± 5 mm/min. Tensile testing was conducted following ASTM D412 to evaluate the mechanical properties of the rubber samples. Three specimens were prepared from rubber sheets through a casting process with a thickness of 3 mm and cured at 30 ± 5 °C (room temperature) for 7 days under UV light (fluorescent light irradiation, 480-570 nm visible light range) and allowed to dry. After curing and drying for 7 days, the natural rubber sheet samples were cut into two pieces using a clean blade to obtain surfaces without additional surface treatment for the self-healing test. The cut surfaces were immediately aligned and manually brought into close contact to ensure proper interface matching during the healing process. No external pressure was applied during healing, and the rejoined samples were maintained at 30 ± 5 °C (room temperature, under UV light (fluorescent light irradiation, 480-570 nm visible light range)) for healing periods ranging from 24 to 120 h. During this period, self-crosslinking occurred at the rejoined interface between the two surfaces, leading to the healing of the damaged region. The rejoined samples were subsequently subjected to uniaxial tensile loading until failure, and the tensile strength at break was recorded.

$$TS = \sigma = \frac{F}{A} \quad (5)$$

where TS is tensile strength at break, σ is Uniaxial stress (N/m^2 or Pa), F is the applied load (N), and A is the original cross-sectional area (m^2)

2.6 Young's modulus in the linear elastic region

At low strain, the tensile behavior of the natural rubber sheets followed Hooke's law. The modulus of elasticity, or Young's modulus, was calculated from the slope of the stress-strain curve in the linear, elastic region, as shown in Eq. (6) (Roylance, 2001; Treloar, 1975).

$$E = \frac{Stress}{Strain} = \frac{\sigma}{\varepsilon} = slope = \frac{\Delta\sigma}{\Delta\varepsilon} \quad (6)$$

where E is Young's modulus or modulus of elasticity, σ is stress (MPa), and ε is strain

2.7 Healing efficiency

Healing efficiency was evaluated by comparing the tensile strength at break obtained from the stress–strain curves of the healed samples with that of the original samples, following the method reported by Xu *et al*. (2016), as shown below:

$$Healing\ efficiency\ (\%) = \frac{TS_{after\ healing}}{TS_{before\ healing}} \times 100 \quad (7)$$

where $TS_{after\ healing}$ is tensile strength at break after healing

$TS_{before\ healing}$ is tensile strength at break before healing

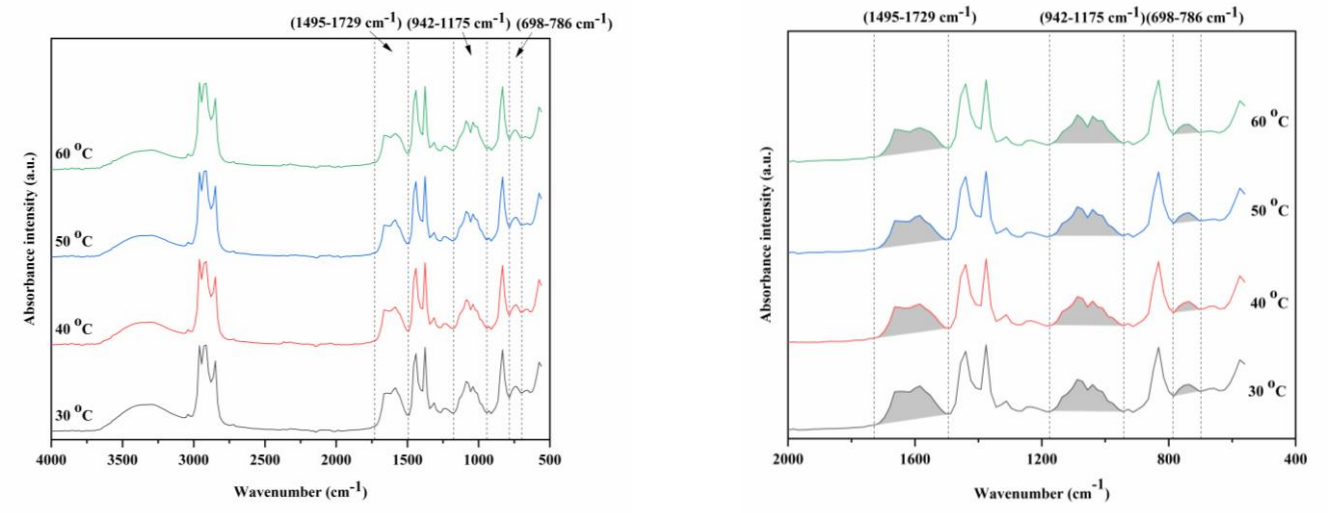
3. Results and Discussion

3.1 Effect of curing temperature and curing time on crosslinking reaction of natural rubber sheets

The natural rubber sheets were prepared using a controlled crosslinking approach through sulfur vulcanization.

The crosslinking reaction primarily occurred at the carbon–carbon double bonds (C=C) along the natural rubber chains. Fourier transform infrared (FT-IR) spectroscopy was employed to investigate the changes in the characteristic functional groups associated with the vulcanization process.

The FT-IR spectra (Figure 1) together with the peak area analysis (Figure 2) revealed significant changes after curing under different temperature conditions. The absorbance peak (Figure 1) and peak area in the range of 1495-1729 cm^{-1} (Figure 2(c)), corresponding to the C=C bonds (Coran, 1965; Lu and Hsu, 1987), gradually decreased as the curing temperature increased. In contrast, the absorbance peaks (Figure 1) and peak areas at 942-1175 cm^{-1} (Figure 2(b)) and 698-786 cm^{-1} (Figure 2(a)), attributed to C-S bonds (Coran, 1965; Lu and Hsu, 1987), increased with increasing curing temperature. Furthermore, the peak area ratios presented in Figure 2(d) supported the same trend. These results indicated that higher curing temperatures promoted sulfur crosslink formation and accelerated the vulcanization reaction within the natural rubber network.



(a) FT-IR spectra

(b) peak areas of FT-IR spectra

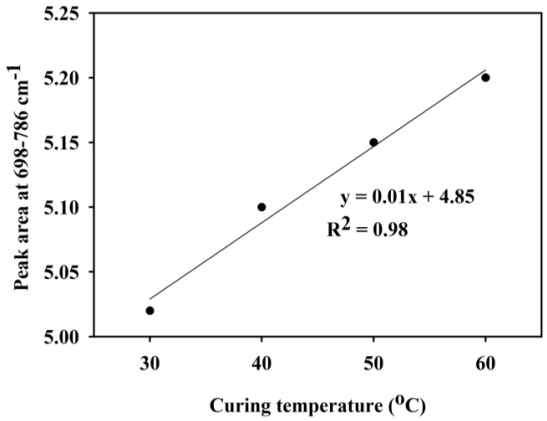
Figure 1 FT-IR spectra showed the effect of curing temperature on the vulcanization reaction of natural rubber at 30 °C, 40 °C, 50°C and 60°C.

3.2 Effect of curing time on crosslinking reaction of natural rubber sheets

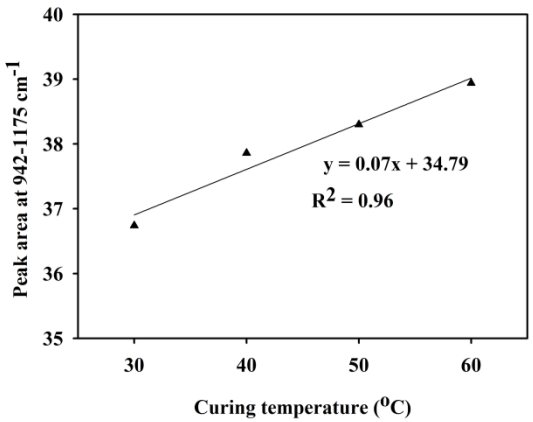
The FT-IR spectra shown in Figure 3 and the corresponding peak area analysis presented in Figure 4 demonstrated clear changes with increasing curing time. The absorbance peak (Figure 3) and peak area at 1495-1729 cm^{-1} (Figure 4(c)), assigned to C=C bonds (Coran, 1965; Lu and Hsu, 1987), gradually decreased as the curing time increased. In contrast, the absorbance peaks (Figure 3) and peak areas at 942-1175 cm^{-1} (Figure 4(b)) and 698-786 cm^{-1} (Figure 4(a)), corresponding to C-S bonds (Coran, 1965; Lu and Hsu, 1987), increased with longer curing time. In addition, the peak area ratios presented in Figure 4(d) confirmed the same trend. The reduction in C=C peak intensity together with the increase in C-S peak intensity indicated the gradual formation of sulfur crosslinks within the rubber network as curing progressed. These findings suggested

that self-crosslinking reactions could proceed slowly under room-temperature conditions when sufficient curing time was provided.

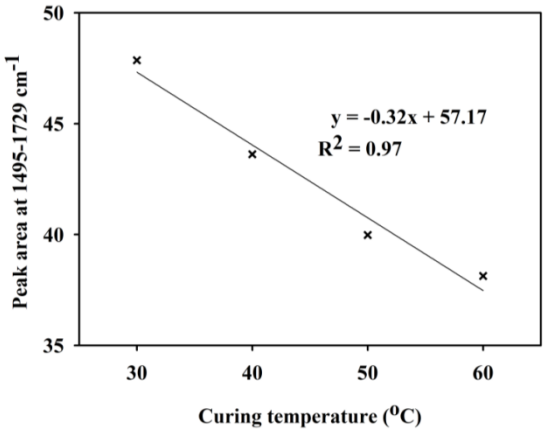
Furthermore, the peak area ratio slopes shown in Figures 2(d) and 4(d) indicated that the vulcanization reaction progressed more rapidly with increasing curing temperature than with prolonged curing time. Although elevated temperature accelerated crosslink formation, curing under low-temperature conditions with controlled curing time preserved a greater amount of remaining reactive sites within the rubber structure. Consequently, controlled curing at room temperature was considered more suitable for preparing natural rubber sheets with self-healing capability.



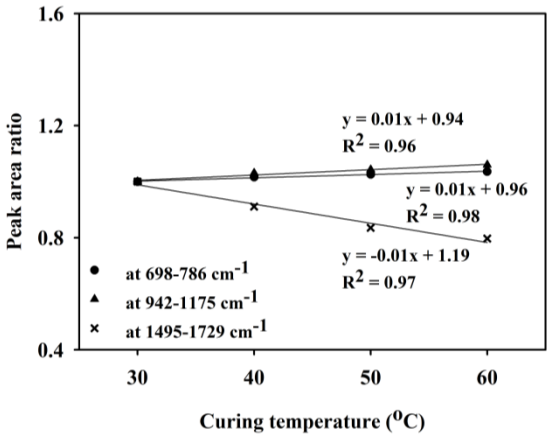
(a) peak areas of 698-786 cm^{-1} and curing temperature



(b) peak areas of 942-1175 cm^{-1} and curing temperature

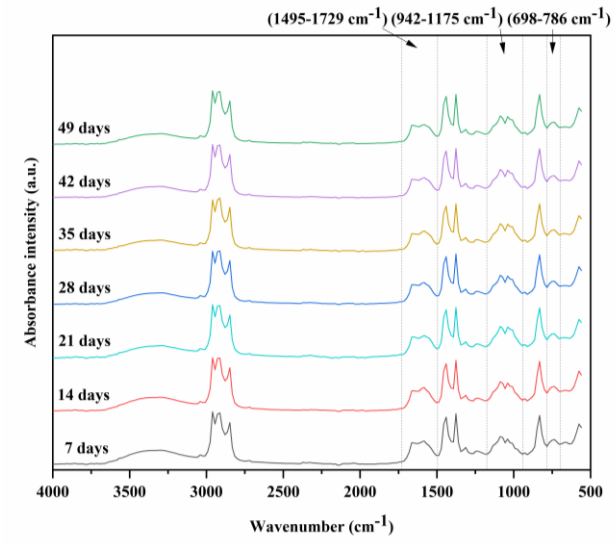


(c) peak areas of 1495-1729 cm^{-1} and curing temperature

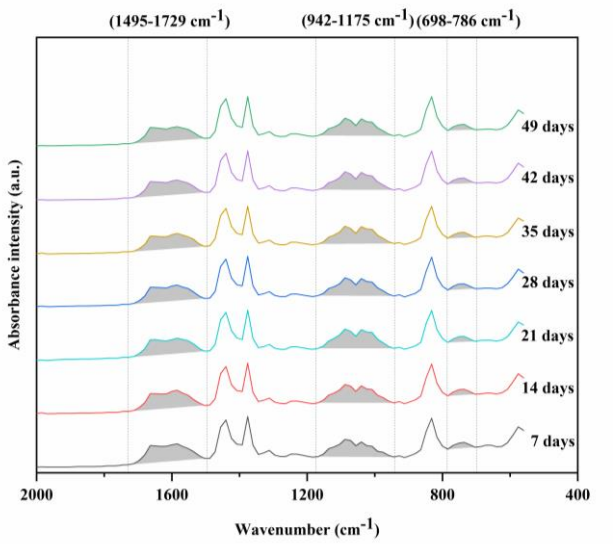


(d) peak area ratio and curing temperature

Figure 2 The peak areas (a-c) and (d) peak area ratio showed the effect of curing temperature on the vulcanization reaction of natural rubber at 30°C, 40°C, 50°C and 60°C.

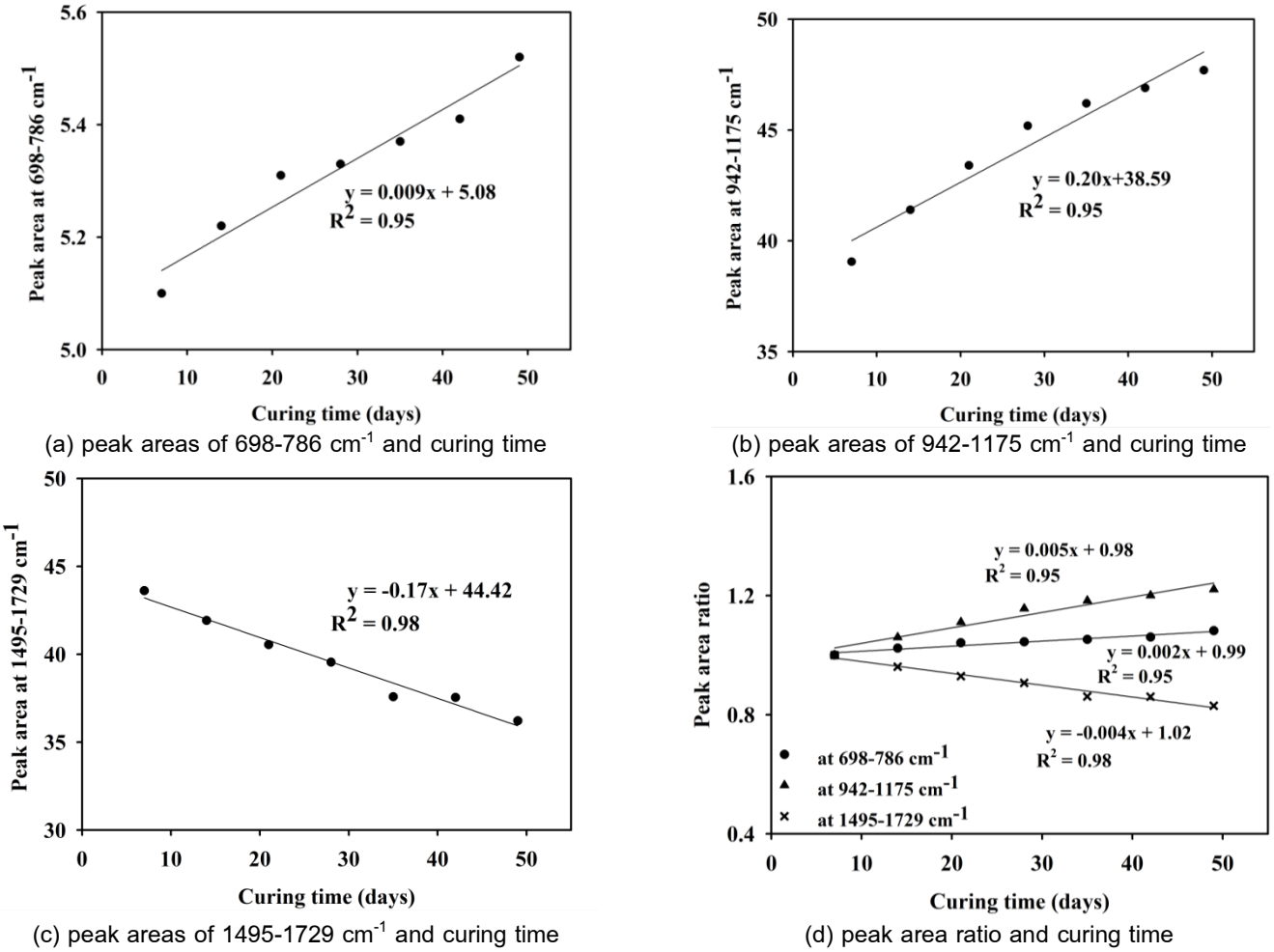


(a) FT-IR spectra



(b) peak areas of FT-IR spectra

Figure 3 The FT-IR spectra showed the effect of curing time on the vulcanization reaction of natural rubber at 30 ± 5 °C (room temperature) for curing periods of 7, 14, 21, 28, 35, 42, and 49 days.



(a) peak areas of 698-786 cm^{-1} and curing time

(b) peak areas of 942-1175 cm^{-1} and curing time

(c) peak areas of 1495-1729 cm^{-1} and curing time

(d) peak area ratio and curing time

Figure 4 The peak areas (a-c) and (d) peak area ratio showed the effect of curing time on the vulcanization reaction of natural rubber at 30 ± 5°C (room temperature) for curing time of 7, 14, 21, 28, 35, 42, and 49 days.

3.3 Analysis of swelling behavior and crosslink density

This section investigated the influence of curing temperature and curing time on the swelling behavior and the crosslink density of the natural rubber sheets. Variations in these properties provided important information regarding the development of the rubber network structure under different curing conditions.

The swelling behavior and calculated crosslink density of the rubber sheets, shown in Figures 5 and 6, revealed that crosslink density gradually increased while swelling behavior decreased with increasing curing temperature and curing time. The reduction in swelling indicated the formation of a denser crosslinked network that restricted solvent penetration into the rubber matrix. In contrast, the increase in crosslink density confirmed the progressive formation of sulfur crosslinks during vulcanization. Furthermore, the slope of the crosslink density results demonstrated that samples cured through extended curing time at room temperature possessed lower crosslink density compared with samples cured at elevated temperatures. These findings suggested that room-temperature curing promoted slower and more controlled network formation, which was favorable for maintaining polymer-chain mobility associated with self-healing behavior.

3.4 Stress-strain behavior and self-healing properties of a natural rubber sheet

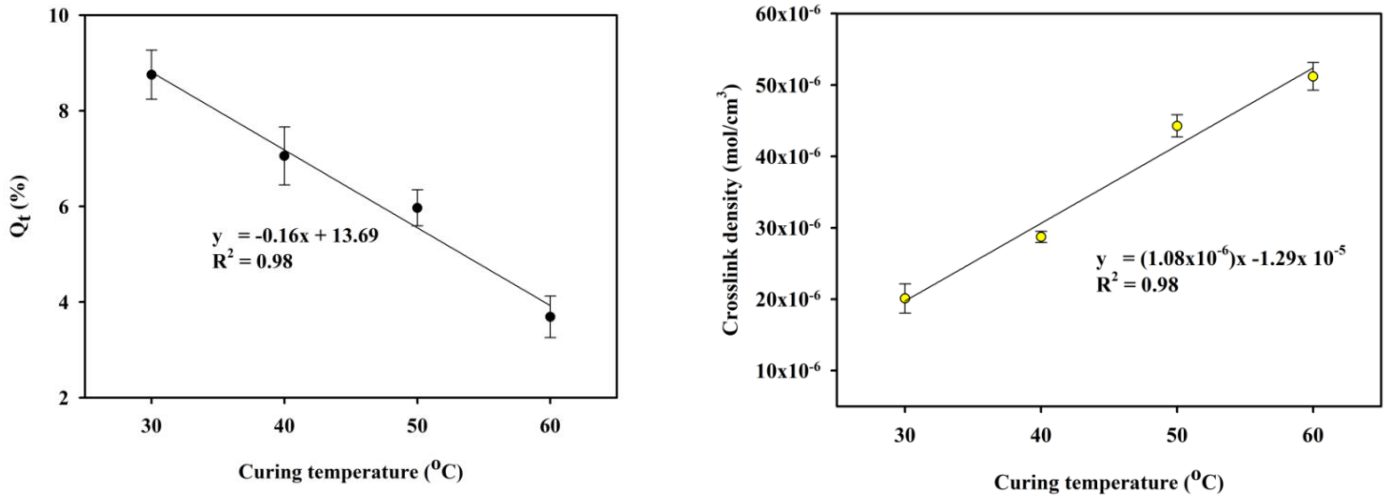
The natural rubber sheets were vulcanized using a sulfur-based curing system at 30 ± 5 °C for 7 days. After curing, each sample was cut into two pieces and immediately rejoined to evaluate the self-healing behavior through self-crosslinking under controlled temperature and healing-time conditions. The rejoined samples were maintained at 30 ± 5°C for different healing periods before mechanical testing.

The stress-strain curves shown in Figure 7(a) revealed that both stress at break and strain at break gradually increased with increasing self-healing time. These results indicated progressive recovery of the mechanical properties during the healing process. In addition, Young's modulus, determined from the slope of the stress-strain curve within the linear elastic region, also increased with longer healing time, as presented in Figure 7(b) and Figure 8(a). The increase in modulus suggested the gradual development of additional crosslinked structures within the rubber network during the self-healing process. Figure 8(b)

shows the relationship between self-healing time and healing efficiency of the natural rubber sheets. The healing efficiency gradually increased as the healing time increased from 24 to 120 h. At shorter healing times, only a small recovery in healing efficiency was observed, indicating that the interfacial reconnection between the cut surfaces was still limited during the early stage of healing. As the healing time increased to 48 and 72 h, the healing efficiency continuously improved, suggesting that additional self-crosslinking reactions occurred at the rejoined interface. The progressive increase in healing performance indicated that polymer chain diffusion and network rearrangement became more effective with longer healing periods (Xu *et al*., 2016).

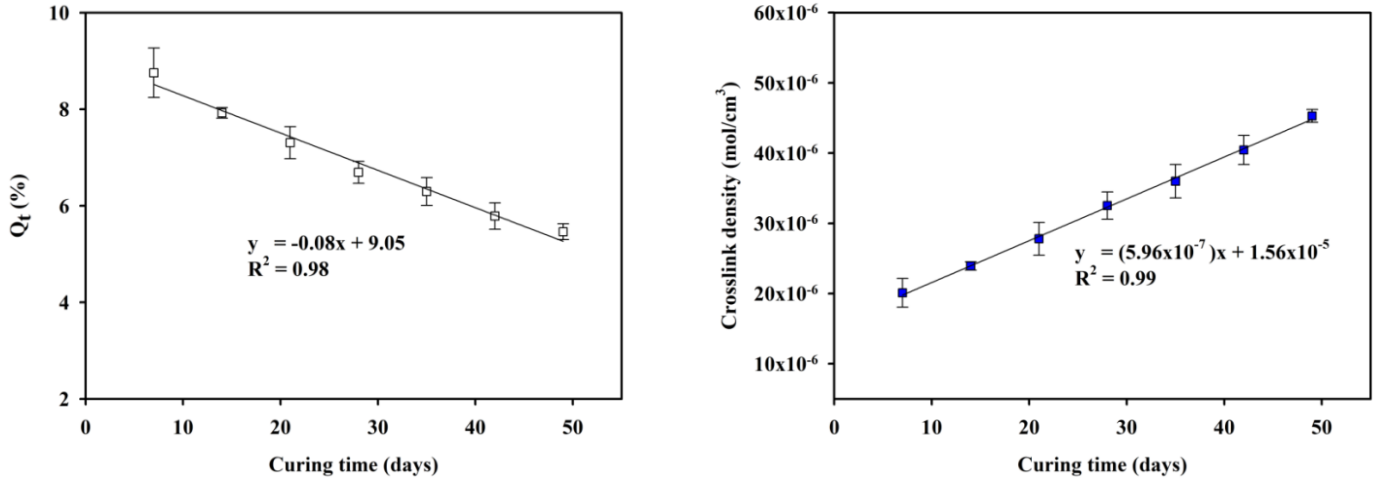
A slight increase was also observed at 96 h, showing that the healing process remained active under room-temperature conditions. The highest healing efficiency was obtained at 120 h, where a significant increase in recovery was observed compared with the earlier healing periods. This behavior suggested that prolonged healing time promoted further interfacial interaction and crosslink formation between the damaged surfaces.

The results demonstrated that the self-healing behavior of the natural rubber sheets strongly depended on healing duration, and longer healing periods enhanced the recovery of mechanical properties through continued self-crosslinking within the rubber network. This result was supported by the swelling behavior (Figure 9(a)) and crosslink density analysis (Figure 9(b)).



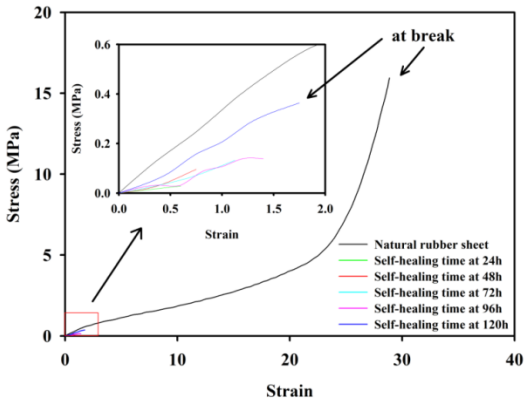
(a) swelling properties and curing temperature (b) crosslink density and curing temperature

Figure 5 The effect of curing temperature on (a) the swelling properties and (b) the crosslink density.

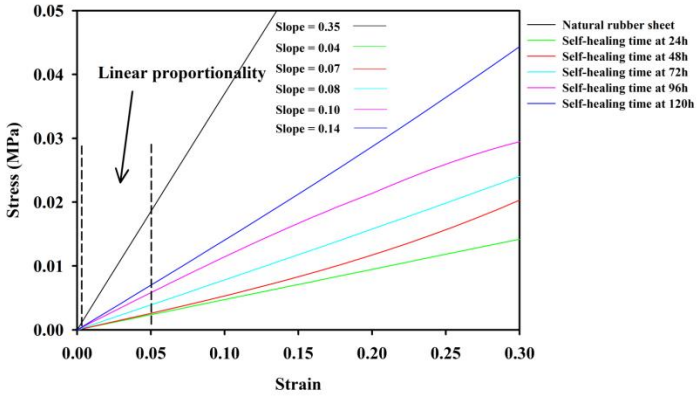


(a) swelling properties and curing time (b) crosslink density and curing time

Figure 6 The effect of curing time on (a) the swelling properties and (b) the crosslink density.

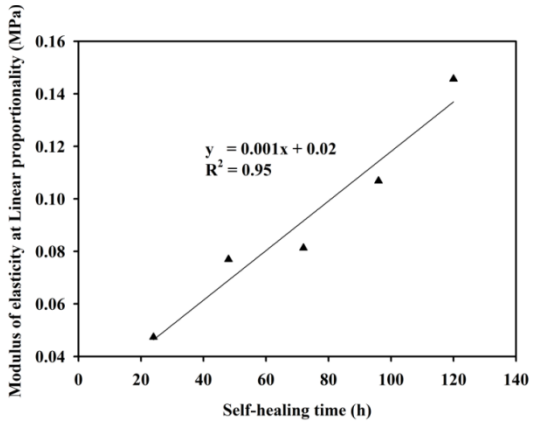


(a) stress-strain behavior

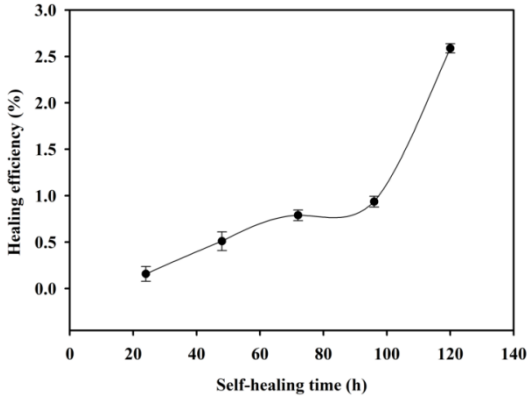


(b) slope of Young's modulus in the linear elastic region

Figure 7 (a) the stress-strain behavior and (b) slope of Young's modulus in the linear elastic region of the natural rubber sheets at different self-healing time.

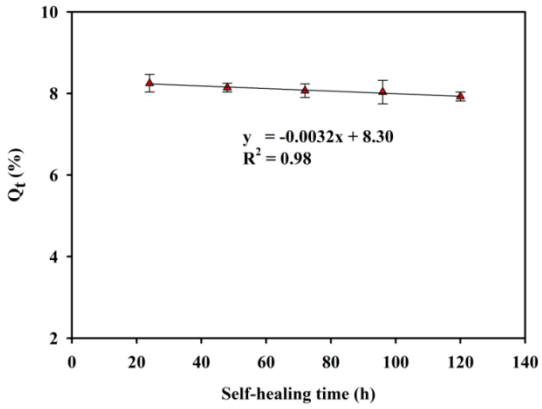


(a) modulus of elastic in the linear elastic region and self-healing time

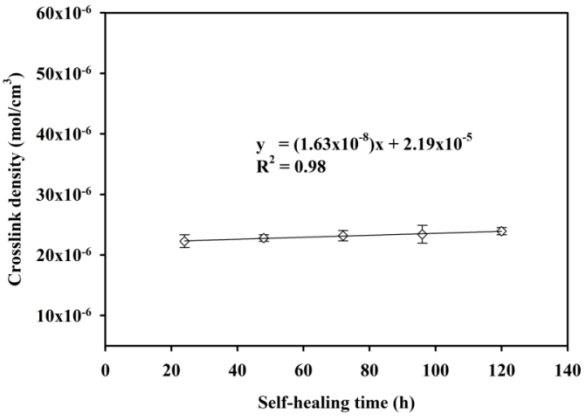


(b) healing efficiency and self-healing time

Figure 8 (a) modulus of elastic in the linear elastic region and (b) healing efficiency of natural rubber sheets at different self-healing time.



(a) swelling behavior and self-healing time



(b) crosslink density and self-healing time

Figure 9 (a) swelling behavior and (b) crosslink density with self-healing time of natural rubber sheets.

The swelling values (Figure 9(a)) gradually decreased with increasing healing time, indicating that the rubber network became more compact due to the formation of additional crosslinks within the material. In contrast, the calculated crosslink density (Figure 9(b)) increased progressively during the healing process, confirming the continued development of the crosslinked network structure at room temperature. The increase in crosslink density suggested that self-crosslinking reactions occurred continuously at the rejoined interface between the damaged surfaces. This enhanced network

formation restricted solvent penetration, resulting in lower swelling behavior. Consequently, the improved crosslink structure contributed directly to the higher healing efficiency and better recovery of mechanical properties observed after longer healing periods. These findings demonstrated that the self-healing performance of the natural rubber sheets was closely related to the gradual formation of crosslinked structures during the healing process.

For the discussion, the FT-IR results demonstrated that the crosslinking reaction mainly occurred through the consumption of carbon–carbon double bonds (C=C) in the natural rubber chains during sulfur vulcanization. The reduction of the C=C absorbance peak area together with the increase in the C-S peak areas confirmed the formation of sulfur-containing crosslinked structures within the rubber network. Increasing the curing temperature accelerated the vulcanization reaction. At higher temperatures, the C=C peak area decreased more rapidly, while the C-S peak areas increased significantly. This behavior indicated that sulfur crosslink formation became more active under elevated curing temperatures. In contrast, curing at 30 ± 5 °C resulted in slower crosslink formation, leaving a larger amount of unreacted C=C bonds in the rubber structure. The remaining unsaturated bonds provided active sites for further self-crosslinking reactions during the healing process. Therefore, room-temperature curing conditions were considered more suitable for preparing self-healing rubber sheets.

The effect of curing time showed a similar trend to that of curing temperature. Longer curing time gradually reduced the C=C bond content and increased the C-S bond formation, indicating continuous network development even under room-temperature conditions. These results suggested that self-crosslinking could proceed slowly when sufficient curing time was provided. The comparison of peak area ratio slopes between curing temperature and curing time revealed that temperature had a stronger effect on the vulcanization reaction than time. Although higher temperatures accelerated crosslinking more effectively, excessive crosslink formation reduced the availability of reactive sites required for self-healing. Consequently, controlled curing at low temperature with extended curing time provided a better balance between network formation and healing capability.

The swelling behavior and crosslink density analysis further supported the FT-IR results. The decrease in swelling behavior with increasing curing temperature and curing time indicated the formation of a denser rubber network that restricted solvent penetration. At the same time, the increase in calculated crosslink density confirmed the progressive development of sulfur crosslinks within the material. The lower crosslink density observed under room-temperature curing conditions suggested that the rubber chains retained greater mobility compared with samples cured at higher temperatures. This remaining chain mobility was important for promoting interfacial diffusion and rearrangement during the self-healing process.

The stress-strain behavior of the healed rubber sheets demonstrated that both tensile strength and elongation at break improved with increasing healing time. These improvements indicated that the damaged interfaces gradually reconnected through self-crosslinking reactions and polymer chain diffusion across the cut surfaces.

The increase in Young's modulus with healing time suggested that the rubber network became mechanically stronger as additional crosslinks formed during the healing process. This result confirmed that the healing mechanism involved gradual reconstruction of the crosslinked network structure at the damaged interface.

Healing efficiency increased continuously from 24 to 120 h, indicating that longer healing periods promoted a more effective recovery of mechanical properties. During the early stage of healing, only limited interfacial interaction occurred between the rejoined surfaces. However, prolonged healing time allowed greater chain diffusion, molecular rearrangement, and formation of additional sulfur crosslinks at the interface (Xu *et al*., 2016).

The swelling and crosslink density results after healing strongly supported the mechanical recovery behavior. The reduction in swelling together with the increase in crosslink density demonstrated that self-crosslinking reactions continued during the healing period. The development of a more compact network structure restricted solvent absorption and enhanced the mechanical integrity of the healed samples.

Overall, the results demonstrated that controlled room-temperature curing successfully produced natural rubber sheets capable of self-healing through gradual self-crosslinking reactions. The balance between moderate crosslink density and sufficient chain mobility played an important role in achieving effective healing behavior under mild conditions without the need for complex chemical modification or external heating.

This study showed strong potential for the preparation of smart rubber materials with self-crosslinking-driven self-healing behavior. These materials could be applied in products requiring damage recovery capability. The self-healing behavior and practical advantages of the natural rubber sheets also demonstrated their potential as a new class of functional rubber materials. In addition, this approach provided an alternative strategy for increasing the value and advanced utilization of locally produced natural rubber latex.

4. Conclusion

This study investigated the effect of controlled curing temperature and curing time on the crosslinking behavior and self-healing performance of natural rubber sheets prepared through a sulfur vulcanization casting process. The work addressed an important limitation found in many previously reported self-healing rubber systems, which often required

complex chemical modification, high processing temperatures, or complicated fabrication procedures that limited large-scale application. In this study, a simpler room-temperature curing approach was proposed to produce self-healing natural rubber sheets through gradual self-crosslinking reactions under mild conditions. FT-IR analysis confirmed that the vulcanization reaction occurred through the conversion of carbon-carbon double bonds into sulfur-containing crosslinked structures. Increasing curing temperature accelerated the crosslinking reaction, while extended curing time promoted slower network formation under room-temperature conditions. The results demonstrated that curing at 30 ± 5 °C preserved a greater amount of remaining unsaturated bonds, which later contributed to the self-healing process. This condition provided a suitable balance between crosslink formation and polymer-chain mobility, allowing further network rearrangement during healing.The swelling behavior and crosslink density analysis supported the FT-IR spectroscopic results. Higher curing temperature and longer curing time reduced swelling behavior and increased crosslink density, indicating the development of a denser rubber network. However, samples cured under room-temperature conditions maintained lower crosslink density and greater chain mobility compared with those cured at elevated temperatures. This remaining molecular mobility played an important role in promoting interfacial diffusion and self-crosslinking during healing. Mechanical testing demonstrated that the self-healing performance improved continuously with increasing healing time. Tensile strength, elongation at break, Young's modulus, and healing efficiency all increased as the healing period extended from 24 to 120 h. The gradual recovery of mechanical properties suggested that polymer-chain diffusion and additional crosslink formation occurred continuously at the damaged interface.

The reduction in swelling behavior together with the increase in crosslink density after healing further confirmed the progressive reconstruction of the rubber network during the self-healing process. The results demonstrated that effective self-healing behavior could be achieved without external heating, sophisticated reversible chemistry, or complex processing methods. Instead, the healing mechanism depended mainly on controlled room-temperature self-crosslinking and sufficient polymer-chain mobility within the natural rubber structure. This finding provided an alternative strategy for developing practical self-healing rubber materials using a relatively simple and cost-effective preparation method.

Overall, the study demonstrated that controlled room-temperature curing successfully produced natural rubber sheets with self-crosslinking-driven self-healing capability. The developed approach showed potential for future applications in smart rubber materials requiring damage recovery properties, including flexible rubber components, protective materials, rubber tubing, and artificial skin-like systems. In addition, the proposed method offered a promising route for increasing the value and advanced utilization of natural rubber latex through the development of functional self-healing rubber products.

5. Acknowledgments

The authors would like to gratefully acknowledge the Faculty of Science and Technology, Princess of Naradhiwas University, the laboratory and equipment for this research.

6. References

American Society for Testing and Materials. 2019. ASTM D3616-95(2019): **Standard test method for rubber-Determination of gel, swelling index, and dilute solution viscosity**. West Conshohocken, PA: ASTM International.

American Society for Testing and Materials. 2021. ASTM D412-16(2021): **Standard test methods for vulcanized rubber and thermoplastic elastomers-Tension**. West Conshohocken, PA: ASTM International.

Boden, J., Bowen, C.R., Buchard, A., Davidson, M.G. and Norris, C. 2022. Understanding the effects of cross-linking density on the self-healing performance of epoxidized natural rubber and natural rubber. **ACS Omega** 7(17): 15098-15105.

Chakraborty, S., Bandyopadhyay, S., Ameta, R., Mukhopadhyay, R. and Deuri, A. S. 2007. Application of FTIR in characterization of acrylonitrile-butadiene rubber (nitrile rubber). **Polymer Testing** 26(1): 38-41.

Coran, A.Y. 1965. Vulcanization. part VII. kinetics of sulfur vulcanization of natural rubber in presence of delayed-action accelerators. **Rubber Chemistry and Technology** 38(1): 1-14.

Flory, P.J. and Rehner, J.Jr. 1943. Statistical mechanics of cross-linked polymer networks II. Swelling. **The Journal of Chemical Physics** 11(11): 521-526.

Flory, P.J. 1953. **Principles of Polymer Chemistry**. Ithaca, NY: Cornell University Press.

Gunasekaran, S., Natarajan, R.K. and Kala, A. 2007. FTIR spectra and mechanical strength analysis of some selected rubber derivatives. **Spectrochimica Acta Part A: Molecular and Biomolecular Spectroscopy** 68(2): 323-330.

Gong, Z., Huang, J., Cao, L., Xu, C. and Chen, Y. 2022. Self-healing epoxidized natural rubber with ionic/coordination crosslinks. **Materials Chemistry and Physics** 285: 126063.

Hernández, M., Grande, A.M., Dierkes, W., Bijleveld, J., Van Der Zwaag, S. and García, S.J. 2016. Turning vulcanized natural rubber into a self-healing polymer: Effect of the disulfide/polysulfide ratio. **ACS Sustainable Chemistry & Engineering** 4(10): 5776-5784.

Han, H., Zhang, X., Kuang, W., Tian, H. and Wang, X. 2023. Self-healing and recyclable elastomer based on epoxidized

natural rubber and carboxylated-chitosan. **Composites Communications** 40: 101594.

Kumnuantip, C. and Sombatsompop, N. 2003. Dynamic mechanical properties and swelling behaviour of NR/reclaimed rubber blends. **Materials Letters** 57(21): 3167-3174.

Kong, L., Yang, Y., Wu, M., Teng, X., Wang, Y. and Xu, C. 2022. Design of epoxidized natural rubber/poly(lipoic acid) elastomer with fast and efficient self-healing under a mild temperature. **International Journal of Biological Macromolecules** 223: 446-457.

Lu, F.J. and Hsu, S.L. 1987. A vibrational spectroscopic analysis of the structure of natural rubber. **Rubber Chemistry and Technology** 60: 647-658.

Mandal, S., Malanin, M., Ghanti, B., Banerjee, S., Sawada, J., Tada, T. and Das, A. 2023. Design of sacrificial network in modified natural rubber leads to strikingly improved mechanical performance with self-healing capability. **Chemical Engineering Journal** 474: 145838.

Mooibroek, H. and Cornish, K. 2000. Alternative sources of natural rubber. **Applied Microbiology and Biotechnology** 53(4): 355-365.

Nimpaiboon, A. and Sakdapipanich, J. 2013. A model study on effect of glucose on the basic characteristics and physical properties of natural rubber. **Polymer Testing** 32(8): 1408-1416.

Ngudsuntear, K., Limtrakul, S., Vatanatham, T. and Arayapranee, W. 2022. Mechanical and aging properties of hydrogenated epoxidized natural rubber and its lifetime prediction. **ACS Omega** 7(41): 36448-36456.

Omar, M.F., Ali, F., Jami, M.S., Azmi, A.S., Ahmad, F., Marzuki, M.Z. and Kim, M.P. 2025. A comprehensive review of natural rubber composites: Properties, compounding aspects, and renewable practices with natural fibre reinforcement. **Journal of Renewable Materials** 13(3). 497-538.

Olejnik, O. and Masek, A. 2023. Recent progress in bio-based elastomers with intrinsic self-healing mechanisms Part I: Natural rubber modifications. **Journal of Saudi Chemical Society** 27(4): 101676.

Rahman, M.A., Sartore, L., Bignotti, F. and Di Landro, L. 2013. Autonomic self-healing in epoxidized natural rubber. **ACS Applied Materials & Interfaces** 5(4): 1494-1502.

Rehman, A., Ismail, H., Sani, N.F.M., Othman, N., Majid, N.A., Islam, A. and Shuib, R.K. 2024. Enhancing self-healing efficiency of natural rubber composites using halloysite nanotubes. **Polymer Composites** 45(1): 424-437.

Roylance, D. 2001. **Stress-Strain Curves**. Massachusetts Institute of Technology study, Cambridge.

Supramaniam, J., Low, D.Y.S., Wong, S.K., Leo, B.F., Goh, B.H. and Tang, S.Y. 2022. Nano-engineered ZnO/CNF-based epoxidized natural rubber with enhanced strength for novel self-healing glove fabrication. **Chemical Engineering Journal** 437(2): 135440.

Treloar, L.R.G. 1975. **The Physics of Rubber Elasticity** (3rd ed.). Oxford University Press.

Trinh, B., Owen, P., VanderHeide, A., Gupta, A. and Mekonnen, T. H. 2023. Recyclable and self-healing natural rubber vitrimers from anhydride-epoxy exchangeable covalent bonds. **ACS Applied Polymer Materials** 5(11): 8890-8906.

Xu, C., Cao, L., Lin, B., Liang, X. and Chen, Y. 2016. Design of self-healing supramolecular rubbers by introducing ionic cross-links into natural rubber via a controlled vulcanization. **ACS Applied Materials & Interfaces** 8(27): 17728-17737.

Yan, C., Liu, T., Zhang, G., Zhang, W., Ma, J., Wu, Y. and Huang, W. 2024. Self-healing natural rubber based on the double cross-linked networks for fabrication of the flexible electronic sensor. **ACS Applied Electronic Materials** 6(8): 6102-6112.

Zhao, W., Huang, B., Zhu, L., Feng, X., Xu, J., Zhang, H. and Yan, S. 2022. Printable hydrogels based on starch and natural rubber latex with high toughness and self-healing capability. **International Journal of Biological Macromolecules** 218: 580-587.

Recent Science and Technology 2026, Vol. 18(3): e267961

Recent Science and Technology

Journal homepage: https:// www.tci-thaijo.org/index.php/rmutsvrj/index

ISSN: 3057-0786 (Online)

Research Article

Evaluation of a Commercial β-Mannanase for Konjac Glucomannan Hydrolysis: Activity and Molecular Weight Analysis

Chompoonuch Phuenpipob [a,b *], Chaleeda Borompichaichartkul [a], Kittipong Rattanaporn [c], Putthapong Phumsombat [d], Supuksorn Masavang [b] and Duangkamol Tungsatitporn [b]

[a] *Department of Food Technology, Faculty of Science, Chulalongkorn University, Bangkok 10330, Thailand.*

[b] *Division of Food Technology, Faculty of Home Economics Technology, Rajamangala University of Technology Phra Nakhon, Bangkok 10330, Thailand.*

[c] *Department of Biotechnology, Faculty of Agro-Industry, Kasetsart University, Bangkok 10900, Thailand.*

[d] *School of Food Industry, King Mongkut's Institute of Technology, Ladkrabang, Bangkok 10520, Thailand.*

Article history:

Received: 2025-06-09
Revised: 2026-03-17
Accepted: 2026-05-18

Keywords:

β-Mannanase;
Konjac glucomannan;
Enzymatic activity;
Molecular weight;
Mannooligosaccharides

ABSTRACT

β-Mannanase (endo-1,4-β-D-mannanase) is a glycoside hydrolase with potential for producing mannooligosaccharides (MOS), which are recognized for their prebiotic properties. However, the applicability of commercial enzymes to specific substrates such as konjac glucomannan (KGM) remains insufficiently evaluated. This study investigated the hydrolytic activity and estimated the molecular weight of a commercial β-mannanase (Mannanase BGM "AMANO" 10) toward KGM. The enzyme exhibited measurable activity under the tested conditions, with a specific activity of approximately 100,574 U g^{-1} protein and a corresponding reducing sugar yield. SDS-PAGE analysis indicated an apparent molecular weight in the range of 50–75 kDa. These findings provide preliminary insights into the performance of the commercial enzyme on KGM and establish baseline information for its potential application in MOS production.

© 2026 Phuenpipob, C., Borompichaichartkul, C., Rattanaporn, K., Phumsombat, P., Masavang, S. and Tungsatitpornb, D. Recent Science and Technology published by Rajamangala University of Technology Srivijaya

1. Introduction

β-Mannans are among the major hemicellulosic polysaccharides found in nature and exhibit considerable structural diversity, including linear mannan, glucomannan, galactomannan, and galactoglucomannan (Singh *et al.*, 2018b; Zhang *et al.*, 2021). Among these, konjac glucomannan (KGM) has attracted considerable interest as a promising substrate for the production of mannooligosaccharides (MOS) because of its abundance, water solubility, and well-defined β-(1⟶4)-linked glucomannan backbone composed mainly of D-mannose and D-glucose residues (Singh *et al.*, 2018a; Sun *et al.*, 2023). Controlled depolymerization of KGM can generate MOS, typically with a degree of polymerization (DP) of 2-6, which have received increasing attention due to their potential prebiotic functionality (Jana *et al.*, 2021; Singh *et al.*, 2019; Zhang *et al.*, 2019). Because MOS are selectively utilized by beneficial gut microorganisms and are associated with gut-health-related applications, the efficient conversion of KGM into structurally defined oligosaccharides is of growing interest in functional food research (Hughes, 2020; Liu *et al.*, 2022; Magengelele *et al.*, 2021).

*** Corresponding author.**

E-mail address: *chompoonuch.p@rmutp.ac.th*

Cite this article as:

Phuenpipob, C., Borompichaichartkul, C., Rattanaporn, K., Phumsombat, P., Masavang, S. and Tungsatitporn, D. 2026. Evaluation of a Commercial β-Mannanase for Konjac Glucomannan Hydrolysis: Activity and Molecular Weight Analysis. **Recent Science and Technology** 18(3): e267961.

https://doi.org/10.65411/rst.2026.267961

The enzymatic degradation of β-mannan-containing polysaccharides may involve several glycoside hydrolases, including endo-β-mannanase, β-mannosidase, and accessory enzymes acting on substituted side groups (Kaur and Dhawan, 2007; Malgas *et al*., 2015), as classified in the CAZy database. Among these, β-mannanase (EC 3.2.1.78) is particularly important because it catalyzes the cleavage of internal β-(1 ⟶ 4)-mannosidic linkages within the mannan backbone, thereby initiating depolymerization and facilitating MOS production (Cai *et al*., 2022; Kaur *et al*., 2007; Malgas *et al*., 2015). For this reason, β-mannanases have been widely studied for the conversion of mannan-rich substrates into functional oligosaccharides (Arunrattanamook *et al*., 2020; Hu *et al*., 2020; Magengelele *et al*., 2021; Pomsang *et al*., 2024). However, the efficiency of MOS generation is strongly influenced by substrate structure, enzyme source, and hydrolysis conditions (Hu *et al*., 2020; Murillo-Franco *et al*., 2025; Srivastava and Kapoor, 2017). Previous studies have primarily focused on β-mannanases derived from microbial sources or purified enzyme systems, whereas comparatively less attention has been given to the characterization of commercially formulated enzymes for KGM hydrolysis. Consequently, although enzymatic hydrolysis of mannan-containing substrates has been widely investigated, the substrate-specific performance of commercially available β-mannanase preparations toward KGM remains insufficiently characterized (Dawood and Ma, 2020; Magengelele *et al*., 2021), with only limited information available for an enzyme such as Mannanase BGM “AMANO” 10 under defined experimental conditions. This study therefore provides baseline experimental data on the hydrolytic activity and molecular weight of a commercial β-mannanase toward KGM.

Commercial enzyme preparations are of practical interest because they represent readily accessible biocatalysts for applied research and future process development (Arunrattanamook *et al*., 2020; Murillo-Franco *et al*., 2025; Zhou *et al*., 2021). Therefore, evaluating their performance on specific substrates is important for reducing uncertainty in enzyme selection and for establishing baseline information for subsequent MOS production studies. In this context, Mannanase BGM “AMANO” 10 was selected as a commercially available β-mannanase for preliminary characterization against KGM. This study aimed to determine its hydrolytic activity using the DNS assay and to estimate its molecular weight by SDS-PAGE. The findings are expected to serve as a useful reference for the selection and utilization of commercial β-mannanases in future research on KGM hydrolysis and MOS production.

2. Materials and Methods

2.1 Enzyme activity assay

Enzymatic activity was determined using the 3,5-dinitrosalicylic acid (DNS) method by measuring the release of reducing sugars at 540 nm, as described by Miller (1959).

2.1.1 Substrate, chemicals, and enzyme

KGM was obtained from Thai Union (Thailand). Commercial β-mannanase (Mannanase BGM “AMANO” 10) was purchased from Amano Enzyme Inc (Japan). 3,5-dinitrosalicylic acid (DNS) and other analytical-grade chemicals were obtained from Sigma-Aldrich (USA).

2.1.2 Mannose standard curve

A standard curve was prepared using mannose solutions in the range of 0-2 mg mL-1. Absorbance was measured at 540 nm using a microplate reader (BioTek Synergy HTX Multi-Mode Reader, BioTek Instruments, USA). All measurements were performed in triplicate and corrected using a reagent blank.

2.1.3 Substrate preparation

A 1% (w/v) KGM stock solution was prepared in 50 mM sodium acetate buffer (pH 5.0) and stirred until fully dissolved. For the enzyme assay, 100 µL of the KGM solution was used as the substrate.

2.1.4 Enzyme preparation

The enzyme stock solution (2 mg mL-1) was diluted with distilled water to obtain a range of working concentrations before the enzyme activity assay. Preliminary experiments were conducted to determine appropriate dilution levels for the DNS assay. Based on the observed absorbance values, enzyme dilutions in the range of 1000- to 6000-fold were selected to ensure that measurements fell within the linear range of the mannose standard curve. All selected dilution levels (1000-, 2000-, 3000-, 4000-, 5000-, and 6000-fold) were used as independent experimental conditions for activity measurements, as presented in Table 1. Heat-inactivated enzyme samples were prepared by boiling the enzyme solution for 10 min, followed by rapid cooling, and were used as negative controls.

2.1.5 Enzyme reaction

The reaction mixture consisted of 100 µL enzyme solution and 100 µL substrate solution. The mixtures were vortexed and incubated at 70°C for 30 min. All assays were performed in triplicate.

2.1.6 DNS assay

After incubation, 200 µL DNS reagent was added, and the mixtures were boiled for 10 min. The reaction was stopped by cooling in an ice bath, then diluted with 2 mL of distilled water. Absorbance was measured at 540 nm using a microplate reader. (BioTek Synergy HTX Multi-Mode Reader, BioTek Instruments, USA). All measurements were performed in triplicate and corrected using a reagent blank.

2.1.7 Determination of enzyme activity

One unit (U) of β-mannanase activity was defined as the amount of enzyme required to release 1 µmol of reducing sugar (mannose equivalent) per minute under the assay conditions. The total activity was calculated using Equation (1)

$$\text{Total activity (U mL}^{-1}\text{)} = \frac{(\text{OD sample} - \text{OD control}) \times 1000 \times \text{Dilution factor}}{\text{Slope} \times \text{MW} \times \text{Time} \times \text{Reaction volume}} \quad (1)$$

OD sample = absorbance of the enzyme solution
OD control = absorbance of control
Dilution factor = dilution (times)
Slope = m value of the standard curve
Mw = molecular weight of mannose (180.16 g mol^{-1})
Time = reaction time (min)
Reaction volume = the total assay volume (mL)

2.1.8 Specific activity

Specific activity was calculated as the ratio of total activity to protein concentration using Equation (2). Protein concentration was determined by the Bradford method using bovine serum albumin (BSA) as a standard (Bradford, 1976).

$$\text{Specific activity (U mg}^{-1}\text{ protein)} = \frac{\text{Total activity (U mL}^{-1}\text{)}}{\text{Protein concentration (mg mL}^{-1}\text{)}} \quad (2)$$

2.1.9 Statistical analysis

All experiments were performed in triplicate. Results are expressed as mean ± standard deviation (SD). Data analysis was performed using Microsoft Excel (Microsoft Corp., USA).

2.2 Determination of mannanase molecular mass by SDS-PAGE

The molecular mass of the mannanase was determined by SDS-PAGE according to the method of Laemmli (1970).

2.2.1 Sample preparation

The enzyme sample was mixed with an equal volume of 2× Laemmli sample buffer (0.125 M Tris-HCl, pH 6.8, 20% glycerol, 4% SDS, 0.004% bromophenol blue, and 10% β-mercaptoethanol) at a ratio of 1:1 (v/v). The mixture was heated at 95°C for 10 min to denature the protein.

2.2.2 Gel electrophoresis

SDS-PAGE was performed using a vertical slab gel system with a 12% resolving gel. A volume of 25 µL of the prepared sample and a molecular weight marker (10–250 kDa, Bio-Rad, USA) were loaded into the wells. Electrophoresis was carried out at a constant voltage of 100 V for approximately 2 h until the dye front reached the bottom of the gel.

2.2.3 Gel staining and destaining

After electrophoresis, the gel was stained with Coomassie Brilliant Blue R-250 solution for 1h and subsequently destained using a solution of methanol: acetic acid: water (40:10:50, v/v/v) until clear protein bands were visible. The molecular mass of the enzyme was estimated by comparison with the protein marker. A protein molecular weight marker (10–250 kDa, Bio-Rad, USA) was used.

3. Results and Discussion

3.1. Enzyme assay of β-mannanase

A mannose calibration curve was constructed to quantify reducing sugars released during konjac glucomannan (KGM) hydrolysis using the DNS assay (Miller, 1959). The calibration curve showed a linear relationship between absorbance at 540 nm and mannose concentration over the tested range, with the regression equation y = 0.3012x - 0.0103 and an R^2 value of 0.9991 (Figure 1), indicating a high degree of linearity within the working range.

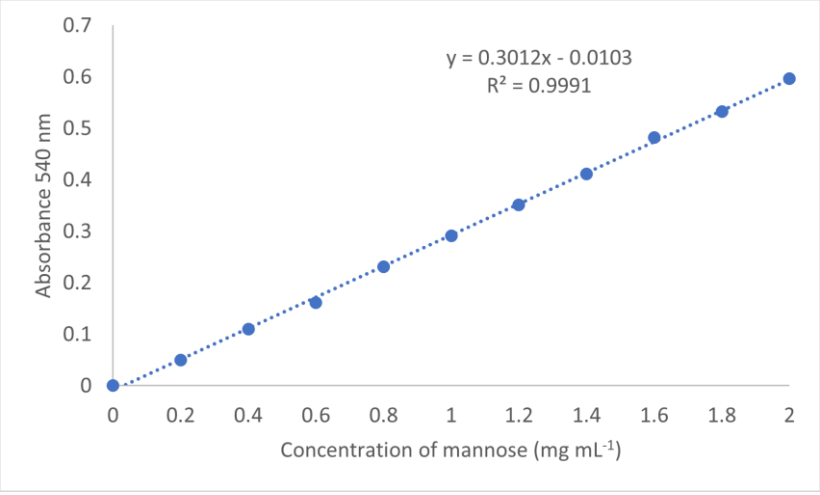


Figure 1 Linear calibration curve showing the relationship between absorbance at 540 nm and mannose concentration (0–2.0 mg mL^{-1}) obtained using the DNS method (R^2 = 0.9991).

Table 1 Absorbance values at 540 nm, reducing sugar concentration, total reducing sugar, reducing sugar yield, total activity, and specific activity of commercial β-mannanase determined by the DNS assay.

Enzyme dilution	Absorbance (540 nm)	Reducing sugar conc. (mg mL^{-1})	Total reducing sugar (mg)	Reducing sugar yield (μmol)	Total activity (U)	Specific activity (U g^{-1} protein)
1000-fold	0.758± 0.007	2.552	0.510	1.418	0.0469	156,392
2000-fold	0.715± 0.015	2.409	0.482	1.338	0.0443	147,643
3000-fold	0.636± 0.023	2.147	0.429	1.193	0.0395	131,569
4000-fold	0.540± 0.017	1.828	0.366	1.016	0.0336	112,036
5000-fold	0.523± 0.024	1.769	0.354	0.983	0.0325	108,441
6000-fold	0.484± 0.011	1.641	0.328	0.912	0.0302	100,574

Note: One unit (U) of β-mannanase activity was defined as the amount of enzyme required to release 1 μmol of reducing sugar (mannose equivalents) per minute under the assay conditions. The amount of protein used in each assay was 3.0×10^{-4} mg. Absorbance values are expressed as the mean ± standard deviation (SD) from triplicate measurements.

The hydrolysis of KGM by the commercial β-mannanase was evaluated under the tested conditions using different enzyme dilutions (1000–6000-fold), and the results are summarized in Table 1. The measured absorbance values (mean ± SD) were converted to mannose-equivalent reducing sugar concentrations using the calibration curve.

The release of reducing sugars increased with hydrolysis, observed at the 1000-fold dilution. Under these conditions, the highest absorbance (0.758 ± increasing enzyme concentration, with the highest 0.007), reducing sugar concentration (2.552 mg mL-1), reducing sugar yield release (1.418 μmol), total activity (0.0469 U), and specific activity (156.39 U mg-1 protein) were obtained (Table 1). As the enzyme dilution increased from 1000- to 6000-fold, all measured parameters decreased accordingly, indicating a dilution-dependent reduction in hydrolytic activity.

For quantitative analysis, measurements within the linear range of the calibration curve were considered. The 6000-fold dilution (0.484 ± 0.011) was therefore selected as a representative condition, as it provided absorbance values within the central region of the calibration curve, thereby ensuring reliable quantification under the applied assay conditions. The relatively low standard deviations observed across replicates indicate good reproducibility of the assay.

The specific activity values obtained in this study were higher than the manufacturer's stated minimum activity. However, this comparison should be interpreted with caution, as total activity measurements are strongly influenced by assay conditions, including substrate type and detection method (Ghose, 1987; Zhu *et al*., 2022). In the present study, KGM was used as the substrate, whereas commercial specifications are often based on galactomannan substrates. Structural differences between these polysaccharides may influence enzyme accessibility and hydrolysis behavior. KGM is a glucomannan composed of β-(1⟶4)-linked mannose and glucose units, whereas galactomannan contains a β-(1⟶4)-mannan backbone substituted with galactose side chains (BeMiller, 2019; Zhang *et al*., 2021). Variations in side-chain substitution have been reported to affect enzyme–substrate interactions and catalytic performance (Chai *et al*., 2020).

In addition, the DNS assay detects reducing ends generated during hydrolysis and is known to be sensitive to short-chain oligosaccharides (Miller, 1959; Zhu *et al*., 2022). This differs from alternative methods such as the Somogyi–Nelson assay, which is based on copper ion reduction and may exhibit different sensitivities depending on sugar composition (Bailey *et al*., 1992; Slavin, 2015; Song *et al.,* 2018). These methodological differences may contribute to variations in reported total activity values.

Furthermore, no information regarding enzyme purity was provided by the manufacturer, and purity was not independently verified in this study. Therefore, the reported specific activity values should be interpreted as apparent values rather than absolute indicators of enzyme purity. Protein concentration was determined using the Bradford assay, which may introduce variability depending on protein composition and the choice of standard protein.

It is important to note that total activity in this study was evaluated under a single reaction condition (pH 5.0 and 70°C) using only KGM as the substrate. Therefore, no conclusions can be drawn regarding catalytic efficiency, substrate specificity, optimum conditions, thermostability, or pH stability. Furthermore, hydrolysis products were not characterized; thus, the potential for MOS production is discussed only as a possible application rather than a confirmed outcome.

Further studies should include kinetic analysis (Km and Vmax), substrate comparison, stability profiling, and product characterization to provide a more comprehensive understanding of the catalytic properties and application potential of the commercial β-mannanase.

3.2 Molecular mass of mannanase

SDS-PAGE was performed under reducing conditions to estimate the molecular mass of the commercial β-mannanase (Figure 2)

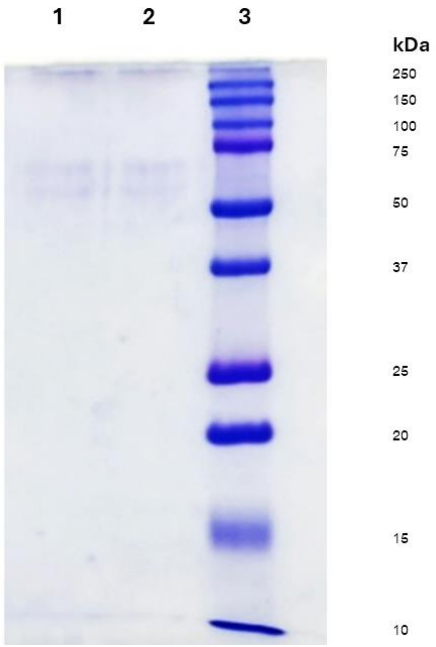


Figure 2 SDS-PAGE analysis of commercial β-mannanase (BGM "AMANO" 10) under reducing conditions. Lane 1–2: β-mannanase samples (1 mg mL^{-1}). Lane 3: molecular weight marker (10-250 kDa, Bio-Rad, USA). Faint protein bands were observed in the approximate molecular weight range of 50–75 kDa, consistent with the reported size range of β-mannanases. The low band intensity may be attributed to limited protein loading or staining sensitivity.

The electrophoretic profile revealed two distinct protein bands within the molecular weight range of 50–75 kDa. Based on comparison with the molecular weight marker, the bands were estimated to have molecular masses of approximately 55 kDa and 70 kDa. The presence of two protein bands suggests that the commercial enzyme preparation is not a single purified enzyme but rather a mixture of protein components, which may represent isoenzymes or co-purified proteins. Similar observations have been reported for β-mannanases derived from fungal sources, where multiple isoforms and post-translational modifications, such as glycosylation, can influence electrophoretic mobility (Chai *et al*., 2020; Yang *et al*., 2015).

The banding pattern was consistent across replicate lanes, indicating reproducibility of the electrophoretic analysis. However, SDS-PAGE under reducing conditions provides information only on the apparent molecular mass of denatured proteins and does not allow conclusions to be drawn regarding native structure, enzyme purity, or subunit composition.

Therefore, although the observed molecular weight range is consistent with previously reported β-mannanases, further analyses such as non-reducing SDS-PAGE, zymography, or LC–MS would be required to confirm protein identity and to better characterize the enzyme composition.

4. Conclusion

This study evaluated the total activity and molecular mass of a commercial β-mannanase using KGM as a substrate under defined assay conditions. The enzyme exhibited measurable activity, with activity values dependent on enzyme concentration. SDS-PAGE analysis revealed two protein bands with approximate molecular masses in the range of 50 and 75 kDa. As the enzyme activity was assessed under a single reaction condition and no product characterization was performed, the results should be interpreted as preliminary. Therefore, no conclusions can be drawn regarding catalytic efficiency, substrate specificity, or stability. These findings provide initial evidence supporting the potential use of the commercial β-mannanase for KGM hydrolysis. Further studies are required to evaluate its catalytic properties, substrate interactions, and product profile for potential applications.

5. Acknowledgments

The authors gratefully acknowledge that the financial support and technical assistance were generously provided by Chulalongkorn University and Rajamangala University of Technology Phra Nakhon for the experimental work. The authors also thank Kasetsart University for their valuable support in instrumental analysis and technical consultation during the research.

6. References

Arunrattanamook, N., Wansuksri, R., Uengwetwanit, T. and Champreda, V. 2020. Engineering of β-mannanase from *Aspergillus niger* to increase product selectivity towards medium chain length mannooligosaccharides. **Journal of Bioscience and Bioengineering** 130(5): 443-449.

Bailey, M.J., Biely, P. and Poutanen, K. 1992. Interlaboratory testing methods for assay of xylanase activity. **Journal of Biotechnology** 23(3): 257–270.

BeMiller, J. N. 2019. **Carbohydrate Chemistry for Food Scientists**. (3rd ed.). Woodhead Publishing, Elsevier

Bradford, M.M. 1976. A rapid and sensitive method for the quantitation of microgram quantities of protein utilizing the principle of protein-dye binding. **Analytical Biochemistry** 72(1): 248-254.

Cai, H., Zhou, Y. and Liu, S. 2022. Optimization of β-mannanase hydrolysis and fermentation characteristics of mannooligosaccharides. **Food Chemistry** 390: 133257.

CAZy database. 2024. **Carbohydrate-active enzymes database**. Available at: http://www.cazy.org, April 5, 2026.

Chai, Y., Wang, L., Liu, Y. and Chen, H. 2020. Classification and mechanism of β-mannanases from different microbial sources. **Applied Microbiology and Biotechnology** 104(14): 6237–6251.

Dawood, A. and Ma, K. 2020. Applications of Microbial β-Mannanases. **Frontiers in Bioengineering and Biotechnology** 8: 598630.

Ghose, T.K. 1987. Measurement of cellulase activities. **Pure and Applied Chemistry** 59(2): 257–268.

Hughes, R.L. 2020. A review of the role of the gut microbiome in personalized sports nutrition. **Frontiers in Nutrition** 6: 191.

Hu, X., Yu, J., Wang, X. and Wang, Y. 2020. High-level expression and characterization of a thermostable β-mannanase for mannooligosaccharide production. **International Journal of Biological Macromolecules** 151: 1075-1083.

IUPAC. 2018. Terminology of bioanalytical methods (IUPAC Recommendations 2018). **Pure and Applied Chemistry** 90(4): 641–684.

Jana, U.K., Kango, N. and Pletschke, B.I. 2021. Mannooligosaccharides: Production, characterization and bioactive applications. **Food Chemistry** 347: 129017.

Kaur, G., Kumar, V. and Sharma, N. 2007. Microbial β-mannanases: Production and applications. **Applied Microbiology and Biotechnology** 75(2): 287-300.

Kaur, J. and Dhawan, S. 2007. Microbial mannanases: An overview of production and applications. **Critical Reviews in Biotechnology** 27(4): 197-216.

Laemmli, U.K. 1970. Cleavage of structural proteins during the assembly of the head of bacteriophage T4. **Nature** 227(5259): 680–685.

Liu, Y., Wang, X., Chen, H., Zhang, J. and Zhang, H. 2022. Effects of dietary mannooligo saccharides on gut microbiota and intestinal barrier function. **Food Research International** 154: 110997.

Magengelele, M., Hlalukana, N., Malgas, A., Rose, S. H., Zyl, W.H. and Pletschke, B.I. 2021. Production and in vitro evaluation of prebiotic mannano-oligosaccharides prepared with a recombinant *Aspergillus niger* endo-mannanase, Man26A. **Enzyme and Microbial Technology** 150: 109893.

Malgas, S., van Dyk, J.S. and Pletschke, B.I. 2015. A review of the enzymatic hydrolysis of mannans and synergistic interactions between β-mannanase, β-mannosidase and α-galactosidase. **World Journal of Microbiology and Biotechnology** 31(8): 1167-1175.

Miller, G.L. 1959. Use of dinitrosalicylic acid reagent for the determination of reducing sugar. **Analytical Chemistry** 31(3): 426–428.

Murillo-Franco, S.L., Galvis-Nieto, J.D. and Orrego, C. E. 2025. Mannooligosaccharide production from açaí seeds by enzymatic hydrolysis: Optimization through response surface methodology. **Environmental Science and Pollution Research** 32: 27860–27871.

Pomsang, P., Ayuni, D., Phumsombat, P., Eugelio, F., Fanti, F., Compagnone, D. and Borompichaichartkul, C. 2024. Enzymatic hydrolysis and biological activities of Konjac glucomannan hydrolysate in different degree of polymerisation. **International Journal of Food Science and Technology** 59(11): 8341-8350.

Singh, R., Kaur, N. and Kennedy, J.F. 2018a. Chemistry and applications of konjac glucomannan. **International Journal of Biological Macromolecules** 112: 1030-1040.

Singh, S., Singh, G. and Arya, S.K. 2018b. Mannans: An overview of properties and applications in food products. **International Journal of Biological Macromolecules** 119: 79–95.

Singh, V., Patel, S. and Shah, N. 2019. Manno-oligosaccharides as prebiotics: Production, characterization, and applications. **International Journal of Food Microbiology** 301: 108197.

Slavin, J. 2013. Fiber and prebiotics: Mechanisms and health benefits. **Nutrients** 5(4): 1417-1435.

Song, Y.J., Sun, W.Y., Fan, Y.L., Xue, Y.F., Liu, D.D., Ma, C.P. and Zhang, T.C. 2018. Galactomannan degrading enzymes from the mannan utilization gene cluster of alkaliphilic *Bacillus* sp. N16-5 and their synergy on galactomannan degradation. **Journal of Agricultural and Food Chemistry** 66: 11055-11063.

Srivastava, P.K. and Kapoor, M. 2017. Production, properties, and applications of endo-β-mannanases. **Biotechnology Advances** 35(1): 1-19.

Sun, Y., Xu, X., Zhang, Q., Zhang, D., Xie, X., Zhou, H., Wu, Z., Liu, R. and Pang, J. 2023. Review of konjac glucomannan structure, properties, gelation mechanism and application in medical biology. **Polymers** 15(8): 1852.

Yang, H., Shi, P., Lu, H., Wang, H., Luo, H., Huang, H., Yang, P. and Yao, B. 2015. A thermophilic β-mannanase from Neosartorya fischeri P1 with broad pH stability and

significant hydrolysis ability of various mannan polymers. **Food Chemistry** 173: 283-289.

Zhang, H., Liu, W., Zhang, J. and Chen, Y. 2019. Prebiotic potential of konjac glucomannan oligosaccharides and their effects on gut microbiota. **Food & Function** 10(10): 6424-6433.

Zhang, W., Li, M., Wang, L. and Gong, Y. 2021. Structural properties and functional potential of konjac glucomannan: A review. **Food Hydrocolloids** 120: 106987.

Zhou, Y., Tan, C., Zhang, X. and Li, L. 2021. Techno-economic evaluation of mannooligosaccharide production from biomass resources. **Bioresource Technology** 337: 125428.

Zhu, Y., Li, T., Zhang, L., Chen, X. and Wang, Y. 2022. Advances in analytical methods for carbohydrate quantification in food systems. **Food Chemistry** 374: 131812.

Recent Science and Technology 2026, Vol. 18(3): e269280

Recent Science and Technology

Journal homepage: https:// www.tci-thaijo.org/index.php/rmutsvrj/index

ISSN: 3057-0786 (Online)

Research Article

Organic Chinese Radish (*Raphanus sativus* L.) Cultivation in Raised Beds with Organic Amendments in Thailand

Pattana Somniyam [a] and Vimolchat Somniyam [a *]

[a] *Division of Agriculture, Faculty of Agriculture, Uttaradit Rajabhat University, Mueang, Uttaradit 53000, Thailand.*

Article history:

Received: 2025-09-23
Revised: 2026-07-02
Accepted: 2026-07-02

Keywords:

Chinese radish;
Raised bed;
Organic amendments;
Animal manure;
Plant-based residues

ABSTRACT

This study investigated the effects of combining animal manures and plant-based organic amendments on the growth and yield of Chinese radish under raised-bed cultivation in Thailand, in response to the increasing demand for chemical-free produce and national organic farming initiatives. A 3 × 6 factorial experiment arranged in a Completely Randomized Design (CRD) with three replications was conducted using three animal manures (cattle, poultry, and pig manure) and six plant-based residues (copper pod leaves, dried rice straw, rice husk biochar, rain tree leaves, old mushroom lumps, and filter cake). The results showed that animal manures primarily affected stem growth and root yield, whereas plant residues mainly influenced leaf characteristics. The interaction between animal manures and plant residues significantly affected leaf length, leaf biomass, and root size. Pig manure produced the tallest plants (28.94 cm) and enhanced canopy width, leaf dry weight, and root yield (40.26 cm, 19.31 g, 20.46 g fresh weight, and 1.39 g dry weight, respectively). Rice husk biochar significantly increased leaf width, leaf length, and leaf area (5.54 cm, 12.97 cm, and 45.79 cm², respectively). The combination of poultry manure and rice straw resulted in the highest leaf fresh and dry weights (310.54 and 29.34 g, respectively), while pig manure combined with filter cake produced the largest root diameter (64.16 mm), root circumference (19.33 cm), and root fresh weight (31.79 g). In contrast, poultry manure combined with mushroom lumps resulted in reduced growth and biomass accumulation compared with other treatment combinations. These findings demonstrate that appropriate combinations of organic amendments can improve nutrient availability, plant growth, and root development under raised-bed cultivation systems. The study highlights the potential of locally available organic materials for sustainable and chemical-free Chinese radish production in limited cultivation areas.

© 2026 Somniyam, P. and Somniyam, V. Recent Science and Technology published by Rajamangala University of Technology Srivijaya

1. Introduction

Chinese radish (*Raphanus sativus* L.) is a widely cultivated root vegetable in Thailand, appreciated for its culinary versatility, nutritional value, and economic significance. Traditionally grown in open-field systems, its production often relies on synthetic fertilizers and pesticides, which can deteriorate soil health, pollute water sources, and pose risks to consumer safety. Particularly concerning is the repeated cultivation of radish in the same plots two to three times per year, which may further deplete soil fertility over time (Thai Post, 2025). In response to growing consumer demand for chemical-free produce and national initiatives to expand organic farming, such as Thailand's plan to develop over 208,000 hectares of organic farmland (ASEAN Post, 2020). Thus, sustainable cultivation practices have garnered increasing attention. Moreover, limited agricultural land, rising demand for safe and sufficient food, an aging society, and labor shortages in the agricultural sector have collectively driven a shift in production processes and farming techniques. Under these constraints, intensive production systems and technological innovations have become essential to enhance efficiency and productivity. Among these, raised bed systems present a promising alternative to conventional field cultivation, particularly in tropical regions (Norsuwan *et al.*, 2021). Raised-bed cultivation provides another promising solution for small-scale chemical-free vegetable production. By

*** Corresponding author.**

E-mail address: *Vimolchat.som@uru.ac.th*

Cite this article as: Somniyam, P. and Somniyam, V. 2026. Organic Cultivation of Chinese Radish (*Raphanus sativus L.*) Using Raised Beds and Organic Amendments in Thailand. **Recent Science and Technology** 18(3): e269280.

https://doi.org/10.65411/rst.2026.269280

elevating the growing medium above ground level. Recent studies indicate that raised-bed systems can increase crop yields compared to conventional planting (Khwunsakun, 2022). These systems improve drainage, reduce soil-borne interference, and allow for precise control of growing media composition (Elizabeth *et al*., 2018). When paired with organic amendments, raised beds can enhance root development and minimize pest pressure, supporting chemical-free production (Brown, 2023; Sharma, 2021). One of the greatest advantages of raised bed is the ability to amend the soil for the bed. Diverse agricultural by- products can be used for growing substrates for the raised bed. Organic amendments such as rice husk biochar, mushroom waste, and sugarcane filter cake have shown potential to improve soil fertility, microbial activity, and nutrient retention. Rice husk biochar, for instance, increases cation exchange capacity and supports microbial diversity in degraded soils (De la Rosa *et al*., 2023). Filter cake, a byproduct of sugarcane processing, is rich in phosphorus and potassium, contributing to long-term soil productivity (Ketrot *et al*., 2026). Mushroom waste also offers high organic matter content and beneficial microbial populations, which can enhance water retention and plant vigor (Aiduang *et al*., 2025). The raw materials come from different origins, which may limit the amount of nutrients to crop requirements. The need for it combines with the animal manure, cattle, poultry, and pig manure, which are normally used as organic sources to obtain more nutritionally complete sources (Santos *et al*., 2025). Although previous studies have demonstrated the benefits of raised-bed cultivation and organic amendments for vegetable production, most studies have focused on the effects of individual organic materials or general organic fertilizer applications. Limited information is available regarding the combined use of locally available animal manures and plant-based residues under raised-bed systems, particularly for Chinese radish production in tropical environments. In addition, the compatibility of different organic amendment combinations and their influence on both vegetative growth and root development remain insufficiently understood. Therefore, this study aimed to evaluate the effects of combining different animal manures and plant-based organic materials on the growth and yield of Chinese radish cultivated under raised-bed conditions in Thailand.

Table 1 Chemical properties of planting materials amended with different animal manures after 60 days of fermentation.

Treatments	pH	EC (mS/cm)	OM (%)	Total N (%)	P (%)	K (%)
1. copper pod leaves + cattle manure	7.48	0.98	20.15	0.61	0.19	0.84
2. dried rice straw + cattle manure	7.80	1.00	11.90	0.47	0.13	1.09
3. rice husk biochar + cattle manure	7.53	0.88	13.70	0.38	0.16	0.47
4. rain tree leaves + cattle manure	7.58	0.89	14.23	0.53	0.13	0.87
5. old mushroom lumps + cattle manure	7.88	0.98	19.65	0.68	0.15	0.58
6. filter cake + cattle manure	7.42	1.01	18.42	0.85	0.74	0.82
7. copper pod leaves + poultry manure	7.65	1.80	21.11	1.01	1.44	0.60
8. dried rice straw + poultry manure	7.72	3.63	17.86	1.05	1.60	0.91
9. rice husk biochar + poultry manure	7.48	0.98	20.15	0.61	0.19	0.46
10. rain tree leaves + poultry manure	7.80	1.00	11.90	0.47	0.13	0.60
11. old mushroom lumps + poultry manure	7.90	2.31	23.44	0.97	1.33	0.82
12. filter cake + poultry manure	6.59	1.70	22.24	0.84	0.71	0.61
13. copper pod leaves + pig manure	7.40	1.92	18.92	1.00	1.50	0.86
14. dried rice straw + pig manure	6.60	1.94	19.78	0.82	1.87	0.62
15. rice husk biochar + pig manure	6.76	1.07	11.50	0.32	0.94	0.43
16. rain tree leaves + pig manure	6.55	1.17	14.30	0.84	0.69	0.49
17. old mushroom lumps + pig manure	7.38	1.32	23.14	0.86	0.73	0.68
18. filter cake + pig manure	6.67	2.16	19.35	0.92	1.28	1.00

Source: adapted from Somniyam *et al*. (2025a)

2. Materials and Methods

The effects of different organic amendments from plant-based and animal manures on the growth and yield of Chinese radish were studied. The study was performed at the plant nursery of the Faculty of Agriculture, Uttaradit Rajabhat University, Thailand, from May to July 2023. The experimental design was a 3 × 6 factorial arrangement in a Completely Randomized Design (CRD) with three replications. The two factors were: Factor A is the type of animal manure (three levels), including cattle manure, poultry manure, and pig

manure. Factor B is the type of plant-based organic matter (six levels), consisting of copper pod leaves (*Peltophorum pterocarpum* (DC.) K.Heyne), dried rice straw, rice husk biochar, rain tree leaves (*Samanea saman* (Jacq.) Merr.), old mushroom lumps, and filter cake (a sugarcane processing byproduct). All organic materials were air-dried and chopped or ground as appropriate before being mixed according to the treatment combinations at a ratio of 1:2:3 (soil: animal manure: organic material, v/v). The mixtures were composted for 60 days prior to use. The chemical properties of the composted were previously analyzed and reported by Somniyam *et al*. (2025a) as shown in Table1. Chinese radish seedlings were initially grown in seedling trays for 14 days and subsequently transplanted into black perforated plastic containers (66 cm in diameter and 53 cm in height), each filled with 20 L of the respective growing media. The containers were placed on steel bench shelves positioned 80 cm above ground level to facilitate drainage and reduce soil-borne interference, thereby simulating a raised-bed cultivation system. All containers were arranged randomly in the nursery and managed under standard organic cultivation practices. No synthetic fertilizers or pesticides were applied, and weed control was performed manually. Irrigation was provided via a micro-sprinkler system. Growth and yield data were recorded 45 days after transplanting. Growth parameters included plant height, number of leaves, leaf width and length, leaf area, canopy width, leaf greenness, leaf fresh weight, and leaf dry weight. Leaf greenness was measured using a SPAD-502DL chlorophyll meter (Minolta, Japan). Yield parameters included root length, root diameter, root circumference, root fresh weight, and root dry weight per plant. Root circumference was measured at the widest part of the root using a measuring tape. Leaf and root dry weights were determined after oven drying at 70°C until constant weight was achieved. Growth and yield measurements were recorded from all three plants within each container, and the average value per container was used for statistical analysis. Therefore, each container was considered one experimental unit. All data were subjected to analysis of variance (ANOVA) using IBM SPSS Statistics version 26. When significant differences were detected, means were compared using Duncan's New Multiple Range Test (DMRT) at a significance level of $p \leq 0.05$.

3. Results and Discussion

3.1 Growth characteristics of Chinese radish

The growth performance of Chinese radish was significantly influenced by the type of animal manure and plant-based organic matter used in the growing media. Analysis of variance revealed that animal manure type (Factor A) significantly affected stem height and number of leaves ($p \leq 0.05$), while plant-based organic matter (Factor B) significantly influenced leaf width and leaf length ($p \leq 0.05$ and $p \leq 0.01$, respectively). The interaction between Factors A and B was significant only for leaf length. Among the animal manures, pig manure resulted in the tallest plants (28.94 cm) and a high number of leaves (16.72), followed closely by poultry manure. In contrast, cattle manure produced significantly lower growth (24.52 cm, 14.17 leaves). These findings are consistent with the higher nutrient content of pig and poultry manures compared with cattle manure; pig manure provides a balanced nutrient profile with moderate nitrogen and phosphorus levels, supporting sustained vegetative growth (Somniyam *et al*., 2025a; Zhang *et al*., 2020). Both pig and poultry manure are known for their rapid mineralization and availability of N and P, which promote vegetative growth. Poultry manure, on the other hand, is rich in readily available nitrogen, which promotes rapid leaf development but may require careful management due to its high salt content (Bhattacharyya *et al*., 2015). Leaf width and length were less affected by manure type, with no significant differences detected.

Among plant residues, rice husk biochar produced the largest leaves, with the highest leaf width (5.54 cm) and leaf length (12.97 cm), followed closely by rain tree leaves (5.16 cm width, 12.78 cm length). These results align with biochar's ability to improve soil porosity, aeration, and water-holding capacity (Chen *et al*., 2017; Wang *et al*., 2022), creating a more favorable root-zone environment for nutrient and water uptake (Santos *et al*., 2025). Elshony *et al*. (2025) stated that radish plants cultivated in soil amended with biochar were positively correlated with increasing the added rate of biochar. Rain tree leaves may have contributed additional organic acids and moderate nutrient release, enhancing vegetative growth (Sangchote, 2008). In contrast, copper pod leaves and rice straw tended to produce narrower and shorter leaves (4.18, 4.25 cm width; 10.39, 10.55 cm length). The relatively lower performance of rice straw substrates can be attributed to their higher bulk density and slower decomposition rate, which may have limited nutrient availability during the growth period (Somniyam *et al*., 2025a; Bhattacharyya *et al*., 2015). The interaction between manure type and plant substrate significantly affected only the leaf length. The longest leaves (14.73 cm) were observed in the cattle manure plus rice husk biochar treatment, suggesting that biochar may have improved the utilization of nutrients supplied by cattle manure. Similarly, cattle manure + rain tree leaves and cattle manure + mushroom lumps also produced longer leaves (13.43,12.50 cm), indicating synergistic effects when cattle manure is supplemented with nutrients or organic matter-rich residues. In contrast, certain combinations performed poorly: poultry manure + mushroom lumps (8.80 cm) and pig manure + copper pod leaves (8.80 cm) resulted in the shortest leaves. These outcomes suggest possible nutrient imbalances or suboptimal decomposition when these residues were combined with nutrient-rich manures. For example, mushroom lumps, although high in organic matter, may temporarily immobilize nitrogen during decomposition,

while copper pod leaves have a high C:N ratio that could delay nutrient release (Somniyam *et al*., 2025b; Sangchote, 2008). These results demonstrate that both manure and substrate type contribute uniquely to radish growth. Plants amended with pig and poultry manure exhibited greater vegetative growth, reflected by significantly greater stem height than those receiving cattle manure. This may be associated with their relatively higher nutrient concentrations and EC values (Table 1), which could have enhanced nutrient availability during vegetative growth. Meanwhile, biochar and rain tree leaves improved leaf expansion, likely due to their favorable effects on physical properties and gradual nutrient release. The significant interaction for leaf length indicates that the choice of substrate can modulate the effectiveness of animal manures, either enhancing or suppressing growth depending on compatibility (Santos *et al*., 2025; Elshony *et al*., 2025). In practice, pairing cattle manure with biochar or rain tree leaves could overcome the nutrient limitations of cattle manure alone, while careful attention should be given to combinations like poultry manure with mushroom residues that may cause growth suppression (Table 2). The effects of animal manures and plant-based organic substrates demonstrate that both individual and combined organic amendments significantly influenced canopy development, leaf greenness, and biomass accumulation. Animal manure type significantly affected leaf greenness and dry weight. Poultry and pig manures enhanced canopy size (37.43, 40.26 cm) and leaf dry weight (19.31 g), compared with cattle manure, which resulted in smaller canopies (32.53 cm) and lower dry weight (13.89 g). These results are consistent with Zhang *et al*. (2020), who reported improved nutrient availability and vegetative growth under poultry-based amendments. These findings align with Jin *et al*. (2024), who demonstrated that supplementing organic fertilizer with reduced chemical input increased radish yield by 12.92 % and improved nutritional quality. Cattle manure produced the highest SPAD value (39.15), possibly due to slower but sustained N release maintaining chlorophyll levels (Fathi, 2022). No significant differences were observed in leaf area or fresh weight, indicating that manure type alone may not fully determine vegetative expansion. Plant-based type (factor B) significantly influenced leaf area and greenness ($p < 0.01$) and dry weight ($p < 0.05$). Rice husk biochar and rain tree leaves promoted larger leaf areas (45.79 cm^2 and 41.71 cm^2); biochar has been reported to enhance microbial diversity and nutrient retention in amended soils (Chen *et al*., 2017). Copper pod leaves resulted in the highest SPAD value (40.72), possibly due to their rapid decomposition and nutrient release (Sangchote, 2008).

Rain tree leaves supported higher dry biomass (>20 g), aligning with Bhattacharyya *et al*. (2015), who emphasized the efficacy of lignocellulosic residues in sustaining vegetative growth. Significant interactions were observed for leaf fresh weight ($p < 0.01$) and dry weight ($p < 0.05$), highlighting the synergistic impact of manure-substrate combinations. The combination of poultry manure + dried rice straw produced the highest leaf fresh weight (310.54 g) and dry weight (29.34 g), suggesting optimal nutrient synergy and microbial activity (Liu *et al*., 2018; Lesing and Anugoolprasert, 2016). Consistent with this result, Pavitra *et al*. (2024) and Suman *et al*. (2024) reported that poultry manure-based organic amendments improved vegetative growth, yield, and soil fertility. Conversely, some treatment combinations, particularly poultry manure combined with old mushroom substrate, produced relatively low leaf biomass. This response may have been partially associated with temporary nutrient immobilization during organic matter decomposition, which could reduce short-term nutrient availability of essential nutrients for plant uptake. In addition, differences in decomposition rates and nutrient release patterns between poultry manure and old mushroom substrate may have affected nutrient synchronization with crop demand, thereby limiting vegetative growth. These findings suggest that the effectiveness of organic amendment combinations depends not only on their nutrient content but also on the dynamics of nutrient mineralization and availability during plant growth. However, this effect was not clearly reflected in root yield parameters (Table 3, 4).

3.2 Root growth and yield characteristics of Chinese radish

Root traits showed moderate responses. Pig manure produced the largest root diameter (44.57 mm) and highest root fresh and dry weight (20.46 and 1.39 g), statistically similar to poultry manure (1.34 g), while cattle manure was lowest (1.04 g). This reflects pig and poultry manure's greater nutrient contributions (Somniyam *et al*., 2025a; Bhattacharyya *et al*., 2015). Among the plant residues, filter cake produced the highest radish yield, with the longest roots (139.51 mm) and greatest root biomass, confirming its effectiveness as a nutrient-rich organic amendment (Inthasan *et al*., 2023). Rice straw resulted in shorter roots and the lowest biomass, consistent with its slower mineralization. Significant interactions occurred for root diameter and circumference. Pig manure + filter cake produced the most vigorous roots (151.70 mm length, 64.16 mm diameter, 19.33 circumference, 31.79 g fresh weight, 1.60 g dry weight), showing strong synergy between high-nutrient manure and filter cake. By contrast, the combination of cattle manure and copper pod leaves produced relatively small roots, possibly due to low nutrient availability and reduced nutrient retention. Limited nutrient supply may have restricted carbohydrate allocation to the storage root, resulting in reduced root growth (Dong *et al*., 2025; Liang *et al*., 2024) (Table1, 4).

Table 2 Effects of animal manures and plant-based organic materials on vegetative growth of Chinese radish grown in raised beds.

Source of variation	Treatment	Stem height (cm)	Number of leaves	Leaf width (cm)	Leaf length (cm)
A	cattle manure	24.52±3.15^{b}	14.17±2.94^{b}	4.85±1.11	12.06±2.23
Animal manures	poultry manure	26.73±3.57^{ab}	16.94±2.08^{a}	4.89±0.92	11.61±2.16
	pig manure	28.94±4.08^{a}	16.72±2.86^{a}	4.64±1.03	11.18±1.90
B	copper pod leaves	27.78±3.23	15.44±2.29	4.18±0.82^{b}	10.39±2.11^{b}
Plant-based	dried rice straw	26.56±6.41	16.22±4.35	4.25±0.65^{bc}	10.55±1.68^{b}
organic materials	rice husk biochar	27.33±5.29	15.55±3.28	5.54±1.01^{a}	12.97±1.60^{a}
	rain tree leaves	25.26±2.95	16.11±5.75	5.16±1.19^{ab}	12.78±1.64^{a}
	old mushroom lumps	25.87±1.84	15.22±1.85	4.84±0.96^{abc}	11.35±2.65^{ab}
	filter cake	27.58±2.90	17.11±3.01	4.78±0.89^{abc}	11.65±1.69^{ab}
A x B interaction	cattle manure+copper pod leaves	25.50±1.48	16.66±1.52	4.79±1.01	10.92±1.12^{bcd}
	cattle manure+dried rice straw	20.60±3.56	12.00±2.00	4.06±0.51	9.00±0.52^{cd}
	cattle manure+rice husk biochar	27.43±3.82	15.00±5.19	4.10±0.78	14.73±0.50^{a}
	cattle manure+rain tree leaves	22.90±1.65	13.33±3.78	5.86±0.61	13.43±1.90^{ab}
	cattle manure+old mushroom lumps	24.77±1.40	13.66±1.15	6.20±1.32	12.50±1.08^{ab}
	cattle manure+filter cake	25.90±2.46	14.33±2.30	4.60±0.36	11.80±2.46^{abcd}
	poultry manure+copper pod leaves	29.57±4.71	15.66±1.15	4.30±0.88	11.46±3.21^{abcd}
	poultry manure+dried rice straw	29.50±8.07	18.66±3.51	4.90±0.96	11.40±1.05^{bcd}
	poultry manure+rice husk biochar	31.73±3.62	13.66±0.57	4.33±0.20	12.43±1.45^{ab}
	poultry manure+rain tree leaves	28.70±1.32	20.00±8.88	5.56±1.62	12.83±2.15^{ab}
	poultry manure+old mushroom lumps	25.77±1.56	15.00±1.73	4.93±0.80	8.80±2.06^{d}
	poultry manure+filter cake	28.37±2.96	18.66±2.08	4.40±0.95	12.76±0.40^{ab}
	pig manure+copper pod leaves	27.77±3.23	14.00±3.46	5.23±0.68	8.80±0.52^{d}
	pig manure+dried rice straw	26.56±6.41	18.00±4.35	3.60±0.45	11.26±2.12^{bcd}
	pig manure+rice husk biochar	27.33±5.28	18.00±1.00	4.33±1.01	11.76±0.83^{abcd}
	pig manure+rain tree leaves	25.26±2.95	15.00±1.73	5.20±0.88	12.10±1.12^{abc}
	pig manure+old mushroom lumps	25.87±1.84	17.00±1.00	4.36±0.80	12.76±2.84^{ab}
	pig manure+filter cake	27.58±2.90	18.33±3.05	5.53±1.25	10.40±1.00^{bcd}
F-test	A	*	*	ns	ns
	B	ns	ns	*	**
	A x B	ns	ns	ns	*
C.V. (%)		12.76	20.91	19.07	14.51

Data are presented as mean ± standard error (n = 3). ns, *, and ** indicate non-significant, significant at $P < 0.05$, and significant at $P < 0.01$, respectively. Means followed by different letters within the same column are significantly different according to Duncan's Multiple Range Test (DMRT) at $P \leq 0.05$.

Table 3 Effects of animal manure and organic planting substrate on leaf morphology and biomass of Chinese radish grown in raised beds.

Source of variation	Treatment	Leaf area (cm^2)	Canopy width (cm)	Greenness (SPAD)	Leaf fresh weight (g)	Leaf dry weight (g)
A	cattle manure	37.91±15.43	32.53±5.10^{b}	39.15±2.61^{a}	161.77±66.32	13.89±5.58^{b}
Animal manures	poultry manure	35.87±12.89	37.43±5.61^{a}	35.28±5.79^{b}	180.02±86.08	19.31±9.13^{a}
	pig manure	32.75±11.63	40.26±6.81^{a}	33.63±6.77^{b}	177.62±69.99	19.31±8.20^{a}
B	copper pod leaves	27.59±11.63^{b}	35.47±6.81	40.72±5.31^{a}	182.32±64.09	19.09±8.20
Plant-based	dried rice straw	28.02±6.58^{b}	32.90±7.37	32.93±8.59^{b}	200.08±104.64	19.72±8.76
organic materials	rice husk biochar	45.79±12.85^{a}	39.96±8.48	36.84±2.22^{ab}	141.55±26.15	14.55±3.64
	rain tree leaves	41.71±15.13^{a}	35.83±4.76	35.95±3.87^{b}	197.17±53.96	21.01±5.30
	old mushroom lumps	35.34±14.61^{ab}	36.92±6.82	35.61±4.96^{b}	163.29±87.48	14.35±7.65
	filter cake	34.59±10.16^{ab}	39.35±2.98	34.08±5.65^{b}	154.41±80.31	16.29±10.07
A x B	cattle manure+copper pod leaves	26.22±5.66	29.00±4.67	40.83±4.18	184.71±33.08^{bcd}	16.81±2.95^{abcd}
interaction	cattle manure+dried rice straw	23.40±5.75	26.10±2.00	40.73±0.20	125.45±77.60^{bcd}	10.16±6.12^{cd}
	cattle manure+rice husk biochar	55.58±3.82	35.73±1.47	37.26±1.45	162.55±5.59^{bcd}	13.29±2.55^{bcd}
	cattle manure+rain tree leaves	52.38±18.10	34.90±1.47	36.73±3.68	179.82±31.55^{bcd}	17.29±2.79^{abcd}
	cattle manure+old mushroom lumps	35.86±3.49	31.26±4.18	38.96±0.23	236.82±75.47^{ab}	18.42±6.16^{abcd}
	cattle manure+filter cake	34.00±16.49	38.20±4.27	40.40±0.72	81.25±46.08^{d}	7.36±4.53^{d}
	poultry manure+copper pod leaves	36.79±16.76	38.10±1.91	38.50±5.11	226.01±48.68^{abc}	24.40±5.06^{ab}
	poultry manure+dried rice straw	29.18±2.10	34.53±4.90	32.53±8.83	310.54±54.20^{a}	29.34±3.89^{a}
	poultry manure+rice husk biochar	43.04±18.84	38.96±11.00	37.33±1.96	117.98±29.80^{cd}	13.92±4.09^{bcd}
	poultry manure+rain tree leaves	41.94±14.80	38.53±8.44	39.30±1.15	178.28±47.37^{bcd}	19.71±5.32^{abcd}
	poultry manure+old mushroom lumps	24.91±11.28	34.96±2.50	33.36±6.92	77.29±21.88^{d}	7.19±1.13^{d}
	poultry manure+filter cake	39.36±5.21	39.50±2.71	30.70±5.80	170.03±59.81^{bcd}	21.30±12.70^{abc}
	pig manure+copper pod leaves	19.77±2.50	39.33±8.03	42.83±7.43	136.24±83.15^{bcd}	16.06±14.45^{abcd}
	pig manure+dried rice straw	31.48±9.17	38.06±8.73	25.53±6.63	164.26±79.13^{bcd}	19.66±10.07^{abcd}
	pig manure+rice husk biochar	38.74±7.84	45.20±9.75	35.93±3.45	144.14±17.67^{bcd}	16.44±4.62^{abcd}
	pig manure+rain tree leaves	30.83±4.57	34.06±0.76	31.83±1.44	233.40±73.83^{ab}	26.03±3.90^{ab}
	pig manure+old mushroom lumps	45.24±20.10	44.53±4.67	34.50±4.92	175.74±70.74^{bcd}	17.45±8.89^{abcd}
	pig manure+filter cake	30.42±7.32	40.36±2.51	31.16±2.01	211.95±82.09^{abc}	20.22±6.56^{abcd}
F-test	A	ns	**	**	ns	*
	B	**	ns	*	ns	ns
	A x B	ns	ns	ns	**	*
C.V.(%)		32.09	15.24	12.53	33.11	38.98

Data are presented as mean ± standard error (n = 3). ns, *, and ** indicate non-significant, significant at $P < 0.05$, and significant at $P < 0.01$, respectively. Means followed by different letters within the same column are significantly different according to Duncan's Multiple Range Test (DMRT) at $P \leq 0.05$.

4. Conclusion

This study demonstrates that the combination of specific animal manures and plant-based residues significantly influences the growth and yield of Chinese radish under raised bed systems. The results indicated that animal manures mainly influenced stem growth and root yield, while plant residues primarily affected leaf characteristics. Their combinations significantly influenced leaf length, leaf biomass, and root size. Among the tested manures, pig manure was the most effective in promoting plant growth and root yield. Among residues, rice husk biochar improved structural conditions and leaf expansion, rain tree leaves promoted both leaf and root development, and filter cake provided high nutrient content for robust root growth.

These findings highlight the importance of matching nutrient-rich manures with suitable plant residues to optimize growing media conditions. Effective combinations enhanced plant growth, whereas unsuitable mixtures reduced crop performance. The raised bed system likely further improved root-zone conditions, contributing to greater yield and root development in Chinese radish and potentially other edible root crops.

Table 4 Effects of animal manures and plant-based organic materials on root growth and yield characteristics of Chinese radish grown in raised beds.

Source of variation	Treatment	Root length (mm)	Root diameter (mm)	Root circumference (cm)	Root fresh weight (g)	Root dry weight (g)
A	cattle manure	114.34±34.98	41.25±8.53	13.96±2.61	17.13±7.18	1.04±0.36^{b}
Animal manures	poultry manure	130.45±27.71	42.24±8.84	14.25±2.47	18.75±5.54	1.34±0.39^{a}
	pig manure	129.58±31.83	44.57±14.48	14.44±3.48	20.46±7.92	1.39±0.35^{a}
B	copper pod leaves	110.39±36.74	44.68±8.56	14.78±2.65	19.91±5.72	1.34±0.35
Plant-based	dried rice straw	107.11±42.95	38.20±8.96	13.04±2.73	16.27±7.42	1.07±0.42
organic matter	rice husk biochar	134.26±22.72	41.69±10.43	13.70±2.47	16.43±6.94	1.14±0.36
	rain tree leaves	130.88±33.42	43.80±8.83	14.60±2.40	18.37±4.69	1.44±0.27
	old mushroom lumps	126.59±14.50	40.38±9.04	13.68±2.81	19.60±7.29	1.14±0.37
	filter cake	139.51±27.26	47.93±17.00	15.48±3.82	22.10±9.02	1.39±0.49
A x B interaction	cattle manure+copper pod leaves	82.23±41.86	39.50±2.65^{b}	13.00±1.12^{b}	17.97±3.39	1.21±0.26
	cattle manure+dried rice straw	83.13±42.65	35.30±9.84^{b}	12.16±3.19^{b}	13.79±9.83	0.92±0.59
	cattle manure+rice husk biochar	138.03±16.45	41.66±3.54^{b}	14.40±1.77^{b}	17.59±7.50	1.13±0.43
	cattle manure+rain tree leaves	116.06±8.45	47.16±11.25^{ab}	15.30±2.85^{ab}	17.52±2.33	1.25±0.12
	cattle manure+old mushroom lumps	136.30±19.97	47.23±13.26^{ab}	15.86±4.24^{ab}	22.16±13.49	0.80±0.34
	cattle manure+filter cake	130.29±33.69	38.38±4.85^{b}	13.03±1.10^{b}	13.78±3.76	0.91±0.35
	poultry manure+copper pod leaves	123.66±16.21	51.25±9.67^{ab}	16.76±2.80^{ab}	20.66±6.22	1.44±0.44
	poultry manure+dried rice straw	131.76±28.03	44.69±8.98^{b}	15.03±2.60^{ab}	19.81±7.47	1.23±0.47
	poultry manure+rice husk biochar	123.65±20.24	34.84±6.80^{b}	11.93±0.75^{b}	10.78±0.27	0.84±0.05
	poultry manure+rain tree leaves	144.01±60.72	46.85±9.25^{ab}	15.56±2.61^{ab}	21.91±6.20	1.59±0.33
	poultry manure+old mushroom lumps	123.04±4.18	34.52±2.36^{b}	12.10±0.60^{b}	18.61±1.99	1.28±0.10
	poultry manure+filter cake	136.56±28.49	41.26±4.15^{b}	14.10±1.20^{b}	20.73±0.86	1.67±0.31
	pig manure+copper pod leaves	125.30±39.99	43.30±9.20^{b}	14.60±2.87^{ab}	21.11±8.48	1.38±0.45
	pig manure+dried rice straw	106.43±54.77	34.63±7.01^{b}	11.93±2.00^{b}	15.23±6.21	1.07±0.30
	pig manure+rice husk biochar	141.10±33.53	48.56±15.34^{ab}	14.76±3.70^{ab}	20.91±7.52	1.46±0.24
	pig manure+rain tree leaves	132.56±10.81	37.40±2.69^{b}	12.93±1.37^{b}	15.67±3.68	1.48±0.27
	pig manure+old mushroom lumps	120.43±14.44	39.40±4.70^{b}	13.10±1.37^{b}	18.03±3.43	1.35±0.41
	pig manure+filter cake	151.70±25.76	64.16±22.73^{a}	19.33±4.68^{a}	31.79±7.95	1.60±0.47
F-test	A	ns	ns	ns	ns	*
	B	ns	ns	ns	ns	ns
	A x B	ns	*	*	ns	ns
C.V. (%)		25.44	22.63	17.97	34.59	28.63

Data are presented as mean ± standard error (n = 3). ns, *, and ** indicate non-significant, significant at P < 0.05, and significant at P < 0.01, respectively. Means followed by different letters within the same column are significantly different according to Duncan's Multiple Range Test (DMRT) at p< 0.05

5. Acknowledgments

We would like to thanks to the Faculty of Agriculture, Uttaradit Rajabhat University, for providing facilities and utilities that greatly contributed to the research process.

6. References

Aiduang, W., Jatuwong, K., Kiatsiriroat, T., Kamopas, W., Tiyayon, P., Jawana, R., Xayyavong, O. and Lumyong, S. 2025. Spent mushroom substrate-derived biochar and its

applications in modern agricultural systems: An extensive overview. **Life** 15(2): 317.

ASEAN Post. 2020. **Organic farming in southeast Asia**. The ASEAN Post. Available Source: https://theaseanpost .com/article/organic-farming-southeast-asia, November 11, 2020.

Bhattacharyya, R., Kundu, S., Sharma, A.R. and Singh, R.K. 2015. Relative efficacy of organic amendments for improving growth and yield of vegetable crops. **Sustainable Agriculture Reviews** 14: 129-161.

Brown, E. 2023. **10 soil additions that supercharge raised beds and 5 that will do the opposite.** Complete Gardening. Available Source: https://completegardening.com, August 10, 2025.

Chen, B., Zhou, D. and Zhu, L. 2017. Use of biochar for sustainable agriculture: Benefits and environmental impacts. **Journal of Soil Science and Plant Nutrition** 17(3): 553–565.

De la Rosa, J.M., Pérez-Dalí, S.M., Campos, P., Sánchez-Martín, Á., González-Pérez, J.A. and Miller, A.Z. 2023. Suitability of volcanic ash, rice husk ash, green compost and biochar as amendments for a Mediterranean alkaline soil. **Agronomy** 13(4): 1097.

Dong, H.T., Li, Y., Brown, P., Akbar, D. and Xu, C.Y. 2025. Effects of nitrogen application on soluble sugar and starch accumulation during sweet potato storage root formation. **Horticulturae** 11: 837.

Elizabeth, A.M., Sarah, T.L. and Sam, E.W. 2018. Raised beds for vegetable production in urban agriculture. **Urban Agriculture and Regional Food System** 3(1): 1-9.

Elshony, M., Farid, I.M., Alkamar, F., Abbas, H.H., Mohamed, I. and Abbas, M.H.H. 2025. Effects of organic amendments on soil productivity, its physical and chemical properties: A review of compost and biochar applications. **Biochar and Compost Technology** 2(1): 72-91.

Fathi, A. 2022. Role of nitrogen (N) in plant growth, photosynthesis pigments, and N use efficiency: A review. **Agrisost** 28: 1-8.

Inthasan, J., Suwanpingka, T. and Dechjiraratthanasiri, C. 2023. Effects of sugarcane filter cake on chemical properties of soil series group No.35. **Journal of Agriculture** 39(1): 59-70.

Jin, D., Lu, Z., Song, X., Ahammed, G.J., Yan, Y. and Chen, S. 2024. Improvement of yield and quality properties of radish by the organic fertilizer application combined with the reduction of chemical fertilizer. **Agronomy** 14(8): 1847.

Ketrot, D., Saribut, S., Sombatcharoennon, A., Peungyam, W., Poomsong, K., Jaroenchasri, R. and Wisawapipat, W. 2026. Release of nitrogen, phosphorus, and potassium from filter cake, filter cake biochar, and sugarcane bagasse ash in a laboratory study. **International Journal of Recycling of Organic Waste in Agriculture** 15(1): 24-31.

Khwunsakun, C. 2022. Research and development of growing bench for quality vegetables production. **Agriculture and Technology** 3(1): 60-74.

Lesing, S. and Anugoolprasert, O. 2016. Efficacy of high-quality organic fertilizer on growth and yield of Chinese kale. **Thai Science and Technology** 24(2): 320-332.

Liang, D., Ning, Y., Ji, C., Zhang, Y., Wu, H., Ma, H., Zhang, J. and Wang, J. 2024. Biochar and manure co-application increases rice yield in low productive acid soil by increasing soil pH, organic carbon, and nutrient retention and availability. **Plants** 13(7): 973.

Liu, X., Zhang, Y., Han, W., Tang, A., Shen, J., Cui, Z. and Zhang, F. 2018. Enhanced crop yields and soil quality improvements under organic amendments in intensive agriculture: A meta-analysis. **Agronomy** 110(1): 1-11.

Norsuwan, T., Utthasuk, K., Punyasai, T., Saltikulnukarn, T., Chaima, R., Suppakittpaisarn, P., Yaipimol, E., Surinseng, V., Charoenlertthanakit, N. and Kaeomuangmoon, T. 2021. Urban agriculture and BCG economic model. **Agricultural Research and Extension** 38(3): 100-116.

Pavitra, K., Thakur, V., Sharma, S. and Bhat, S.A. 2024. Efficacy of organic amendments and biofertilizers on yielding, biochemical and soil nutritional attributes of radish (*Raphanus sativus L.*). **International Journal of Recycling of Organic Waste in Agriculture** 13(4): 132447.

Sangchote, H. 2008. **Effects of leaf-litter decomposition of forest and fruit tree species on soil chemical properties**. Master of Science (Soil Science), Chiang Mai University. (in Thai)

Santos, M.G.B.d., Paiva, A.B., Viana, R.d. S.R., Jindo, K. and Figueiredo, C.C. 2025. Biochar as a feedstock for sustainable fertilizers: Recent advances and perspectives. **Agriculture** 15(8): 894.

Sharma, A. 2021. Raised bed cultivation: A regenerative planting technology to stimulate vegetable production. **Gri Meet** 1(11): 1-13.

Somniyam, P., Pupakdeepan, W., Phatdiphanpreeda, P. and Somniyam, V. 2025a. Effect of composted plant based and animal derived materials on Chinese kale (*Brassica oleracea var. alboglabra*) performance in raised beds. **International Journal of Agricultural Technology** 21(5): 2007-2020.

Somniyam, P., Somniyam, V., Pupakdeepan, W., Phatdiphanpreeda, P. and Bunyat, P. 2025b. **The potential of local materials on some of organic vegetables production by using growing bench technique: Case study Uttaradit PGS farmer group**. Final report. Faculty of Agriculture, Uttaradit Rajabhat University. (in Thai)

Suman, S., Singh, S.K. and Bhati, D. 2024. Nutrient management through organic amendments to ensure sustainable and economic cultivation of radish. **Plant Science Today** 11(2).

Thai Post. 2025. **Khon Kaen's prolonged cold weather boosts radish farming: Large, white, plump roots fetch high prices**. Thai Post. Available Source: https://www.thaipost.net/district-news/735651, February 6, 2025. (in Thai)

Wang, H., Cheng, Y., Jin, M., Liu, Z., Shi, L. and Lu, C. 2022. Effects of rice husk biochar on nitrogen conversion and fixation in sheep manure composting. **Chinese Agricultural Science Bulletin** 38(27): 51-59.

Zhang, H., Zhao, X., Wang, X. and Wang, G. 2020. Effects of different animal manures on nutrient availability and growth of leafy vegetables. **Journal of Plant Nutrition** 43(8): 1156-1166.

Recent Science and Technology 2026, Vol. 18(3): e270270

Recent Science and Technology

Journal homepage: https:// www.tci-thaijo.org/index.php/rmutsvrj/index

ISSN: 3057-0786 (Online)

Research Article

Physical and Combustion Properties of Charcoal Briquettes Produced from Mangrove Wood and Coconut Shell Waste

Wasu Suksuwan [a], Prateep Tippracha [a], Sopida Jornden [b], Pacharakron Chantaramanee [c], Suwat Rattanapan [d] and Suchart Chantaramanee [b *]

[a] *Department of Mechanical Engineering, Faculty of Engineering, Rajamangala University of Technology Srivijaya, Songkhla 90000, Thailand.*
[b] *Department of Industrial Engineering, Faculty of Engineering, Rajamangala University of Technology Srivijaya, Songkhla 90000, Thailand.*
[c] *Department of Mechanical and Mechatronics Engineering, Faculty of Engineering, Prince of Songkla University, Songkhla 90112, Thailand.*
[d] *Department of Science, Faculty of Science and Technology, Rajamangala University of Technology Srivijaya, Nakhon Si Thammarat Campus (Sai Yai), Nakhon Si Thammarat 80110, Thailand.*

Article history:

Received: 2025-12-22
Revised: 2026-06-12
Accepted: 2026-07-02

Keywords:

Charcoal briquettes;
Biomass fuel;
Physical properties;
Calorific value;
Combustion characteristics

ABSTRACT

This research examines the physical and combustion properties of charcoal briquettes produced from mangrove wood and coconut shell agricultural residues, which were fabricated using a cylindrical compression mould. The seven formulations were prepared with mangrove wood and coconut shell ratios of 100 : 0, 90 : 10, 80 : 20, 70 : 30, 60 : 40, 50 : 50, and 0 : 100. The entire mixture consists of 0.5 kg of tapioca starch (binding agent) and 3 L of tap water. The charcoal briquettes have an outer diameter of 40 mm, an inner diameter of 14 mm, and a height of 80 mm. The properties analysed included physical properties: particle size, true density, moisture content and combustion properties: total heat value, and fuel usage characteristics. The particle size analysis revealed that mangrove charcoal powder had a finer average particle size of 48.2 ± 1.75 µm compared to coconut shell charcoal powder of 285.4 ± 20.36 µm. The true densities of mangrove wood and coconut shell charcoals were 1.3690 ± 0.0019 g/cm^3 and 1.4095 ± 0.0016 g/cm^3, respectively, indicating similar intrinsic density. Every formulation satisfied the Community Product Standard for Charcoal Briquettes (M.P.Ch. 238/2547) and had a gross calorific value ranging from 5,897 ± 510 kcal/kg to 6,886 ± 420 kcal/kg and a moisture content ranging from 4.211 ± 0.127% to 4.887 ± 0.164%. A higher coconut-shell fraction generally increased calorific value. During combustion, formulation M60C40 ignited fastest (7 min) and had the longest burn-to ash-time, 223 min, making it well-suited for long-duration applications. No formulation produced sparks during usability tests. In summary, the M70C30 formula releases little smoke and provides a consistent medium flame, indicating excellent performance for this research.

© 2026 Suksuwan, W., Tippracha, P., Jornden, S., Chantaramanee, P., Rattanapan, S. and Chantaramanee, S. Recent Science and Technology published by Rajamangala University of Technology Srivijaya

1. Introduction

Renewable energy continues to grow in importance amid global anxiety over climate change (Lomunyak *et al*., 2024). The Earth's surface temperature tends to rise continuously. The scientific consensus suggests that the increase in temperature should be limited to 2 °C or less (Malte *et al*., 2009). The rise in global temperatures is mainly due to the continued expansion of fossil fuel use and various human activities that increase the concentration of greenhouse gases in the atmosphere. To address the significant impacts of climate change, international cooperation and agreements are initiated to control and reduce greenhouse gas emissions. Thailand has embraced international approaches to mitigate and adapt to such changes through its active participation in the 26th Conference of the Parties (COP 26) within the United Nations Framework Convention on Climate Change. The 13th National Economic and Social Development Plan (2023-2027) integrates

* **Corresponding author.**
E-mail address: *suchart.c@rmutsv.ac.th*

Cite this article as:

Suksuwan, W., Tippracha, P., Jornden, S., Chantaramanee, P., Rattanapan, S. and Chantaramanee, S. 2026. Physical and Combustion Properties of Charcoal Briquettes Produced from Mangrove Wood and Coconut Shell Waste. **Recent Science and Technology** 18(3): e270270.
https://doi.org/10.65411/rst.2026.270270

the concept of bio-circular economy-green economy (BCG Model) with a special emphasis on the green economy dimension, with a focus on the sustainable use of natural resources and environmental management, in line with Strategic Goal 10 to promote a circular economy and a low-carbon society (Jomsurang and Anamai, 2024). This approach is also in line with Sustainable Development Goal 13, which focuses on urgent action to address climate change and its impacts (Winfried and Claudia, 2018). The conceptual framework and operational approach serve as an important mechanism to support the development of a variety of renewable energy sources, such as solar energy, hydroelectric and hydro power, wind energy, waste-to-energy, geothermal energy, and biomass energy (Department of Renewable Energy Development and Conservation, 2024). This study focuses mainly on biomass energy as a potential alternative energy source. It focuses on utilizing agricultural waste generated after harvest (Saleem, 2022). According to 2023 data, Thailand has about 101.82 million km^2 of rainforest area, while the total agricultural area is 153,184,527 km^2, or 47.77% of the country's total area. The agrarian terrain that covers this large area generates substantial biomass waste, which can be efficiently processed into solid fuel (Pattaraanong *et al*., 2021).

Previous studies have examined the potential of various biomass sources for producing charcoal briquettes. The feasibility of using pineapple peel as a raw material for briquettes was assessed by reviewing different weight-based mixing ratios 80 : 20, 70 : 30, 60 : 40, and 50 : 50. The resulting cylindrical briquettes with an outer diameter of 4 cm, an inner diameter of 1 cm and a length of 10 cm have calorific values ranging from 5,051.51 cal/g to 5,240.95 cal/g (Titiporn and Chotika, 2018). Briquettes made from agricultural waste include coconut shells (tall varieties), dried lamut leaves, and durian sawdust, reported heating values of 4,910.82 cal/g, 3,195.757 cal/g, and 5,067.55 cal/g, respectively (Roseleena *et al*., 2019). The influence of composite materials on the mechanical and thermal properties of coconut shell briquettes resulted in an average moisture content of 5.6% and a maximum average calorific value of 5,515.33 cal/g (Amnouy *et al*., 2019). The briquettes developed from longan wood charcoal powder, water, and tapioca starch in a ratio of 0.47:0.47:0.06 have a moisture content of 6.65 ± 0.03% and a calorific value of 5,509.85 ± 0.65 cal/g (Kritsada and Nirubol, 2020). The use of waste materials from durian and mangosteen plantations, by combining large branches, small branches, leaves, and fruits in a ratio of 1:1:1:1, with tapioca starch and molasses as binders at weight ratios of 8:2 and 7:3, resulted in briquettes having calorific values ranging from 5,100 to 5,840 cal/g and 5,205-5,640 cal/g, respectively (Amon, 2021). The grapefruit peel cubes have an average calorific value of 5,344 cal/g and a moisture content ranging from 8.35% to 11.14% (Sirichai and Changwat, 2022). Only four bamboo charcoal briquette formulations complied with the community product standards for charcoal briquettes (M.P.Ch. 238/2004) (Jutapol *et al*., 2022). The fuel briquettes are produced from biowaste materials, including municipal wastewater sludge, agricultural waste, and tapioca starch sludge as binders at mixing ratios of 0.35:0.40:0.25 and 0.65:0.15:0.20 (kg:kg:kg), with a calorific value of 5,158.09 cal/g (Ratchatorn and Jaruwan, 2022). Overall, most previous studies have indicated that briquettes obtained from various biomass sources and mixing ratios can achieve acceptable calorific values. Moisture content and related properties that comply with the requirements of the Community Product Standard M.P.Ch. 238/2547. However, other high-potential local biomass sources, such as mangrove charcoal and coconut shells, have not been comprehensively studied or evaluated, so further investigation is needed (Kabir *et al*., 2022). This study investigated charcoal derived from coconut shells as a biomass fuel, with particular emphasis on its calorific value, which reached 19.4 MJ/kg, and its moisture content of 5.6%, both of which exceeded previously reported values. Additionally, charcoal briquettes are biomass fuels produced from agricultural residues, such as sawdust, rice husks, and coconut shells. They provide consistent heat, long burning duration, and low smoke and ash emissions, while reducing waste, lowering costs, and promoting sustainable, renewable energy use.

Therefore, this research aims to investigate the physical and combustion properties of composite charcoal briquettes made from waste mangrove wood charcoal and coconut shell charcoal using a cylindrical compression mold. This sustainable energy alternative can indirectly help reduce greenhouse gas concentrations by replacing fossil fuels in everyday activities like cooking, thereby alleviating environmental concerns.

2. Materials and Methods

2.1 Raw materials

This research utilized agricultural waste materials consisting of various sizes of mangrove wood scraps from the species Rhizophora mucronata (Nuryawan *et al*., 2025) and coconut shell fragments from native coconut varieties are dense, durable, and resistant to breakage and abrasion due to their composition of lignin, cellulose, and hemicellulose, which were obtained from a community forest in the mangrove area of Songkhla Province, Thailand.

2.2 Sample preparation

The charcoal samples were prepared by carbonizing the raw agricultural waste residues, specifically the mixed-sized mangrove wood and coconut shell waste, to serve as the primary materials for composite briquette production. Each type of waste was separately carbonized using a 200 L charcoal kiln. This charcoal kiln consists of (1) the furnace body, (2) a smoke pipe for observing combustion, (3) three smoke pipes for releasing smoke from the furnace, (4) a chimney pipe, (5)

a wood vinegar collection chamber, (6) a fuel feeding inlet, and (7) a front furnace cover, as shown in the Figure 1.

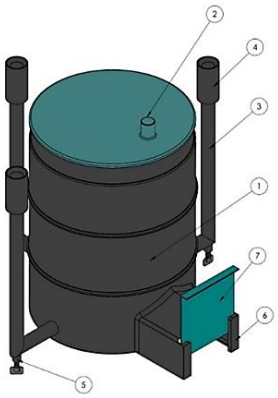


Figure 1 The illustration of a 200-litre charcoal kiln.

For efficient carbonization, the waste materials were uniformly distributed within the kiln to ensure even heat distribution and complete charring. After loading, the kiln lid was sealed. The combustion process was initiated through the fuel feeding port. Smoke emissions were monitored for 15 min. to ensure complete discharge of the initial, toxin-rich plume. After 3 h, when the smoke had turned white, the kiln lid and fuel-feeding port were sealed tightly with clay-soaked cloths. After an additional 2 h, three clay-wrapped "poultices" were used to seal the ends of the left, right, and rear smoke pipes, leaving only the accelerating air vent open. When the smoke emanating from this vent became diluted, the vent was sealed, allowing the charring process to complete within the kiln. The kiln carbonizes biomass by pyrolysis heating in limited oxygen at roughly 300-800 °C. This process effectively drives out moisture from the wood, transforming the material into charcoal. The resulting charcoal was black in appearance and was retrieved from the kiln on the following day, as shown in Figure 2.



(A) (B)

Figure 2 Charcoal types (A) Mangrove charcoal and (B) Coconut shell charcoal.

2.3 Preparation of charcoal powder and mixture design

Following the carbonization process, both mangrove wood charcoal and coconut shell charcoal were separately ground into fine powder using a grinding machine equipped with a 5 hp motor operating at 2,890 revolutions per minute (rpm) was used, and the mixing process was conducted for 20 min.

Subsequently, mixtures were prepared for the fabrication of cylindrical charcoal briquettes. A total of seven experimental ratios were designed based on the weight percentages of mangrove wood charcoal (M) and coconut shell charcoal (C) as follows: 100:0, 90:10, 80:20, 70:30, 60:40, 50:50, and 0:100. These ratios were designated as M100C0, M90C10, M80C20, M70C30, M60C40, M50C50, and M0C100, respectively. For all mixtures, cassava starch (Siwakorn *et al*., 2026) was consistently used as a binder at a fixed volume of 0.5 kg, and tap water was added at a constant volume of 3 L. All measurements were performed precisely using a digital weighing scale (Model SF 400) with a resolution of ± 1 g. The detailed experimental design is presented in Table 1.

Table 1 Experimental design showing the mixing ratios of mangrove charcoal and coconut shell charcoal.

Recipe name	Mixing ratio	Raw Materials			
		Mangrove (kg)	Coconut shell (kg)	Tapioca starch (kg)	Water (L)
M100C0	100 : 0	100	0	0.5	3
M90C10	90 : 10	90	10	0.5	3
M80C20	80 : 20	80	20	0.5	3
M70C30	70 : 30	70	30	0.5	3
M60C40	60 : 40	60	40	0.5	3
M50C50	50 : 50	50	50	0.5	3
M0C100	0 : 100	0	100	0.5	3

Once the desired weights of the ingredients were obtained, the finely ground charcoal powder, cassava starch, and tap water were thoroughly mixed to achieve a homogenous consistency. The prepared mixture was then fed into a cylindrical compression mould at a predetermined quantity. A TMC hydraulic press, with a maximum compaction force of 160 N was used to compress the mixture into briquettes. Immediately after compression, while still moist, the cylindrical briquette samples were carefully demoulded.

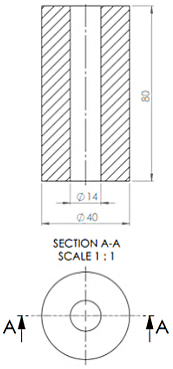


Figure 3 The illustration of a green charcoal.

The resulting "green charcoal" briquettes had an outer diameter of 40 mm, an inner hole diameter of 14 mm, and a height of 80 mm, as illustrated in the Figure 3 and representative green charcoal briquette specimens for different mixing ratios in Figure 4.

2.4 Physical properties testing

Figure 5 illustrates the charcoal powder utilized for the particle size analysis of the initial raw materials, specifically the

mixed-sized mangrove wood charcoal powder and coconut shell charcoal powder. Random samples of the fine-ground powder were sieved and then analyzed using a Laser Particle Size Analyzer (LPSA2), ANLYSETTE 22 Nano Tec, FRITSCH, and Germany.

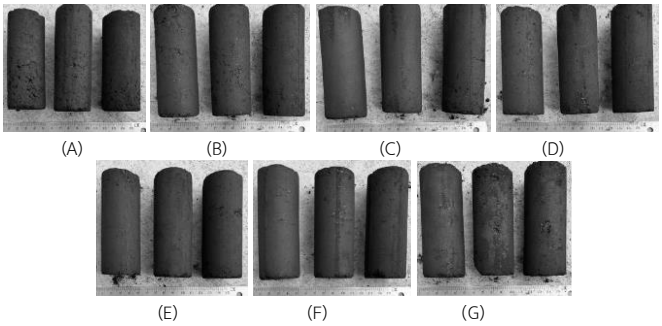
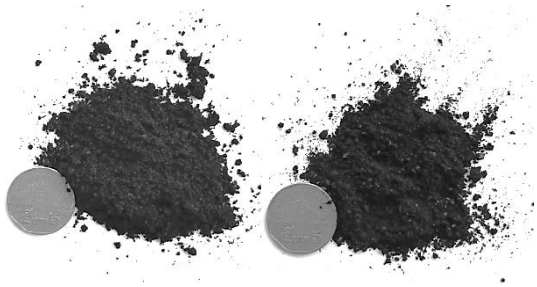


Figure 4 Representative green charcoal briquette specimens for different mixing ratios: (A) M100C0, (B) M90C10, (C) M80C20, (D) M70C30, (E) M60C40, (F) M50C50, and (G) M0C100.

This instrument can analyze particle size in both liquid and air dispersed media, covering a range from 0.01 µm to 2,000 µm in liquid and 0.1 µm to 2,000 µm in air. Furthermore, the true density of the mixed-sized mangrove wood charcoal powder and coconut shell charcoal powder was determined. Random samples of the fine-ground powder were analyzed using a True Density Analyzer, AccuPyc II 1340, U.S.A., Mettler Toledo Density Meter D4. All measurements were performed in triplicate (n = 3). This instrument operates by inducing vibrations through electromagnetic waves within a U-shaped glass tube. A sensor then measures the oscillation period, which is correlated to the true density.



(A) (B)

Figure 5 Types of charcoal powder: (A) Mangrove and (B) Coconut shell.

2.5 Gross calorific value analysis

The gross calorific value of the moulded cylindrical briquette samples was analyzed. After shaping, the briquettes were sun-dried until completely dry. Random samples were then collected from various locations for each of the seven mixing ratios, all measurements were performed in triplicate (n = 3), as shown in Figure 4. According to the Community Product Standard for Charcoal Briquettes (M.P.Ch. 238/2547), the testing method adheres to ASTM D 5865 (ASTM International, 2019)

A Bomb Calorimeter (C5000, IKA, Germany) was used to determine the calorific value. The principle of this method involves the combustion of the material in an oxygen-rich environment, releasing heat. This heat is absorbed by a surrounding water tank, and the resulting temperature increase of the water is measured to calculate the calorific value.

2.6 Moisture content analysis

The moisture content (expressed as a percentage of analysis sample) of the composite charcoal briquette samples was determined. After being mixed and moulded into cylindrical shapes, the briquettes were sun-dried to a ready-to-use condition. Random samples were then collected from various locations for all seven mixing ratios, as depicted in Figure 4. The testing procedure adhered to ASTM D3173 (Canales *et al*., 2022), as specified by the Community Product Standard for Charcoal Briquettes (M.P.Ch. 238/2547). Samples were heated in a hot air oven (Memmert) at a controlled temperature of 110 ± 1°C. The oven maintained a heating rate of 2 to 4 times per minute, with an internal air atmosphere humidity of 1.9 mg L-1 or less. All measurements were performed in triplicate (n = 3). The percentage moisture content of the charcoal briquette samples was calculated using Equation 1.

$$\text{Moisture in analysis sample, \%} = ((W_1-W_2)/W_1) \times 100\% \quad (1)$$

where: W_1 is the mass of the sample before drying (g)

W_2 is the mass of the sample after drying (g)

2.7 Thermal and combustion properties

In these tests, a constant briquette weight of 0.5 kg and a fixed water volume of 1 L were used for all formulations. Each experiment lasted for a total of 60 min and was replicated four times. The heat generated resulted in varying boiled water temperatures across different time intervals. For all formulations, the highest water temperature was consistently recorded at the 20-minute mark. Beyond this point, as the burning time increased, the water temperature began to decrease, which is attributed to the continuous consumption of the charcoal briquettes as fuel, leading to a reduction in their effective burning volume.

2.8 Fuel properties and usability testing

This section details the evaluation of the fuel properties and usability of the briquettes by determining the combustion duration per unit of mass. For this test, a charcoal briquette sample weighing 0.5 kg was used as fuel to boil 1 kg of water. The experiment recorded time intervals at 0, 20, 40, and 60 min to assess ignition time, time to boiling water, and boiling water temperature. The overall usability of each of the seven briquette formulations, as shown in Figure 4, was evaluated from the initial ignition until complete ash formation.

3. Results and Discussion

The results and discussion on the physical, calorific, and combustion properties of composite charcoal briquettes made from waste mangrove wood charcoal and coconut shell charcoal, fabricated using a cylindrical compression mould, yielded the following key findings:

3.1 Particle size analysis

The particle size distribution analysis of the mixed charcoal powder derived from mangrove wood and coconut shells was conducted to evaluate the relationship between particle size (in micrometres) and cumulative particle volume (in percentage), as presented in Figure 6.

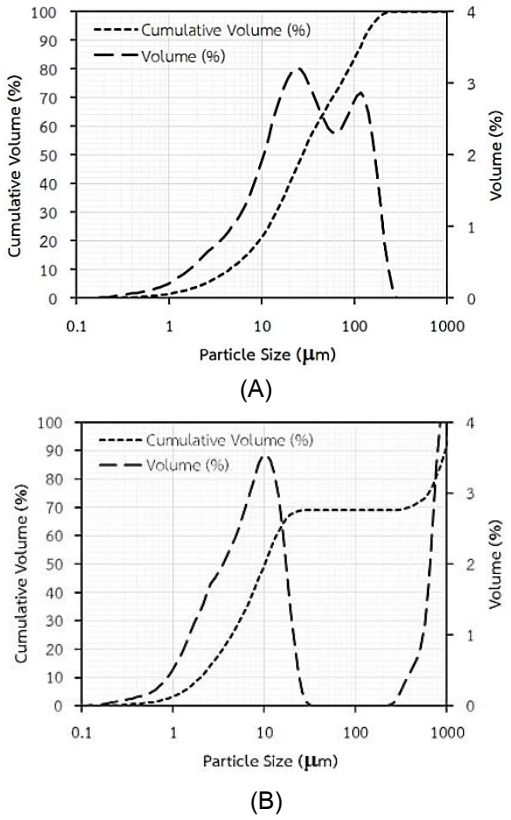


Figure 6 Particle size distribution graphs for (A) Mangrove wood charcoal and (B) Coconut shell charcoal.

As presented in the Figure 6(A), the particle size distribution for mangrove wood charcoal powder exhibited a bimodal distribution, with two distinct peaks observed in the volume percentage graph, indicating two primary particle size populations. The d_{10}, d_{50}, and d_{90} values were 4.3 µm, 27.0 µm, and 128.4 µm, respectively, with an average particle size of 48.2 ± 1.75 µm. This broad distribution, spanning from very fine particles (d_{10} = 4.3 µm) to relatively coarse particles (d_{90} = 128.4 µm), suggests that the grinding process produced a wide range of particle sizes (Zamora *et al*., *2015).*

In contrast, for coconut shell charcoal powder, depicted in Figure 6(B), the volume percentage graph primarily showed a prominent peak in the range of 8-12 µm, indicating a significant fraction of fine particles. However, the cumulative volume percentage curve rose sharply beyond 100 µm, culminating in d_{10}, d_{50}, and d_{90} values of 2.0 µm, 10.4 µm, and 972.6 µm, respectively, with a much larger average particle size of 285.4 ± 20.36 µm. The exceptionally high d_{90} value for coconut shell charcoal powder (972.6 µm) highlights the presence of a considerable proportion of very large particles, despite the fine primary peak. This suggests a highly heterogeneous particle size distribution for coconut shell charcoal (Yuliah *et al*., 2017*).*

In summary, a direct comparison reveals that while both charcoal types contain fine particles (indicated by low d_{10} values), the overall average particle size of mangrove wood charcoal powder (48.2 ± 1.75 µm) was considerably finer and more uniformly distributed than that of the coconut shell charcoal powder (285.4 ± 20.36 µm), which exhibited a broader and more heterogeneous distribution with very large particles. These distinct particle size characteristics are expected to influence the compaction behavior and final physical properties of the briquettes, particularly affecting density and structural integrity. The finer and more diverse particle sizes of mangrove wood charcoal may facilitate better particle packing and inter-particle bonding during compression. Consistent with the findings of Anan *et al*. (2022), fine grinding and mixing of the ingredients enabled the compression molding process to produce charcoal with higher true density and calorific value.

3.2 True density analysis

The true density of the powdered charcoal particles, derived from carbonized mixed-sized mangrove wood and coconut shell waste, was analysed. Random samples of each charcoal powder type were collected from their respective piles and tested at room temperature, specifically within a range of 25.37 °C to 25.93 °C. The results showed that mangrove wood charcoal powder had a true density of 1.3690 ± 0.0019 g/cm^3, while coconut shell charcoal powder had a true density of 1.4095 ± 0.0016 g/cm^3. These results indicate that the true densities of both charcoal powders are very similar, with a minimal difference of only 0.0405 g/cm^3. This similarity in true density, despite differences in particle size distribution, suggests that the intrinsic material properties of the charcoals are comparable. This is similar to studies on mata buaya (Bruguiera sexangula), which has a density of 0.9 g/cm^3 (Hardiansyah *et al*., 2023).

3.3 Gross calorific value analysis

Table 2 presents the results of the gross calorific value analysis of charcoal briquettes and illustrates the relationship between the briquette formulations and their respective calorific values. Briquettes made solely from coconut-shell charcoal powder (M0C100) exhibited a calorific value of 6,886 ± 420 kcal/kg. In comparison, briquettes composed entirely of mangrove wood charcoal powder (M100C0) yielded a lower calorific value of 5,897 ± 510 kcal/kg (Rahman *et al*., 2019; Kabir *et al*., 2022). When examining the calorific values across the composite formulations, a clear trend emerged. Starting from

the M100C0 formulation, which had the lowest calorific value, and progressing towards the M0C100 formulation, which had the highest at 6,886 ± 420 kcal/kg, the calorific value generally increased with an increasing proportion of coconut shell charcoal powder (from C10, C20, C30, C40, to C50 ratios). The calorific values for the mixed formulations were 6,021 ± 145, 5,917 ± 108, 6,141 ± 570, 6,389 ± 214, and 6,292 ± 500 kcal/kg, respectively. This indicates that coconut shell charcoal contributes significantly to the overall heat content of the briquettes, as its high density and carbon content yield a rigid, dense cellulose structure during combustion. Additionally, the moisture content for all tested formulations ranged between 4.211 ± 0.127% and 4.887 ± 0.164%.

Every briquette formulation successfully met the Community Product Standard for Charcoal Briquettes (M.P.Ch. 238/2547). This standard stipulates a minimum gross calorific value of not less than 5,000 cal g^{-1} (equivalent to 5,000 kcal/kg) and a maximum moisture content of not exceeding 8% by weight. All formulations developed in this study, with calorific values ranging from 5,897 ± 510 kcal/kg to 6,886 ± 420 kcal/kg and moisture contents between 4.211 ± 0.127% and 4.887 ± 0.164%, were found to satisfy these criteria.

Table 2 Gross calorific values of charcoal briquette formulations.

Recipe Name	Mangrove (kg)	Coconut Shell (kg)	Gross Calorific Value (kcal/kg)	Moisture in analysis (%)
M100C0	100	0	5,897 ± 510	4.887 ± 0.164
M90C10	90	10	6,021 ± 145	4.211 ± 0.127
M80C20	80	20	5,917 ± 108	4.446 ± 0.136
M70C30	70	30	6,141 ± 570	4.676 ± 0.152
M60C40	60	40	6,389 ± 214	4.427 ± 0.130
M50C50	50	50	6,292 ± 500	4.842 ± 0.158
M0C100	0	100	6,886 ± 420	4.489 ± 0.142

3.4 Thermal and combustion properties

Table 3 presents the results of the thermal properties testing for each formulation of mangrove wood and coconut shell charcoal briquettes, showing the boiling water temperature at various time intervals. In these tests, a constant briquette weight of 0.5 kg and a fixed water volume of 1 L were used for all formulations. Each experiment lasted for a total of 60 min and was replicated four times. The heat generated resulted in varying boiled water temperatures across different time intervals. For all formulations, the highest water temperature was consistently recorded at the 20 min mark. Beyond this point, as the burning time increased, the water temperature began to decrease, which is attributed to the continuous consumption of the charcoal briquettes as fuel, leading to a reduction in their effective burning volume.

Upon analysing the data in Table 3 in conjunction with the calorific values presented in Table 2, a clear correlation emerges. The M0C100 formulation, which exhibited the highest gross calorific value (6,886 ± 420 kcal/kg), also demonstrated the highest water temperature at 20 min (93.5 °C), as this duration was sufficient for the charcoal to fully ignite, resulting in efficient heat transfer and greater energy release that enabled the water to reach its boiling point. On the other hand, the M100C0 formulation, with the lowest calorific value (5,897 ± 510 kcal/kg), yielded a comparatively lower maximum temperature at 20 min (95.8 °C). However, M100C0 unexpectedly reached a slightly higher water temperature (95.8 °C) than M0C100 (93.5 °C), possibly reflecting experimental variability or ignition efficiency. The overall trend suggests that higher calorific values generally lead to better thermal performance. Formulations with a higher proportion of coconut shell charcoal, such as M0C100, tended to achieve higher water temperatures, aligning with their higher energy content. Furthermore, the highest value was observed for the M90C10 formulation at 20 minutes This result can be attributed to the higher proportion of coconut shell charcoal relative to mangrove wood charcoal in the mixture. This correlation highlights the direct impact of the briquette's energy density on its practical thermal performance for heating applications (Wasu *et al*., 2021).

Table 3 Results of the water boiling test.

Recipe Name	0 minute	20 minutes	40 minutes	60 minutes
	°C	°C	°C	°C
M100C0	32.2	95.8	86.3	73.6
M90C10	32.6	98.1	85.8	80.3
M80C20	32.1	86.2	85.9	77.2
M70C30	32.3	84.7	77.9	71.2
M60C40	32.4	91.1	83.5	72.8
M50C50	32.1	89.9	81.8	74.5
M0C100	32.2	93.5	85.6	78.4

In addition to heat output, Table 4 details other key combustion properties, including ignition time, time to burn to ash, and actual combustion time. These characteristics varied among the different briquette formulations, primarily influenced by the true density of the briquettes and the specific composition of each mixture. The ignition time, defined as the duration from initial lighting until stable flame combustion, ranged from 7 min (M60C40) to 19 min (M80C20). Notably, the M60C40 formulation exhibited the shortest ignition time (7 min), indicating its superior ease of initial lighting. Regarding the overall burning duration, the M60C40 formulation demonstrated the longest time to burn to ash (223 min), followed by M80C20 and M0C100 (210 min each). This indicates that the M60C40 briquettes sustained combustion for the longest period until complete ash formation. The actual combustion time, which excludes the initial ignition phase, also showed M60C40 having the longest duration of 216 min (Onuegbu *et al*., 2011).

In addition to the quantitative thermal and combustion metrics, Table 5 presents the qualitative usability test results for each charcoal briquette formulation, focusing on smoke

emission, flame characteristics, spark generation, and ease of ignition.

Table 4 Combustion test results.

Recipe Name	Ignition Time (min)	Time to Burn to Ash (min)	Actual Combustion Time (min)
M100C0	17	192	175
M90C10	16	200	184
M80C20	19	210	191
M70C30	9	204	195
M60C40	7	223	216
M50C50	8	211	203
M0C100	10	210	200

Table 5 Fire characteristics.

Recipe Name	Fire characteristics			
	Smoke	Flame	Sparks	Ignition
M100C0	Little	Much	None	Slow
M90C10	Moderate	Moderate	None	Slow
M80C20	Moderate	Little	None	Slow
M70C30	Little	Moderate	None	Moderate
M60C40	Moderate	Moderate	None	Fast
M50C50	Much	Moderate	None	Fast
M0C100	Little	Little	None	Moderate

One key result was the absence of spark generation across all tested formulations, indicating a safer burning characteristic. When considering minimal smoke emission, the M70C30 formulation proved to be the most suitable for practical use. This formulation also exhibited moderate levels of flame and ignition characteristics, striking a balance between ease of lighting and clean burning (Chaney, 2010).

4. Conclusion

Charcoal briquettes made from agricultural residues, specifically a blend of mangrove wood charcoal and coconut shell charcoal, represent a significant alternative biomass energy source. These briquettes offer a promising solution to replace fossil fuels in essential daily activities such as cooking, grilling and heating, while simultaneously contributing to the reduction of environmental problems. This research investigated the physical, calorific, and combustion properties of these composite briquettes. Key findings from the study are as follows:

The average particle size of ground mangrove wood charcoal was 48.2 ± 1.75 μm, while that of coconut shell charcoal was 285.4 ± 20.36 μm. This indicates that mangrove charcoal powder is generally finer than coconut shell charcoal powder, a characteristic that influences compaction and briquette integrity.

The true densities of mangrove charcoal powder (1.3690 ± 0.0019 g/cm^3) and coconut shell charcoal powder (1.4095 ± 0.0016 g/cm^3) were found to be very similar, with only a minor difference of 0.0405 g/cm^3. All briquette formulations met the Community Product Standard for Charcoal Briquettes (M.P.Ch.238/2547), requiring a minimum of 5,000 cal/g. The calorific values ranged from 5,897 ± 510 kcal/kg (M100C0) to 6,886 ± 420 kcal/kg (M0C100). A clear trend showed that increasing the proportion of coconut shell charcoal led to higher calorific values. The moisture content across all formulations was low, ranging between 4.211 ± 0.127% and 4.887 ± 0.164%, well within the standard's limit of 8% by weight. The moisture content is still high, so it should be dried or sun-dried before being used as fuel. In the water boiling tests, all formulations reached their highest water temperature at the 20-minute mark. The M60C40 formulation demonstrated the shortest ignition time (7 min.) and the longest time to burn to ash (223 min.), making this formulation the most suitable choice for applications requiring prolonged and sustained burning. No spark generation was observed in any formulation. The M70C30 formulation produced minimal smoke while exhibiting moderate flame and ignition characteristics, making it suitable for practical household applications. Notably, its heating value of 6,141 ± 570 kcal/kg was substantially higher than that reported for briquettes prepared with a 5% cow dung binder of 4,794.38 kcal/kg. This finding suggests that the M70C30 formulation offers greater energy efficiency and improved fuel quality while maintaining desirable combustion characteristics. In summary, the research results indicate that M70C30 blended charcoal briquettes made from mangrove wood and coconut shells are an efficient and suitable alternative biomass fuel. They possess excellent physical properties, high calorific value, and excellent combustion characteristics, meeting relevant standards and practical application requirements. To facilitate commercial implementation, a detailed break-even analysis should be undertaken to evaluate economic feasibility and identify the conditions that yield the greatest profit per unit.

5. Acknowledgments

The authors would like to express their sincere gratitude to the Faculty of Engineering, Rajamangala University of Technology Srivijaya, for providing the laboratory facilities and supporting the research work. Special thanks are also extended to the invaluable research assistants: Mr. Baramet Wongsakulwong, Mr. Korawit Kaewchucherd, Mr. Pachara Doungthong, and Miss Katesinee Momta, for their dedicated assistance in material and equipment preparation, support, and initial data collection for this research.

6. Declaration of Generative AI Use

During the preparation of this manuscript, the authors used ChatGPT (OpenAI) solely for language editing and improvement of readability. All research design, data collection, analysis, interpretation, and conclusions were performed by the authors.

The authors assume full responsibility for the content of this manuscript.

7. References

Amnouy, K., Worapot, S., Peerawat, L. and Reungruthai, S. 2019. A study of the effect of mixture material in coconut shell charcoal briquette on mechanical and thermal properties. **Thai Industrial Engineering Network Journal** 5(2): 67–75.

Amon, V. 2021. Utilization of fruit orchard waste: Durian and mangosteen for charcoal briquette production. **Rajamangala University of Technology Tawan-Ok Research Journal** 14(2): 66–71.

Anan, W., Khunnapat, S., Wimol, P., Peerapong, N., Sujitra, S., Kittikhun, S., Apichart, H. and Chinoros, I. 2022. Charcoal briquette production process from industrial waste charcoal. **Science Journal, Chandrakasem Rajabhat University** 32(2): 89–94.

ASTM International. 2019. **ASTM D5865/D5865M-19: Standard test method for gross calorific value of coal and coke.** ASTM International. doi.org Available Source: https://store.astm.org/d5865_d5865m-19.html, December 18, 2025.

Canales, R., Prieto, F., Prieto, J., Acevedo, O. and Otazo, E. 2022. Evaluation of three lignocellulose biomass materials (barley husk, corn cobs, agave leaves) as precursors of activated carbon. **Revista Facultad de Ciencias Universidad Nacional de Colombia, Sede Medellín** 11(1): 17–39.

Chaney, J. 2010. **Combustion characteristics of biomass briquettes.** Doctor of Philosophy (thesis). University of Nottingham.

Department of Alternative Energy Development and Efficiency. 2024. **Renewable energy**. Available Source: http://services.dede.go.th/opendata/index.html, September 15, 2024.

Hardiansyah, T., Arif, N., Apri, H.I., Iwan, R., Mohammad, B. and Widya, F. 2023. Briquettes made of branches wood of three mangrove species bonded by starch adhesive. **Materials** 16: 5266.

Jomsurang, V. and Anamai, D. 2024. Applying the principles of diffusion theory to drive international SDGs towards sustainable development at the localizing in the form of the BCG model. **Asian Political Science Review** 8(1): 27–38.

Jutapol, J., Lumpoon, L., Pitinan, A. and Surasing, A. 2022. Study of the optimal ratios and properties of charcoal briquettes from bamboo. **Agriculture and Technology Journal** 3(3): 81–93.

Kabir, A.R., Anwar, S.S., Yusup, S., Sham, D.S., Inayat, M. and Aminu, U.H. 2022. Exploring the potential of coconut shell biomass for charcoal production. **Ain Shams Engineering Journal** 13(1): 101499.

Kritsada, B. and Nirubol, C. 2020. Study of charcoal briquette from longan wood. **Naresuan Phayao Journal** 13(2): 51–56.

Lomunyak, G., Osodo, B., Njoka, F. and Kombe, E. 2024. Characterization, optimization and emission analysis of manually-made charcoal dust briquettes with starch, paper and algae binders. **Heliyon** 10: e40991.

Malte, M., Nicolai, M., William, H., Sarah, C.B.R., Katja, F., Reto, K., David, J.F. and Myles, R.A. 2009. Greenhouse-gas emission targets for limiting global warming to 2 °C. **Nature** (458): 1158–1162.

Nuryawan, A., Simatupang, J., Risnasari, I., Nur, T.B., Fatriasari, W., Basyuni, M., Tambunan, H., Utami, S.S. and Jeong, B. 2025. Physical, chemical, mechanical, and thermal properties of charcoal briquettes produced from mangrove branch wood. **Frontiers in Materials** (12): 1611316.

Onuegbu, T.U., Ekpunobi, U.E., Ogbu, I.M., Ekeoma, M.O. and Obumselu, F.O. 2011. Comparative studies of ignition time and water boiling test of coal and biomass briquettes blend. **International Journal of Research and Reviews in Applied Sciences** 7(2): 153–159.

Pattaraanong, K., Warunee, T., Adisak, N. and Somchart, S. 2021. Assessment of seasonal availability and spatial distribution of bio-feedstock for power generation in Thailand. **BioEnergy Research** 14: 70–90.

Rahman, R., Widodo, S., Azikin, B. and Tahir, D. 2019. Chemical composition and physical characteristics of coal and mangrove wood as alternative fuel. **Journal of Physics: Conference Series** 1341: 052008.

Ratchatorn, T. and Jaruwan, W. 2022. Utilization of waste from biomass for fuel briquettes production. **Thai Science and Technology Journal** 30(6): 124–136.

Roseleena, A., Rodeeyah, C. and Nurmayamean, S. 2019. Production of charcoal from agricultural residues. **YRU Journal of Science Technology** 4(1): 47–53.

Saleem, M. 2022. Possibility of utilizing agriculture biomass as a renewable and sustainable future energy source. **Heliyon** 8: e08905.

Sirichai, J. and Changwat, C. 2022. The study on the production of charcoal briquettes from pomelo peels. **Kasem Bundit Engineering Journal** 12(1): 55–74.

Siwakorn, N., Nuttaphon, S., Pasawat, S., Wiriya, S., Kantapong, K., Chanin, O., Kanchana, S. and Kittipong, L. 2026. Insights into the co-utilization of cassava industry waste and invasive woody biomass for charcoal briquettes production. **Carbon Resources Conversion** 100416: 2588–9133.

Titiporn, C. and Chotika, Y. 2018. Utilization of briquettes charcoal from pineapple peel. **Life Sciences and Environment Journal** 19(2): 280–286.

Suksuwan, W., Hayee-asae, N., Hemma, I., Batcha, M.F.M., Palamanit, A. and Wae-hayee, M. 2021. Effect of equivalent ratio on thermal energy and exhaust gas properties from gasification of oil palm empty fruit bunch using household gasifier. **IOP Conference Series: Earth and Environmental Science** (765): 012070.

Winfried, H. and Claudia, K. 2018. The UN sustainable development goals (SDGs) in the transnational multilevel system. **Heidelberg Journal of International Law** 2: 375.

Yuliah, Y., Kartawidjaja, M., Suryaningsih, S. and Ulfi, K. 2017. Fabrication and characterization of rice husk and coconut shell charcoal based bio-briquettes as alternative energy source. **IOP Conference Series: Earth and Environmental Science** (65): 012021.

Zamora, C.R., Sessions, J., Smith, D. and Marrs, G. 2015. Effect of grinder configuration on forest biomass bulk density, particle size distribution and fuel consumption. **Biomass and Bioenergy** (81): 44–54.

Recent Science and Technology 2026, Vol. 18(3): e271479

Recent Science and Technology

Journal homepage: https:// www.tci-thaijo.org/index.php/rmutsvrj/index

ISSN: 3057-0786 (Online)

Research Article

Development of Biodegradable Plant Pots from Chitosan Reinforced with Natural Fibers for Agricultural Applications

Thanchanok Kanlaoong [a], Sopida Jornden [a] and Uraiwan Sookyung [b] *

[a] *Department of Industrial Engineering, Faculty of Engineering, Rajamangala University of Technology Srivijaya, Muang District, Songkhla 90000, Thailand.*

[b] *Materials Processing Technology Research Unit, Department of Industrial Engineering, Faculty of Engineering, Rajamangala University of Technology Srivijaya, Muang District, Songkhla 90000, Thailand.*

Article history:

Received: 2026-04-01
Revised: 2026-06-12
Accepted: 2026-07-02

Keywords:

Chitosan composite;
Biodegradable pot;
Natural fiber

ABSTRACT

This study aimed to develop biodegradable composite materials based on chitosan reinforced with natural fibers, including pineapple leaf fiber (PL), rice straw (RI), and sugarcane bagasse (BG), for use as biodegradable plant pots. The fibers were incorporated into a chitosan matrix at fiber-to-chitosan ratios of 1:0.08, 1:0.12, 1:0.16, 1:0.20, and 1:0.24 by weight, with glycerol used as a plasticizer. The composites were then fabricated using a molding and drying process. The effects of fiber type and composition on density, water absorption, thickness swelling, and biodegradation behavior were investigated. The results showed that fiber type significantly influenced the composite properties. PL-reinforced composites exhibited the highest density, water absorption, thickness swelling, and biodegradation rate, attributed to their high cellulose content and fibrillated structure. PL-reinforced composites exhibited the highest density (0.907 g/cm³) and biodegradation (97%), attributed to their high cellulose content and fibrillated structure. In contrast, RI composites showed the lowest density and biodegradation, while BG composites demonstrated intermediate behavior. Increasing chitosan content improved dimensional stability by reducing thickness swelling. Soil burial tests confirmed that all composites were biodegradable, with degradation increasing over time. Among the formulations investigated, the fiber-to-chitosan ratio of 1:0.16 was selected as the most suitable formulation for pot fabrication and plant cultivation tests due to its balanced dimensional stability and biodegradation performance. Furthermore, the developed composites were successfully fabricated into hollow pot structures using a two-part mold system. A plant cultivation test demonstrated that all biodegradable pots supported plant growth without visible toxicity and exhibited performance comparable to conventional plastic nursery bags.

© 2026 Kanlaoong, T., Jornden, S. and Sookyung, U. Recent Science and Technology published by Rajamangala University of Technology Srivijaya

1. Introduction

The increasing use of plastic materials in agricultural applications, particularly nursery bags and plant pots, has led to significant environmental concerns due to their persistence and resistance to degradation. Over time, these materials fragment into microplastics (particles smaller than 5 mm), which are increasingly recognized as a critical environmental pollutant (Ghosh *et al*., 2025). These microplastics accumulate in agricultural soils and can alter soil physicochemical properties, disrupt microbial communities, and impair plant growth, ultimately posing risks to food security and human health. In agricultural systems, microplastics originate from various sources, including plastic mulching, irrigation systems, and the application of contaminated organic amendments, leading to their continuous accumulation in soil environments. Therefore, the development of biodegradable alternatives derived from renewable and natural resources has gained increasing attention as a sustainable approach to mitigate plastic pollution, particularly for short-term agricultural applications such as plant cultivation (Srisunont *et al*., 2024; Ghosh *et al*., 2025).

Numerous studies have investigated the development of biodegradable pots using a variety of natural and waste-derived

* **Corresponding author.**

E-mail address: *uraiwan.so@rmutsv.ac.th*

Cite this article as: Kanlaoong, T., Jornden, S. and Sookyung, U. 2026. Development of Biodegradable Plant Pots from Chitosan Reinforced with Natural Fibers for Agricultural Applications. **Recent Science and Technology** 18(3): e271479.
https://doi.org/10.65411/rst.2026.271479

materials. Agricultural residues such as water hyacinth, rice straw, sawdust, and coconut coir have been widely used due to their availability and biodegradability, often combined with cassava starch or other natural binders to enhance structural integrity (Tanpaiboonkul, 2022; Chaichan, 2019; Iriany, 2022; Manafi-Dastjerdi, 2022). These materials have been evaluated in terms of physico-chemical and mechanical properties, biodegradation behavior, and their suitability for plant nursery applications. More complex formulations incorporating multiple biomass sources, such as coffee grounds and rubber wood sawdust, as well as alternative wastes including coconut bagasse, tobacco dust, compost, and cow manure, have also been explored to improve performance and degradability (Chaichan, 2017; Somakul, 2020; Juming, 2022). In addition, lignocellulosic residues such as straw and palm-based wastes have been applied in bio-containers with additives like cellulose or molasses to enhance structural stability (Piyang, 2018; Tibalia, 2023). Overall, while biodegradable pots can be produced from a wide range of materials, their performance strongly depends on material selection and processing conditions, and achieving a balance between mechanical strength during use and effective biodegradation after disposal remains a key challenge.

Although various biodegradable materials have been developed for plant pot applications, most studies have primarily focused on starch-based, latex-based, or lignocellulosic binder systems, while limited attention has been given to chitosan-based composites. Chitosan is a natural biopolymer with excellent biodegradability, biocompatibility, and film-forming properties; it was selected in this study because it can act as a biodegradable binder while providing sufficient cohesion between natural fiber particles. However, its application in structural products such as plant pots remains limited due to its hydrophilic nature, which results in high water absorption and dimensional instability under moist conditions. In addition, chitosan-based materials generally exhibit relatively low mechanical strength, particularly when exposed to water, making it difficult to maintain structural integrity during use. These limitations highlight the need for material modification strategies, such as reinforcement with natural fibers, to improve the performance of chitosan-based systems. Recent studies have demonstrated the potential of chitosan-based composites in agricultural applications, including biodegradable mulch films, controlled-release fertilizer systems, and plant growth substrates, owing to their biodegradability and environmental compatibility. However, information regarding chitosan composites reinforced with different agricultural fibers for biodegradable pot applications remains limited. Furthermore, the influence of different agricultural fibers on the physical properties, water-related behavior, biodegradation, and practical plant cultivation performance of chitosan composites has not been systematically investigated. The novelty of this work lies in the comparative evaluation of pineapple leaf fiber, rice straw, and sugarcane bagasse as reinforcements in chitosan-based biodegradable pots, with emphasis on their effects on dimensional stability, biodegradation behavior, and plant growth performance. Therefore, this study aims to develop biodegradable plant pots from chitosan reinforced with pineapple leaf fiber, rice straw, and sugarcane bagasse, and to evaluate their density, water absorption, thickness swelling, biodegradation behavior, and plant growth performance.

2. Materials and Methods

2.1 Materials

Chitosan (derived from shrimp shells) and acetic acid (food grade, 99.85%) were commercially obtained and used without further purification. Commercial glycerol was used as a plasticizer. Rice straw (RI), sugarcane bagasse (BG), and pineapple leaf fiber (PL) were used as natural fiber reinforcements.

2.2 Preparation of natural fibers

Rice straw, sugarcane bagasse, and pineapple leaf fiber were selected as natural fibers. The materials were sun-dried for 5-10 days until completely dried. The dried fibers were then mechanically ground using a grinder to obtain the desired particle size. The ground fibers were subsequently sieved through a 40-mesh sieve to obtain a more uniform particle size prior to composite preparation.

2.3 Preparation of fiber/chitosan composites

A 3% (w/v) chitosan solution was prepared in 2% (v/v) acetic acid under continuous stirring. Rice straw, sugarcane bagasse, and pineapple leaf fiber were then added at fiber-to-chitosan ratios of 1:0.08, 1:0.12, 1:0.16, 1:0.20, and 1:0.24 (by weight). Glycerol was incorporated as a plasticizer at a fiber-to-glycerol ratio of 1:1.5 (by weight). The mixture was stirred until homogeneous, poured into a rectangular mold, and dried at 100 °C for 7 h. The samples were then cooled to room temperature and removed for further characterization.

2.4 Preparation of fiber/chitosan composite pots

The prepared fiber/chitosan composite mixture was stirred until a homogeneous consistency was obtained. The mixture was then poured into a two-part mold equipped with an inner core to form a hollow pot structure, while the outer mold maintained the external shape and wall thickness. The assembled mold was placed in a drying oven at 100 °C for 7 h. After drying, the samples were allowed to cool to room temperature and then removed from the mold to obtain the final biodegradable pots. The preparation process is illustrated in Figure 1.



Figure 1 Preparation of fiber/chitosan composite pots: (a) mixing of the composite mixture, (b) molding and drying in an oven, and (c) final biodegradable pots.

2.5 Testing and characterization

All measurements were performed in triplicate, and the average values are reported.

The density of the samples was measured using an electronic densimeter (MD-200S, Alfa Mirage, Japan) according to the instrument's standard procedure.

Water absorption was determined by immersing the dried samples in water at room temperature for 24 h. After immersion, the samples were removed, surface water was gently wiped off, and the samples were weighed. The water absorption was calculated using the following equation:

$$Water\ Absorption\ (\%) = \frac{Ww - Wd}{Wd} \times 100 \quad (1)$$

where *Wd* is the initial dry weight and *Ww* is the weight after immersion.

Thickness swelling was evaluated by measuring the sample thickness before and after immersion in water at room temperature for 24 h. The swelling percentage was calculated using the following equation:

$$Thickness\ Swelling\ (\%) = \frac{T2 - T1}{T1} \times 100 \quad (2)$$

where $T1$ is the initial thickness and $T2$ is the thickness after immersion.

Biodegradation was evaluated using a soil burial test. The samples were buried at a depth of 10 cm below the soil surface. To simulate practical environmental conditions, the soil was watered every two days throughout the burial period. The samples were buried in soil for 15 and 30 days. After the specified period, the samples were removed, cleaned, dried, and weighed. The weight loss was calculated using the following equation:

$$Weight\ Loss\ (\%) = \frac{Wi - Wt}{Wi} \times 100 \quad (3)$$

where Wi is the initial weight and Wt is the weight after burial.

3. Results and Discussion

3.1 Fiber characteristics and density

Natural fibers are mainly composed of cellulose, hemicellulose, and lignin, with additional components such as silica and ash depending on the plant source. Pineapple leaf fibers contain high cellulose content and exhibit porous lumen structures, which contribute to their high hydrophilicity (Asim *et al.*, 2015, Sufian *et al.*, 2020). Rice straw fibers are characterized by the presence of significant silica content, which influences their rigidity and water interaction behavior (Rosado *et al.*, 2021; Sharma *et al.*, 2023). In contrast, bagasse fibers contain relatively higher lignin content, resulting in lower hydrophilicity and improved dimensional stability (Hajiha and Sain, 2015; Niju and Swathika, 2019). The typical chemical compositions of these fibers are summarized in Table 1.



Figure 2 Macroscopic appearance of natural fibers used in this study: PL, RI, and BG.

The density of the fiber/chitosan composites, as shown in Figure 3, was significantly influenced by the type of natural fiber used. Among the three fiber types, the composites reinforced with PL showed the highest density, followed by BG, while those reinforced with RI showed the lowest density across all fiber. This trend can be explained based on the macroscopic structure of the fibers observed in Figure 2. PL fibers display a fine and fibrillated structure with high aspect ratio and large specific surface area. Such morphology promotes efficient packing and strong interfacial contact within the composite matrix, resulting in a more compact structure with reduced void content. In contrast, RI fibers exhibit an irregular, particle-like morphology, which limits packing efficiency and increases internal void formation. BG fibers show intermediate characteristics, consisting of short and relatively coarse fibers, leading to moderate packing behavior and density values. The observed results are consistent with previously reported density values of natural fibers. PL fiber is generally considered a relatively high-density lignocellulosic fiber, with reported values in the range of approximately 0.80-1.60 g/cm³ (Chokshi *et al.*, 2022; Chaves *et al.*, 2024). In contrast, rice straw is categorized as a low-density agricultural residue, particularly when processed into particleboard or bulk form, where densities are typically much lower due to its loose structure, generally ranging from approximately 0.30-0.50 g/cm³ depending on processing conditions and compaction level (Yang *et al.*, 2003; Zhang *et al.*, 2012, Chaves *et al.*, 2024). Similarly, sugarcane bagasse is also considered a low-density biomass material, although its density can vary depending on fiber processing and structural refinement, generally ranging from approximately 0.50-0.90

g/cm³ for bulk or fiber-based forms (Yogeshwaran and Priya 2020; Mahmud *et al*., 2025).

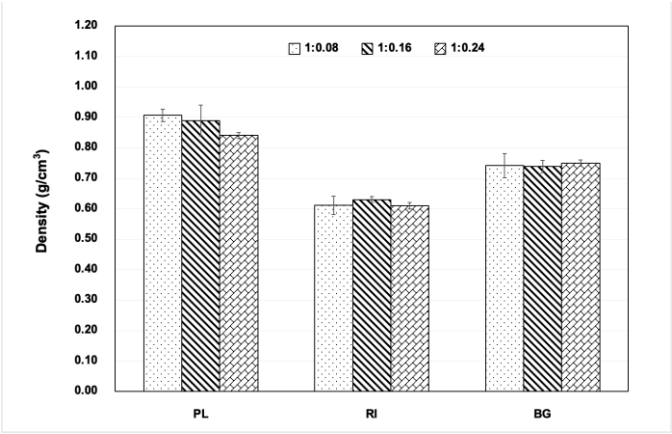


Figure 3 Density of fiber/chitosan composites reinforced with PL, RI, and BG at different fiber-to-chitosan ratios.

3.2 Water absorption and thickness swelling

The water absorption and thickness swelling of the fiber/chitosan composites are presented in Figure 4(a) and (b), respectively. The results indicate that both properties were influenced by fiber type and content of chitosan. PL composites exhibited the highest water absorption and thickness swelling, while BG showed the lowest water absorption but slightly higher thickness swelling than RI. PL composites showed the highest values due to their high cellulose content and highly fibrillated structure, which increase hydrophilicity and provide a larger specific surface area for water interaction (Asim *et al*. 2015, Sethupathi *et al*. 2024). These characteristics facilitate water penetration into the composite matrix, leading to both higher water uptake and greater structural expansion. BG composites exhibited the lowest water absorption, which can be attributed to their relatively higher lignin content that reduces water affinity (Kamande *et al*., 2026). However, BG showed slightly higher thickness swelling than RI, indicating that although less water is absorbed, the composite structure can still undergo expansion once water penetrates. This behavior suggests that the fibrous structure of BG allows more flexibility or rearrangement in the thickness direction. RI composites showed moderate water absorption but lower thickness swelling. This behavior is likely related to the presence of silica and the more rigid, particle-like structure of rice straw fibers, which restrict dimensional expansion even when water is absorbed.

In addition, the effect of chitosan content on thickness swelling was clearly observed. Increasing the chitosan ratio resulted in a decrease in thickness swelling for all fiber types. This behavior can be attributed to the formation of a more compact and stable matrix, which restricts water penetration and limits structural expansion during immersion. As a result, higher chitosan content enhances the dimensional stability of the composites. Although the composites showed relatively high water absorption, this property may be beneficial for biodegradable plant pot applications. The absorbed water can help retain moisture in the growing medium and support plant growth during cultivation. In addition, water uptake may promote degradation of the pots after disposal. However, excessive water absorption may reduce dimensional stability during use. Therefore, an appropriate fiber-to-chitosan ratio is important to achieve a balance between usability and biodegradability.

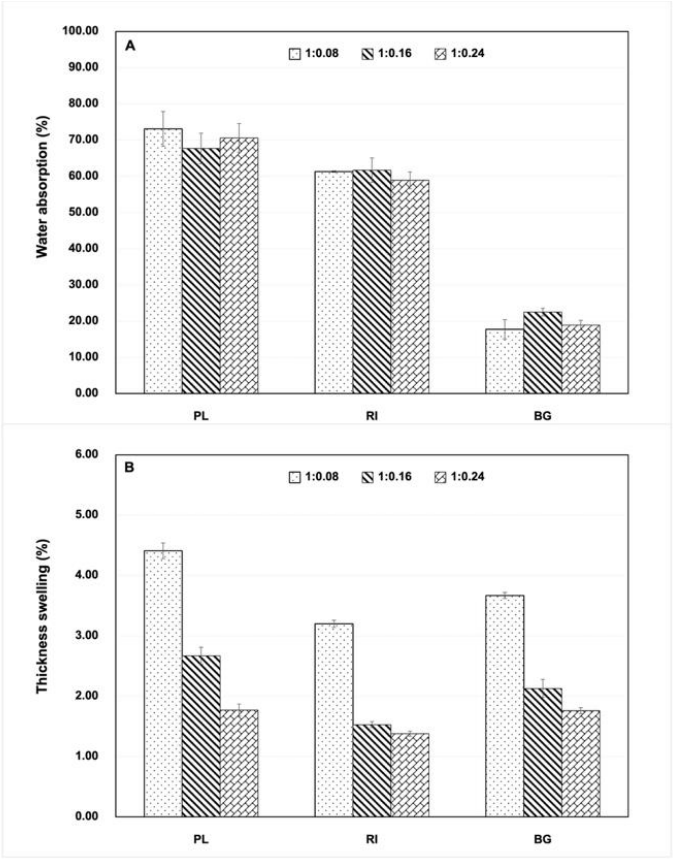


Figure 4 Water absorption (A) and Thickness swelling (B) of fiber/chitosan composites reinforced with PL, RI, and BG at different fiber-to-chitosan ratios.

3.3 Biodegradation behavior under soil burial

The biodegradation behavior of the fiber/chitosan composites under soil burial conditions is presented in Figure 5(a) and (b), corresponding to 15 and 30 days of burial, respectively. The results show that weight loss increased with burial time for all composites, indicating progressive biodegradation in the soil environment. Among the different fiber types, PL composites exhibited the highest weight loss, followed by BG, while RI showed the lowest weight loss at both time intervals.

Table 1 Chemical composition and structural characteristics of natural fibers used in this study.

Fiber type	Cellulose (%)	Hemicellulose (%)	Lignin (%)	Other components	Reference
PL	70-82	5-12	5-13	Wax, Ash	(Asim *et al*., 2015; Sufian *et al*., 2020)
RI	32-47	19-27	5-24	Silica 10-15%	(Rosado *et al*., 2021; Sharma *et al*., 2023)
BG	40-50	25-35	18-24	Ash	(Hajiha and Sain, 2015; Niju and Swathika, 2019)

At 15 days (Figure 5(a)), all samples showed moderate weight loss, with PL composites demonstrating slightly higher degradation compared to BG and RI. After 30 days (Figure 5(b)), the differences became more pronounced, where PL composites exhibited a significant increase in weight loss, while BG showed intermediate degradation and RI remained the most resistant. This trend indicates that the degradation process becomes more evident with prolonged exposure to soil conditions. The higher biodegradation of PL composites can be attributed to their high cellulose content and highly fibrillated structure, as discussed in Section 3.1. These characteristics enhance water absorption (Figure 4) and increase the accessibility of microorganisms to the composite matrix. As reported by (Ibrahim *et al*., 2025), water uptake can induce structural swelling in cellulose, thereby opening the matrix and allowing microbial enzymes to penetrate more easily. This improved accessibility promotes microbial activity and enzymatic degradation, resulting in a higher weight loss. BG composites exhibited moderate biodegradation behavior. Although BG showed the lowest water absorption, its fibrous structure and relatively higher lignin content provide a balance between resistance and degradability. As observed in Section 3.2, BG composites exhibited slightly higher thickness swelling than RI, suggesting that some structural expansion occurs after water penetration. This expansion may allow partial accessibility of microorganisms into the composite structure, contributing to moderate degradation. In contrast, RI composites exhibited the lowest biodegradation. This behavior can be attributed to the presence of silica and the more rigid, particle-like structure of rice straw fibers. As discussed previously, RI composites showed lower thickness swelling, indicating limited structural expansion. This restricts microbial penetration and reduces the accessibility of degradable components, resulting in lower weight loss during soil burial.

The visual appearance of the fiber/chitosan composites before and after 30 days of soil burial is presented in Table 2. Clear physical changes can be observed for all samples after burial, confirming the biodegradation behavior discussed in Figure 5. PL composites exhibited the most severe structural deterioration after soil burial. The samples lost their original shape, showing fragmentation, surface erosion, and disintegration into smaller pieces, particularly at lower chitosan content (1:0.08 and 1:0.16).

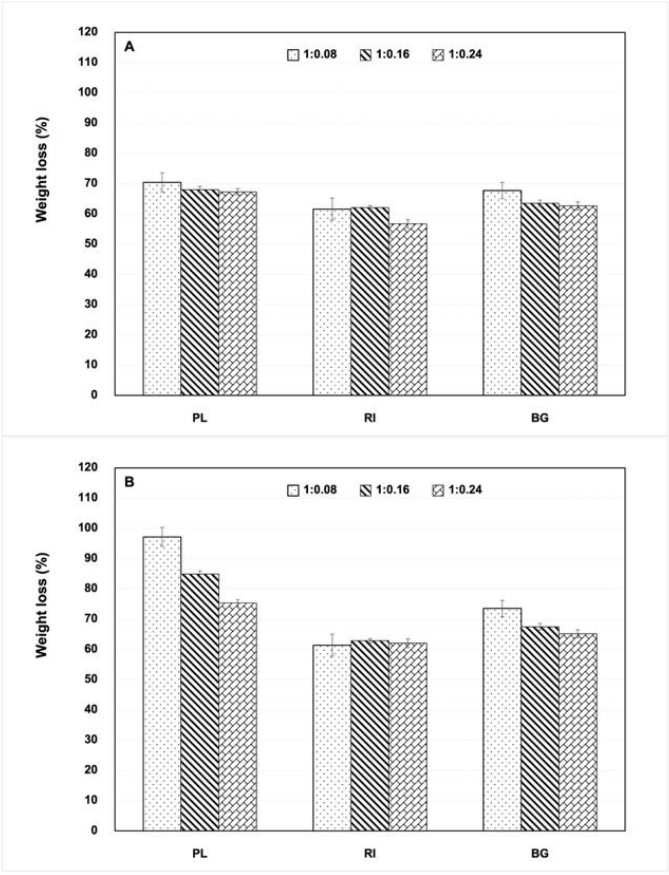


Figure 5 Weight loss (%) of fiber/chitosan composites reinforced with PL, RI, and BG during soil burial test after (a) 15 days and (b) 30 days.

This observation is consistent with the highest weight loss values obtained in Figure 5, indicating extensive biodegradation. The pronounced degradation of PL composites can be attributed to their high cellulose content and fibrillated structure, which facilitate water absorption and microbial penetration, accelerating the breakdown of the material. BG and RI composites exhibited relatively less pronounced visual changes after soil burial compared to PL. Most samples generally retained their overall shape, with observable surface roughness, localized cracking, and partial fragmentation after burial. These changes indicate that degradation occurred, although the structural integrity of the composites was still partially

maintained. The visual observations are consistent with the weight loss results in Figure 5, where BG and RI showed lower to moderate biodegradation compared to PL.

In addition, the effect of chitosan content on visual degradation can also be observed. Composites with higher chitosan ratios (1:0.24) generally retained their structural integrity better than those with lower ratios, showing less fragmentation and surface damage. This supports the previous findings (Section 3.2), where higher chitosan content contributed to a more compact and stable matrix, thereby slowing down the degradation process.

Table 2 Appearance of fiber/chitosan composites before and after 30 days of soil burial.

Sample	Before soil burial	After soil burial 30 days
PL 1:0.08		
PL 1:0.16		
PL 1:0.24		
RI 1:0.08		
RI 1:0.16		

Table 2 Appearance of fiber/chitosan composites before and after 30 days of soil burial. (Continuous).

Sample	Before soil burial	After soil burial 30 days
RI 1:0.24		
BG 1:0.08		
BG 1:0.16		
BG 1:0.24		

3.4 Application test for plant cultivation

The application performance of the fiber/chitosan composites as biodegradable plant pots was evaluated through a plant growth test, as shown in Figure 6. All samples were able to support plant growth over a period of one month, indicating that the developed materials are suitable for agricultural use. No visible signs of plant toxicity, such as leaf discoloration, growth inhibition, or plant death, were observed in any of the samples. This suggests that the presence of chitosan and glycerol in the composite matrix did not adversely affect plant development. The growth performance of plants cultivated in the biodegradable pots was comparable to that of the conventional plastic nursery bag. The quantitative plant growth data are summarized in Table 3. Plants grown in all biodegradable pots exhibited comparable growth to those cultivated in the conventional plastic nursery bag, with plant heights ranging from 12.5 to 14.5 cm and leaf numbers ranging from 8 to 10 after 30 days of cultivation. The highest plant height was observed for PL:CS (14.5 cm), whereas the highest number of leaves was recorded for RI:CS (10 leaves). These results indicate that the

developed composites provide a suitable environment for plant growth without causing harmful effects. The results demonstrate that the fiber/chitosan composites are not only biodegradable but also functionally viable as plant-growing containers, supporting their potential application as eco-friendly alternatives to conventional plastic pots.

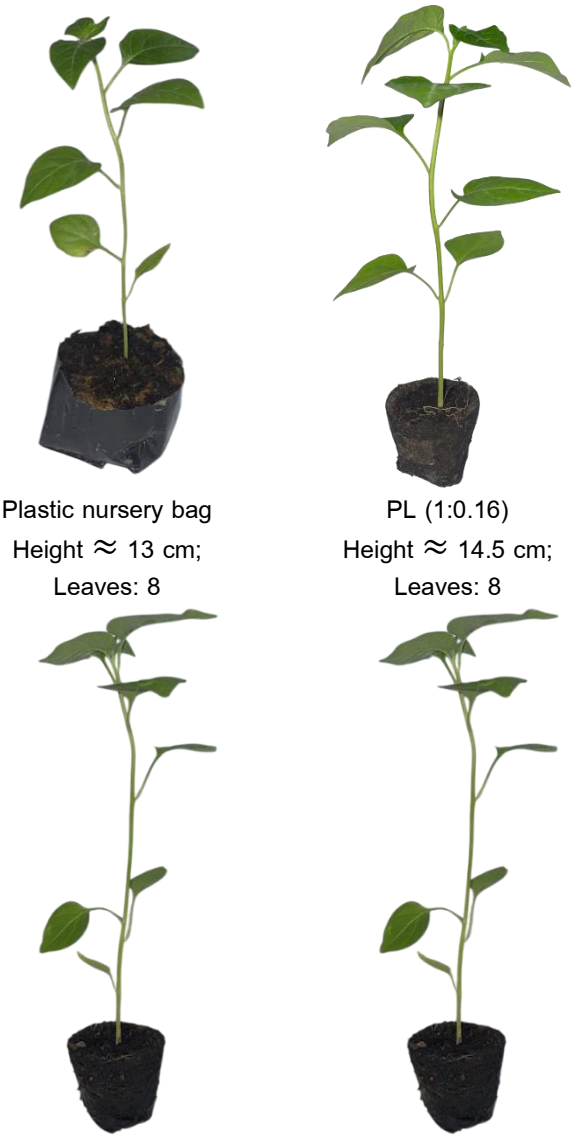


Figure 6 Chili plant growth in biodegradable pots (PL, RI, BG) and plastic nursery bag after 1 month of cultivation.

Table 3 Plant growth performance after 30 days of cultivation in different pot types.

Pot type	Plant height (cm)	Number of leaves
Plastic nursery bag	13.0	8
PL (1:0.16)	14.5	8
BG (1:0.16)	12.5	9
RI (1:0.16)	13.5	10

4. Conclusion

This study successfully developed biodegradable fiber-reinforced chitosan composites using pineapple leaf fiber (PL), rice straw (RI), and sugarcane bagasse (BG). The results showed that fiber type significantly influenced density, water absorption, thickness swelling, and biodegradation behavior. PL composites exhibited the highest density, water uptake, and biodegradation due to their high cellulose content and fibrillated structure, while RI showed the lowest values and BG demonstrated intermediate behavior. Increasing chitosan content improved dimensional stability by reducing thickness swelling. All composites were biodegradable under soil burial conditions and could be fabricated into hollow pot structures. The plant cultivation test confirmed that the developed pots supported plant growth without visible toxicity and showed comparable performance to conventional plastic nursery bags. These findings highlight the potential of fiber/chitosan composites as eco-friendly and biodegradable alternatives for agricultural applications. The 1 : 0 . 1 6 fiber-to-chitosan ratio showed a balanced combination of dimensional stability and biodegradation performance, making it the most suitable formulation for biodegradable pot production. The developed materials show potential for use as sustainable nursery pots in agricultural applications. However, this study focused primarily on physical properties and biodegradation behavior. Future work should include mechanical characterization and advanced material analyses to further evaluate their practical performance and long-term applicability.

5. Acknowledgments

The authors gratefully acknowledge the Department of Industrial Engineering, Faculty of Engineering, Rajamangala University of Technology Srivijaya, for providing laboratory facilities and technical support.

6. Declaration of Generative AI Use

ChatGPT was used only for English grammar correction and language refinement. All AI-assisted text was reviewed and edited by the authors, who take full responsibility for the final content of the manuscript.

7. References

Asim, M., Abdan, K., Jawaid, M., Nasir, M., Dashtizadeh, Z., Ishak, M.R. and Hoque, M.E. 2015. A review on pineapple leaves fibre and its composites. **International Journal of Polymer Science** 2015(1): 950567.

Chaichan, W. and Sawain, A. 2017. **Plant pots from co-production of spent coffee grounds, shell lime and rubber wood sawdust**. Rajamangala University of Technology Srivijaya.

Chaichan, W., Sawain, A. and Chaichan, W. 2018. Plant nutrients and biodegradable period of biological plant pot. **Wichcha Journal** 37: 12-26.

Chaichan, W., Sawain, A. and Chaichan, W. 2019. Optimum ratio for co-producing plant pot from organic residues. **Journal of Southern Technology** 12(1): 193-205.

Chaves, D.M., Araújo, J.C., Gomes, C.V., Gonçalves, S.P., Fangueiro, R. and Ferreira, D.P. 2024. Extraction, characterization and properties evaluation of pineapple leaf fibers from Azores pineapple. **Heliyon** 10(4): e26698.

Chokshi, S., Parmar, V., Gohil, P. and Chaudhary, V. 2022. Chemical composition and mechanical properties of natural fibers. **Journal of Natural Fibers** 19(10): 3942-3953.

Ghosh, S., Verma, D., Kumar, K., Pramanik, R., Balo, S., Mahata, D., Saini, A.K. and Mani, A. 2025. Microplastics in agricultural soils: An emerging threat to soil health, microbial ecology, crop productivity, and food safety. **International Journal of Plant & Soil Science** 37(5): 61-74.

Hajiha, H. and Sain, M. 2015. The use of sugarcane bagasse fibres as reinforcements in composites, pp. 525-549. In Faruk, O. and Sain, M., eds. **Biofiber Reinforcements in Composite Materials**. 2015: 525-549.

Ibrahim, F.H., Setiawan, R.A., Steven, S. and Mardiyati, Y. 2025. Towards sustainable composites: Fabrication, characterization, and biodegradation of all-cellulose composites (ACC) from ramie and luffa. **Results in Engineering** 26: 104695.

Iriany, A., Chanan, M., Hasanah, F. and Hariyanti, N.Y. 2022. Biodegradable pot made from water hyacinth and banana pseudostem for cocoa nursery. **IOP Conference Series: Earth and Environmental Science** 985(1): 012005.

Juming, N., Doloh, R., Khanong, P. and Kaewmanee, J. 2022. Production of plant pots from coffee grounds, water hyacinth and coconut fiber. **Proceedings of the National Science and Technology Conference**: 10-11.

Kamande, S.W., Kariuki, S.W. and Murithi, G. 2026. Impact of lignin on water absorption and thickness swelling of particleboard: A comprehensive review. **Advances in Materials Science and Engineering** 2026(1): 9065314.

Mahmud, M.A., Abir, N., Belal, S.A. and Gafur, M.A. 2025. Chemical characterization and tensile properties of a sugarcane bagasse-chemically modified starch composite structure developed for packaging purposes. **Results in Materials** 25: 100634.

Manafi-Dastjerdi, M., Ebrahimi-Nik, M., Rohani, A. and Lawson, S. 2022. Production of biodegradable pots from cattle manure and wood waste. **Environmental Science and Pollution Research** 29(14): 20265-20278.

Niju, S. and Swathika, M. 2019. Delignification of sugarcane bagasse using pretreatment strategies for bioethanol production. **Biocatalysis and Agricultural Biotechnology** 20: 101263.

Piyang, T., Chaichan, W. and Sagulsawasdipan, K. 2018. Environment-friendly plant pot production from palm oil sludge and mushroom waste. **Rajamangala University of Technology Srivijaya Research Journal** 10(3): 497-511.

Rosado, M.J., Rencoret, J., Marques, G., Gutiérrez, A. and Del Río, J.C. 2021. Structural characteristics of the guaiacyl-rich lignins from rice husks and straw. **Frontiers in Plant Science** 12: 640475.

Sethupathi, M., Khumalo, M.V., Skosana, S.J. and Muniyasamy, S. 2024. Recent developments of pineapple leaf fiber utilization in polymer composites. **Separations** 11(8): 245.

Sharma, N., Allardyce, B.J., Rajkhowa, R. and Agrawal, R. 2023. Rice straw-derived cellulose: A comparative study of various pre-treatment technologies and its conversion to nanofibres. **Scientific Reports** 13(1): 16327.

Somakul, P. and Ngencharoen, S. 2020. Biodegradable nursery pot from beverage labelling waste and coconut bagasse. **Proceedings of the KU SRC Annual Conference** 28.

Srisunont, T., Wongsakoonkan, W., Tongphanpharn, N., Ratanasongtham, P. and Srisunont, C. 2024. A brief overview of biodegradable pots for sustainable environment in Thailand. **Current Applied Science and Technology**: e0260109.

Sufian, A.A.M., Othman, S.A., Hasrin, N.I. and Harun, S.N.I. 2020. Future of pineapple leaf paper: A review. **International Journal of Engineering Advanced Research** 1(2): 1-5.

Tanpaiboonkul, N., Budnumpetch, T., Sukaranandara, K. and Phothilangka, P. 2022. Biodegradable pots from water hyacinth using cassava starch and cassava pulp as binder. **Huachiew Chalermprakiet Science and Technology Journal** 8(1): 56-69.

Tibalia, E.M.S.E., Wintoko, J. and Purnomo, C.W. 2023. Biodegradable food container from rice straw and sugarcane bagasse. **IOP Conference Series: Earth and Environmental Science** 1275(1): 012012.

Yang, H.S., Kim, D.J. and Kim, H.J. 2003. Rice straw–wood particle composite for sound absorbing wooden construction materials. **Bioresource Technology** 86(2): 117-121.

Yogeshwaran, V. and Priya, A. 2020. Removal of hexavalent chromium from aqueous solution using treated sugarcane bagasse powder. **Journal of the Indian Chemical Society** 97(9b): 1467-1477.

Zhang, Y., Ghaly, A. and Li, B.X. 2012. Physical properties of rice residues under different conditions. **American Journal of Applied Sciences** 9: 1757-1768.

Recent Science and Technology 2026, Vol. 18(3): e271665

Recent Science and Technology

Journal homepage: https:// www.tci-thaijo.org/index.php/rmutsvrj/index

ISSN: 3057-0786 (Online)

Research Article

Enrichment of Bioactive Compounds from Lotus (*Nelumbo nucifera* 'Roseum Plenum') Tea through Fermentation

Udomrat Chueasuwanachai [a], Nuntaporn Pungsungvorn [a] and Nipaporn Kanthong [a *]

[a]*Department of Biotechnology, Faculty of Science and Technology, Rajamangala University of Technology Tawan-ok, Sriracha, Chonburi 20110, Thailand.*

Article history:

Received: 2026-04-16
Revised: 2026-07-09
Accepted: 2026-07-09

Keywords:

Nelumbo nucifera;
Bioactive compounds;
Lotus flavonoids;
Lotus tea;
Lotus tea wine

ABSTRACT

Lotus tea, tea made from the Double red lotus (*Nelumbo nucifera* 'Roseum Plenum'). This advantageous characteristic is caused by its bioactive compounds, which include flavonoids and alkaloids. However, stirring the tea with hot water rapidly extracts the active compounds, which may result in a lower overall yield. Additionally, the related flavonoids and alkaloids have good solubility in alcohol. This study aimed to evaluate the feasibility of using lotus tea as a substrate for wine fermentation and to investigate the effect of fermentation on the extraction and enrichment of bioactive compound. Lotus tea and tea infusion used as substrate for the fermentation and HPLC utilized for measuring interesting bioactive compounds. The results indicate that both lotus tea and tea infusion underwent steady fermentation, producing ethanol levels of approximately 6% (v/v) within the first 7 days. All samples displayed characteristics typical of sweet wine, with alcohol content ranging from 6-8% (v/v) by day 28. Fermentation increased the concentrations of bioactive compounds, including catechin, epigallocatechin gallate (EGCG), and nuciferine, to approximately 2–5 times those in the original tea infusion, indicating enhanced extraction during fermentation. While fermentation increased the content of bioactive compounds in lotus tea, further in vivo and clinical investigations are necessary to establish the biological relevance of these findings and assess any potential health effects.

© 2026 Chueasuwanachai, U., Pungsungvorn, N. and Kanthong, N. Recent Science and Technology published by Rajamangala University of Technology Srivijaya

1. Introduction

The lotus flower (*Nelumbo nucifera* Gaertn) is a plant commonly used in the daily lives of Thai Buddhists and has also been used in traditional medicine. Especially the Sattabongkot cultivar, double red lotus (*Nelumbo nucifera* "Roseum Plenum"), claimed to support neurological function, cardiovascular health, antioxidant, reduce inflammation, improve sleep quality, and antidiabetic activities (Mukherjee *et al.*, 2009; Tungmunnithum *et al.*, 2018). The bioactive flavonoids and alkaloids present in lotus tissues are the main reasons for these health benefits.

Lotus tea made from lotus flower, stamen and petal and aromatic herbs. The main bioactive compounds as effect to health like quercetin, kaempferol, catechin, and nuciferine were limited water solubility (Lin *et al.*, 2009; Sharma *et al.*, 2017). Additionally, hot- water infusion is the common method for preparing lotus tea; however, this approach leads to inefficient extraction, resulting in beverages with suboptimal phytochemical content and diminished health benefits (Chen *et al.*, 2012).

Ethanol is widely used as an effective solvent for extracting flavonoids and alkaloids. However, the high alcohol concentration beverage is unsuitable for functional foods and health products because of safety, sensory, and regulatory concerns. Wine, alcoholic fermentation is the strategy that combines the advantage in food processing with a healthy perspective. Ethanol produced during the fermentation process acts as a green extraction solvent, facilitating the extraction of bioactive compounds from plant materials (Chemat *et al*., 2012). During alcoholic fermentation, ethanol concentrations typically remain below 14% (v/v), enabling the gradual extraction of compounds with limited water solubility. In addition, ethanol generated by yeast enhances the solubility and extraction

* **Corresponding author.**

E-mail address: *Nipaporn_ka@rmutto.ac.th*

Cite this article as: Chueasuwanachai, U., Pungsungvorn, N. and Kanthong, N. 2026. Enrichment of Bioactive Compounds from Lotus (*Nelumbo nucifera* 'Roseum Plenum') Tea through Fermentation. **Recent Science and Technology** 18(3): e271665.
https://doi.org/10.65411/rst.2026.271665

efficiency of relatively less polar phytochemicals, while microbial enzymes degrade plant cell walls, promoting the release of intracellular bioactive constituents. Fermentation also induces biochemical transformations and structural modifications within the plant matrix, which can improve the release, stability, and bioaccessibility of phytochemicals, including flavonoids and alkaloids (Hussain *et al.*, 2016; Luo *et al.*, 2024). Collectively, these processes contribute to the enrichment of bioactive compounds in fermented lotus tea products.

The aim of this study was to utilize alcoholic wine fermentation as a method to enhance the extraction of bioactive flavonoids and alkaloids from lotus tea. We compared the phytochemical profiles of lotus tea infusion and fermented lotus wine, with a focus on weakly water-soluble compounds such as kaempferol and nuciferine. We hypothesized that the gradual increase in low-level ethanol concentration (approximately 6–8% v/v) over 28 days of fermentation would improve the solubilization of these compounds. This process would result in a fermented lotus tea beverage with higher bioactive content.

2. Materials and Methods

2.1 Raw materials and yeast culture

Dried lotus tea, stamens, petals, and herbal ingredients as aroma herb were sourced from the community enterprise Thanacha Wellness Organic Farm (Chonburi, Thailand). The commercial active dry yeast, Saccharomyces cerevisiae from Lalvin EC-1118™ (Lallemand Inc, Montreal, Canada).

2.2 Preparation of lotus tea wine

Lotus tea wine fermentation was performed using tea powder, lotus stamens, and petals in four treatments. The quantities of lotus stamens (24 g) and petals (96 g) were equivalent to their respective proportions in 150 g of the lotus tea mixture (Table 1).

Table 1 Raw materials and ingredient composition of the wine.

Treatment	Sample	Raw materials	Weight (g)
1	Tea infusion	Tea powder	150
2	Tea	Tea powder	150
3	Stamen	Lotus stamen	24
4	Petals	Lotus petals	96

Nine liters of water were prepared, and granulated sugar was added to adjust the total soluble solids (TSS) to 20 °Brix, as sugar composition can influence yeast metabolism. Ingredients were added according to each treatment and boiled for 30 minutes. Solid residues were removed, leaving approximately 20%, except in the tea treatment (treatment 2) where residues were retained. The mixture was cooled and transferred to a 10 L fermentation tank.

Prior to inoculation, 5 g of active dry yeast (Lalvin EC-1118™, Canada) was added to 100 mL of warm lotus tea infusion and incubated for 30 min to obtain a rehydrated starter culture. Fermentation was conducted at an inoculation rate of 0.5 g/L and carried out at ambient temperature (28–30 °C) for 28 days. After fermentation, the clear supernatant was collected, bottled, and stored at 4 °C.

2.3 Monitoring of the fermentation process

Samples of fermentation were collected every seven days. A hand refractometer was used to measure TSS as °Brix using the AOAC method (AOAC, 2019). The pH was determined using a pH meter (pH 700, Eutech Instruments, Singapore) following the manufacturer's recommended. Ebulliometry was used to determine the alcohol content in accordance with OIV-MA-AS312-01A (OIV, 2012). Results are shown as mean ± standard deviation (SD), and all experiments were conducted in triplicate.

2.4 Sample and standard solution preparation for bioactive compound analysis

The lotus tea wine sample underwent direct analysis. For the tea infusion samples, one tea bag (containing 2 g of tea powder) was steeped in 250 mL of hot water for five minutes to prepare the first tea infusion samples. To prepare ethanol extracts, petals (9.6 g) were soaked in 10 mL of 70% (v/v) ethanol as a conventional solvent system and extracted at ambient temperature (28–30 °C) for 28 days.

The HPLC reference standards, quercetin hydrate, kaempferol hydrate, catechin hydrate, nuciferine, and troxerutin were obtained from TCI (Tokyo, Japan) and epigallocatechin gallate (EGCG) from Sigma-Aldrich (St. Louis, MO, USA). Stock standard solutions (100 ppm) were prepared in a mobile phase consisting of 1% (v/v) acetic acid in deionized water and acetonitrile (9:1, v/v). All samples and standards solutions were filtered through a 0.22 µm nylon syringe filter prior to HPLC analysis.

2.5 HPLC analysis of bioactive compounds

Bioactive compounds were analyzed using a Shimadzu Prominence-i LC-2050C i-Series HPLC system equipped with a UV–Vis detector (Shimadzu Corporation, Tokyo, Japan). Separation was performed on a reverse-phase C18 column (Shim-pack GIST, 4.6 × 250 mm, 3 µm particle size). The mobile phase consisted of solvent A (1% acetic acid in water) and solvent B (acetonitrile) under isocratic elution (90:10, v/v). The flow rate was 0.7 mL/min, column temperature was maintained at 35 °C, injection volume was 10 µL, and total run time was 60 min. Detection was carried out at 272 nm.

Compound identification was based on retention time comparisons with authentic standards analyzed under identical conditions. Quantification was achieved using external calibration curves derived from peak areas, following the method described by Seal (Seal, 2016).

2.6 Statistical analysis

All fermentation treatments were conducted in triplicate. Statistical analyses were performed using GraphPad Prism

version 9 (GraphPad Software, San Diego, CA, USA). Data for total soluble solids (TSS), alcohol content, and selected bioactive compound concentrations were analyzed by one-way analysis of variance (ANOVA). When significant differences were detected, means were compared using Tukey's honestly significant difference (HSD) post hoc test at a significance level of $p < 0.05$.

3. Results and Discussion

3.1 Feasibility of lotus tea as a substrate for wine fermentation

The use of non-fruit plant or herbs as fermentation substrates could markedly reduce yeast growth and fermentation efficiency. Because of variations in nutrient composition and the presence of inhibitory phytochemicals (Fletcher and Baetz, 2020). These results have demonstrated the potential of lotus tea as a raw material for wine fermentation. The level of alcohol and alterations in TSS serve as the primary criterion for wine characterization to identify wine fermentation performance.

The initial sugar concentration of 20 °Brix (~200 g/L) theoretically support a maximum alcohol yield of approximately 11–12% (v/v) (Duncan and Acton, 1967). In this study, alcohol production of tea infusion, tea and petals treatment at day 7 reached approximately 6–7% (v/v), representing about 50–70% of the theoretical yield, suggesting that fermentation had progressed into the late fermentation phase (Figure 1-2, Table 2).

The absence of significant differences ($p > 0.05$) in both TSS reduction and alcohol production between days 7, 14, and 28 for tea infusion, tea and petals treatment indicates that fermentation may have effectively ceased after 7 days. This behavior is consistent with typical yeast fermentation kinetics, where rapid sugar conversion occurs within the first few days, followed by a plateau phase.

In contrast, lotus stamens showed continued changes up to day 14, implying prolonged fermentation. This may be attributed to its lower nutrient availability or the presence of bioactive compounds that inhibit yeast activity, delaying alcohol production. This fermentation process of lotus tea sample is reliable with previous reports on non-fruit and herbal wine production, which often requires extended fermentation periods depending on its raw material composition (Awasthi, 2022; Shaik *et al.*, 2023).

On day 28 of fermentation, all lotus tea wine exhibited an alcohol content of 6–8% (v/v) and TSS of 7–11 °Brix, with a clear brown appearance (Figure 2). Based on alcohol and TSS levels, the product can be classified as a sweet white wine (Jackson, 2020).

To further confirm the type and concentration of sugars present, the addition HPLC analysis was conducted on both lotus tea infusion and tea wine samples. The results revealed that fructose was the predominant sugar in both types of wine, with concentrations of 1.13 g/100 mL and 0.83 g/100 mL, respectively. This is consistent with yeast metabolism, where glucose is preferentially utilized over fructose during fermentation (Fleet, 1990).

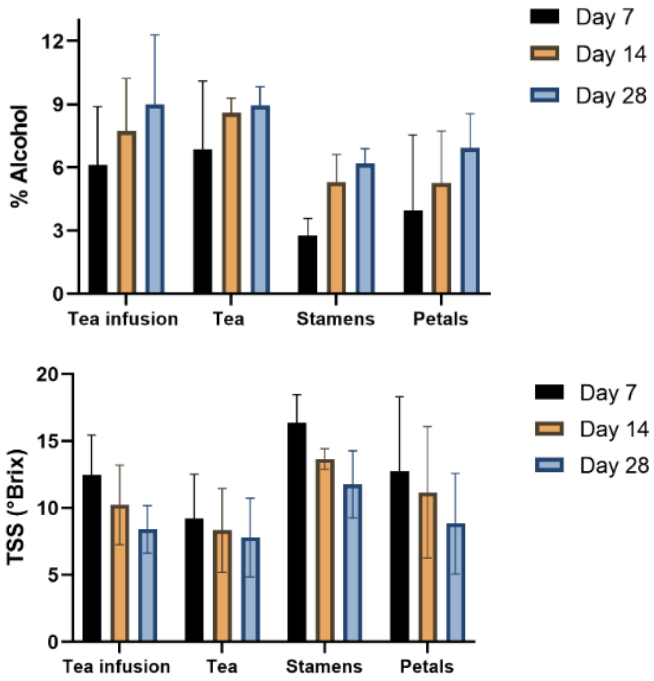


Figure 1 Alcohol content (up) and TSS (low) of lotus tea samples during wine fermentation.



Figure 2 Color of lotus wine after 28 days of fermentation (from left to right): Petals wine, stamens wine, tea infusion wine, and lotus tea wine.

3.2 Effect of wine fermentation on the extraction of bioactive compounds

The extraction efficiency of bioactive compounds from lotus tea, tea infusion, stamens, and petals using a wine fermentation process combined with maceration for 28 days was evaluated and compared with conventional hot water extraction. The total concentration of bioactive compounds varied significantly based on the solvent properties and extraction conditions, as demonstrated by quantitative analysis using HPLC. (Figure 3 and Table 3).

Flavonoids, including quercetin, kaempferol, catechin, and EGCG, as well as alkaloids such as nuciferine, exhibited distinct solubility behaviors in aqueous and alcoholic media, which

directly influenced their extraction efficiency (Dai and Mumper, 2010; Nguyen *et al.*, 2021).

EGCG, which is highly soluble in both water and organic solvents (Liu *et al.*, 2019), was detected at approximately two-fold higher levels in tea wine than in hot water extracts. No significant difference was observed between tea infusion wine and tea wine, indicating that residual tea material during fermentation did not affect extraction yield. The detection of EGCG in stamens and petals wines further confirms its origin from the lotus plant.

Catechin, which has limited solubility in water but increased solubility at higher temperatures and in alcohol (Cuevas-Valenzuela *et al.*, 2014), was detected at higher levels in tea wine than in tea infusion wine. This result suggests that ethanol enhances the extraction of moderately polar compounds, while lotus tea material during fermentation further contributes to increased extraction yield.

Quercetin exhibits low water solubility, with increased solubility under alkaline conditions and precipitation in acidic environments (pH < 4)(Srinivas *et al.*, 2010). Accordingly, only trace amounts were detected in tea infusion and lotus tea wines and none in stamen and petal wines, likely due to the acidic conditions (pH 3–4) after 28 days of fermentation. In contrast, ethanol extracts of lotus petals, which does not create acidic conditions, yielded higher quercetin levels.

Kaempferol, a flavonoid with strong antioxidant activity but very low water solubility (Deng *et al.*, 2019), was detected in minimal amounts in aqueous-based extracts and was absent in systems with higher water content. The highest levels were observed in lotus petals ethanol extracts, consistent with its preference for less polar solvents.

Nuciferine, an alkaloid with negligible water solubility but high solubility in organic solvents such as ethanol, methanol, and chloroform (Du *et al.*, 2016), was found in significantly higher concentrations in tea wine and was approximately four times higher than in tea infusions. The highest levels were detected in petals ethanol extracts, reflecting both solvent compatibility and compound distribution within plant tissues.

This study demonstrates that integrating wine fermentation with maceration is an effective green extraction strategy for enhancing the recovery of bioactive compounds, particularly those with high alcohol solubility. However, solvent composition, pH, and the solubility characteristics of individual compounds remain critical factors for maximizing the concentration of bioactive compounds in the extract.

3.3 Functional implications

The presence of interested flavonoids and alkaloids, including catechin, EGCG, quercetin and nuciferine, in lotus tea wine highlights its potential as a functional beverage with multiple health-promoting properties. These compounds have been extensively reported to exhibit antioxidant, anti-inflammatory, immunomodulatory, and cardioprotective effects (Chen *et al.*, 2019; Zhao *et al.*, 2023). The enrichment of such bioactive constituents through fermentation, with levels increasing approximately more than twofold compared to the original tea infusion, suggests that the fermentation process may enhance the extraction, transformation, or stability of these compounds.

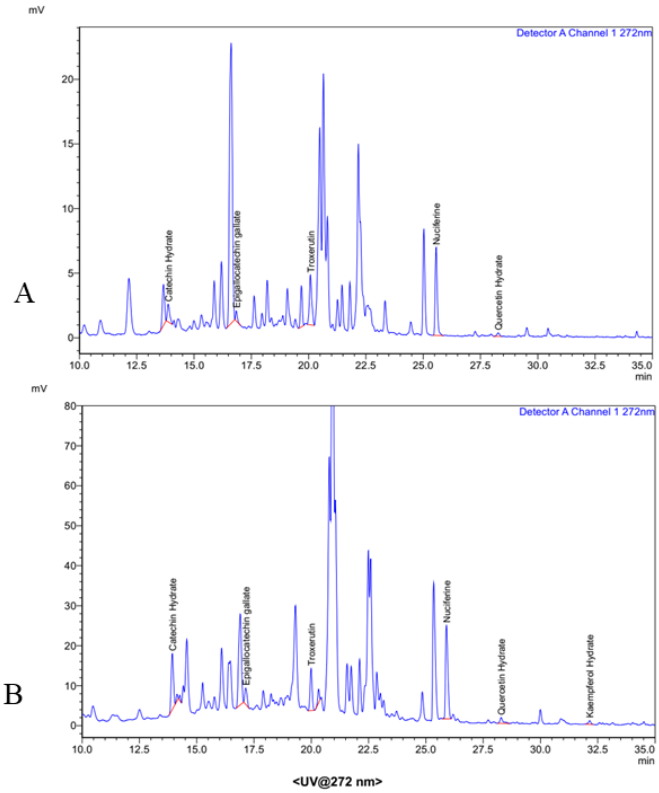


Figure 3 HPLC chromatogram of selected bioactive compounds in tea infusion (A) and lotus tea wine (B).

In particular, nuciferine has attracted attention due to its potential neuropharmacological effects. Previous studies have demonstrated that nuciferine may improve sleep quality by modulating multiple neurotransmitter systems and reducing neuronal hyperexcitability associated with insomnia (Zhang *et al.*, 2024). These findings highlight the potential of lotus tea wine as a functional beverage, with benefits extending beyond its increased nuciferine concentration to potential neuroprotective and other health-promoting effects.

However, it is important to note that the actual health benefits derived from these compounds are influenced not only by their increased concentrations but also by factors such as daily intake, bioavailability, metabolism, and individual physiological variability. Polyphenols such as catechin and EGCG are known to have limited bioavailability due to rapid metabolism and low absorption rates, which may reduce them in vivo efficacy (Cai *et al.*, 2018; Yang *et al.*, 2025).

4. Conclusion

This study demonstrates that lotus tea is a feasible alternative substrate for wine fermentation, despite the inherent

limitations of non-fruit raw materials. The fermentation process successfully supported yeast activity and moderate ethanol production of approximately 6–8% (v/v), which corresponds to about 50–70% of the theoretical yield based on an initial sugar concentration. In addition to ethanol production, Lotus tea wine markedly increased the concentrations of several bioactive constituents, particularly catechin, epigallocatechin gallate (EGCG), and the poorly water-soluble alkaloid nuciferine, which were present at levels approximately 2–5-fold higher than those in the corresponding tea infusions. These findings demonstrate that lotus tea wine fermentation not only enables ethanol production but also improves the recovery of bioactive phytochemicals, especially compounds with limited water solubility.

Table 2 Changes in TSS (°Brix) and alcohol concentration (% v/v) during wine fermentation.

No.	Treatment	Day 7		Day 14		Day 28	
		TSS (°Brix)	Alcohol (% v/v)	TSS (°Brix)	Alcohol (% v/v)	TSS (°Brix)	Alcohol (% v/v)
1	Tea infusion	12.46 ± 2.96^{a}	6.09 ± 2.79^{a}	10.23 ± 2.97^{a}	7.74 ± 2.48^{a}	8.40 ± 1.76^{a}	8.99 ± 3.29^{a}
2	Tea	9.20 ± 3.32^{ab}	6.87 ± 3.22^{a}	8.33 ± 3.12^{ab}	8.59 ± 0.69^{ab}	7.80 ± 2.94^{a}	8.95 ± 0.87^{ab}
3	Stamens	16.36 ± 2.10^{ac}	2.77 ± 0.81^{a}	13.66 ± 0.75^{ac}	5.30 ± 1.31^{ac}	11.76 ± 2.50^{a}	6.19 ± 0.70^{ac}
4	Petals	12.73 ± 5.57^{abc}	3.96 ± 3.58^{a}	11.16 ± 4.90^{abc}	5.25 ± 2.47^{abc}	8.83 ± 3.75^{a}	6.93 ± 1.62^{abc}

*Values are expressed as mean ± standard deviation (n = 3). Different superscript letters within the same column indicate significant differences ($p < 0.05$)

Table 3 Concentrations of selected bioactive compounds in tea infusion, tea wine and ethanol extracts (mg/mL).

Sample	EGCG	Catechin	Quercetin	Kaempferol	Nuciferine
Tea infusion	1.18 ± 0.13^{a}	2.37 ± 1.66^{a}	0.29 ± 0.00^{a}	0.06± 0.00^{a}	1.84 ± 1.30^{a}
Tea infusion wine	2.85 ± 0.26^{b}	1.27 ± 0.51^{ab}	0.27 ± 0.01^{ab}	0.32 ± 0.07^{ab}	4.10 ± 0.69^{b}
Tea wine	2.67 ± 0.38^{b}	11.70 ± 0.87^{ac}	0.49 ± 0.15^{ac}	0.10 ± 0.02^{ac}	5.13 ± 1.98^{b}
Stamens wine	1.21 ± 0.01	1.15 ± 0.51	ND	0.06± 0.00	0.68 ± 0.11
Petals wine	2.48 ± 0.27	0.71 ± 0.27	ND	0.06± 0.00	4.18 ± 0.20
Petals ethanol extract	15.97± 00.30	11.87±0.45	1.06±1.10	2.53±0.03	46.41±0.79

* Data are expressed as mean ± SD (n = 3 for tea infusion, stamens and petals wine and petals ethanol extract; n = 7 for tea and tea infusion wine). Different superscript letters within the same column indicate significant differences ($p \leq 0.05$). The statistical analysis excludes the stamen wine, petal wines, and petal ethanol extract.

5. Declaration of Generative AI and AI-assisted Technologies

During the preparation of this manuscript, ChatGPT was used to assist with language translation from Thai to English and sentence rephrasing for clarity. In addition, Grammarly and QuillBot were used for grammar checking, spelling correction, and language polishing.

The use of these tools was limited to improving the quality and readability of the English language. No generative AI tool was used to create or modify the scientific content, including the research design, experimental procedures, data analysis, results, or conclusions. All content is based on original experimental work conducted by the authors, who take full responsibility for the integrity and accuracy of the manuscript.

6. References

Cai, Z.Y., Li, X.M., Liang, J.P., Xiang, L.P., Wang, K.R., Shi, Y.L., Yang, R., Shi, M., Ye, J.H., Lu, J.L., Zheng, X.Q. and Liang, Y.R. 2018. Bioavailability of tea catechins and its improvement. **Molecules** 23(9): 2346.

Chemat, F., Vian, M.A. and Cravotto, G. 2012. Green extraction of natural products: Concept and principles. **International Journal of Molecular Sciences** 13(7): 8615-8627.

Chen, G., Zhu, M. and Guo, M. 2019. Research advances in traditional and modern use of *Nelumbo nucifera*: Phytochemicals, health promoting activities and beyond. **Critical Reviews in Food Science and Nutrition** 59(sup1): S189-S209.

Chen, S., Fang, L., Xi, H., Guan, L., Fang, J., Liu, Y., Wu, B. and Li, S. 2012. Simultaneous qualitative assessment and quantitative analysis of flavonoids in various tissues of lotus (*Nelumbo nucifera*) using high performance liquid chromatography coupled with triple quad mass spectrometry. **Analytica Chimica Acta** 724: 127-135.

Cuevas-Valenzuela, J., González-Rojas, Á., Wisniak, J., Apelblat, A. and Pérez-Correa, J.R. 2014. Solubility of (+)-catechin in water and water-ethanol mixtures within the temperature range 277.6–331.2 K: Fundamental data to design polyphenol extraction processes. **Fluid Phase Equilibria** 382: 279-285.

Dai, J. and Mumper, R.J. 2010. Plant phenolics: Extraction, analysis and their antioxidant and anticancer properties. **Molecules** 15(10): 7313-7352.

Deng, S.-P., Yang, Y.-L., Cheng, X.-X., Li, W.-R. and Cai, J.-Y. 2019. Synthesis, spectroscopic study and radical scavenging activity of kaempferol derivatives: Enhanced water solubility and antioxidant activity. **International journal of molecular sciences** 20(4): 975.

Du, X.-F., Pan, X., Guo, L. and Zhu, Y. 2016. Extractions and purification of nuciferine from Lotus leaves. **Advance Journal of Food Science and Technology** 10(2): 153-159.

Duncan, P. M. and Acton, G. W. B. 1967. **Progressive Winemaking: A Textbook Covering Fully the Theory and Practice of Winemaking, and a Guide to the Production of Superior Wines of Popular Types**. Amateur Winemaker.

Fleet, G.H. 1990. Growth of yeasts during wine fermentations. **Journal of Wine Research** 1(3): 211-223.

Fletcher, E. and Baetz, K. 2020. Multi-faceted systems biology approaches present a cellular landscape of phenolic compound inhibition in saccharomyces cerevisiae. **Frontiers in Bioengineering and Biotechnology** (8)2020: 539902.

Hussain, A., Bose, S., Wang, J.-H., Yadav, M.K., Mahajan, G.B. and Kim, H. 2016. Fermentation, a feasible strategy for enhancing bioactivity of herbal medicines. **Food Research International** 81: 1-16.

Jackson, R.S. 2020. **Wine Science: Principles and Applications**. Academic press.

Lin, H.-Y., Kuo, Y.-H., Lin, Y.-L. and Chiang, W. 2009. Antioxidative effect and active components from leaves of Lotus (*Nelumbo nucifera*). **Journal of agricultural and food chemistry** 57(15): 6623-6629.

Liu, B., Asadzadeh, B., and Yan, W. 2019. Solubility determination and modeling of EGCG peracetate in 12 pure solvents at temperatures from 278.15 to 318.15 K. **Journal of Chemical & Engineering Data** 64(12): 5218-5224.

Luo, X., Dong, M., Liu, J., Guo, N., Li, J., Shi, Y. and Yang, Y. 2024. Fermentation: ถ mprovement of pharmacological effects and applications of botanical drugs. **Frontiers in Pharmacology** 2024(15): 1430238.

Recent Science and Technology 2026, Vol. 18(3): e268061

Recent Science and Technology

Journal homepage: https:// www.tci-thaijo.org/index.php/rmutsvrj/index

ISSN: 3057-0786 (Online)

Research Article

Calcium Ion Adsorption-Desorption Behavior on Maize Residue-Derived Biochar for Soil Nutrient Retention

Patcharee Intanoo [a *] and Sakkarin Khaedaeng [b]

[a] *Department of Industrial Chemistry Innovation, Faculty of Science, Maejo University, Chiang Mai 50290, Thailand.*

[b] *Department of Industrial Chemistry and Textile Technology, Faculty of Science, Maejo University, Chiang Mai 50290, Thailand.*

Article history:

Received: 2025-06-18
Revised: 2026-07-06
Accepted: 2026-07-13

Keywords:

Biochar;
Calcium ion;
Adsorption-desorption;
Freundlich isotherm;
Nutrient retention

ABSTRACT

This research investigated the adsorption and desorption behavior of calcium ion (Ca^{2+}) on maize residue-derived biochar prepared by pyrolysis at 400 °C for 3 h under oxygen-limited conditions. Batch adsorption experiments were conducted by mixing 1.0 g biochar with 30 mL Ca^{2+} solutions at initial concentrations of 50-90 mg/L and shaking at 100 rpm until equilibrium. The produced biochar had an alkaline pH of 8.11, a specific surface area of 22.51 m^2/g, a pore volume of 0.04 cm^3/g, and oxygen-containing functional groups including -OH, -COOH/C=O, C-O, and phenolic groups. Adsorption equilibrium was reached after 240 min. The adsorption data fitted the Freundlich model (R^2 = 0.9828; KF = 1.6792 L/g; 1/n = 1.6567) better than the Langmuir model (R^2 = 0.8478), while negative Langmuir parameters indicated that the monolayer assumption was not appropriate for this system. Kinetic analysis showed better agreement with the pseudo-second-order model (R^2 = 1.00; qe, cal = 1.170 mg/g), suggesting that surface complexation or ion-exchange interactions contributed to the first adsorption layer. Subsequent retention might involve weaker adsorbate-adsorbate interactions on heterogeneous sites, consistent with Freundlich-type multilayer adsorption. The hysteresis index (HI = 1.37) suggested relatively strong calcium retention with limited desorption in deionized water. These findings indicate that maize residue-derived biochar has potential as a calcium-retention soil amendment; however, soil incubation and plant-response studies are required to validate agricultural performance under practical conditions.

© 2026 Intanoo, P. and Khaedaeng, S. Recent Science and Technology published by Rajamangala University of Technology Srivijaya

1. Introduction

Maize productivity in Thailand has gradually declined over the past decade, largely due to soil degradation caused by intensive monoculture, excessive fertilizer application, and post-harvest residue burning (Office of Agricultural Economics, 2023; Aumtong *et al*., 2024). These practices reduce soil organic matter, deteriorate soil structure, and decrease cation exchange capacity (CEC), thereby weakening the soil's ability to retain exchangeable nutrient cations and accelerating nutrient losses through leaching (Khongdee *et al*., 2022; Omara *et al*., 2023). Among essential plant nutrients, calcium (Ca^{2+}) is particularly susceptible to leaching in acidic and highly weathered soils despite its indispensable roles in cell wall stabilization, membrane integrity, intracellular signaling, and plant tolerance to biotic and abiotic stresses (Wdowiak *et al*., 2024). Consequently, improving calcium retention while maintaining its availability has become an important challenge for sustainable agricultural production.

Calcium is an essential secondary macronutrient that regulates numerous physiological processes, including enzyme activation, root development, and cellular signaling, in addition to its structural role in plant cell walls (Wdowiak *et al*., 2024). However, because Ca^{2+} is relatively weakly retained by soil colloids compared with many other nutrient cations, it is readily lost through leaching, particularly in coarse-textured and acidic soils. Therefore, effective soil amendments should not only enhance calcium retention but also allow its gradual release to satisfy plant nutrient demand throughout the growing season (Omara *et al*., 2023). This requirement has stimulated growing

* **Corresponding author.**

E-mail address: *patchareeintanoo@gmail.com*

Cite this article as: Intanoo, P. and Khaedaeng, S. 2026. Calcium Ion Adsorption-Desorption Behavior on Maize Residue-Derived Biochar for Soil Nutrient Retention. **Recent Science and Technology** 18(3): e268061.

https://doi.org/10.65411/rst.2026.268061

interest in developing sustainable soil amendments capable of improving nutrient retention without restricting nutrient availability.

Among the available soil amendments, biochar has emerged as a promising material because of its porous structure, large specific surface area, high cation exchange capacity, and abundant oxygen-containing functional groups generated during oxygen-limited pyrolysis (Amalina *et al*., 2022; Phadtare and Kalbande, 2022; Kabir *et al*., 2023). These physicochemical properties promote nutrient retention through cation exchange, electrostatic attraction, and surface complexation while simultaneously improving soil physical properties (Kabir *et al*., 2023; Omara *et al*., 2023). Nevertheless, high adsorption capacity alone does not necessarily ensure improved nutrient use efficiency if adsorbed nutrients cannot subsequently be released for plant uptake. Therefore, comprehensive evaluation of both adsorption and desorption behavior is essential for assessing the practical agricultural performance of biochar. In this context, hysteresis analysis provides valuable information on nutrient retention and release behavior beyond conventional adsorption capacity.

Existing studies have demonstrated that biochar effectively adsorbs various metal cations owing to its porous structure and oxygen-containing functional groups (Chen *et al*., 2024; Mei *et al*., 2025). However, most investigations have focused on the removal of heavy metals and other environmental contaminants rather than nutrient cations such as Ca^{2+}. Moreover, previous studies have primarily emphasized adsorption equilibrium, while calcium desorption behavior, hysteresis characteristics, and the relationships among adsorption isotherms, adsorption kinetics, and nutrient release remain insufficiently understood. Consequently, it remains unclear whether calcium adsorbed onto biochar can be retained strongly enough to minimize nutrient loss while still being gradually released to satisfy plant nutrient requirements, particularly in maize residue-derived biochar.

Maize residues are among the most abundant agricultural by-products generated annually in northern Thailand and are frequently disposed of by open-field burning, resulting in greenhouse gas emissions and the loss of valuable biomass resources. Compared with many agricultural residues, maize residues are inexpensive, locally available, and produced in large quantities, making them an attractive feedstock for biochar production. Furthermore, biochar produced from maize residues under relatively low pyrolysis temperatures has been reported to preserve abundant oxygen-containing functional groups that favor nutrient cation adsorption (Janu *et al*., 2022; Barszcz *et al*., 2024). Low-temperature pyrolysis (approximately 400 °C) preserves these reactive functional groups while maintaining adequate pore development, whereas higher pyrolysis temperatures promote aromatic carbon formation and reduce surface oxygen functionalities involved in cation adsorption (Janu *et al*., 2022; Barszcz *et al*., 2024).

Based on these considerations, this study aims to characterize the physicochemical properties of maize residue-derived biochar and systematically investigate calcium absorption, adsorption kinetics, desorption behavior, and hysteresis characteristics. Unlike previous studies that mainly evaluated adsorption equilibrium of contaminant metals, this work integrates physicochemical characterization, adsorption isotherm analysis, kinetic modeling, desorption experiments, and hysteresis evaluation to provide a comprehensive understanding of calcium retention and release mechanisms on maize residue-derived biochar. The findings are expected to provide a more realistic assessment of biochar performance as a sustainable nutrient-retention material capable of simultaneously minimizing calcium loss through leaching while maintaining adequate nutrient availability for plant uptake.

2. Materials and Methods

2.1 Maize residue preparation

The maize residue used for biochar production was collected from local farmers in the Jedee Maekrua community, Mae Faek Mai, San Sai, Chiang Mai, Thailand. The collected maize residues were sun-dried for 7 days to remove moisture. After drying, the residues were mechanically ground at a rotational speed of 14,000 rounds per minute (rpm) for 3 minutes. The ground material was then sieved through a 60-mesh screen to obtain fine maize residue powder. This powder was stored in a desiccator to prevent moisture absorption before further use.

2.2 Conversion of maize residue into biochar

The maize residue powder, previously sieved through a 60-mesh screen, was converted into biochar by using a pyrolysis process. The pyrolysis process was conducted under oxygen-limited conditions at a temperature of 400 °C, with a heating rate of 5 °C per minute, for a duration of 3 hours. This process yielded fine black biochar powder. The fine black biochar powder was subsequently sieved again using a 60-mesh screen to ensure uniform particle size. The biochar powder was then stored in a desiccator to prevent moisture absorption prior to use.

2.3 Chemical composition and physical property analysis of biochar

The chemical composition analysis of biochar was performed to identify and confirm the presence of functional groups on the biochar surface, such as hydroxyl (–OH), carboxyl (–COOH), and carbonyl (C=O) groups. This was carried out using a Fourier Transform Infrared Spectrometer (FTIR) (Perkin Elmer, England/Spectrum) over a wavenumber range of 400–4000 cm^{-1}. The chemical properties of the biochar were further assessed by measuring pH using a pH meter (Mettler-Toledo AG) and cation exchange capacity (CEC) following the method described by Intanoo and Kongklay (2022). For physical characterization, the specific surface area, pore size, and pore

volume of the biochar were analyzed using a surface area and porosity analyzer based on the Brunauer–Emmett–Teller (BET) method (Quantachrome/Autosorb 1 MP).

2.4 The adsorption and release behavior of calcium ions on the surface of biochar

The adsorption behavior of calcium ions on the biochar surface was studied based on adsorption equilibrium theories using the Langmuir model (Equations (1)–(2)) (Langmuir, 1918) and the Freundlich model (Equations (3)–(4)) (Freundlich, 1906). Both models describe the relationship between the amount of adsorbate (calcium ions) adsorbed per unit mass of adsorbent (biochar) in mg/g, and the equilibrium concentration of calcium ions remaining in the solution at a given temperature in mg/L. The adsorption and release behavior was conducted in two stages: (1) the determination of equilibrium sorption time, and (2) the analysis of calcium ion adsorption behavior. Calcium concentrations were quantified using atomic absorption spectrophotometry (GBC Scientific Equipment/ SavantAA) following calibration with a five-point standard curve (0–100 mg/L). The calibration curve exhibited $R^2 > 0.999$.

$$q_e = \frac{q_m K_L C_e}{1 + K_L C_e} \quad (1)$$

$$\frac{C_e}{q_e} = \frac{1}{K_L q_m} + \frac{C_e}{q_m} \quad (2)$$

$$q_e = K_F C^{\frac{1}{n}} \quad (3)$$

$$\log q_e = \log K_F + \frac{1}{n} \log C_e \quad (4)$$

$$HI = \frac{1/n_{desorbed}}{1/n_{adsorped}} \quad (5)$$

where: q_e is the amount of adsorbate adsorbed per unit mass of adsorbent at equilibrium (g/g); C_e is the equilibrium concentration of the adsorbate remaining in the solution at a given temperature (g/mL); q_m is the maximum adsorption capacity for monolayer coverage per unit mass of adsorbent (g/g); K_L is the Langmuir constant related to the affinity of binding sites (L/mg); K_F is the Freundlich constant indicating the multilayer adsorption capacity (g/g).

2.4.1 Equilibrium sorption time determination

The determination of equilibrium sorption time of calcium ions onto the biochar surface was carried out by adding 30 mL of a calcium standard solution at a certain concentration to 1 gram of biochar. The mixture was then shaken at the speed of 100 rounds per minute (rpm) for various durations time: 4, 10, 15, 30, 60, 120, 240, 360, 480, and 900 minutes, respectively. After each specified shaking time, the samples were collected, and the solution was separated by filtration through a 0.45-micron nylon membrane filter. The calcium concentration in the filtrate was determined as described in Section 2.4. All equilibrium adsorption experiments were independently performed in five replicates (n = 5).

2.4.2 Calcium ion adsorption behavior

The study of calcium ion adsorption behavior on the biochar surface was conducted by introducing 30 mL of calcium standard solutions with the concentrations of 50, 60, 70, 80, and 90 mg/L into 1 gram of biochar. The selected calcium concentration range of 50–90 mg/L was chosen as a controlled laboratory range suitable for evaluating adsorption isotherm behavior without causing immediate saturation of adsorption sites. This range also provided sufficient analytical sensitivity for calcium determination by atomic absorption spectrophotometry while allowing adsorption behavior to be compared across increasing initial calcium concentrations. The solution volume-to-biochar ratio of 30 mL/g was used to ensure adequate contact between calcium ions and the biochar surface under batch adsorption conditions. (Udawatta *et al*., 2023). The mixtures were agitated using a shaker at a speed of 100 rpm for a duration corresponding to the previously determined equilibrium sorption time. A blank control containing calcium solution without biochar was simultaneously prepared under identical experimental conditions to distinguish calcium adsorption from possible precipitation during the adsorption experiment. After shaking, the solution was collected and filtered through a 0.45-micron nylon membrane filter. The calcium concentration in the filtrate was determined as described in Section 2.4. All adsorption experiments were independently performed in five replicates (n = 5).

2.4.3 The release of calcium ion from biochar surface

The release behavior of calcium ions (Ca^{2+}) from biochar surface was investigated using the hysteresis index (HI) as an indicator to assess the ease or difficulty of calcium ion desorption after adsorption onto biochar (Guedes *et al*., 2021). The hysteresis index is calculated as the ratio of the slope of the adsorption curve to that of the desorption curve at the same equilibrium concentration, as shown in Equation (5). In this study, the calcium-loaded biochar (obtained from the adsorption procedure described in section 2.4.2) was immersed in 30 mL of deionized water and agitated at 100 rpm using a shaker at the equilibrium sorption time. The aqueous solution was then collected and filtered through a 0.45-micron nylon membrane filter. The concentration of desorbed calcium ions was analyzed using an atomic absorption spectrophotometer (GBC Scientific Equipment/SavantAA).

2.5 Statistical analysis

Experimental results are presented as mean ± standard deviation (SD). The mean and standard deviation were calculated from five independent experiments using Microsoft Excel 2021. Adsorption isotherm and kinetic parameters were estimated by linear regression analysis.

3. Results and Discussion

3.1 Properties of biochar

The produced biochar exhibited a cation exchange capacity (CEC) of 1,670.96 ± 44.66 cmol/kg and a pH of 8.12 ± 0.22, representing approximately 38.0-fold and 1.15-fold increases, respectively, compared with the untreated soil (soil CEC = 44.00 ± 1.50 cmol/kg). These properties indicated a high density of exchangeable surface sites together with moderately alkaline characteristics that were favorable for nutrient retention. In addition, the produced biochar exhibited a specific surface area of 22.51 m²/g and a pore volume of 0.04 cm³/g, suggesting a porous structure that can facilitate interactions between nutrient ions and the biochar surface.

The relatively high CEC observed in the present study might be attributed to the preservation of oxygen-containing functional groups and the presence of mineral ash generated during low-temperature pyrolysis, both of which contribute to the formation of negatively charged adsorption sites for nutrient cations (Kabir *et al*., 2023; Omara *et al*., 2023; Chen *et al*., 2024). Previous studies had similarly reported that biochars produced at relatively low pyrolysis temperatures (300–500 °C) generally exhibit higher CEC because oxygen-containing functional groups were better preserved than those produced at higher temperatures, thereby enhancing cation exchange capacity (Ippolito *et al*., 2020; Joseph *et al*., 2021).

The high CEC observed in this study is consistent with the potential of biochar to improve soil nutrient retention. For example, Intanoo and Kongklay (2022) reported that incorporating biochar into soil increased soil CEC by 10.33% compared with untreated soil and was associated with improved chlorophyll content and higher yields of kale and eggplant. Although the present study did not include soil incubation or plant growth experiments, the high CEC and porous structure of the produced maize residue-derived biochar suggest its potential as a nutrient-retention material for agricultural soils. Further soil and plant studies are required to verify its agronomic performance under field conditions.

The FTIR analysis of produced biochar is shown in Figure 1. As seen in Figure 1, it was found that produced biochar revealed the presence of several key functional groups on its surface. These included hydroxyl groups (O–H stretching at 3,600–3,200 cm^{-1}), carboxylic groups (C=O stretching at 1,740–1,700 cm^{-1}), and ether groups (C–O stretching at 1,110–1,030 cm^{-1}). Additionally, aromatic structures (C=C, C=O stretching at 1,630–1,600 cm^{-1}) and phenolic groups (O–H bending at 1,392 cm^{-1}) were also detected. The dominant oxygen-containing functional groups were mainly found on biochar surface. They were attributed to partial oxidation reactions during the pyrolysis of maize residue under low-temperature (400 °C) and oxygen-limited conditions. Under such conditions, organic structures like cellulose, hemicellulose, and lignin decompose and undergo chemical transformations, leading to the development of new surface functional groups. For the porosity of biochar, it originates from the thermal decomposition of these organic structures, which generates volatile compounds such as CO, CO_2, CH_4, H_2, and water vapor. As these volatiles release, they leave behind the cavities within the carbon matrix, by which creating the porous structure that characterizes biochar. These features collectively enhance the functionality of biochar in improving soil structure, water retention, and nutrient-retaining capacity.

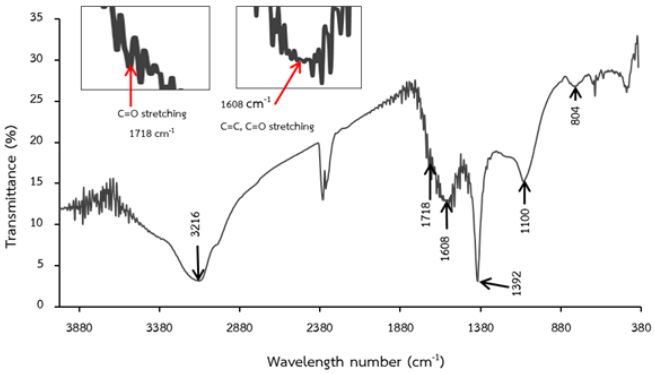


Figure 1 FTIR spectra of biochar produced from maize residue.

The presence of various functional groups on the biochar surface has attracted significant attention due to their role in enhancing the soil's cation exchange capacity (CEC). These surface functional groups, such as carboxylic (–COOH), hydroxyl (–OH), and carbonyl (C=O), can dissociate to form negatively charged sites (e.g., R–COOH ⟶ R–COO^-), thereby enabling the adsorption of nutrient cations from soil solution. Therefore, the incorporating biochar into agricultural soils, might enhance the nutrient retention by reducing leaching losses, as the negatively charged sites on the biochar surface bind positively charged nutrient ions. Furthermore, elevated CEC contributes to improved fertilizer use efficiency, enriches soil fertility, and ultimately increases crop productivity.

3.2 Calcium ion adsorption behavior on the surface of biochar

3.2.1 Equilibrium sorption time determination

To determine the equilibrium sorption time of calcium ions on the biochar surface, a relationship was established between the amount of calcium adsorbed per unit mass of biochar at a given time (q_t) and the adsorption time, as illustrated in Figure 2. According to Figure 2, the amount of calcium ions adsorbed on the biochar surface increased with time and eventually stabilized after 240 minutes of adsorption. This indicates that adsorption beyond 240 minutes does not significantly affecte to the quantity of calcium ions adsorbed on biochar surface. In other words, once the biochar becomes saturated with calcium ions, some ions began to desorb, creating new vacant sites for subsequent ions to occupy. Eventually, the rate of adsorption equaled to the rate of

desorption, a condition known as equilibrium. This phenomenon occurred after more than 240 minutes of the adsorption. Therefore, it can be concluded that the equilibrium sorption time of this study was longer than 240 minutes.

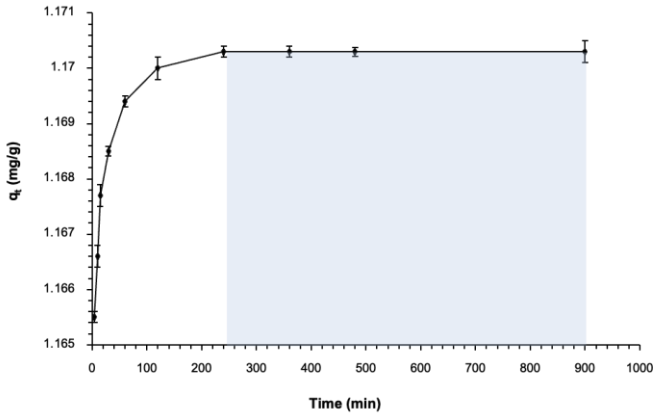


Figure 2 The adsorption of calcium ions on biochar surface at different contact times at room temperature (values represent mean ± SD (n = 5)).

3.2.2 Calcium ion adsorption behavior analysis

The adsorption behavior of calcium ions on the biochar surface was evaluated using the Langmuir and Freundlich adsorption isotherm models. The experimental equilibrium adsorption data obtained at initial Ca^{2+} concentrations of 50–90 mg/L are summarized in Table 1. These data were subsequently used for fitting the Langmuir and Freundlich adsorption isotherm models. The linearized Langmuir plot (Figure 3 a) yielded negative values for both the maximum adsorption capacity (q_m) and the Langmuir constant (K_L) (Table 2). Such negative parameters indicated that the fundamental assumptions of the Langmuir model, namely homogeneous adsorption sites and monolayer adsorption, were not satisfied under the present experimental conditions (Hu *et al*., 2022; Mei *et al*., 2025). Consequently, the Langmuir model was considered unsuitable for describing calcium adsorption onto maize residue-derived biochar, and its parameters were not interpreted quantitatively. In contrast, the Freundlich model exhibited a higher coefficient of determination (R^2 = 0.98) than the Langmuir model (R^2= 0.85), indicating better agreement with the experimental data (Lonappan *et al*., 2016; Khan *et al*., 2018). This finding suggested that calcium adsorption occurred predominantly on heterogeneous adsorption sites through a multilayer adsorption process, which was consistent with the assumptions of the Freundlich isotherm.

The heterogeneous adsorption behavior might be associated with the physicochemical characteristics of the produced biochar. Biochar prepared at the relatively low pyrolysis temperature of 400 °C under oxygen-limited conditions generally retained abundant oxygen-containing functional groups while limiting the development of highly condensed aromatic structures (Janu *et al*., 2022; Barszcz *et al*., 2024; Malik *et al*., 2025). The coexistence of different functional groups likely generated adsorption sites with varying binding affinities for calcium ions, thereby promoting heterogeneous and multilayer adsorption rather than uniform monolayer adsorption. These observations were consistent with previous studies reporting that low-temperature biochars commonly exhibit heterogeneous surface characteristics that are better described by the Freundlich adsorption model (Mei *et al*., 2025).

Based on the adsorption isotherm analysis, the Freundlich model suggested that calcium adsorption on maize residue-derived biochar occurred predominantly on heterogeneous adsorption sites through a multilayer adsorption process. As illustrated in Figure 4, the initial adsorption layer was likely associated with interactions between Ca^{2+} ions and oxygen-containing functional groups on the biochar surface, including hydroxyl and carboxyl groups. These surface interactions were generally attributed to electrostatic attraction, ion exchange, and surface complexation, which collectively contribute to relatively strong adsorption at the biochar surface (Udawatta *et al*., 2023). Once the primary adsorption sites became occupied, additional calcium ions were likely retained through interactions with previously adsorbed ions, forming subsequent adsorption layers via relatively weak intermolecular forces, such as van der Waals and dipole–dipole interactions. This combination of strong surface interactions followed by weaker adsorbate–adsorbate interactions is consistent with the heterogeneous and multilayer adsorption behavior described by the Freundlich isotherm.

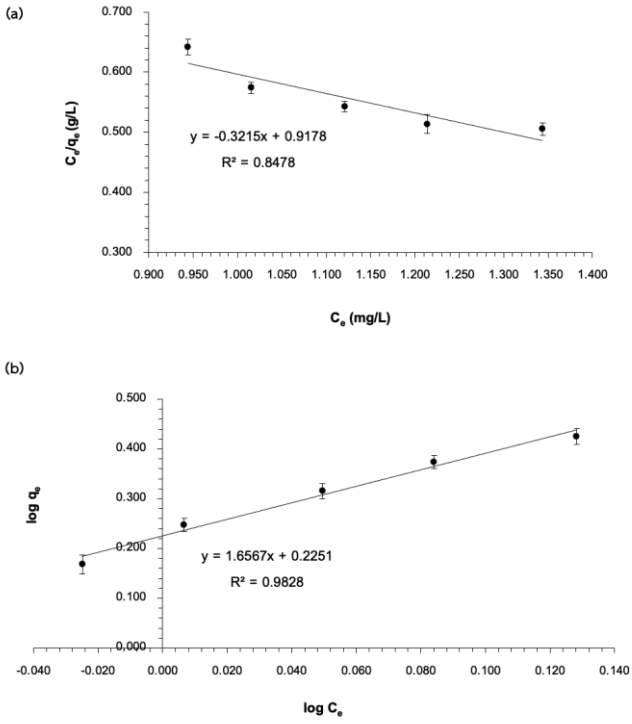


Figure 3 The adsorption behavior of calcium on biochar surface based on (a) the Langmuir and (b) the Freundlich isotherm models (values represent mean ± SD (n = 5)).

In the Freundlich isotherm model, the adsorption behavior was further interpreted using the constants K_F and $^1/_n$, which represented the adsorption capacity and adsorption intensity, respectively. The obtained $^1/_n$ value of 1.66 suggested that calcium adsorption deviated from ideal monolayer behavior and further supported the heterogeneous nature of the biochar surface. This observation was consistent with the superior fit of the Freundlich model and indicated that calcium adsorption likely occurred through multiple adsorption sites with different binding energies rather than uniformly distributed adsorption sites. The relatively high K_F value also reflected the favorable affinity of maize residue-derived biochar for calcium ions within the investigated concentration range. Values of $^1/_n$ greater than unity might indicate cooperative adsorption behavior or suggested that the Freundlich model only partially described the adsorption process over the investigated concentration range (Foo and Hameed, 2010; Tran *et al*., 2017).

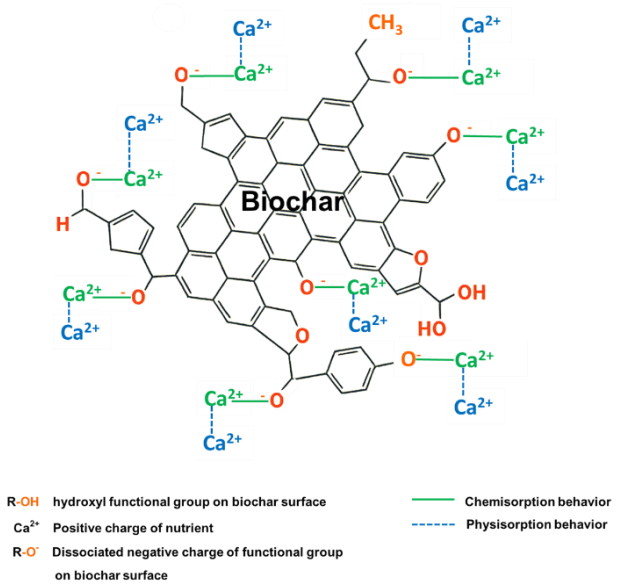


Figure 4 Schematic drawing of multilayer adsorption following the Freundlich adsorption isotherm model.

3.2.3 Adsorption kinetics

The study of calcium ion adsorption kinetics on the biochar surface provides insights into the adsorption efficiency, which might be governed either by the diffusion of calcium ions toward the biochar surface, as described by the pseudo-first-order kinetic model (Equation (6)), or by the formation of chemical bonds between calcium ions and the surface functional groups of the biochar, as explained by the pseudo-second-order kinetic model (Equation (7)) (Udawatta *et al*., 2023).

$$\log(q_e - q_t) = \log q_e - \frac{k_1}{2.303}t \quad (6)$$

$$\frac{t}{q_t} = \frac{1}{k_2 q_e^2} + \frac{t}{q_e} \quad (7)$$

where: k_1 is the rate constant of the pseudo-first-order kinetic model (min^{-1}), q_t is the amount of adsorbate adsorbed per unit mass of adsorbent at time t (mg/g), q_e is the amount of adsorbate adsorbed per unit mass of adsorbent at equilibrium (mg/g), and t is the adsorption time (minutes).

The adsorption kinetics of calcium ions onto maize residue-derived biochar were evaluated using the pseudo-first-order and pseudo-second-order kinetic models. Linear plots generated from Equations (6) and (7) are presented in Figure 5, and the corresponding kinetic parameters are summarized in Table 3. The pseudo-second-order model exhibited a higher coefficient of determination (R^2 = 1.00) than the pseudo-first-order model, indicating better agreement with the experimental data. In addition, the equilibrium adsorption capacity predicted by the pseudo-second-order model ($q_{e_{cal}}$) closely matched the experimentally determined value ($q_{e_{exp}}$) of 1.170 mg/g, further supporting the suitability of this kinetic model for describing calcium adsorption onto the biochar surface.

The superior fit of the pseudo-second-order model suggested that the adsorption process was likely governed by surface interactions between calcium ions and reactive sites on the biochar rather than by simple diffusion-controlled adsorption alone. Similar kinetic behavior had been reported for calcium adsorption onto biochar and other carbonaceous adsorbents, where ion exchange and surface complexation were considered important adsorption pathways (Udawatta *et al*., 2023). Nevertheless, the kinetic analysis alone could not conclusively identify the adsorption mechanism. Therefore, the adsorption mechanism proposed in this study was interpreted collectively based on adsorption isotherm analysis together with FTIR characterization and hysteresis behavior. Overall, these complementary results suggested that calcium adsorption on maize residue-derived biochar likely involved relatively strong surface interactions during the initial adsorption stage, followed by weaker interactions contributing to multilayer adsorption, which is consistent with the Freundlich adsorption model.

3.3 Calcium ion desorption from biochar surface

The desorption behavior of calcium ions from maize residue-derived biochar was evaluated using the hysteresis index (HI), which reflected the reversibility of the adsorption–desorption process. In general, low HI values indicated weak nutrient retention and a greater risk of nutrient loss through leaching, whereas excessively high HI values suggested that adsorbed nutrients might become strongly retained and less available for plant uptake (Guedes *et al*., 2021). Therefore, an appropriate balance between adsorption and desorption was essential for biochar intended for agricultural applications.

In the present study, the calculated HI value was 1.37, indicating that calcium ions were retained on the biochar surface while remaining potentially releasable under appropriate environmental conditions. This result suggested that maize residue-derived biochar possesses a favorable balance

between calcium retention and release rather than exhibiting either excessively weak or irreversible adsorption. The observed hysteresis behavior was also consistent with the Freundlich isotherm, which indicated heterogeneous adsorption sites and multilayer adsorption. Calcium ions initially associated with reactive oxygen-containing functional groups may be retained more strongly, whereas ions adsorbed in subsequent layers were expected to be more readily desorbed through weaker intermolecular interactions.

Although the present study was conducted under controlled laboratory conditions, the obtained HI value suggested that the produced biochar had the potential to function as a nutrient-retention material capable of reducing calcium loss while maintaining nutrient availability. Such adsorption–desorption behavior might contribute to improved nutrient use efficiency in agricultural soils. However, the actual release of calcium under field conditions was expected to be influenced by various environmental factors, including soil pH, moisture content, competing ions, and microbial activity. Therefore, soil incubation and plant growth experiments were required to verify the practical agronomic performance of the produced biochar.

Although the present study provided insight into the adsorption and desorption behavior of calcium ions on maize residue-derived biochar under controlled laboratory conditions, several limitations should be acknowledged. The adsorption experiments were performed using standard calcium solutions rather than soil systems, and solution pH was not continuously monitored during adsorption. Consequently, the possible influence of solution chemistry on calcium precipitation cannot be completely excluded. Furthermore, the agricultural implications proposed in this study should be considered preliminary until validated through soil incubation and plant growth experiments. Future studies should therefore investigate calcium retention under realistic soil conditions while incorporating pH monitoring and blank control experiments.

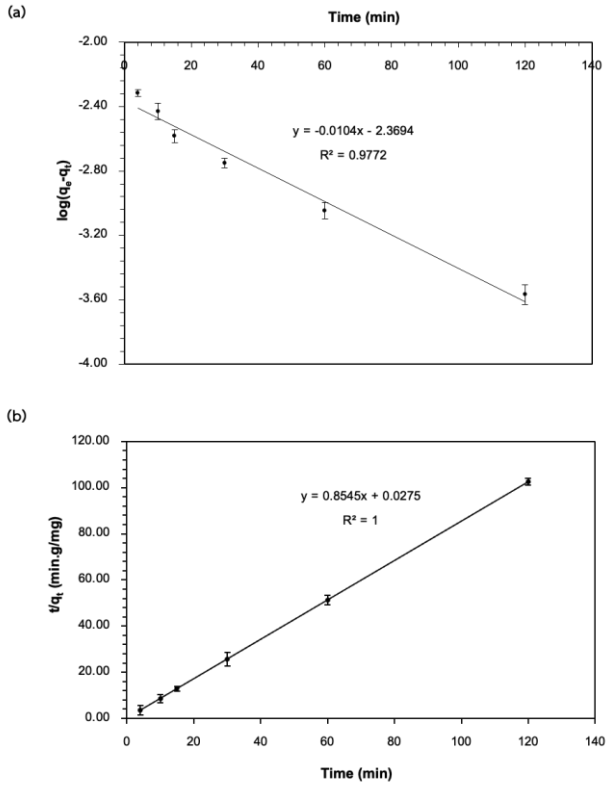


Figure 5 The adsorption kinetics of calcium ion on biochar surface based on (a) the pseudo-first-order and (b) the pseudo-second-order reaction rate (values represent mean ± SD (n = 5)).

Table 1 The calcium ion adsorption data on 1 gram of biochar were analyzed using the Langmuir and Freundlich isotherm model at room temperature.

Concentration (mg/l)		q_e (mg/g)	C_e (mg/l)	$\frac{C_e}{q_e}$ (g/l)	$\log C_e$	$\log q_e$
Initial	Adsorbed					
50	49.06	1.472	0.944	0.642	-0.025	0.168
60	58.98	1.770	1.015	0.574	0.007	0.248
70	68.88	2.066	1.121	0.542	0.050	0.315
80	78.79	2.364	1.214	0.513	0.084	0.374
90	88.66	2.660	1.344	0.505	0.128	0.425

Table 2 The parameters that describe the adsorption behavior according to the Langmuir and the Freundlich isotherm model.

Langmuir adsorption isotherm			Freundlich adsorption isotherm		
q_m (mg/g)	K_L (L/mg)	R^2	K_F (L/g)	$1/n$	R^2
-3.1104	-0.3503	0.8478	1.6792	1.6567	0.9828

Table 3 The kinetic constants of calcium ion adsorption on biochar based surface on the pseudo-first-order and pseudo-second-order reaction rate.

$q_{e\ (exp)}$* (mg g^{-1})	Pseudo-first order reaction rate			Pseudo-second order reaction rate		
	$q_{e\ (cal)}$** (mg g^{-1})	k_1 (min^{-1})	R^2	$q_{e\ (cal)}$** (mg g^{-1})	k_2 (g mg^{-1} min^{-1})	R^2
1.170	0.00427	0.0239	0.9772	1.170	26.56	1.00

Note: q_e (exp)* is calcium absorption capacity at equilibrium obtained from the experiment.
q_e (cal)** is calcium adsorption capacity at equilibrium obtained from the calculation.

4. Conclusion

The study of calcium ion adsorption behavior on the biochar surface revealed that the adsorption mechanism aligns with the Freundlich isotherm model. This reflects adsorption on heterogeneous surface sites of biochar and supports multilayer adsorption. The adsorption process was found to involve both chemisorption and physisorption mechanisms. In the first adsorption layer, calcium ions bind to surface functional groups containing oxygen atoms such as –OH, –COOH, and C=O through chemical bonding, which corresponded to the pseudo-second-order kinetic model. In subsequent layers, additional calcium ions are adsorbed onto the initially adsorbed calcium ions through physical forces such as electrostatic interactions and van der Waals forces. These interactions further support the occurrence of multilayer adsorption, consistent with the heterogeneous nature of the biochar surface. Furthermore, desorption analysis showed that the hysteresis index (HI) was greater than 1.00, indicating the adsorbed calcium ions were strongly retained on the biochar surface. These results suggested that the produced biochar demonstrated promising calcium ion retention capability.

5. Acknowledgments

The author would like to acknowledge the financial support provided by the Faculty of Science, Maejo University, under the departmental budget grant for the fiscal year of 2024 (Project Code: MJ.2-67-026). Special thanks are extended to the Jedee Maekrua community, Mae Faek Mai Subdistrict, San Sai District, Chiang Mai Province, for providing the maize residue used in this study. Appreciation is also given to the Industrial Chemical Innovation Program, Faculty of Science, Maejo University, for the equipment, instruments, and facilities that made the successful completion of this research possible.

6. References

Amalina, F., Razak, A.S.A., Krishnan, S., Sulaiman, H., Zularisam, A.W. and Nasrullah, M. 2022. Biochar production techniques utilizing biomass waste-derived materials and environmental applications: A review. **Journal of Hazardous Materials Advances** 7: 100134.

Barszcz, W., Łożyńska, M. and Molenda, J. 2024. Impact of pyrolysis process conditions on the structure of biochar obtained from apple waste. **Scientific Reports** 14: 10501.

Chen, J., Zhou, J., Zheng, W., Leng, S., Ai, Z., Zhang, W., Yang, Z., Yang, J., Xu, Z., Cao, J., Zhang, M., Leng, L. and Li, H. 2024. A complete review on the oxygen-containing functional groups of biochar: Formation mechanisms, detection methods, engineering, and applications. **Science of the Total Environment** 946: 174081.

Foo, K.Y. and Hameed, B.H. 2010. Insights into the modeling of adsorption isotherm systems. **Chemical Engineering Journal** 156(1): 2–10.

Freundlich, H. 1906. Over the adsorption in solution. **Zeitschrift für Physikalische Chemie** 57: 387–470.

Guedes, R.S., Pinto, D.A., Ramos, S.J., Dias, Y.N., Junior, C.F.C., Gastauer, M., Filho, W.M.S. and Fernandes, A.R. 2021. Biochar and conventional compost reduce hysteresis and increase phosphorus desorbability in iron mining waste. **Revista Brasileira de Ciência do Solo** 45: e0200174.

Hu, Y., Li, P., Yang, Y., Ling, M. and Li, X. 2022. Preparation and characterization of biochar from four types of waste biomass under matched conditions. **BioResources** 17(4): 6464–6475.

Intanoo, P. and Kongklay, K. 2022. A study of kale and eggplant growth growing in biochar-based growing media. **Journal of Agricultural Research and Extension** 40(1): 1–14.

Ippolito, J.A., Cui, L., Kammann, C., Wrage-Mönnig, N., Estavillo, J.M., Fuertes-Mendizabal, T., Novak, J.M., Spokas, K.A., Borchard, N. and Cayuela, M.L. 2020. Biochar as a sustainable strategy to improve soil properties and nutrient use efficiency: A review. **Agronomy** 10(10): 1567.

Janu, R., Mrlik, V., Ribitsch, D., Hofman, J., Sedláček, P., Bielská, L. and Soja, G. 2022. Biochar surface functional groups as affected by biomass feedstock, biochar composition and pyrolysis temperature. **Carbon Resources Conversion** 5(1): 36–46.

Joseph, S., Cowie, A.L., Van Zwieten, L., Bolan, N., Budai, A., Buss, W., Cayuela, M.L., Graber, E.R., Ippolito, J.A., Kuzyakov, Y., Luo, Y., Ok, Y.S., Palansooriya, K.N.,

Shepherd, J., Stephens, S., Weng, Z. and Lehmann, J. 2021. How biochar works, and when it doesn't: A review of mechanisms controlling soil and plant responses to biochar. **GCB Bioenergy** 13(11): 1731–1764.

Kabir, E., Kim, K.H. and Kwon, E.E. 2023. Biochar as a tool for the improvement of soil and environment. **Frontiers in Environmental Science** 11: 1324533.

Khan, M.A., Khan, S., Ding, X., Khan, A. and Alam, M. 2018. The effects of biochar and rice husk on adsorption and desorption of cadmium onto soils with different water conditions (upland and saturated). **Chemosphere** 193: 1120–1126.

Khongdee, N., Tongkoom, K., Iamsaard, K., Mawan, N., Yimyam, N., Sanjunthong, W., Khongdee, P. and Wicharuck, S. 2022. Closing yield gap of maize in Southeast Asia by intercropping systems: A review. **Australian Journal of Crop Science** 16(11): 1224–1233.

Langmuir, I. 1918. The adsorption of gases on plane surfaces of glass, mica and platinum. **Journal of the American Chemical Society** 40(9): 1361–1403.

Lonappan, L., Rouissi, T., Das, R.K., Brar, S.K., Ramirez, A.A., Verma, M., Surampalli, R.Y. and Valero, J.R. 2016. Adsorption of methylene blue on biochar microparticles derived from different waste materials. **Waste Management** 49: 537–544.

Malik, S. and Laura, J.S. 2025. Evaluating biochar properties derived from various agro-residues via pyrolysis: A comparative study. **Oriental Journal of Chemistry** 41(1): 120–126.

Mei, Y., Zhuang, S. and Wang, J. 2025. Adsorption of heavy metals by biochar in aqueous solution: A review. **Science of the Total Environment** 968: 178898.

Office of Agricultural Economics. 2023. **Agricultural statistics of Thailand report**. Ministry of Agriculture and Cooperatives, Bangkok. (in Thai)

Omara, P., Singh, H., Singh, K., Sharma, L., Otim, F. and Obia, A. 2023. Short-term effect of field application of biochar on cation exchange capacity, pH, and electrical conductivity of sandy and clay loam temperate soils. **Technology in Agronomy** 3: 16.

Pandian, K., Vijayakumar, S., Mustaffa, M.R.A.F., Subramanian, P. and Chitraputhirapillai, S. 2024. Biochar: A sustainable soil conditioner for improving soil health, crop production and environment under changing climate: A review. **Frontiers in Soil Science** 4: 1376159.

Phadtare, P.D. and Kalbande, S.R. 2022. Biochar production technologies from agricultural waste, its utilization in agriculture and current global biochar market: A comprehensive review. **International Journal of Environment and Climate Change** 12(11): 1010–1031.

Tran, H.N., You, S.J., Hosseini-Bandegharaei, A. and Chao, H.P. 2017. Mistakes and inconsistencies regarding adsorption of contaminants from aqueous solutions: A critical review. **Water Research** 120: 88–116.

Udawatta, M.M., Silva, R.C.L.D. and Silva, D.S.M.D. 2023. Surface modification of *Trema orientalis* wood biochar using natural coconut vinegar and its potential to remove aqueous calcium ions: Column and batch studies. **Environmental Engineering Research** 28(1): 210522.

Wdowiak, A., Podgórska, A. and Szal, B. 2024. Calcium in plants: An important element of cell physiology and structure, signaling, and stress responses. **Acta Physiologiae Plantarum** 46: 108.

Zeng, S. and Kan, E. 2022. Sustainable use of $Ca(OH)_2$ modified biochar for phosphorus recovery and tetracycline removal from water. **Science of the Total Environment** 839: 156159.

Recent Science and Technology 2026, Vol. 18(3): e271208

Recent Science and Technology

Journal homepage: https:// www.tci-thaijo.org/index.php/rmutsvrj/index

ISSN: 3057-0786 (Online)



Research Article

Design and Development of a Microcontroller-Based Control System for a Semi-Automatic Bean Sprout Cultivation Machine

Panot Sripakarach [a *]

[a]*Department of Electrical Engineering, Faculty of Engineering, Thonburi University, Bangkok 10160, Thailand.*

Article history:

Received: 2026-03-11
Revised: 2026-05-07
Accepted: 2026-07-22

Keywords:

Closed-loop control;
Thermoelectric cooling;
Precision agriculture;
Food safety;
Bean sprout cultivation

ABSTRACT

The cultivation of high-quality bean sprouts is often hindered by inconsistent environmental control and hazardous chemical contamination. This research develops a closed-loop environmental control system, utilizing an Arduino Mega 2560 microcontroller to actively manage the microclimate within a semi-automatic cultivation machine. The system integrates thermoelectric (Peltier) cooling to effectively dissipate accumulated metabolic heat, combined with a precision humidity control mechanism. Performance was evaluated in triplicate (n = 3) against traditional timer-based irrigation systems. Statistical analysis (one-way ANOVA, $p < 0.05$) demonstrated that the prototype successfully stabilized water temperature (22–25 °C) and relative humidity (80–90%) throughout the cultivation period. These optimal conditions led to a 31–65% increase in total net yield compared to traditional chemical-free methods. While this yield remains slightly lower than intensive commercial practices that rely on growth-accelerating chemicals, laboratory tests by an ISO/IEC 17025 accredited facility confirmed undetectable levels of formaldehyde and sulfur dioxide. This study provides a novel engineering framework for chemical-free precision agriculture, demonstrating significant potential for enhancing food safety and reducing manual labor in commercial-scale production.

© 2026 Sripakarach, P. Recent Science and Technology published by Rajamangala University of Technology Srivijaya

1. Introduction

Bean sprouts are a widely consumed economic crop, valued for their high nutritional content and their rapid cultivation cycle of only three to four days. However, cultivating high-quality and uniform bean sprouts requires strict environmental control (Wannawas and Riansut, 2020). Traditional cultivation methods are heavily reliant on manual labor, requiring continuous monitoring and watering every two to three hours. Suboptimal temperatures or insufficient humidity often result in poor-quality yields, characterized by excessively long roots, thin stems, or a high susceptibility to fungal rot.

To mitigate these issues, commercial producers frequently resort to the illicit application of hazardous chemicals to reduce spoilage and artificially enhance the physical appearance of the sprouts. For instance, formaldehyde is commonly used to improve crispness and extend shelf life, while sulfur dioxide (SO_2) serves as a bleaching agent to maintain a fresh aesthetic. These substances pose severe health risks. Notably, the World Health Organization (WHO) classifies formaldehyde as a known human carcinogen, strictly prohibiting its use as a food additive (World Health Organization, 2006). A preliminary laboratory analysis conducted in this study on a 600-gram random sample of commercially available bean sprouts detected formaldehyde contamination at levels up to 0.5 mg/kg. This finding underscores an urgent public health issue that directly motivates the objective of this study: to replace chemical dependency with precise, automated control of the physical cultivation environment.

Biologically, the seed germination process is exothermic, releasing substantial amounts of metabolic heat that accumulates within the cultivation environment (Mirek *et al.*, 2023). Maintaining ambient and water temperatures between 22 and 25 °C is intended to dissipate this accumulated heat, thereby limiting the conditions that favor rot-causing microorganisms and reducing the need for

* **Corresponding author.**

E-mail address: *mintandmos@thonburi-u.ac.th*

Cite this article as: Sripakarach, P. 2026. Design and Development of a Microcontroller-Based Control System for a Semi-Automatic Bean Sprout Cultivation Machine. **Recent Science and Technology** 18(3): e271208.

https://doi.org/10.65411/rst.2026.271208

chemical interventions. Furthermore, water temperature strongly influences the germination, stem elongation, and yield of mung bean sprouts (Hanif *et al*., 2019), whereas a high relative humidity (maintained at 80–90% in this study) minimizes seedling transpiration and promotes cellular expansion, resulting in longer sprouts and a significantly higher fresh weight than those grown under low-humidity conditions (Amitrano *et al*., 2020).

To achieve these optimal conditions and overcome the limitations of manual labor, automated technologies are increasingly being integrated into bean sprout cultivation systems. For example, Bamrungkul (2021) demonstrated that an automated cultivation machine, utilizing a timer-controlled water pump operating at three-hour intervals, reduced energy consumption while yielding robust sprouts. The application of microcontrollers in this domain is also well-documented. Hakim *et al*. (2023) developed a prototype automated watering system using an open-source Arduino-based controller, which significantly reduced labor time and increased crop yields compared to traditional practices.

However, a critical knowledge gap remains. While previous studies have successfully implemented automated irrigation to manage humidity, they primarily rely on open-loop or simple timer-based strategies. Consequently, these systems lack precise, systematic, and closed-loop control over both water and ambient temperatures. Although solid-state thermoelectric cooling has emerged as a viable, eco-friendly solution in hydroponics (Kanasri, 2018), its integration into closed-loop sprout cultivation, specifically to actively counteract metabolic heat, remains largely underexplored.

To bridge this technological gap and address the aforementioned health concerns, this study aims to design and develop a closed-loop environmental control system for a chemical-free, semi-automatic bean sprout cultivation machine. Distinct from previous prototypes that focused mainly on irrigation frequency, this research introduces an integrated climate-control framework designed to actively dissipate metabolic heat, a critical factor often overlooked in existing designs. The proposed system regulates relative humidity and water temperature in real-time through a coordinated sensor-actuator network. The novelty of this work lies in the integration of thermoelectric cooling within a closed-loop logic to maintain thermal stability, thereby ensuring optimal morphology and food safety without chemical dependency. This approach offers a more sophisticated and scalable engineering solution than current timer-based systems, establishing a new baseline for precision sprout cultivation.

2. Materials and Methods

This section details the design and development of a microcontroller-based system for a chemical-free, semi-automatic bean sprout cultivation machine. The system utilizes embedded technology to maintain an optimal microclimate for plant growth. The research methodology comprises five primary phases: physical structure design, hardware architecture design, equipment sizing and calculation, algorithm development, and performance evaluation.

2.1 Physical structure design

The physical architecture of the cultivator was designed based on vertical farming principles, which optimize spatial efficiency and environmental control in closed systems (Beacham *et al*., 2019). The cultivation chamber consists of an opaque container measuring 31 × 58 × 37.5 cm (width × length × height), yielding a total volumetric capacity of 0.067 m³. The use of an opaque enclosure is a critical design parameter, as it prevents light-induced greening of the sprouts; light exposure increases the accumulation of chlorophylls and carotenoids and reduces dry matter compared with dark-grown sprouts (Mastropasqua *et al*., 2020). The interior is engineered as a closed-loop environment to facilitate precise temperature and humidity regulation. As illustrated in Figure 1, the structure is functionally compartmentalized into four primary zones.

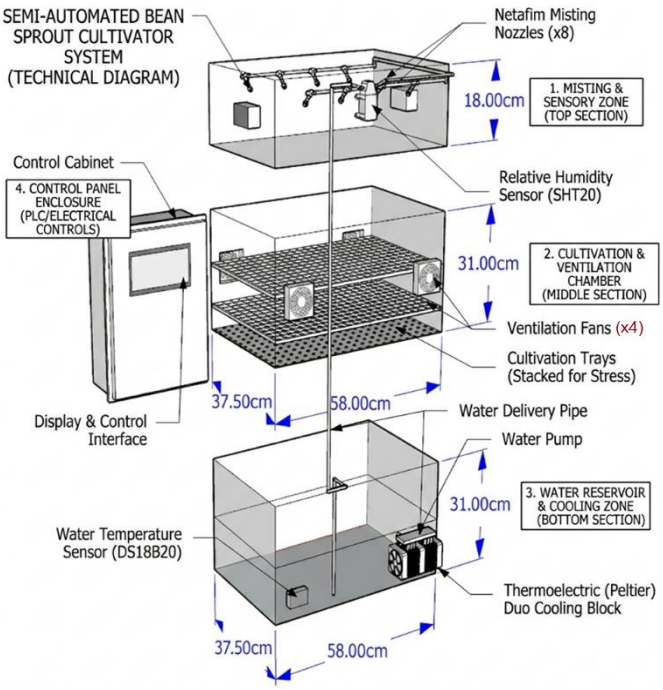


Figure 1 The physical structure and functional zones of the semi-automatic bean sprout cultivation machine.

2.1.1 Top section (Misting and sensory zone)

Located at the ceiling of the chamber, this zone is equipped with eight Netafim misting nozzles. These nozzles are evenly distributed along the container's length to ensure uniform spray coverage over the cultivation area, effectively eliminating dry spots. An SHT20 temperature and relative humidity sensor is also mounted in this uppermost area. This placement protects the sensor from direct exposure to water droplets while allowing for accurate measurement of the chamber's ambient conditions.

2.1.2 Middle section (Cultivation and ventilation chamber)

Serving as the primary cultivation area, this zone accommodates a three-tier stacked planting grid. This

configuration maximizes spatial efficiency and utilizes the weight of the upper tiers to exert constant physical stress on the underlying sprouts. Applying mechanical stress is a proven agricultural technique to stimulate lateral stem expansion and suppress excessive vertical elongation, yielding thicker sprouts that meet commercial quality standards (Biddington, 1986). In addition, four 12 VDC ventilation fans are integrated into the side walls to exhaust accumulated carbon dioxide and metabolic heat, thereby mitigating the risk of mold growth associated with excess moisture.

2.1.3 Bottom section (Water reservoir and cooling zone)

The lower compartment acts as a water reservoir and recirculating sump, collecting excess runoff from the upper cultivation tiers via a gravity drain system. A solid-state thermoelectric (Peltier) module is integrated into the reservoir wall to actively extract heat from the circulating water. Additionally, a submersible DS18B20 temperature sensor provides continuous real-time feedback to the microcontroller, ensuring that the recirculated misting water is strictly maintained within the optimal 22–25 °C range.

2.1.4 Control box and HMI zone

The control system is housed in an isolated enclosure, entirely separated from the high-humidity cultivation chamber. This physical isolation is essential to prevent electrical short circuits and protect sensitive electronic components. The control box contains the main processing unit (Arduino Mega 2560), power driving modules, a switching power supply, and solid-state relays (SSRs). For system interaction, an ESP32-S3 touchscreen is mounted on the front panel at an ergonomic viewing angle, serving as the primary Human-Machine Interface (HMI) for real-time monitoring and operational mode configuration.

2.2 Hardware architecture and control system

The control system architecture of the semi-automatic bean sprout cultivation machine employs a centralized processing design with robust power distribution. The system manages data and signal flow according to a logical framework comprising four functional domains: processing, inputs, outputs, and bi-directional communication (as illustrated in Figure 2). This framework ensures that environmental regulation remains precise, safe, and resilient against electromagnetic interference (EMI) (Horowitz and Hill, 2015). The hardware architecture is divided into the following primary components.

2.2.1 Power management system

To guarantee stable operation, the power distribution and electrical circuit isolation were designed as follows:

Main DC power distribution: A 50 A switching power supply converts the 220 VAC mains input into 12 VDC to drive high-current actuators, including four ventilation fans, the thermoelectric (Peltier) cooling module, and the circulating water pump. Simultaneously, a step-down converter (Hi-Link module) provides a stable 5 VDC regulated supply for the Arduino Mega 2560 and the ESP32-S3 HMI, protecting sensitive logic components from voltage fluctuations.

High-voltage isolation for the misting pump: The misting system pump operates on a dedicated 12 VDC adapter. To mitigate EMI generated by this inductive load, the pump is switched on the alternating current (AC) side using a solid-state relay (SSR). This provides galvanic isolation, ensuring that high-voltage switching transients do not interfere with the microcontroller's logic operations (OMRON Corporation, n.d.).

2.2.2 Main processing unit (Process)

An Arduino Mega 2560 microcontroller serves as the central processing unit of the system. It functions as the core logic hub, executing embedded environmental control algorithms to process acquired sensor data and independently command the various actuator modules based on real-time conditions.

2.2.3 Signal acquisition and parameter measurement system (Input system)

The signal acquisition system facilitates real-time, unidirectional data transfer from high-precision sensors to the microcontroller, ensuring continuous, low-latency monitoring of the internal microclimate. The system relies on two primary sensing modules:

Water temperature sensing: A submersible DS18B20 sensor monitors the temperature of the recirculating water. Operating via the 1-Wire protocol through a specialized adapter board, this digital sensor provides high noise immunity and ensures accurate temperature feedback, which is essential because water temperature significantly affects the germination rate, stem length, and yield of mung bean sprouts (Hanif *et al*., 2019).

Ambient humidity and temperature measurement: Two SHT20 digital sensors measure the air temperature and relative humidity inside the cultivation chamber. Because both sensors share identical hardware addresses, they communicate with the microcontroller via a TCA9548A I2C multiplexer to prevent data collisions. This architectural choice allows the Arduino Mega 2560 to switch communication channels effectively, maintaining high signal integrity and reliable data synchronization across multiple sensing nodes (Texas Instruments, 2014).

Before installation, all sensors were calibrated against standard laboratory instruments to ensure measurement accuracy. Furthermore, the control system was programmed with a data sampling interval and control loop frequency of 60 seconds.

2.2.4 Actuator control and output system

The central processing unit regulates the internal microclimate by transmitting digital control signals to various power-driving modules. These modules serve as intermediaries to drive high-current actuators based on predefined

environmental set-points. The output architecture comprises the following sub-systems:

Humidity and ventilation control: To mitigate excessive relative humidity (RH) and accumulated metabolic heat, the microcontroller interfaces with a MOSFET D4184 electronic switch module. This module controls four 12 VDC ventilation fans, which are activated when the ambient RH exceeds 90%. This facilitates rapid air exchange, removing the moisture and metabolic heat that accumulate in the closed chamber (Mirek *et al*., 2023) and thereby limiting the stagnant, high-moisture conditions often associated with fungal proliferation.

Water temperature regulation: A 2-channel electro-mechanical relay module controls the cooling sub-system, comprising a thermoelectric (Peltier) plate and a circulation pump. This setup maintains the reservoir water within the optimal 22–25 °C range. The relay provides robust switching capable of handling the Peltier module's high current demands, ensuring efficient heat extraction (Zhao and Tan, 2014).

Misting system control: A solid-state relay (SSR) manages the high-pressure misting pump to maintain adequate humidity. When the sensor detects an RH below 80%, the SSR activates the pump, delivering atomized water through eight misting nozzles. An SSR is specifically utilized here for its ability to endure frequent switching cycles without mechanical wear and to suppress electromagnetic interference (EMI) that could otherwise compromise sensor accuracy (OMRON Corporation, n.d.).

Operational status notification: A piezoelectric buzzer provides audible feedback to the user. It is programmed to emit a continuous rhythmic alert upon the completion of a cultivation cycle, signaling that the sprouts are ready for harvest.

2.2.5 Human-machine interface and bi-directional communication

The system employs bi-directional communication between the touchscreen interface and the main processing unit, enabling direct user interaction and real-time monitoring. An ESP32-S3 HMI module equipped with a capacitive touchscreen communicates with the Arduino Mega 2560 via the I2C protocol. This master-slave architecture ensures reliable data exchange and bus integrity, adhering to standard practices for multi-microcontroller embedded systems (Ibrahim, 2006). The HMI operations are divided into two primary functions:

User input (Command interface): Operators can select predefined cultivation modes–such as TON1 for short-stemmed sprouts or TON2 for long-stemmed sprouts–directly via the touchscreen. These commands are transmitted to the Arduino Mega 2560, which updates the operational logic accordingly.

Data visualization (System monitoring): The ESP32-S3 serves as a real-time dashboard, displaying critical environmental parameters (water temperature, air temperature, and relative humidity) alongside the elapsed operational time received from the main controller. This visual feedback aligns with precision agriculture monitoring principles, facilitating immediate process evaluation and fault detection (Shamshiri *et al*., 2018).

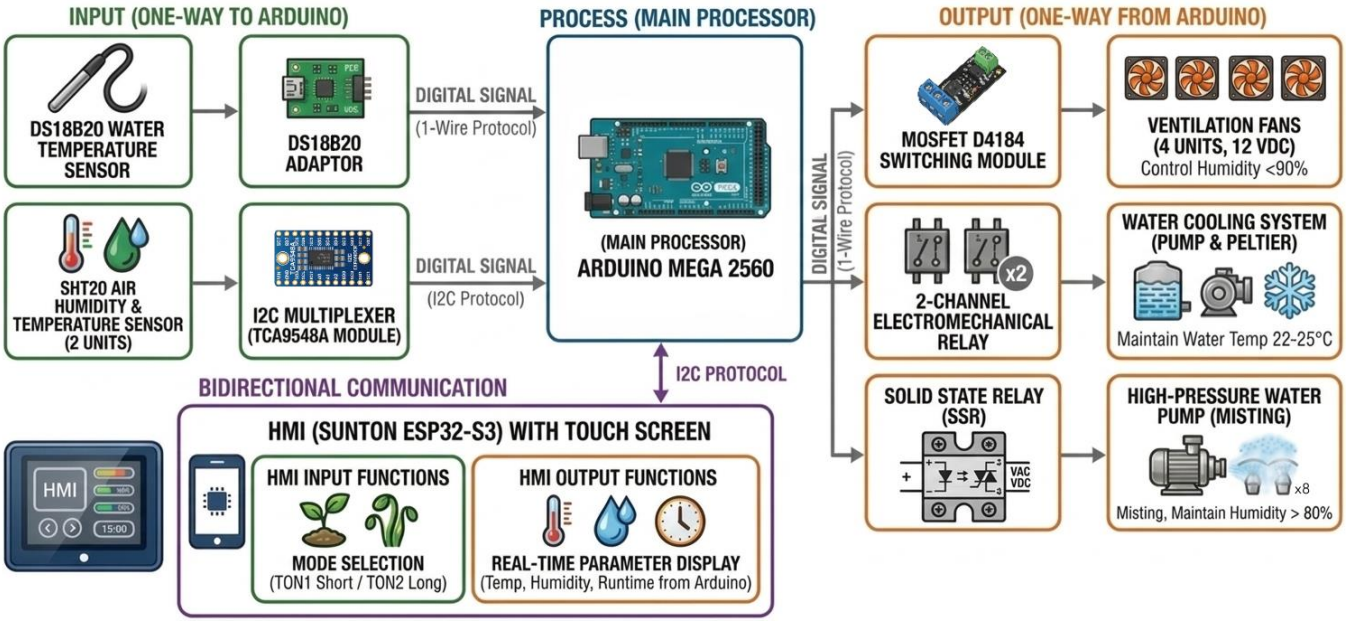


Figure 2 Block diagram of the hardware architecture and control system for the semi-automatic bean sprout cultivation machine.

2.3 Engineering calculations and equipment sizing

To design an effective environmental control system for the semi-automatic bean sprout cultivation machine, engineering parameters were calculated to determine precise equipment specifications. These calculations ensure that component capacities align with both the operational loads and the biological requirements of the plants. The key sizing and design procedures are detailed below.

2.3.1 Cultivation chamber sizing

The cultivation chamber was designed as a closed system to minimize external environmental disturbances and ensure control system stability. The chamber dimensions are 31 × 58 × 37.5 cm (width × length × height), yielding a total volume of 0.067 m³. The interior features a vertical arrangement of three cultivation trays (N_{layer}), providing a net surface area of 5,394 cm². This capacity was evaluated to accommodate a maximum initial seed weight of 600 grams, distributed equally at 200 grams per tier. This spatial distribution minimizes seed overlap and facilitates uniform moisture penetration throughout the cultivation area.

2.3.2 Cooling load calculation and Peltier sizing

The cooling system is designed to reduce the supplied water temperature from ambient levels to the optimal range for bean sprout growth. The specific target is to cool a 15 kg water mass from 30 °C to 22 °C within 30 minutes. The minimum sensible heat load is calculated using the fundamental heat transfer equation (Çengel and Boles, 2015):

$$Q_{water} = \frac{m.c.\Delta T}{t} \quad (1)$$

where:

Q_{water} = Heat load or energy to be extracted from the water (Watts or J/s)

m = Mass of the supplied water in the system (15 kg)

c = Specific heat capacity of water (4,184 J/kg. °C)

ΔT = Required temperature reduction (30 °C - 22 °C = 8 °C)

t = Target cooling time (30minutes = 1,800 seconds)

Based on Equation (1), the system requires a minimum energy of approximately 278.93 W to compensate for heat loss and the latent heat generated by plant respiration. Consequently, the system was designed to utilize two 12 V, 178 W thermoelectric (Peltier) modules operating in tandem. This configuration provides a combined theoretical maximum cooling capacity of 356 W. Because the total cooling capacity exceeds the required heat load (356 W > 278.93 W), it ensures that the system possesses sufficient reserve capacity to achieve and maintain the target water temperature at 22–25 °C.

2.3.3 Misting system and water film thickness calculation

The irrigation system was designed to provide comprehensive coverage across the cultivation area while preventing waterlogging. Eight Netafim misting nozzles were utilized, operating at a nominal flow rate of 0.125 L/min per unit, based on the manufacturer's technical specifications (Netafim, 2022). The water volume per spray cycle and the resulting water film thickness are calculated as follows:

1) Water volume per spray cycle (V_{spray})

$$V_{spray} = (N_{nozzle} \times q_{nozzle}) \times \frac{t_{spray}}{60} \times 1000 \quad (2)$$

where:

V_{spray} = Water volume sprayed in one operational cycle (cm^3 or ml)

N_{nozzle} = Number of misting nozzles (8 nozzles)

q_{nozzle} = Water flow rate per nozzle (0.125 L/min)

t_{spray} = Pump operation time per cycle (10 seconds)

Applying Equation (2) yields an approximate water volume of 166.67 cm^3 per cycle (a rounded reference value of 166 cm^3 was utilized for subsequent structural designs).

2) Water film thickness (h)

$$h = \frac{V_{spray}}{W \times L \times N_{layer}} \quad (3)$$

where:

h = Average thickness of the water film falling on the cultivation area (cm)

W = Width of the cultivation tray (31 cm)

L = Length of the cultivation tray (58 cm)

N_{layer} = Number of stacked cultivation layers (3 layers)

(Note: The total cross-sectional area of the 3-layer cultivation is 5,394 cm²)

Using Equation (3), the average water film thickness evaluates to approximately 0.0307 cm, or 0.31 mm.

These calculations demonstrate that a 10-second misting duration generates an average water film of just 0.31 mm. This micro-layer is adequate to sustain the target relative humidity of 80–90% without inducing waterlogging. Furthermore, this specific thickness promotes optimal oxygen diffusion into the plant roots, mitigating the risk of root rot. These parameters strictly align with established water management criteria for soilless culture systems (Grewal *et al*., 2011; Lakhiar *et al*., 2018; Design Innovation Center, 2020).

2.3.4 Main DC power supply sizing

The primary power supply delivers direct current (DC) to all system components, excluding the high-pressure water pump, which is galvanically isolated via an SSR. To determine a safe operational power rating, the system was evaluated under maximum load conditions–specifically when both the thermoelectric cooling sub-system and the ventilation fans operate concurrently:

$$P_{total} = P_{peltier} + P_{fan} + P_{control} \quad (4)$$

where:

P_{total} = Maximum total power required by the system (W)

$P_{peltier}$ = Combined power consumption of two thermoelectric modules (2 x 178 W = 356 W)

P_{fan} = Combined power consumption of four 12 V, 0.3 A ventilation fans (4 x 3.6 W = 14.4 W)

$P_{control}$ = Estimated power consumption of the microcontroller, sensors, and relay modules (≈15 W)

According to Equation (4), the maximum operational load (P_{total}) is 385.4 W. To ensure power supply longevity and effectively accommodate transient surge currents, a Safety Factor (S.F.) of 1.25 was applied. This strictly adheres to standard electrical engineering practices for continuous loads (NFPA, 2020), as modeled in Equation (5):

$$P_{supply} \geq P_{total} \times S.F. \quad (5)$$

Applying Equation (5), the minimum required power supply rating is 481.75 W. Consequently, a 12 V, 50 A industrial switching power supply was selected, providing a maximum capacity of 600 W. Because this capacity comfortably exceeds the minimum requirement (600 W > 481.75 W), this oversizing approach mitigates the risk of voltage drops during full-load operations, thereby preserving the accuracy and long-term stability of the logic and sensory systems.

2.4 Algorithm and control logic design

The software control system employs a closed-loop architecture to stabilize the microclimate within the cultivation chamber, tailored specifically for automated sprout production (Shamshiri *et al*., 2018; Hakim *et al*., 2023). The Arduino Mega 2560 continuously monitors environmental variables, comparing real-time sensor data against predefined set-points. To ensure efficient multitasking and real-time responsiveness, the control logic implements non-blocking timing functions. This programming approach allows the microcontroller to execute multiple sensor-actuator tasks concurrently without stalling the main program loop. The sequential logic and operational steps of the overall control system are illustrated in the flowchart in Figure 3. The system operates in two primary modes:

2.4.1 TON1 mode (2-day short sprout cultivation)

Initiating the TON1 mode via the ESP32-S3 touchscreen transmits an I2C command to the Arduino Mega 2560, starting a 48-hour master timer. The microcontroller then concurrently executes two environmental regulation loops:

Water temperature control loop: Although a proportional-integral-derivative (PID) control system could offer higher precision, an on-off control strategy with a predefined hysteresis band was intentionally selected. This approach effectively maintains the water temperature between 22 and 25 °C, a set-point range selected to continuously remove the metabolic heat released by the germinating seeds (Mirek *et al*., 2023), since water temperature is a key factor governing the germination, stem elongation, and yield of mung bean sprouts (Hanif *et al*., 2019). The controller activates the Peltier cooling modules at the upper control limit (UCL) of 25 °C and deactivates them at the lower control limit (LCL) of 22 °C. This hysteresis approach prevents rapid relay toggling (short cycling), thereby extending the operational lifespan of the switching components (Dorf and Bishop, 2011).

Humidity and ventilation control loop: Using data from the SHT20 sensors, the system regulates internal moisture levels through two response pathways. First, if the relative humidity (RH) falls below the 80% threshold, the system triggers a 10-second misting cycle. This fine-mist irrigation facilitates adequate moisture absorption and root oxygen diffusion (Lakhiar *et al*., 2018). Conversely, if the RH exceeds 90%, the system activates the ventilation fans via the MOSFET module. This rapid air exchange exhausts excess moisture and accumulated carbon dioxide (CO_2), together with the metabolic heat released by the germinating seeds (Mirek *et al*., 2023), thereby reducing the conditions that promote fungal growth and anaerobic root rot in closed systems.

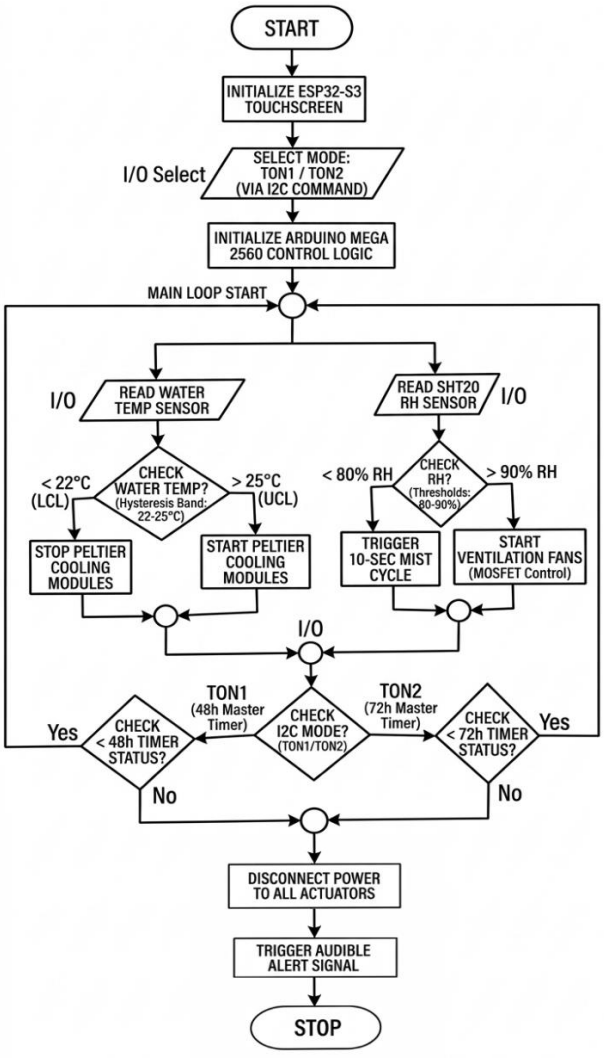


Figure 3 Logic flow of the dual-mode environmental regulation system based on non-blocking timing functions.

Upon concluding the 48-hour cycle, the microcontroller enters a termination state. It safely disconnects power to all actuator loads and triggers an audible alert to notify the user.

2.4.2 TON2 mode (3-day long sprout cultivation)

The TON2 control algorithm uses the same environmental thresholds and logic loops as TON1. The only software distinction is the extension of the master timer to 72

hours (3 days). This extended duration provides the sprouts with sufficient time for hypocotyl elongation and structural stem development prior to system termination.

2.5 Experimental design and evaluation

To evaluate the performance of the developed technology, a comparative experiment was designed between two cultivation systems, as depicted in Figure 4:

Semi-automatic cultivation machine with environmental control (Prototype): This system actively controls both water temperature and relative humidity.

Traditional cultivation machine (Control setup): This system simulates conventional commercial bean sprout cultivation methods commonly used in local markets.

While traditional methods typically rely on chemicals or plant hormones to enhance stem thickness, no chemicals or additives were utilized in either system during this experiment. This strict condition was established to empirically demonstrate the growth outcomes derived exclusively from the precise control of the physical environment. To ensure the reliability and reproducibility of the results, all experimental cases were conducted in triplicate (n = 3 independent batches).



(a) (b)

Figure 4 The cultivation systems used in the comparative experiment: (a) semi-automatic machine with environmental control and (b) traditional cultivation machine.

The experimental conditions and evaluation metrics were established as follows:

2.5.1 Determination of variables and experimental conditions

The experiment utilized black mung beans. The controlled variables, identical across both systems, included an initial seed weight of 600 grams and a total water volume of 10 liters per cycle. The cultivation period was divided into two specific durations: a 2-day period (for short bean sprouts) and a 3-day period (for long bean sprouts). The watering condition, a critical independent variable in this study, varied based on the operational mechanism of each system:

Semi-automatic machine with environmental control (Figure 4(a)): This system employed a feedback control mechanism. The water pump was automatically activated only when the sensor detected the relative humidity inside the cultivation chamber dropping below 80%. During each activation, the watering duration lasted for exactly 10 seconds, a setting designed to conserve both water resources and energy.

Traditional cultivation machine (Figure 4(b)): This system utilized a timer-based watering approach. The watering frequency was divided into three distinct intervals: every 2, 4, and 6 hours. For each watering event in this setup, the duration was set to 10 minutes.

2.5.2 Data collection of yield and physical characteristics

Upon completion of the cultivation periods (2 and 3 days), bean sprouts from each experimental condition were harvested to collect the following data:

Total yield weight: The net fresh weight was measured using a digital scale to compare the growth rates across different conditions.

Physical characteristics: For each batch, 30 bean sprouts were randomly sampled daily (10 sprouts from each of the three cultivation layers), totaling 90 samples per experimental condition (n = 90). The stem length and diameter were measured using a digital Vernier caliper. This measurement aimed to evaluate the physical quality against commercial market standards.

2.5.3 Food safety assessment

To verify the prototype's efficacy in eliminating chemical dependency, bean sprout samples produced by the prototype (Sample A) and samples randomly purchased from a local fresh market (Sample B) were sent to an accredited laboratory for chemical residue analysis. The analysis focused on two specific contaminants: formaldehyde (analyzed using a Test Kit, with a Limit of Detection (LOD) of 0.50 mg/kg) and sulfur dioxide (analyzed using the In-house method TE-CH-018 based on AOAC 2023 990.28, with an LOD of 3.00 mg/kg)

3. Results and Discussion

This study evaluated the performance of the microcontroller-based environmental control system designed for the semi-automatic bean sprout cultivation machine (Prototype: Case 1) in comparison to a traditional timer-based cultivation system. The traditional system served as the control setup and was divided into three distinct operational conditions: watering every 6 hours (Case 2), every 4 hours (Case 3), and every 2 hours (Case 4). To strictly isolate the effects of the physical environment, neither system utilized any chemicals or growth hormones throughout the cultivation process. The experiments were conducted under ambient conditions, characterized by temperatures ranging from 30–35 °C and a relative humidity (RH) of approximately 70%.

The evaluation covered environmental parameters, the morphological characteristics of the yield, and food safety assessments. All cultivation experiments were conducted in triplicate (n = 3 independent batches) to ensure reproducibility. For morphological parameters, 30 sprouts were randomly sampled daily (10 per cultivation layer) per batch, totaling 90 sprouts per condition. Statistical differences among the experimental cases were analyzed using one-way Analysis of Variance (ANOVA) followed by Tukey's post-hoc test, with a significance level set at $p < 0.05$. Furthermore, the percentage of improvement was calculated using Equation (6). All data are presented as Mean ± Standard Deviation (SD).

$$POI\ (\%) = \left(\frac{V_P - V_T}{V_T} \right) \times 100 \quad (6)$$

where:

V_P = The measured value from the prototype machine (Case 1).

V_T = The measured value from the traditional timer-based systems (Control setup: Cases 2, 3, or 4).

POI = The percentage of improvement (%).

3.1 Water temperature profile

The water temperature within the system was continuously monitored at one-hour intervals throughout the cultivation period, which spanned 48 hours for the TON1 mode (short bean sprouts) and 72 hours for the TON2 mode (long bean sprouts).

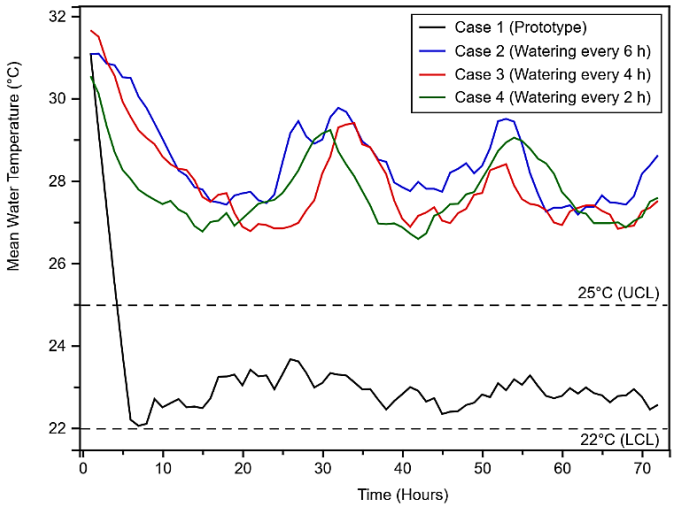


Figure 5 Water temperature profiles (°C) in the prototype and traditional systems. The prototype maintained a high stability with an overall average of 23.17 ± 0.38 °C.

As illustrated in Figure 5, the prototype machine (Case 1) effectively controlled and maintained the water temperature within the target range of 22–25 °C with high stability, achieving an average temperature of 23.17 ± 0.38 °C. The thermoelectric (Peltier) cooling system successfully reduced the temperature to the desired set-point within the first five hours of operation. Maintaining this optimal temperature supports the seed germination process, which is an exothermic reaction. This thermal regulation facilitates the dissipation of metabolic heat (Mirek *et al.*, 2023) and is therefore expected to mitigate the risk of pathogenic microbial proliferation.

Conversely, the traditional systems (Cases 2–4) exhibited significantly higher average water temperatures of 28.49 ± 1.00 °C, 27.91 ± 0.82 °C, and 27.75 ± 0.78 °C, respectively ($p < 0.05$). Although increasing the watering frequency slightly reduced the temperature via evaporative cooling, it failed to lower the temperature to the optimal range due to the overriding influence of the ambient heat. These findings clearly demonstrate the inherent limitations of timer-based irrigation systems lacking active cooling mechanisms, as the metabolic heat released by the germinating seeds continues to accumulate within the cultivation environment (Mirek *et al.*, 2023).

3.2 Relative humidity profile

Relative humidity (RH) within the cultivation chamber is a critical factor influencing plant transpiration.

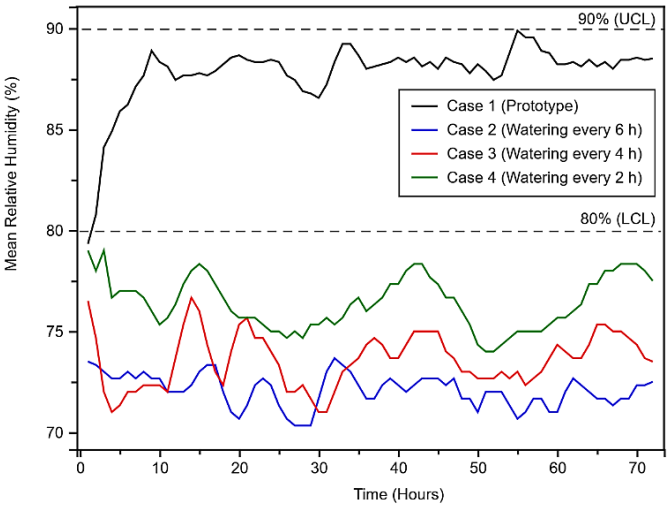


Figure 6 Relative humidity profiles (%) in the prototype and traditional systems. The prototype maintained a stable microclimate with an overall average of 87.82 ± 0.36%.

As illustrated in Figure 6, the prototype machine (Case 1) successfully maintained an average RH of 87.82 ± 0.36%, remaining consistently within the target range of 80–90%. The implementation of a feedback control mechanism, which triggers a 10-second misting cycle when the RH drops below 80% and activates the ventilation fans when the RH exceeds 90%, enabled the system to achieve an equilibrium state within approximately one hour. Maintaining this optimal moisture level effectively mitigates transpiration stress and promotes cellular expansion in the plants (Amitrano *et al.*, 2020).

In contrast, the traditional systems (Cases 2–4) recorded substantially lower average RH values of 72.09 ± 0.35%, 73.57 ± 0.85%, and 76.41 ± 1.00%, respectively ($p < 0.05$). Although increasing the watering frequency contributed to a slight elevation in humidity, none of the traditional setups were able to consistently sustain the RH within the appropriate threshold. This finding

underscores the inefficiency of fixed-interval watering methods in maintaining a stable microclimate (Lakhiar *et al*., 2018).

3.3 Growth in sprout length

As previously detailed, a total of 90 bean sprouts (n = 90 from 3 independent batches) were randomly sampled daily to measure their average length, as presented in Table 1 and Figure 7.

On Day 1, sprouts cultivated in the prototype machine were slightly shorter than those in the traditional systems, reflecting an initial adaptation phase of the seeds to the controlled environment. However, by Day 2 (the conclusion of the TON1 mode), the average sprout length in the prototype rapidly increased to 47.18 ± 1.65 mm, exceeding the average of the traditional systems by 50.4% (statistically significant at $p < 0.05$). This growth trend became substantially more pronounced on Day 3 (the conclusion of the TON2 mode), with the prototype achieving an average length of 118.16 ± 2.44 mm, which was 73.9% longer than the traditional control setups ($p < 0.05$). This accelerated growth is directly attributed to optimal environmental regulation coupled with the applied mechanical stress technique, which synergistically stimulated uniform structural development (Biddington, 1986; Hanif *et al*., 2019).

Table 1 Average length (mm) of bean sprouts throughout the cultivation period (Mean ± SD).

Time (Days)	Case 1 (Prototype)	Case 2 (Every 6h)	Case 3 (Every 4h)	Case 4 (Every 2h)	Mode
Day 1	14.36	15.65	15.96	20.62	-
Day 2	47.18±1.65	30.90±0.85	32.14±1.42	31.08±0.93	TON1
Day 3	118.16±2.44	57.20±1.80	60.10±1.66	86.51±2.24	TON2

3.4 Growth in sprout diameter

Stem thickness is a crucial indicator of commercial quality. The diameter measurement results from the sampled groups (n = 90) are presented in Table 2 and Figure 8.

Table 2 Average diameter (mm) of bean sprouts throughout the cultivation period (Mean ± SD).

Time (Days)	Case 1 (Prototype)	Case 2 (Every 6h)	Case 3 (Every 4h)	Case 4 (Every 2h)	Mode
Day 1	1.93	1.94	1.99	2.06	-
Day 2	2.52±0.12	2.12±0.11	2.19±0.09	2.26±0.10	TON1
Day 3	2.75±0.15	2.33±0.12	2.39±0.13	2.45±0.13	TON2

The morphological development of the sprouts is illustrated in Figure 9 (a: 1-day-old, b: 2-day-old, c: 3-day-old). On Days 2 and 3, the prototype machine produced bean sprouts that were significantly thicker ($p < 0.05$), by approximately 15%, than those from the traditional systems (achieving 2.75 ± 0.15 mm on Day 3 compared to 2.33–2.45 mm in traditional setups). This enhanced plumpness supports the primary hypothesis that maintaining high relative humidity (80–90%) coupled with precise temperature control actively stimulates lateral cellular expansion. Consequently, this controlled environment yields sprouts of high commercial quality without the need for chemical additives.

3.5 Total net yield

The post-harvest fresh weight from all three cultivation trays (n = 3 independent batches) was evaluated to determine the total yield, as presented in Table 3 and Figure 10.

The prototype machine (Case 1) produced the highest total yield in both the TON1 (2.48 ± 0.19 kg) and TON2 (4.93 ± 0.37 kg) modes, outperforming the 2-hour and 6-hour interval traditional cultivation methods by 31.4% and 63.2%, respectively ($p < 0.05$). However, when examining the physical appearance in Figure 11, although the sprouts cultivated in the prototype exhibited a higher biomass than those from the chemical-free traditional systems, the total yield remained lower than that of commercial productions utilizing growth-accelerating chemicals (which typically achieve a yield ratio of 1:10, or 6.00 kg). Nevertheless, these results demonstrate that the engineered system can effectively increase production yield and significantly reduce manual labor, consistent with previous reports that automated irrigation improves sprout quality compared with traditional practices (Hakim *et al*., 2023).

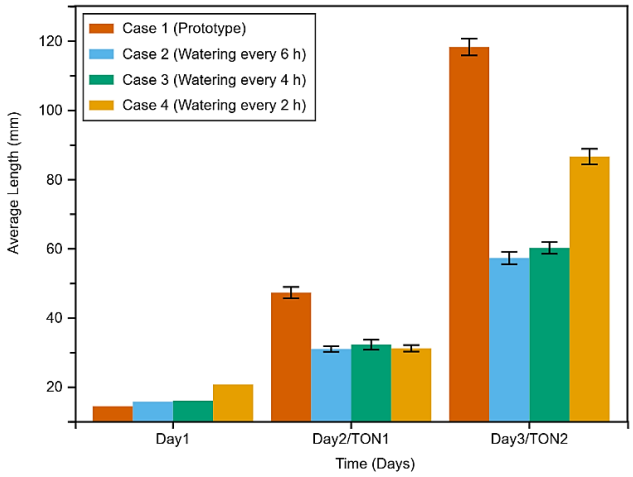


Figure 7 Average length (mm) of bean sprouts in the prototype and timer-based systems (Mean ± SD). Error bars represent standard deviation (SD).

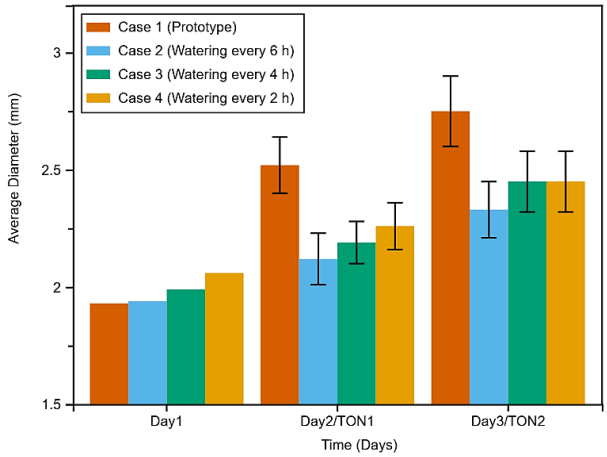
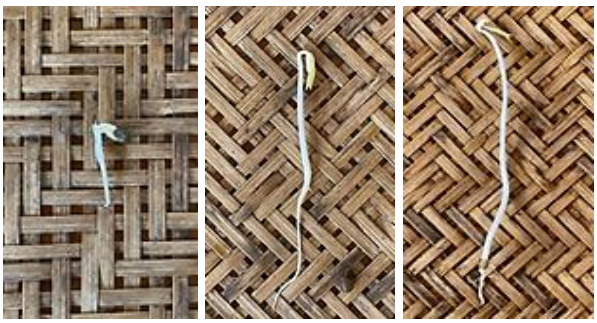


Figure 8 Average diameter (mm) of bean sprouts in the prototype and timer-based systems (Mean ± SD). Error bars represent standard deviation (SD).



(a) (b) (c)

Figure 9 Morphological development of bean sprouts from the prototype machine at (a) day 1, (b) day 2 and (c) day 3.

Table 3 Average total fresh weight (kg) at harvest from an initial seed mass of 600 g (Mean ± SD).

Time (Days)	Case 1 (Prototype)	Case 2 (Every 6h)	Case 3 (Every 4h)	Case 4 (Every 2h)	Mode
Day 1	-	-	-	-	-
Day 2	2.48±0.19	1.50±0.13	2.11±0.17	2.31±0.17	TON1
Day 3	4.93±0.37	3.02±0.25	3.17±0.27	3.75±0.27	TON2

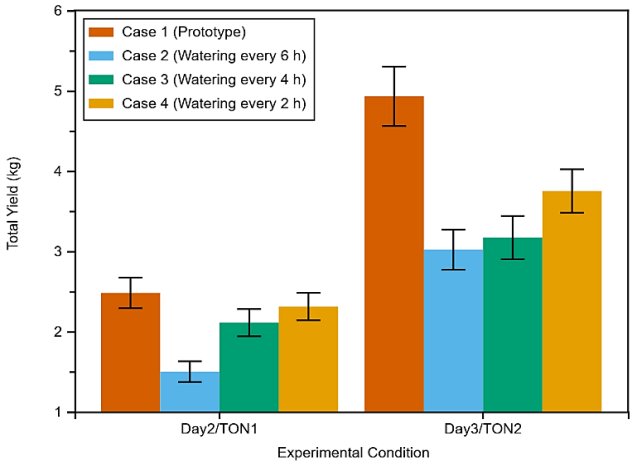


Figure 10 Average total fresh weight (kg) of bean sprouts across different cultivation cases (Mean ± SD). Error bars represent standard deviation (SD).



(a) (b)

Figure 11 Bean sprouts from the prototype (Case 1): (a) 2-day-old short sprouts (TON1), and (b) 3-day-old long sprouts (TON2).

3.6 Food safety and chemical residue test results

To ensure consumer safety, two groups of bean sprout samples-Sample A (from the prototype machine) and Sample B (randomly selected from a local fresh market)- were sent for testing at the Central Laboratory (Thailand) Co., Ltd. The samples were analyzed for formaldehyde and sulfur dioxide (SO_2) contamination in accordance with the ISO/IEC 17025:2017 standard.

Table 4 Comparison of chemical residue test results in bean sprout samples.

Sample Group	Formaldehyde (Test Result)	LOD (mg/kg)	Sulfur Dioxide: SO_2 (Test Result)	LOD (mg/kg)
Sample A	Not Detected	0.5	Not Detected	3.0
Sample B	Detected	0.5	Not Detected	3.0

(Note: Formaldehyde testing was conducted using a test kit. Sulfur dioxide testing utilized the in-house method TE-CH-018 based on AOAC (2023) 990.28.)

4. Conclusion

This study successfully developed a microcontroller-based closed-loop environmental control system for a semi-automatic bean sprout cultivation machine. The system demonstrated superior performance in stabilizing critical microclimate parameters compared to traditional timer-based methods, leading to significantly enhanced growth and higher yields without chemical dependency. Laboratory validations confirmed that the harvested sprouts strictly adhered to international food safety standards. The principal contribution of this research is the provision of an integrated engineering framework that ensures high-quality, chemical-free production while effectively reducing manual labor. Future work should focus on optimizing energy efficiency and conducting a comprehensive economic evaluation, including a formal break-even point (BEP) analysis, to fully establish its commercial viability and scalability.

5. Acknowledgments

The author expresses sincere gratitude to Thonburi University for providing the testing facilities, equipment, and instruments necessary to conduct this research and collect the experimental data. Special thanks are extended to Mr. Adithep Fueangkaeo and Mr. Aatthachai Aumnak for their valuable assistance in developing the electrical control cabinet circuit, system drafting, and control programming. The author also gratefully acknowledges Mr. Kritsada Thongluea and Mr. Nuttapat Kitbumrung for their significant contributions to the structural fabrication and equipment installation. Finally, appreciation is extended to Miss Arisa Chaiphak for her diligent support in seed preparation prior to the experiments and her assistance in data collection.

6. References

Amitrano, C., Arena, C., De Pascale, S. and De Micco, V. 2020. Light and low relative humidity increase antioxidants content in mung bean (*Vigna radiata* L.) sprouts. **Plants** 9(9): 1093.

AOAC. 2023. Method 990.28: Sulfites in foods, optimized Monier-Williams method. In: Latimer, G.W. Jr. (ed.). **Official**

Methods of Analysis of AOAC INTERNATIONAL (22nd ed.). Oxford University Press, New York.

Bamrungkul, P. 2021. ***The bean sprouts crop automatic machine*** [Research Report]. Rajamangala University of Technology Isan, Nakhon Ratchasima. (in Thai)

Beacham, A.M., Vickers, L.H., and Monaghan, J.M. 2019. Vertical farming: A summary of approaches to growing skywards. **The Journal of Horticultural Science and Biotechnology** 94(3): 277–283.

Biddington, N.L. 1986. The effects of mechanically-induced stress in plants – A review. **Plant Growth Regulation** 4: 103–123.

Çengel, Y.A. and Boles, M.A. 2015. **Thermodynamics: An Engineering Approach** (8thed.). McGraw-Hill Education.

Design Innovation Center. 2020. Basics of hydroponics farming. Vigyan Ashram.

Dorf, R.C. and Bishop, R.H. 2011. **Modern Control Systems** (12th ed.). Pearson Education.

Grewal, H.S., Maheshwari, B. and Parks, S.E. 2011. Water and nutrient use efficiency of a low-cost hydroponic greenhouse for a cucumber crop: An Australian case study. **Agricultural Water Management** 98(5): 841–846.

Hakim, M.F., Abraar, M., Alfurqan, M.A., Zainal, Z. and Baharom, M.N.R. 2023. Arduino-based irrigation system for mung bean sprouts cultivation. **Multidisciplinary Applied Research and Innovation** 4(2): 273–279.

Hanif, M., Khattak, M.K., Ul Haq, I., Gul, K., Khan, A., Ullah, K., Khan, A. and Ali, A. 2019. Effects of temperature and water purity on germination and yield of mungbean sprouts. **Sains Malaysiana** 48(4): 711–717.

Horowitz, P. and Hill, W. 2015. **The Art of Electronics** (3rd ed.). Cambridge University Press.

Ibrahim, D. 2006. **Microcontroller Based Applied Digital Control**. John Wiley & Sons.

Kanasri, T. 2018. Control system of water temperature for Chinese celery growing hydroponic vegetables. **EAU Heritage Journal Science and Technology** 12(3): 133–140. (in Thai)

Lakhiar, I.A., Gao, J., Syed, T.N., Chandio, F.A. and Buttar, N.A. 2018. Modern plant cultivation technologies in agriculture under controlled environments: A review on aeroponics. **Journal of Plant Interactions** 13(1): 338–352.

Mastropasqua, L., Dipierro, N. and Paciolla, C. 2020. Effects of darkness and light spectra on nutrients and pigments in radish, soybean, mung bean and pumpkin sprouts. **Antioxidants** 9(6): 558.

Mirek, P., Panowski, M., Słomczyńska, K., Stanek, M. and Bąkowski, T. 2023. Resources and potential for utilization of low-exergy heat from mung bean sprouts cultivation – case study. **Archives of Thermodynamics** 44(4): 507–534.

Netafim. 2022. CoolNet Pro™ fogger system technical datasheet. Netafim Ltd.

NFPA. 2020 . NFPA 70: National electrical code (NEC). National Fire Protection Association.

OMRON Corporation. n.d. **Technical Explanation for Solid-state Relays** (CSM_SSR_TG_E_9_2) [Technical guide]. OMRON Corporation, Kyoto. Retrieved September 29, 2026, from https://www.ia.omron.com/data_pdf/guide/18/ssr_tg_e_9_2.pdf

Shamshiri, R.R., Kalantari, F., Ting, K.C., Thorp, K.R., Hameed, I.A., Weltzien, C., Ahmad, D. and Shad, Z.M. 2018. Advances in greenhouse automation and controlled environment agriculture: A transition to plant factories and urban agriculture. **International Journal of Agricultural and Biological Engineering** 11(1): 1–22.

Texas Instruments. 2014. TCA9548A low-voltage 8-channel I2C switch with reset function [Datasheet].

Wannawas, P. and Riansut, W. 2020. Influence of planting materials and light exposure on bean sprout growth. **Rajamangala University of Technology Srivijaya Research Journal** 12(1): 1–12. (in Thai)

World Health Organization. 2006. **Formaldehyde in drinking-water: Background document for development of WHO guidelines for drinking-water quality**. World Health Organization.

Zhao, D. and Tan, G. 2014. A review of thermoelectric cooling: Materials, modeling and applications. **Applied Thermal Engineering** 66(1-2): 15–24.

Recent Science and Technology 2026, Vol. 18(3): e272461

Recent Science and Technology

Journal homepage: https:// www.tci-thaijo.org/index.php/rmutsvrj/index

ISSN: 3057-0786 (Online)

Research Article

Dual-Heat-Zone Biomass-Assisted Pyrolysis of Polyethylene Waste for Community-Scale Fuel Recovery in Nakhon Phanom, Thailand

Harid Klongdee [a *] and Narongrit Auppapong [a]

[a] *Department of Energy Engineering, That Phanom College, Nakhon Phanom University, That Phanom District, Nakhon Phanom 48110, Thailand.*

Article history:

Received: 2026-06-08
Revised: 2026-07-22
Accepted: 2026-07-23

Keywords:

Pyrolysis;
Plastic waste;
Biomass stove;
Pyrolytic oil;
Waste-to-energy;
Rural community-scale

ABSTRACT

This study aimed to design, fabricate, and evaluate the performance of a dual-heat-zone (central-pipe), biomass-assisted pyrolysis system for converting polyethylene (PE) plastic waste into pyrolytic oil at rural community scale. The developed system incorporated a central heat-transfer pipe inside the pyrolysis reactor, enabling simultaneous heat transfer from both the bottom (external jacket) and the interior (central pipe) of the reactor. Performance was assessed against a conventional reactor, defined here as a bottom-heated reactor of identical volume, wall material, and PE feedstock loading, heated only through the external jacket The performance was measured based on the reactor temperature profile, cumulative oil yield, and energy efficiency (η), defined as the ratio of chemical energy recovered in the pyrolytic oil to the total thermal energy supplied by the biomass fuel over the run using thermodynamic energy equations (Eq. (3)). Experimental results demonstrated that the system could rapidly increase the reactor temperature from approximately 30°C to 420°C within 20 minutes, and up to 520°C within 30 minutes (mean ± SD, n = 3). The heat transfer rate (Q) from the biomass stove to the reactor reached 15.8 kW, while the cumulative oil yield (Y oil) reached approximately 65% at 30 minutes (± SD, n = 3). Under these specific test conditions (single reactor unit, 5.0 kg PE per batch, n = 3 replicates), the energy efficiency of the pyrolysis system was found to be 68.5%, compared with 42.3% for the conventional bottom-heated reactor tested under the same conditions. These results should be interpreted as preliminary, single-configuration findings rather than generalized performance guarantees. A linear regression analysis was applied to correlate reactor temperature with oil yield (R^2 = 0.974, P-value < 0.001). Preliminary, non-replicated field observations at two community sites in Nakhon Phanom Province suggested an income-generation potential of approximately 30,000 THB/month, motivating a more rigorous field-trial protocol as a next step. This economic estimate is based on assumptions regarding oil price, daily production volume, and operating cost, as explicitly stated in Section 3.5, and should be treated as indicative rather than confirmed. Preliminary characterization of the pyrolytic oil indicated properties broadly consistent with a diesel-range fuel; full quality data are required before the product is described as a finished "fuel oil." The fabrication cost of approximately 20,000 THB/unit supports the system's potential viability for community-scale deployment, consistent with the principles of the circular economy and the Sustainable Development Goals. The main limitations of this study include the use of a single plastic type (PE), a single reactor scale, a short 30-minute test duration, and the current lack of data on pyrolytic oil quality and environmental emissions data. These limitations are addressed as priorities for follow-up work.

© 2026 Klongdee, H. and Auppapong, N. Recent Science and Technology published by Rajamangala University of Technology Srivijaya

1. Introduction

Plastic waste pollution is one of the most pressing environmental crises facing Thailand and the greater Mekong River region. The rapid expansion of single-use plastics, combined with inadequate waste management infrastructure in rural and riverside communities, has led to severe ecological, environmental, and public health consequences (ONEP, 2022; DEQP, 2019). Thailand alone generates approximately 28 million tonnes of municipal solid waste (MSW) annually, of which more than 14% is plastics—a fraction that continues to rise

*** Corresponding author.**

E-mail address: *klongdee.harid@gmail.com*

Cite this article as: Klongdee, H. and Auppapong, N. 2026. Dual-Heat-Zone Biomass-Assisted Pyrolysis of Polyethylene Waste for Community-Scale Fuel Recovery in Nakhon Phanom, Thailand. **Recent Science and Technology** 18(3): e272461.

https://doi.org/10.65411/rst.2026.272461

(PCD, 2022). Improper disposal, open burning, and unregulated landfilling exacerbate greenhouse gas (GHG) emissions and contaminate water bodies, threatening biodiversity and human well-being across the region (UNEP, 2021).

In response to these challenges, thermochemical conversion technologies, particularly pyrolysis, have attracted significant global research attention as viable pathways for converting plastic waste into value-added fuel oils (Miandad *et al*., 2016; Anuar Sharuddin *et al*., 2016). Pyrolysis is defined as the thermochemical decomposition of organic materials at elevated temperatures (typically 300–700°C) in the absence of oxygen, producing liquid oil, syngas, and char as primary products (Mohan *et al*., 2006; Bridgwater, 2004). The liquid oil fraction exhibits physicochemical properties closely resembling petroleum-derived diesel fuel, making it suitable for use in internal combustion engines and industrial heating systems (Kaminsky *et al*., 2004; Scheirs and Kaminsky, 2006).

For a batch pyrolysis reactor heated by an external biomass stove, the overall energy balance around the reactor can be expressed as a heat balance specific to the system studied, rather than a generic combustion relation:

$$Q_{biomass} = Q_{pyrolysis} + Q_{sensible} + Q_{loss} \quad (1)$$

where Q_biomass is the thermal energy delivered by the biomass stove (kW), Q_pyrolysis is the energy consumed by the endothermic cracking reactions, Q_sensible is the sensible heat required to raise the reactor and feedstock to reaction temperature, and Q_loss is the heat lost through the reactor walls and fittings (Incropera *et al*., 2011).

Conventional pyrolysis reactors typically supply heat only from the bottom of the vessel, resulting in uneven temperature distribution, prolonged heating times, and high specific energy consumption (Mastral *et al*., 2000; Lee, 2009). Islam *et al*. (2005) demonstrated that non-uniform heat distribution significantly diminishes pyrolysis efficiency (Sakata *et al*., 1999; Islam *et al*., 2005). Bridgwater (2012) concluded that innovative reactor designs capable of achieving rapid and uniform heating are critical for maximizing liquid oil yields (Mastral *et al*., 2002; Bridgwater, 2012).

The integration of renewable energy sources as the heat input for pyrolysis has been widely explored to reduce operating costs and lower net carbon emissions (Demirbas, 2008). Biomass combustion represents an attractive renewable heat source. Agricultural residues, wood chips, and other locally available biomass fuels offer a low-cost, carbon-neutral alternative to fossil fuels (Sajjakulnukit *et al*., 2005; Chamsing *et al*., 2006). Several studies have demonstrated that biomass-fired pyrolysis systems can achieve economic viability at community scale (Demirbas *et al*., 2009). The LEnC framework (Chaiyat *et al*., 2020) and the 3E analytical approach (Pokson and Chaiyat, 2022) offer comprehensive frameworks for evaluating thermodynamic and economic performance.

To address the identified research gaps, this study developed and experimentally evaluated a dual-heat-zone biomass-assisted pyrolysis system, in which heat from a biomass stove is transferred into the reactor through both the reactor base and a central pipe. This dual heat-transfer configuration promotes more rapid and uniform temperature distribution, reduces startup time, and improves oil production efficiency while using locally available renewable biomass as the heat source.

To design and develop a dual-heat-zone biomass-assisted pyrolysis system for plastic waste-to-fuel conversion.

To improve heat transfer efficiency and reduce the time required to initiate the pyrolysis process.

To compare the performance of the developed system against a conventional bottom-heated pyrolysis reactor.

To assess the practical applicability and economic viability of the system for community-scale and local organization use.

The pyrolysis of plastic waste has been extensively studied over the past two decades, providing the comparative literature used throughout this manuscript. Miandad *et al*. (2016) reported that PE and PP can be converted to fuel oil at yields of 50–95% and 50–90% by weight, respectively, depending on temperature, catalyst type, and residence time. Anuar Sharuddin *et al*. (2016) identified temperature as the most critical parameter, with optimal ranges of 300–500°C for most common polymers. Islam *et al*. (2005) highlighted the significant impact of reactor geometry on pyrolysis efficiency. Demirbas (2004) found that higher temperatures generally favor oil production over char formation. Williams and Slaney (2007) reported PE pyrolysis oil yields of approximately 85 wt.% at 500°C; Onwudili *et al*. (2009) demonstrated mixed PE/PP/PS yields of up to 70 wt.% at 500°C. Bridgwater (2012) noted that integrating biomass combustion reduces operating costs. Abnisa and Wan Daud (2014) found that co-pyrolysis of biomass with plastics could improve liquid yield.

Bench-scale reactors using biomass pellets as the heat source for plastic pyrolysis have achieved average reactor temperatures near 412°C with forced-convection combustion, confirming the feasibility of biomass-fired heating but relying on a single (bottom-only) heating zone (Kurniawan *et al*., 2020). Recent work on mixed-plastic pyrolysis has instead focused on predicting oil/wax yields across feedstock compositions without changing the reactor's heat-transfer geometry (Genuino *et al*., 2023). The specific novelty of the present design relative to these and other single-zone reactors is the addition of a central heat-transfer pipe operating in parallel with the external jacket, which increases the effective heat transfer area by approximately 85% (Eq. 8) and is hypothesized to reduce internal temperature gradients across the packed PE bed, a design-level change (heating geometry), rather than a new

theoretical or catalytic mechanism, and evaluated here through directly comparative testing against a bottom-only reactor of otherwise identical specification (Section 2.3).

The reactor operating temperatures of 420°C and 520°C used to define the pyrolysis-onset and stable-operation phases in this study (Section 3.1) fall within the 300–500°C range reported as optimal for common polyolefins, including PE (Anuar Sharuddin *et al*., 2016), and are consistent with reported PE decomposition behaviour. A thermogravimetric analysis (TGA) profile of the specific PE feedstock used in this study is not yet available; the authors intend to attach a TGA curve confirming the onset/major mass-loss temperature range for the batch tested, which will strengthen the rationale for the selected operating temperatures.

Oil-quality criteria relevant to this study include the physicochemical properties expected of a diesel-range pyrolytic oil, namely kinematic viscosity, flash point, density, and gross calorific value, benchmarked against ASTM D975 diesel specifications. Available results are introduced here and reported quantitatively in Section 3.2.1, while full characterization is pending completion of the laboratory analysis.

2. Materials and Methods

2.1 Thermodynamic and economic relations

This section presents the calculation tools used to evaluate the system (Eqs. 3–7), followed by the fabrication details, feedstock, and experimental procedure. The energy efficiency (η) of the pyrolysis system is defined as the ratio of chemical energy recovered in the pyrolytic oil to the total thermal energy supplied by the biomass fuel over the pyrolysis run:

$$\eta = (m_oil \times LHV_oil) / (\dot{m}_fuel \times LHV_fuel \times t) \quad (3)$$

The exergy efficiency (ψ) provides a more thermodynamically rigorous performance indicator:

$$\psi = Ex_oil / Ex_input \quad (4)$$

$$Ex_fuel = \beta \times LHV_fuel \quad (5)$$

where β is the exergy-to-enthalpy correction factor (1.04–1.17 for solid biomass (Dincer and Rosen, 2013). The levelized energy cost (LEnC) is the most widely used metric for economic performance (Chaiyat *et al*., 2020; NREL, 2021):

$$LEnC = [Inv \times CRF + OM] / (W_system \times t_OT) \quad (6)$$

$$CRF = [r \times (1 + r)^n] / [(1 + r)^n - 1] \quad (7)$$

This definition of η is applied consistently throughout the manuscript wherever “efficiency” is reported (Sections 3.3 and 3.4); no alternative definition is used elsewhere in the text.

2.2 System design and fabrication

The heat transfer rate (Q) inside the reactor is governed by:

$$Q = U \times A \times \Delta T \quad (2)$$

where U is the overall heat transfer coefficient (W/m²·K), A is the effective heat transfer area (m²), and ΔT is the temperature difference between the heat source and the pyrolysis material (Cengel and Ghajar, 2014; Holman, 2010).

The dual-heat-zone biomass-assisted pyrolysis system consists of five main components: (1) a pyrolysis reactor vessel, (2) a biomass stove, (3) a central heat-transfer pipe, (4) a vapor transport pipeline and condenser unit, and (5) a product oil collection tank. A schematic diagram is illustrated in Figure 1 and full system specifications are presented in Table 1.

Table 1 Specifications of the dual-heat-zone biomass-assisted pyrolysis system.

Component	Parameter	Value
Pyrolysis Reactor	Inner diameter × Height	400 mm × 600 mm
	Wall thickness (SS304)	3 mm
	Reactor volume	75.4 L
	Max. operating temperature	600°C
Central Heat-Transfer Pipe	Outer diameter	50 mm
	Pipe length in reactor	550 mm
	Material	SS304
Biomass Stove	Fuel type	Wood chips / agri. residues
	Rated heat output	15–20 kW
Condenser Unit	Coolant	Ambient air / water
	Vapor pipe diameter	25 mm
	Insulation	50 mm
Fabrication Cost	Total unit cost	20,000 THB/unit

Hot combustion gases are directed through both the external jacket (bottom heating) and the internal central pipe (central heating), maximizing the effective heat transfer area:

$$A_eff = A_bottom + A_central = \pi r^2_i + \pi d_p \times L_p \quad (8)$$

2.3 Feedstock and fuel

The conventional (baseline) reactor is defined for this study as a bottom-heated pyrolysis reactor of identical inner diameter, height, wall material (SS304, 3 mm), and reactor volume (75.4 L) to the dual-heat-zone system, heated only through the

external jacket (i.e., without the central pipe), and tested with the same PE feedstock mass and the same biomass fuel type and rated heat output. This ensures a like-for-like comparison of heat-transfer configuration as the sole design variable.

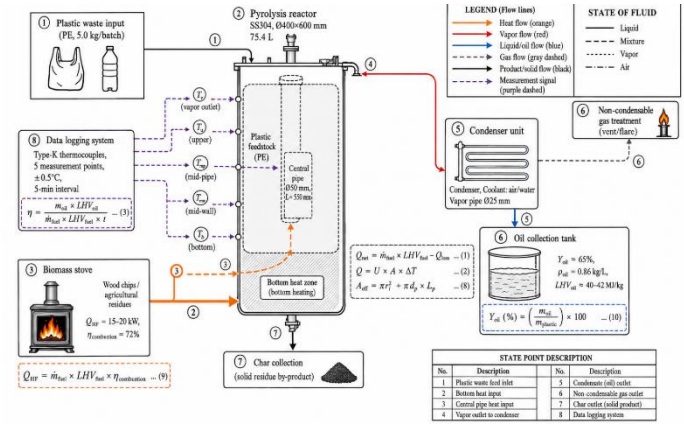


Figure 1 Schematic diagram of the dual-heat-zone biomass-assisted pyrolysis system.

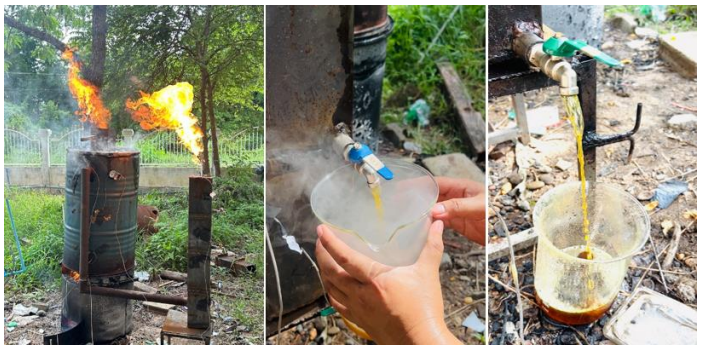


Figure 2 Community-scale fixed-bed pyrolysis reactor (left) with pyrolytic oil collection at the condensate outlet (center and right).

The primary feedstock was polyethylene (PE) plastic waste collected from the local community, pre-sorted, cleaned, and dried prior to each experiment. PE was selected due to its abundance in household waste streams (approximately 35–40% by mass in Thailand) and its high reported oil yield of 50–95 wt.% (Miandad *et al.*, 2016). The mass of plastic feedstock loaded per experiment was 5.0 kg. Biomass fuel consisted of wood chips and agricultural residues (rice husk and corn cobs) with moisture content below 15% and LHV_biomass of 14.5–16.8 MJ/kg (Sajjakulnukit *et al.*, 2005). Feedstock particle size/dimensions, bulk density, and PE grade/source to be inserted from experimental records, for reproducibility. A single representative value of LHV_biomass = 15.6 MJ/kg [to be confirmed against the actual rice husk:corn cob mixing ratio used, or a bomb-calorimeter measurement of the blend] is used in place of the previously reported range, with moisture content maintained below 15% (Sajjakulnukit *et al.*, 2005). The biomass feed rate was. The biomass feed rate was $\dot{m}$_biomass = 5 kg/h, using a rice husk:corn cob ratio of 60:40, fed continuously throughout the run.

2.4 Experimental procedure and measurements

Thermocouples (Type K, ±0.5°C accuracy) were installed at five positions within the reactor. Temperature data were recorded at 5-minute intervals over the 30-minute experiment duration. The heat transfer rate was calculated from:

$$Q_HF = \dot{m}_biomass \times LHV_biomass \times \eta_combustion \quad (9)$$

where η_combustion = 72% based on flue gas temperature measurements.

The specific method used to determine η_combustion (e.g., indirect method from flue-gas temperature and excess-air measurements, instrument model, and governing equation) should be described in full here. The cumulative oil yield (Y_oil) was calculated as:

$$Y_oil\ (\%) = (m_oil / m_plastic) \times 100 \quad (10)$$

Parallel experiments were conducted with a conventional bottom-heated reactor for direct comparison. Three replicate experiments were performed under each condition. Statistical significance was assessed using $R^2 \geq 0.85$ and P-value < 0.05. Standard deviations for every reported value should be inserted from the triplicate raw data referenced above, to demonstrate statistical transparency, per reviewer request. The following procedural details, requested for reproducibility, should be inserted from the experimental log: (i) the vapor/off-gas flow rate measurement method and instrument; (ii) the method used to control reactor temperature during the run (e.g., manual biomass feeding rate adjustment vs. automated damper control); (iii) the method used to measure the mass of pyrolytic oil, non-condensable gas, and solid char residue at the end of each run (for mass-balance closure, Section 3.2.2); and (iv) the condensation conditions (coolant flow rate/temperature and condenser residence time).

Thermocouple calibration method and traceability, and the measurement uncertainty of all instruments used (thermocouples, mass balance, flowmeters), should be reported explicitly to support the statistical reliability claims made in Section 3.

2.5 Oil quality analysis

Analytical methods to be completed: kinematic viscosity at 40°C per ASTM D445; flash point per ASTM D93; density at 15°C per ASTM D4052; higher/lower heating value (HHV/LHV) by bomb calorimetry; water content by Karl Fischer titration (ASTM D6304) or ASTM D95; and compositional analysis by GC-MS and/or FTIR to identify the hydrocarbon fractions present and confirm suitability as a diesel-range fuel. Results, once available, should be compared against ASTM D975 diesel specifications to substantiate any “fuel oil” terminology used in the Abstract and Conclusion.

2.6 Field deployment protocol

A formal field-test protocol, deployment duration, operating schedule, method of recording oil production and sales/income,

and number of operating cycles monitored, should be inserted here to substantiate the ~30,000 THB/month estimate reported in the Abstract and Section 3.5. Until this protocol is documented, the income figure should be presented as a preliminary, non-replicated field observation rather than a validated result.

2.7 Safety considerations

A dedicated safety discussion should be added, covering: eactor pressure control and relief (to prevent over-pressurization during rapid heating); handling of flammable pyrolysis vapors and prevention of gas leaks at pipe/condenser joints; backfire/flashback prevention at the biomass stove inlet; and management of smoke and particulate emissions from biomass combustion during community operation. These measures should be described with the specific safeguards implemented on the fabricated unit (e.g., pressure relief valve rating, joint sealing method, operator PPE, and stove exhaust routing)

3. Results and Discussion

3.1 Temperature profile and heating rate

The experimental temperature profiles of both systems are presented in Figure 3 and summarized in Table 2. The new system achieved a rapid and continuous temperature increase characterized by four distinct phases: (1) Rapid heat-up phase (0–5 min): 30°C to 120°C; (2) Continuous rise phase (5–15 min): temperature reached 320°C; (3) Full pyrolysis entry phase (15–20 min): temperature exceeded 420°C; (4) Stable high-temperature operation (20–30 min): temperature reached 520°C. The average heating rate of the new system in the 0–20 min interval was 19.5°C/min, compared to 10.8°C/min for the conventional system—an improvement of 80.6%. The linear regression correlation was:

$$T = 16.5t + 29.8, \quad R^2 = 0.974, \quad \text{P-value} = 1.8 \times 10^{-10} \quad (11)$$

The high R^2 value of 0.974 and P-value < 0.001 confirm the strong linear relationship between heating time and reactor temperature under the tested experimental conditions, supporting the statistical reliability criterion of $R^2 \geq 0.85$ and P-value < 0.05.

Beyond the statistical fit, the faster heating observed for the dual-heat-zone system is consistent with the underlying heat-transfer mechanism: The central pipe places a conductive heat source directly within the packed PE bed, shortening the internal conduction path relative to a bottom-only jacket and reducing the radial temperature gradient across the reactor cross-section. This more uniform internal temperature field would be expected to bring a larger fraction of the PE bed above the onset temperature for thermal cracking (typically 300–500°C for polyolefins) more quickly and more uniformly than bottom-only heating. This is consistent with both the higher heating rate (Section 3.1) and the higher oil yield (Section 3.2) observed in this study. However, establising a full quantitative relationship with PE cracking kinetics would require in-bed temperature mapping and should be identified as a direction for future work rather than a claim established by the present dataset.

The linear regressions reported in Eqs. (11) – (12) are fitted to sequential time-series measurements from a single run per condition; such data points are not statistically independent (each depends on the reactor state at the prior time step), and the number of distinct time points (n = 7) is limited. The high R^2 values should therefore be interpreted as descriptive of the trend observed in this run rather than as a fully validated statistical inference; independent replicate runs (Section 2.4) with regression performed across replicates, rather than across time within a single run, would provide a more rigorous basis for the reported P-values.

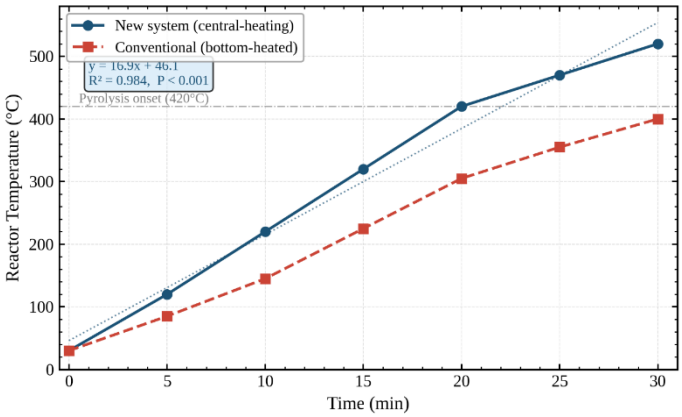


Figure 3 Temperature profile comparison: new dual-heat-zone system vs. conventional bottom-heated reactor.

Table 2 Temperature profile and cumulative oil yield of the biomass-assisted pyrolysis system.

Time (min)	T_new (°C)	T_conv (°C)	ΔT (°C)	Y_oil (% cumulative)
0	30	30	0	0
5	120	85	35	0
10	220	145	75	5
15	320	225	95	18
20	420	305	115	35
25	470	355	115	52
30	520	400	120	65

Note: values are means (n = 3); ± SD to be added per column once triplicate raw data are compiled.

3.2 Oil yield

No oil was produced during the first 5 minutes, consistent with the pre-pyrolysis heating phase. Oil production commenced at approximately 10 minutes (5% yield), corresponding to the reactor temperature reaching approximately 220°C. The cumulative oil yield increased rapidly from 18% at 15 minutes to 35% at 20 minutes, and reached approximately 65% at 30 minutes, consistent with the 50–95% range reported for pure PE (Miandad *et al.*, 2016) and 70 wt.% by Onwudili *et al.* (2009). The linear regression correlation was:

$$Y_oil = 0.168 \times T - 31.4,\ R^2 = 0.965,\ P\text{-value} = 9.2 \times 10^{-11} \quad (12)$$

The high R^2 of 0.965 confirms a strong linear relationship between reactor temperature and cumulative oil yield within the temperature range of 220–520°C under the tested conditions.

This 65% yield is lower than the 50–95 wt.% range reported for pure PE pyrolysis (Miandad *et al*., 2016) and the 70 wt.% reported by Onwudili *et al*. (2009). Three factors likely explain this gap. First, the 30-minute experiment duration used here is shorter than the residence times typically used in the comparator studies, which generally hold the reactor at peak temperature for longer periods to allow near-complete cracking of the polymer chains; the present run may therefore have been terminated before the reaction reached completion. Second, the semi-open vapor transport and condenser configuration used in this fixed-bed, field-deployable design may allow a fraction of lighter, more volatile pyrolysis vapors to escape uncondensed, particularly during the rapid temperature-rise phase, reducing the recovered liquid fraction relative to fully sealed laboratory reactors. Third, feedstock particle size and packing density (Section 2.3) affect internal heat and mass transfer and were not matched to the comparator literature. Because the temperature–yield relationship in Eq. (14) remains strongly linear up to 520°C with no evidence of a plateau within the tested window, it is plausible that extending the experiment beyond 30 minutes at sustained peak temperature would increase cumulative yield further; this is identified as a specific direction for follow-up testing (Section 4) rather than a conclusion drawn from the present dataset.

3.2.1 Oil quality

Placeholder: kinematic viscosity, flash point, density, and gross calorific value of the pyrolytic oil, ideally reported at two or more sampling times/temperatures (e.g., 20 min and 30 min) to show whether reactor temperature affects oil quality as well as quantity, per reviewer request. To be completed once laboratory analysis is available.

3.2.2 Mass balance

Only the liquid oil fraction (Y_oil) is quantified in the present dataset. A complete mass balance for the 5.0 kg PE feed, oil, non-condensable gas (by difference or direct measurement), and solid char residue, should be reported to confirm closure and to contextualize the 65% oil yield against the remaining ~35% of feed mass, which is currently unaccounted for in the manuscript.

3.3 Efficiency calculations

Applying Eq. (3) to the 30-minute run: the plastic feedstock mass was m_plastic = 5.0 kg, giving a recovered oil mass m_oil = Y_oil × m_plastic = 0.65 × 5.0 = 3.25 kg (using ρ_oil = 0.85 kg/L). Using LHV_oil = 40–42 MJ/kg (midpoint 41 MJ/kg), the energy recovered in the oil is m_oil × LHV_oil ≈ 133.3 MJ. The biomass fuel consumed over the run, $\dot{m}$_fuel × t, is [to be inserted from the measured biomass mass consumed during the 30-minute run; this value, together with LHV_fuel = 15.6 MJ/kg, should be substituted into Eq. (3) to reproduce η = 68.5% exactly as reported]. Similarly, the exergy efficiency ψ (Eq. 4) requires Ex_oil and Ex_input = Ex_fuel = β × LHV_fuel (Eq. 5); with β in the range 1.04–1.17 for solid biomass (Dincer and Rosen, 2013), [substitute the measured/assumed β and confirm the resulting ψ = 52.1% as reported].

$$\eta = (m_oil \times LHV_oil) / (\dot{m}_fuel \times LHV_fuel \times t) = 68.5\% \quad (13)$$

$$\psi = Ex_oil / Ex_input = 52.1\% \quad (14)$$

This restores the explicit calculation path linking the raw measurements (Table 1, Table 2) to the summary efficiency figures reported in Section 3.4, addressing the missing equation numbers (13)–(14) in the original submission.

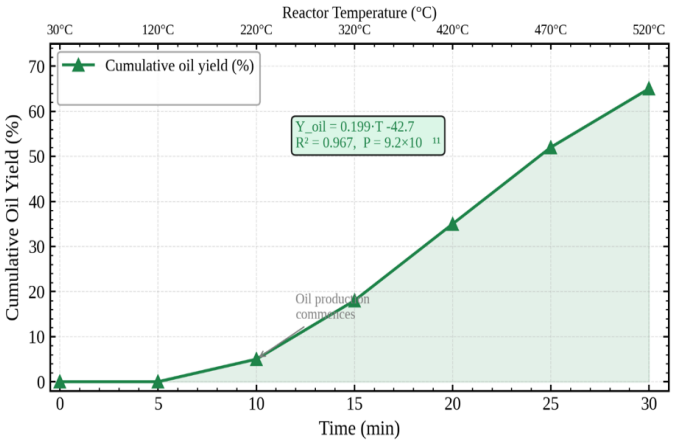


Figure 4 Cumulative oil yield over time in the pyrolysis process.

3.4 Comparison with conventional system

As defined in Section 2.3, the conventional reactor used for this comparison was matched to the dual-heat-zone system in inner diameter, height, wall material, reactor volume, PE feedstock mass, and biomass fuel type/heat output, differing only in the absence of the central heat-transfer pipe; the reported ΔT, η, and ψ differences are therefore attributable to the heating-zone configuration rather than to confounding differences in reactor size or fuel loading.

The temperature difference (ΔT) increased progressively from 35°C at 5 minutes to a maximum of 120°C at 30 minutes. The energy efficiency (η) of the new system was 68.5%, compared to 42.3% for the conventional system—a relative improvement of 62.0%. The exergy efficiency (ψ) was estimated at 52.1%. The regression performance curve of ΔT versus time yielded:

$$\Delta T = 4.05t + 14.5,\ R^2 = 0.989,\ P\text{-value} = 3.7 \times 10^{-12} \quad (15)$$

The near-perfect R^2 of 0.989 indicates that ΔT increases linearly with time throughout the 30-minute experiment, providing a reliable predictive tool for scaling the central-pipe heat-transfer enhancement to larger reactor configurations.

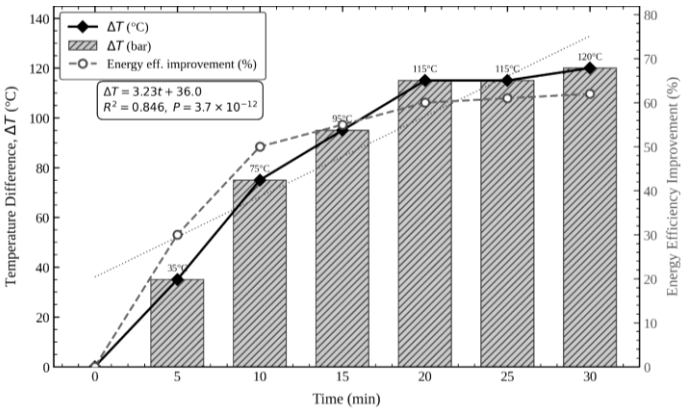


Figure 5 Temperature difference (ΔT) between new and conventional system over time.

3.5 Community-scale suitability and economic analysis

The system's low fabrication cost (20,000 THB/unit), use of locally available biomass, and demonstrated income-generation potential (~30,000 THB/month in two field sites in Nakhon Phanom Province) support its potential viability for community-scale deployment, subject to the economic assumptions below being confirmed. The LEnC was calculated with a system lifespan of 10 years, discount rate of 5.0%, and annual operating time of 2,400 h/year. The LEnC of approximately 2.2 THB/L represents a 93% cost saving compared to diesel at 33 THB/L, yielding a payback period of less than 1 month.

The economic assumptions underlying the 30,000 THB/month income estimate and the <1-month payback period should be stated explicitly, including: the assumed sale price of pyrolytic oil (THB/L); the assumed daily production volume and number of production cycles per day/month; labor cost per cycle; biomass fuel cost (if not self-collected); and routine maintenance cost beyond the OM figure in Table 3. Without these assumptions stated, the income and payback figures cannot be independently verified.

Table 3 Economic analysis of the dual-heat-zone biomass-assisted pyrolysis system.

Parameter	Value
Capital cost of pyrolysis reactor and stove (Z_reactor, THB)	15,000
Capital cost of condenser and piping (Z_condenser, THB)	3,000
Capital cost of oil collection tank (Z_tank, THB)	2,000
Total investment cost (Inv, THB)	20,000
Annual operating & maintenance cost (OM, THB/y)	3,600
Discount rate (r, %)	5.0
System lifespan (n, y)	10
Capital recovery factor (CRF)	0.1295
Annual operating time (t_OT, h/y)	2,400
Annual oil production (L/y, estimated)	6,500
Estimated income increase (THB/month)	30,000
Levelized energy cost (LEnC, THB/L)	2.2

The community settings of Ban Nathon and Ban Khoksawang, Amphoe That Phanom, Nakhon Phanom Province, support the relevance of this design to rural community-scale deployment in Thailand, where locally sourced agricultural residues and small-scale plastic collection are already established practices. The recovered pyrolytic oil has potential applications as a fuel for low-speed diesel engines used in agricultural machinery and for community-level heating, subject to confirmation of oil quality (Section 2.5). This application pathway, rather than direct diesel substitution, is the most realistic near-term use case pending full characterization.

4. Conclusions

This study developed and experimentally evaluated a dual-heat-zone (central-pipe), biomass-assisted pyrolysis system for converting PE plastic waste into pyrolytic oil, directly addressing the four stated objectives:

Objective 1 (design and development): A dual-heat-zone reactor was designed and fabricated (Section 2.2, Table 1), incorporating a central heat-transfer pipe that increased the effective heat transfer area by approximately 85% compared to conventional bottom-heated reactors (Eq. 8).

Objective 2 (heat transfer efficiency / startup time): The new system achieved pyrolysis-onset temperature (420°C) within 20 minutes, with an average heating-rate improvement of 80.6% (from 10.8°C/min to 19.5°C/min).

A cumulative oil yield of approximately 65% was achieved within 30 minutes, consistent with reported yields for pure PE pyrolysis (Section 3.2).

Objective 3 (comparison with conventional system): Against a clearly defined, like-for-like conventional bottom-heated reactor (Section 2.3), the energy efficiency of the new system (68.5%) was higher than that of the conventional system (42.3%) under the matched test conditions described in Section 2.3, a relative improvement of 62.0%.

Linear regression analysis yielded statistically reliable performance correlations ($R^2 \geq 0.965$, P-value < 0.001).

Objective 4 (practical applicability and economic viability): The system's low fabrication cost (~20,000 THB/unit) and an LEnC of 2.2 THB/L (a 93% saving relative to diesel) support economic viability for community-scale deployment, though these efficiency, cost, and income figures are single-configuration, preliminary results (Section 3.5) that should be confirmed by replicate testing and a documented field-trial protocol (Section 2.6) before being generalized.

Limitations: This study is limited to a single plastic type (PE), a single reactor scale (75.4 L), and a short 30-minute test duration per condition; cumulative oil yield beyond 30 minutes was not tested (Section 3.2). Pyrolytic oil quality (Section 2.5, 3.2.1), a complete process mass balance (Section 3.2.2), and the environmental/emissions impact of biomass combustion have not yet been characterized. The reported statistical correlations (Eq. 13–15) are based on a single run per condition and should be interpreted with the caveats noted in Section 3.1. Measured pyrolytic-oil properties, viscosity, flash point, density,

calorific value, should be stated explicitly in this conclusion once available, per reviewer request. For future studies, computational fluid dynamics (CFD) modelling should optimize central-pipe geometry. Catalytic pyrolysis using natural zeolites should be investigated to upgrade pyrolytic oil quality. Life cycle assessment should quantify GHG emission reduction. Extended-duration trials (>30 minutes at sustained peak temperature) should test whether cumulative oil yield can be increased beyond the 65% observed here, directly addressing the reviewer's question on this point. An environmental assessment of smoke and volatile organic compound (VOC) emissions from the biomass stove and from any uncondensed pyrolysis vapor should also be conducted, together with a comparative assessment against alternative plastic waste management routes (e.g., open burning, landfilling, and mechanical recycling) available in the study communities, to fully substantiate the environmental benefit claimed for this system.

5. Acknowledgments

The authors gratefully acknowledge the Energy Engineering Program, Thatphanom College, Nakhon Phanom University, for financial support and research facilities. The authors also thank the two agricultural cooperative groups in Nakhon Phanom Province for their cooperation in the field experiments.

During the preparation of this manuscript, the authors used ChatGPT (OpenAI) solely to assist with English language editing, grammatical correction, and improvement of readability and clarity. All AI-assisted content was carefully reviewed, verified, and revised by the authors to ensure its accuracy, completeness, and objectivity. No generative AI tools were used to create images, figures, graphs, or diagrams in this manuscript. The authors take full responsibility for the accuracy, integrity, originality, and final content of the submitted work.

6. References

Abnisa, F. and Wan Daud, W.M.A. 2014. A review on co-pyrolysis of biomass: An optional technique to obtain a high-grade pyrolysis oil. **Energy Conversion and Management** 87: 71–85.

Anuar Sharuddin, S.D., Abnisa, F., Wan Daud, W.M.A. and Aroua, M.K. 2016. A review on pyrolysis of plastic wastes. **Energy Conversion and Management** 115: 308–326.

Bridgwater, A.V. 2004. Biomass fast pyrolysis. **Thermal Science** 8(2): 21–49.

Bridgwater, A.V. 2012. Review of fast pyrolysis of biomass and product upgrading. **Biomass and Bioenergy** 38: 68–94.

Cengel, Y.A. and Ghajar, A.J. 2014. **Heat and Mass Transfer: Fundamentals and Applications** (5th ed). McGraw-Hill: New York.

Chaiyat, N., Chaongew, S., Ondokmai, P. and Makarkard, P. 2020. Levelized energy and exergy costings per life cycle assessment of a combined cooling, heating, power and tourism system of San Kamphaeng hot spring, Thailand. **Renewable Energy** 146: 828–842.

Chamsing, A., Salokhe, V. and Singh, G. 2006. Energy consumption analysis for small-scale combined rice milling and husk gasification systems. **Agricultural Engineering International**: CIGR Journal 8: Manuscript EE 06 002.

Demirbas, A. 2004. Pyrolysis of municipal plastic wastes for recovery of gasoline-range hydrocarbons. **Journal of Analytical and Applied Pyrolysis** 72(1): 97–102.

Demirbas, A. 2008. Biofuels sources, biofuel policy, biofuel economy and global biofuel projections. **Energy Conversion and Management** 49(8): 2106–2116.

Demirbas, M.F., Balat, M. and Balat, H. 2009. Potential contribution of biomass to sustainable energy development. **Energy Conversion and Management** 50(7): 1746–1760.

Dincer, I. and Rosen, M. A. 2013. **Exergy: Energy, Environment and Sustainable Development** (2nd ed). Elsevier: Oxford.

Genuino, H.C., Pilar Ruiz, M., Heeres, H.J. and Kersten, S.R.A. 2023. Pyrolysis of mixed plastic waste: Predicting the product yields. **Waste Management** 156: 208–215.

Holman, J.P. 2010. **Heat Transfer** (10th ed). McGraw-Hill: New York.

Incropera, F.P., DeWitt, D.P., Bergman, T.L. and Lavine, A.S. 2011. **Fundamentals of Heat and Mass Transfer** (7th ed). Wiley: Hoboken.

Islam, M.N., Islam, M.N., Alam Beg, M.R. and Islam, M.R. 2005. Pyrolytic oil from fixed bed pyrolysis of municipal solid waste and its characterization. **Renewable Energy** 30(3): 413–420.

Kaminsky, W., Predel, M. and Sadiki, A. 2004. Feedstock recycling of polymers by pyrolysis in a fluidized bed. **Polymer Degradation and Stability** 85(3): 1045–1050.

Kurniawan, A., Sugiarto, B. and Perdana, A. 2020. Design of bench scale pyrolysis reactor for plastic waste conversion into liquid fuel using biomass as heating source. **Eksergi** 17(1): 1–6.

Lee, K.H. 2009. Effects of pyrolysis conditions on the pyrolysis of polypropylene. **Journal of Analytical and Applied Pyrolysis** 86(1): 39–44.

Mastral, A.M., Murillo, R., Callen, M.S. and Garcia, T. 2000. Evidence of coal and tire interactions in coal-tire coprocessing for short residence times. **Fuel Processing Technology** 69(2): 127–140.

Mastral, J.F., Esperanza, E., Garcia, P. and Juste, M. 2002. Pyrolysis of high-density polyethylene in a fluidised bed reactor. **Journal of Analytical and Applied Pyrolysis** 63(1): 1–15.

Mohan, D., Pittman, C.U. and Steele, P.H. 2006. Pyrolysis of wood/biomass for bio-oil: A critical review. **Energy & Fuels** 20(3): 848–889.

National Renewable Energy Laboratory (NREL). 2021. **Levelized cost of energy analysis**. NREL: Golden. Available Source: https://www.nrel.gov/analysis/lcoe.html.

Onwudili, J.A., Insura, N. and Williams, P.T. 2009. Composition of products from the pyrolysis of polyethylene and polystyrene in a closed batch reactor. **Journal of Analytical and Applied Pyrolysis** 86(2): 293–303.

Pokson, C. and Chaiyat, N. 2022. Thermal performance of a combined cooling, heating, and power (CCHP) generation system from infectious medical waste. **Case Studies in Chemical and Environmental Engineering** 6: 100221.

Sajjakulnukit, B., Yingyuad, R., Maneekhao, V., Pongnarintasut, V., Bhattacharya, S.C. and Abdul Salam, P. 2005. Assessment of sustainable energy potential of non-plantation biomass resources in Thailand. **Biomass and Bioenergy** 29(3): 214–224.

Sakata, Y., Uddin, M.A. and Muto, A. 1999. Degradation of polyethylene and polypropylene into fuel oil by using solid acid and non-acid catalysts. **Journal of Analytical and Applied Pyrolysis** 51(1–2): 135–155.

Scheirs, J. and Kaminsky, W. 2006. **Feedstock Recycling and Pyrolysis of Waste Plastics**. Wiley: Chichester.

Williams, P.T. and Slaney, E. 2007. Analysis of products from the pyrolysis and liquefaction of single plastics and waste plastic mixtures. **Resources, Conservation and Recycling** 51(4): 754–769.

Recent Science and Technology 2026, Vol. 18(3): e271280

Recent Science and Technology

Journal homepage: https:// www.tci-thaijo.org/index.php/rmutsvrj/index

ISSN: 3057-0786 (Online)

Research Article

Shelf-Life Assessment and Prediction of *Gymnema inodorum* (Lour.) Decne. Jelly under Accelerated Storage Conditions

Natthanicha Banpacha [a], Hiran Janpeng [a] and Rajnibhas Sukeaw Samakradhamrongthai [a, b *]

[a] *Division of Product Development Technology, Faculty of Agro-Industry, Chiang Mai University, Chiang Mai 50100, Thailand.*

[b] *Interdisciplinary and Food Product Development for Wellness Research Unit, Multidisciplinary Research Institute, Chiang Mai University, Chiang Mai 50100, Thailand.*

Article history:

Received: 2026-03-17
Revised: 2026-06-01
Accepted: 2026-07-27

Keywords:

Accelerated storage;
Q10 model;
Shelf-life prediction

ABSTRACT

This study investigated changes in quality and shelf-life prediction of *Gymnema inodorum* jelly (GIJ) under accelerated storage conditions using the Q_{10} model. The GIJ samples were stored at four controlled temperatures (4, 25, 35, and 45 °C) for 10 weeks to evaluate quality deterioration. Quality attributes, including color parameters (L*, a*, b*), syneresis, texture profile analysis (hardness, springiness, gumminess, and chewiness), microbiological quality, and sensory acceptability, were periodically assessed. Storage temperature and duration significantly influenced product quality, with progressive color degradation, increased syneresis, and reduced textural properties observed during prolonged storage, particularly at elevated temperatures. Microbiological analysis showed that total viable counts exceeded acceptable limits earlier at higher storage temperatures, reaching the regulatory threshold at weeks 4 and 6 under storage at 45 °C and 35 °C, respectively. Sensory evaluation showed that the product remained acceptable during the initial storage period, with liking scores above the predefined acceptance threshold, but declined progressively with extended storage. Shelf-life prediction based on the Q_{10} model estimated that GIJ could be stored for approximately 147.6 days (4 months and 27 days) at 4 °C and 63 days (2 months and 3 days) at 25 °C. Under these conditions, the product remained acceptable to consumers and complied with the Thai Community Product Standard (TCPS 519/2547). These findings demonstrate the applicability of the Q_{10} model as a practical tool for predicting the storage stability of functional jelly products while supporting product development, quality control, and commercialization.

© 2026 Banpacha, N., Janpeng, H. and Samakradhamrongthai, R.S. Recent Science and Technology published by Rajamangala University of Technology Srivijaya

1. Introduction

The development of ready-to-eat functional foods derived from local medicinal plants has gained increasing attention due to their potential to add value to agricultural raw materials while meeting the growing consumer demand for health-promoting products. *Gymnema inodorum* (Lour.) Decne (*G. inodorum*), an indigenous plant widely consumed in Southeast Asia, is rich in bioactive compounds, particularly phenolic compounds, flavonoids, and gymnemic acids. These phytochemicals exhibit strong antioxidant properties and have been reported to contribute to glycemic control and other health benefits (Tiwari *et al*., 2014; Tiamyom *et al*., 2019; Dunkhunthod *et al*., 2021; Nunta *et al*., 2023). Consequently, *G. inodorum* has considerable potential for application in various functional food products, including beverages, snacks, and gel-based confectionery.

Jelly products are among the most popular semi-solid foods due to their soft texture, ease of chewing, and high consumer acceptability across different age groups. Their structure is formed by a three-dimensional polymeric gel network capable of retaining a large amount of water, resulting in desirable sensory and textural characteristics (Chaurasia *et al*., 2023; Baiti *et al*., 2024). In recent years, plant-based functional jellies enriched with bioactive compounds from fruits, vegetables, and medicinal plants have gained increasing attention because of their potential health benefits. However, these products often

*** Corresponding author.**

E-mail address: *rajnibhas.s@cmu.ac.th*

Cite this article as: Banpacha, N., Janpeng, H. and Samakradhamrongthai, R.S. 2026. Shelf-Life Assessment and Prediction of *Gymnema inodorum* (Lour.) Decne. Jelly under Accelerated Storage Conditions. **Recent Science and Technology** 18(3): e271280.
https://doi.org/10.65411/rst.2026.271280

exhibit greater formulation complexity due to interactions between bioactive constituents and hydrocolloid networks, which may affect gel stability during storage. In addition, jelly systems typically contain high moisture levels, hydrocolloids, and sugars, which make them susceptible to physical, chemical, and microbiological changes during storage. One of the most common quality defects is syneresis, a phenomenon in which contraction of the polymer network expels water from the gel matrix, leading to reduced firmness and overall product deterioration. In addition, gel softening and microbial growth may occur, further compromising product quality and safety (Arslan and Kadagan, 2021; Arab *et al*., 2022; Lin *et al*., 2023). These changes can negatively affect consumer acceptance and shorten the product's shelf life.

Although food processing can extend product stability, quality degradation and spoilage may still occur during storage. Therefore, shelf-life evaluation is a critical step in food product development, as it determines the period during which a product maintains acceptable quality, safety, and sensory attributes. Accurate shelf-life estimation is also an essential component of good manufacturing practices (Suwan and Suwannakam, 2021). Furthermore, food regulations require manufacturers to clearly declare expiration dates or "best before" information on product labels (Ministry of Public Health, 2024). Conventional shelf-life testing under normal storage conditions can be time-consuming and costly, especially for products with extended stability. Accelerated storage testing offers a practical alternative, as elevated temperatures can hasten physical, chemical, and microbiological deterioration, enabling faster prediction of product stability (Sinchaipanit *et al*., 2022). Among predictive approaches, the Q_{10} model is widely used to estimate shelf life based on the relationship between temperature and reaction rate, assuming that the deterioration rate increases with increasing storage temperature. This approach enables rapid prediction of product stability under normal storage conditions using data obtained from accelerated storage studies (Arboretti *et al*., 2022; Xiao *et al*., 2022)

Despite the growing interest in *G. inodorum* as a functional food ingredient, studies on the storage stability and shelf-life of products developed from this plant remain limited. Therefore, this study aimed to investigate the quality changes of *G. inodorum* jelly (GIJ) during accelerated storage. The products were stored at 4, 25, 35, and 45 °C for 10 weeks, and changes in color parameters, texture profile analysis, syneresis, microbiological quality, and sensory acceptance were evaluated. The findings are expected to provide useful information for determining appropriate storage conditions and estimating the shelf life of the product to ensure quality and consumer safety.

2. Materials and Methods

2.1 Materials and chemicals

G. inodorum leaves were obtained from a local plantation in the Mae-On District of Chiang Mai Province, Thailand. Samples were collected between February and April 2024 without consideration of the specific season or time of collection. The first three pairs of young leaves from the apical regions of the plants were harvested. Carrageenan and konjac powder (food-grade) were purchased from Yok Intertrade (Chiang Mai) Co., Ltd. Citric acid (food-grade) was acquired from Specialfood (Samut Prakan) Co., Ltd. Monk fruit syrup was purchased from Miss Cony, Thailand. 3M™ Petrifilm™ aerobic count plate and 3M™ Petrifilm™ yeast and mold count plate were acquired from 3M company (MN, USA). Peptone was obtained from HiMedia Laboratories Pvt. Ltd. (Nashik, India). Purified water was produced using a Millipore water purification system (Millipore, Bedford, MA, USA).

2.2 Study on quality changes of GIJ products during accelerated storage

Aqueous *G. inodorum* leaf extract was prepared with slight modifications to the method described by Banpacha *et al*. (2025). Briefly, dried *G. inodorum* leaves were weighed and mixed with clean drinking water at 50 °C to obtain a 3% (w/v) concentration. The extraction was carried out for 3 min, after which the mixtures were filtered through a tea filter bag to remove solid residues and allowed to cool to room temperature before use.

For jelly preparation, K-carrageenan and konjac flour were blended at a ratio of 1:1 and incorporated into the aqueous *G. inodorum* leaf extract at a total hydrocolloid concentration of 1.5% (w/v). The selected ratio was based on previous studies reporting improved gel strength, chewiness, and structural stability due to synergistic interactions between K-carrageenan and konjac gum, with the 1:1 ratio identified as optimal for desirable gel characteristics (Tunieva *et al*., 2021; Wang *et al*., 2021). The mixture was allowed to hydrate for 5 min. Monk fruit syrup (12.2%, w/v) was added, and the solution was heated to 85 ± 2 °C with continuous stirring for 10 min to ensure complete dissolution and homogeneity. Heating was discontinued, and citric acid (0.3%, w/v) was added to adjust the formulation. The hot jelly solution was immediately filled into aluminum foil sachets (12 g) and hermetically sealed. Freshly prepared samples were analyzed on day 0 to determine the initial microbial load before storage. Subsequently, the products were stored at controlled temperatures of 4, 25, 35, and 45 °C under laboratory conditions (approximately 65% RH) for 10 weeks. Samples were withdrawn at two-week intervals for quality evaluation.

2.3 Color measurement

Color characteristics were determined using the CIE L*, a*, b* color system with a HunterLab ColorFlex EZ colorimeter (USA). The parameters recorded included lightness (L*),

redness/greenness (a*), and yellowness/blueness (b*), and the average values were reported.

The total color difference (ΔE*) was calculated to evaluate overall color changes during storage according to the following equation:

$$\Delta E^* = \{(\Delta L^*)^2 + (\Delta a^*)^2 + (\Delta b^*)^2\}^{1/2} \quad (1)$$

where ΔL*, Δa*, and Δb* represent the differences between the initial color values (L_1, a_1, b_1) and the measured color values at each storage time (L_2, a_2, b_2), respectively.

2.4 Syneresis of GIJ products during accelerated storage

Syneresis was determined according to the method of Saraboot *et al*. (2018) with slight modifications. Jelly samples (5 g) were weighed and placed on Whatman No. 4 filter paper positioned on a wire mesh screen. The samples were allowed to drain at their respective storage temperatures for 2 h. The syneresis was calculated using the following equation.

$$Syneresis\ (\%) = \frac{Total\ weight\ of\ separated\ liquid\ (g)}{Total\ weight\ of\ sample\ (g)} \times 100 \quad (2)$$

2.5 Texture profile analysis (TPA) of GIJ products during accelerated storage

The TPA (hardness, springiness, gumminess, and chewiness) was performed according to the method described by Kaewpetch *et al*. (2024) with six replications. Measurements were conducted using a texture analyzer (TA.XT plus, Stable Micro System, Surrey, UK) equipped with a P/50 cylinder probe (50 mm diameter). Samples were subjected to two consecutive compression cycles with a 3 s interval between compressions to simulate mastication. The operating parameters were set as follows: pre-test speed of 1 mm/s, test speed of 5 mm/s, post-test speed of 5 mm/s, a strain of 75%, and a trigger force of 5 g.

2.6 Microbiological analysis

Microbiological quality was evaluated throughout storage at 4, 25, 35, and 45 °C. Total viable count (TVC) and yeast and mold (YM) populations were determined according to the methods described by 3M Food Safety (2021) and Schumacher *et al*. (2023) using 3M™ Petrifilm™ plates (3M Company, St. Paul, MN, USA). At each sampling interval, a 10 g portion of sample was aseptically weighed and homogenized with 90 mL of sterile 0.1% peptone water to obtain an initial dilution of 10^{-1}. A decimal dilution series (10^{-1} to 10^{-6}) was subsequently prepared using the same diluent. For enumeration, 1 mL of each dilution was dispensed onto the center of 3M™ Petrifilm™ Aerobic Count plates for TVC and 3M™ Petrifilm™ Yeast and Mold plates. The inoculum was evenly distributed using a sterile plastic spreader and was allowed to solidify for 1 min prior to incubation. All plates were incubated in a calibrated incubator (Gallenkamp, Model: SIZE TWO, UK). Aerobic count plates were incubated at 35 ± 1 °C for 48 ± 3 h, whereas YM plates were incubated at 25 ± 1 °C for 3–5 days. Following incubation, colonies were enumerated according to the manufacturer's interpretation guidelines. Plates containing 25–250 colonies for TVC and fewer than 150 colonies for YM were selected for counting. All analyses were performed in triplicate, and microbial populations were calculated and expressed as colony-forming units per gram of sample (CFU/g).

2.7 Sensory evaluation of GIJ products during accelerated storage

Sensory evaluation was conducted using an untrained panel consisting of 60 participants (38 females and 22 males) aged between 20 and 60 years, who were recruited from Chiang Mai Province, Thailand. This study was approved by the Ethics Committee of Chiang Mai University (approval number: CMUREC 67/071). Written informed consent was obtained from all participants prior to their involvement in the study. Samples were coded by three-digit random numbers and were served in a randomized order determined by random permutation. Distilled water was provided, and panelists were instructed to cleanse their palate between samples (Godoy *et al*., 2013). Participants rated each sample for degree of liking using 9-point hedonic scales, ranging from 1 (dislike extremely) to 9 (like extremely) (Meilgaard *et al*., 2025). Sensory attributes included appearance, color, aroma, flavor, sweetness, sourness, texture, and overall acceptability.

2.8 Determination of quality indices and accelerated shelf-life estimation

2.8.1 End-of-shelf-life criteria

Quality indices representing both product safety and consumer acceptance were established to determine the end of shelf-life. Critical limits (cut-points) were defined based on microbiological safety standards and sensory acceptability criteria.

(1) Microbiological criteria: Microbiological quality was considered the primary criterion for shelf-life determination because consumer safety is a mandatory requirement and microbiological deterioration represents an irreversible quality defect. Microbiological limits were established in accordance with the Community Product Standard for soft jelly issued by the Thai Community Product Standard (TCPS 519/2547). The maximum allowable limits were set at $\leq 1 \times 10^4$ CFU/g for TVC and $\leq$ 100 CFU/g for YM.

(2) Sensory acceptability criteria: Consumer acceptance was determined based on sensory liking scores obtained using a nine-point hedonic scale. The cut-point was defined as a mean score lower than 6 ("like slightly"), below which the product was considered unacceptable to consumers.

Shelf-life was defined as the earliest time point at which either microbiological or sensory criteria exceeded the predefined cut-point.

2.8.2 Accelerated shelf-life estimation using the Q_{10} method

Shelf-life under accelerated storage conditions was estimated using the Q_{10} method, which is widely applied for predicting the shelf-life of food products based on the effect of

temperature on the rate of quality deterioration. The Q_{10} value represents the factor by which the rate of a chemical or physical reaction increases when the temperature is raised by 10 °C. This approach is based on the principle that temperature influences reaction rates, as higher temperatures increase the kinetic energy of molecules, causing them to move more rapidly and collide more frequently. Consequently, the rate of chemical reactions and quality deterioration increases compared with that at lower temperatures (Sinchaipanit *et al*., 2022).

In this study, accelerated storage tests were conducted at 35 and 45 °C to obtain deterioration data, while shelf-life at 4 and 25 °C was predicted based on the temperature dependence of quality loss. The Q_{10} value was calculated using the following equation:

$$Q_{10} = \frac{\theta_{S(T)}}{\theta_{S(T+10)}} \quad (3)$$

where $\theta_{S(T)}$ and $\theta_{S(T+10)}$ represent the estimated shelf-life at temperatures T and T+10, respectively. The temperature coefficient for a 1 °C temperature difference was calculated as:

$$Q_1 = Q_{10}^{0.1} \quad (4)$$

where Q_1 represents the temperature coefficient for a 1 °C change in storage temperature. For temperature differences other than 10 °C, the temperature coefficient was calculated using:

$$Q^{\Delta T} = \frac{\theta_{S(T)}}{\theta_{S(T+\Delta T)}} \quad (5)$$

where $Q^{\Delta T}$ represents the temperature coefficient for a temperature difference of ΔT °C, and ΔT represents the difference between the two storage temperatures.

Shelf-life was defined as the earliest time point at which either microbiological counts exceeded the regulatory limits or sensory scores fell below the predefined acceptance threshold.

2.9 Statistical analysis

Physical properties were analyzed in triplicate, while texture measurements were performed in six replicates for each treatment. SPSS statistics 17.0 (SPSS Inc., Chicago, IL, USA) was used to calculate means, standard deviations (SD), and to perform multivariate analysis. Duncan's multiple range test was used to determine significant differences at a 95% confidence level ($p < 0.05$).

3. Results and Discussion

3.1 Effect of accelerated storage temperature on quality changes of GIJ

3.1.1 Changes in color parameters

Shelf-life evaluation of GIJ products was conducted under accelerated storage conditions at 4, 25, 35, and 45 °C for 10 weeks. The color parameters of the products were evaluated using the CIE color system (Figure 1). The L* value, representing lightness, ranged from 82.35 to 82.47 (Figure 1a). The a* value ranged from 1.80 to 2.44, with positive values indicating a red hue (Figure 1b), while the b* value ranged from 39.45 to 42.44, with positive values indicating a yellow hue (Figure 1c). During storage, noticeable changes in color parameters were observed compared to the initial samples. This was consistent with the total color difference (ΔE*), which progressively increased throughout the storage period in all treatments, ranging from 0.46 to 3.06 (Figure 1d). In general, ΔE* values below 1.5 are considered imperceptible to the naked eye, values between 1.5 and 3.0 are noticeable but generally acceptable, and values greater than 3.0 indicate distinct color differences that may affect consumer acceptance (Chheng *et al*., 2025).

A statistically significant decrease in L* values ($p < 0.05$) was observed from week 6 onward, indicating a gradual darkening of the product. This trend is consistent with the findings of Kamil *et al*. (2023), who reported reduced lightness in probiotic gummy candies during storage. Although no significant differences were detected within the first 4 weeks, a decreasing trend in lightness was still evident, suggesting that early-stage color degradation had begun prior to reaching statistical significance. Similarly, the redness (a*) and yellowness (b*) values showed significant decreasing trends ($p < 0.05$) throughout the storage period, indicating a reduction in redness and yellowness intensity. Collectively, these results demonstrate a progressive fading and darkening of the jelly product during storage. This change may be attributed to the presence of water-soluble phenolic and flavonoid pigments in the product (Goławska *et al*., 2023). Prolonged storage may reduce the water-holding capacity of the gel matrix, leading to moisture migration and surface water exudation. Consequently, these pigments may dissolve and migrate with the released moisture to the product surface, resulting in reduced color intensity. In addition, elevated storage temperatures may accelerate chemical reactions such as oxidation and non-enzymatic browning, further contributing to color deterioration. Similar reductions in lightness and overall color intensity during storage have been reported in guava–pineapple jelly (Molla *et al*., 2022), supporting the hypothesis that thermal exposure and storage duration are critical factors governing color stability in gel-based fruit products.

3.1.2 Changes in syneresis

Regarding gel structural stability, syneresis was used as an indicator of the amount of water released from the gel network during storage. The results showed that syneresis significantly increased ($p < 0.05$) with prolonged storage time (Figure 2), indicating progressive destabilization of the gel matrix. This finding is consistent with the report of Na Ayutthaya and Putduang (2016). The increase in syneresis can be attributed to the contraction of the three-dimensional gel network

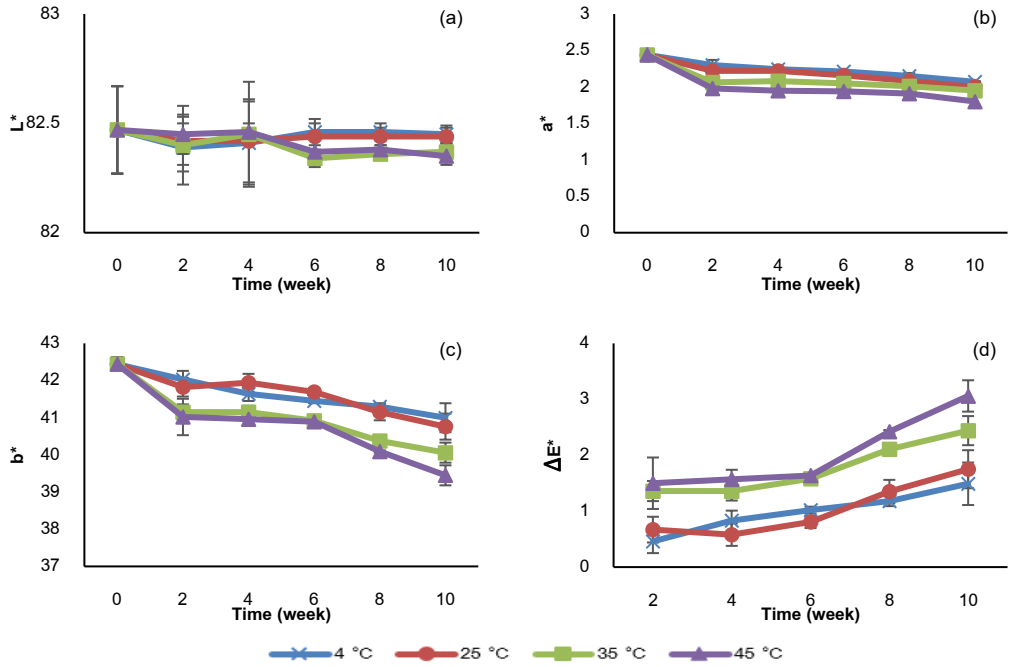


Figure 1 Changes in CIE L* (a), a* (b), b* (c) values and total color difference (ΔE*) (d) of GIJ during storage at different temperatures for 10 weeks.

structure, which exerts pressure on the entrapped water and forces it out of the gel matrix (Arab *et al*., 2023). In addition, elevated storage temperatures may accelerate molecular movement and weaken intermolecular interactions within the gel structure, thereby reducing water-holding capacity and promoting phase separation (Chen *et al*., 2025). These structural changes may adversely affect overall product quality, particularly texture acceptability and visual appearance, due to visible water separation in the jelly product. Excessive syneresis has also been associated with reduced physical stability and shorter shelf life of gel-based food products during storage (Mizrahi, 2010; Petcharat *et al*., 2026).

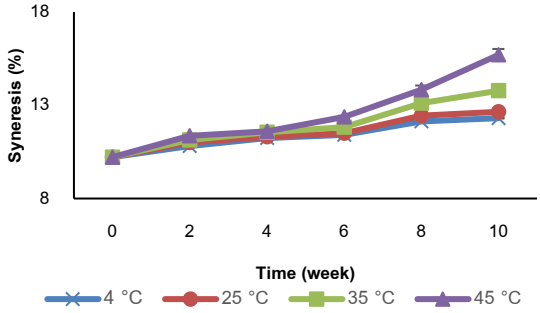


Figure 2 Changes in syneresis of GIJ during storage at different temperatures for 10 weeks.

3.1.3 Changes *in TPA*

The changes in textural properties of GIJ products during accelerated storage at 4, 25, 35, and 45 °C for 10 weeks were evaluated. The results demonstrated that texture parameters, including hardness, springiness, gumminess, and chewiness, significantly decreased ($p < 0.05$) with increasing storage time (Figure 3). These findings indicate that the jelly gel became progressively softer during storage. The softening behavior can be attributed to the deterioration of the gel structure over time. The three-dimensional polymeric network of the gel tends to contract during storage, causing the entrapped water to be expelled from the gel matrix. This effect is more pronounced at elevated temperatures, which accelerate syneresis, defined as water separation from the gel network. Consequently, structural density decreases, intermolecular interactions weaken, and the mechanical strength of the gel is reduced (Na Ayutthaya and Putduang, 2016; Lin *et al*., 2025). Similar decreases in hardness, gumminess, and chewiness during storage were reported by Chheng *et al*. (2025) in Sesban flower extract jelly. The deterioration of textural properties may negatively affect product quality and consumer acceptability, particularly in terms of chewiness and gel consistency, and may ultimately limit the shelf life of the jelly product.

3.1.4 Microbiological properties

The microbiological quality of the jelly products during storage at 4, 25, 35, and 45 °C for 10 weeks is presented in Table 1. TVC and YM counts were evaluated and compared with the Thai Community Product Standard (TCPS. 519/2547), which specifies limits of not more than 1×10^4 CFU/g for total microorganisms and not more than 100 CFU/g for YM.

For TVC, the initial samples and those stored during the early weeks at all temperatures exhibited counts below 10 CFU/g, reflecting satisfactory hygienic quality and appropriate

manufacturing practices. However, with prolonged storage, particularly at elevated temperatures, a marked increase in microbial growth was observed. At 45 °C, TVC exceeded the regulatory limit by week 4 (1.7×10^4 CFU/g). Similarly, samples stored at 35 °C surpassed the permissible level by week 6 (1.3×10^4 CFU/g), while those stored at 25 °C exceeded the standard by week 10 (2.5×10^4 CFU/g). In contrast, samples stored at 4 °C remained within the acceptable limit throughout the storage period. These results indicate that TVC was the primary factor limiting product shelf life, as it was the first quality parameter to reach unacceptable levels under accelerated storage conditions. YM counts also increased gradually during storage; however, all values remained below the regulatory threshold throughout the experiment. The accelerated increase in TVC at higher storage temperatures can be attributed to enhanced microbial metabolic activity and faster rates of cell division under favorable thermal conditions (Qiu *et al*., 2022). Moreover, the microbiological changes were closely associated with the physical deterioration of the jelly matrix observed during storage. As storage temperature increased, degradation of the gel network and greater syneresis were observed, leading to the release of free water from the gel structure. The increased availability of surface moisture may have created a more favorable environment for microbial growth. Therefore, the reduced microbiological stability of the jelly at elevated temperatures was likely the combined result of temperature-induced stimulation of microbial activity and temperature-related deterioration of the gel structure, which enhanced water availability through syneresis (Tarlak, 2023).

3.1.5 Sensory evaluation

Sensory evaluation was conducted using a 9-point hedonic scale to assess consumer preference in terms of appearance, color, aroma, flavor, sweetness, sourness, texture, and overall acceptability. The results showed that GIJ products received liking scores ranging from 6.1 to 7.9 across all attributes during storage, corresponding to “like slightly” to “like very much,” as presented in Table 2. The symbol “–” in the table indicates time points at which sensory evaluation was not performed. This was due to microbial counts exceeding the limits specified by the Thai Community Product Standard No. 519/2547 (TVC $\leq 1 \times 10^4$ CFU/g and YM $\leq$ 100 CFU/g). Sensory testing was therefore discontinued at those time points to ensure panelist safety. Consequently, sensory evaluation was conducted only for samples that met the microbiological safety criteria. Overall, the GIJ products maintained acceptable sensory quality during the early stages of storage. The relatively high scores for appearance and color suggest that the appearance characteristics of the jelly were well maintained, which is an important factor influencing consumer purchase intention. However, a gradual decline in sensory attributes was observed as storage progressed, which may be associated with physicochemical and microbiological changes occurring in the product. Changes in texture could be related to moisture migration or structural modifications in the gel network (Lin *et al*., 2025), while slight reductions in aroma and flavor may result from the degradation or volatilization of flavor compounds during storage. These findings are consistent with the study of Putri *et al*. (2025), who reported a significant decline in consumer liking scores for jelly products during storage. Their study also indicated that storage at 25 °C accelerated quality deterioration compared with storage at 4 °C.

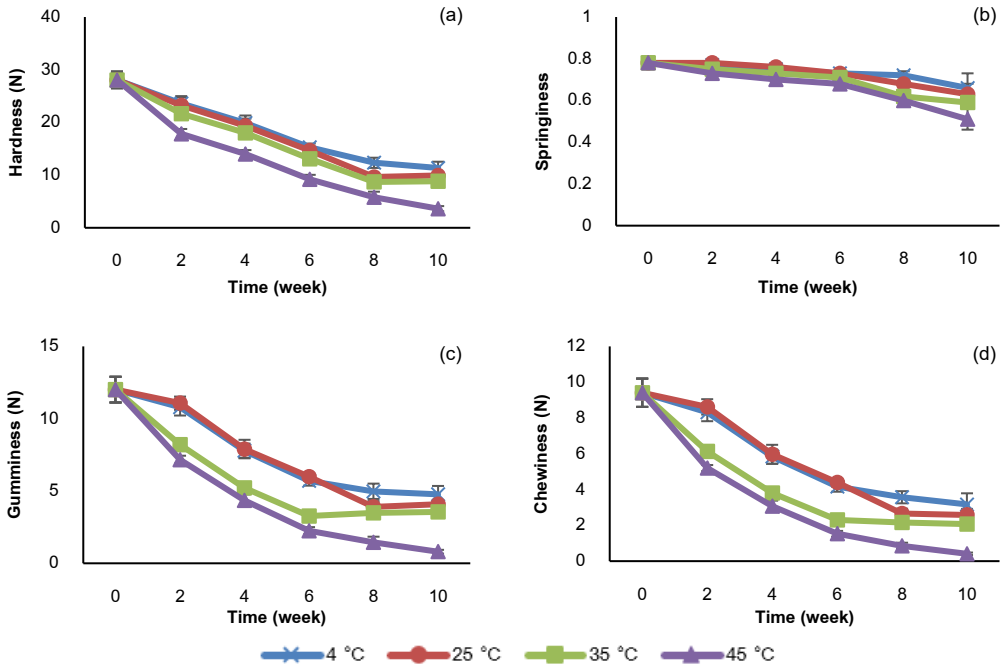


Figure 3 Changes in hardness (a), springiness (b), gumminess (c), and chewiness (d) of GIJ during storage at different temperatures for 10 weeks.

Table 1 Microbial growth of TVC and YM counts in GIJ during storage at different temperatures for 10 weeks.

Properties	Storage temperature (°C)	Storage time (weeks)					
		0	2	4	6	8	10
TVC (CFU/g)	4	<10	<10	<10	<10	3.0×10^{1}	1.4×10^{2}
	25		<10	<10	1.3×10^{1}	5.7×10^{2}	2.5×10^{4}
	35		<10	4.5×10^{2}	1.3×10^{4}	4.5×10^{5}	2.8×10^{6}
	45		2.8×10^{2}	1.7×10^{4}	2.3×10^{5}	6.7×10^{5}	2.4×10^{6}
YM (CFU/g)	4	<10	<10	<10	<10	<10	<10
	25		<10	<10	<10	4.7×10^{1}	8.9×10^{1}
	35		<10	<10	<10	<10	3.2×10^{1}
	45		<10	<10	<10	<10	1.2×10^{1}

Table 2 Sensory evaluation of GIJ during storage at different temperatures for 10 weeks.

Sensory attributes	Storage temperature (°C)	Storage time (weeks)					
		0	2	4	6	8	10
Appearance	4	7.8±0.4	7.7±0.5	7.6±0.8	7.6±0.5	7.6±0.5	7.3±0.8
	25		7.6±0.8	7.6±0.7	7.5±0.5	7.2±0.6	-
	35		7.5±0.7	7.5±0.9	-	-	-
	45		7.6±0.5	-	-	-	-
Color	4	7.8±0.4	7.6±0.7	7.5±0.7	7.5±0.5	7.4±0.5	7.3±0.8
	25		7.7±0.9	7.7±0.8	7.5±0.5	7.2±0.6	-
	35		7.7±0.7	7.7±0.7	-	-	-
	45		7.6±0.5	-	-	-	-
Aroma	4	6.5±1.0	6.6±1.2	6.6±0.8	6.5±0.5	6.3±0.8	6.2±0.8
	25		6.6±1.2	6.5±0.9	6.6±0.5	6.4±0.7	-
	35		6.1±1.2	6.4±0.7	-	-	-
	45		6.0±0.9	-	-	-	-
Flavor	4	7.5±0.9	7.6±1.0	7.3±0.5	7.3±0.5	7.1±0.7	6.9±1.1
	25		7.7±0.5	7.1±1.0	7.0±0.8	7.0±0.8	-
	35		7.3±0.5	6.9±0.6	-	-	-
	45		7.3±0.7	-	-	-	-
Sweetness	4	7.5±0.9	7.6±0.8	7.4±0.7	7.3±0.7	7.3±0.9	7.0±0.9
	25		7.6±0.5	7.3±0.5	7.2±0.4	7.1±0.7	-
	35		7.0±1.1	6.9±0.6	-	-	-
	45		7.1±0.9	-	-	-	-
Sourness	4	6.8±0.6	6.7±0.9	6.7±0.7	6.6±0.5	6.4±0.7	6.1±0.7
	25		6.6±1.1	6.7±0.5	6.6±0.8	6.5±0.7	-
	35		6.3±1.5	6.6±0.7	-	-	-
	45		6.3±0.8	-	-	-	-
Texture	4	7.8±0.8	7.9±0.7	7.5±0.5	7.2±0.8	7.2±0.4	6.8±0.6
	25		7.9±0.6	7.7±0.5	7.1±1.0	7.1±0.7	-
	35		7.2±0.9	7.4±0.7	-	-	-
	45		6.8±0.9	-	-	-	-
Overall liking	4	7.9±0.7	7.7±0.9	7.7±0.7	7.6±0.7	7.4±0.7	6.9±0.7
	25		7.6±0.5	7.6±0.5	7.5±0.5	7.3±0.8	-
	35		7.2±0.6	7.3±0.5	-	-	-
	45		7.2±0.8	-	-	-	-

Note: Each value represents the mean ± SD (n = 60)

3.2 Shelf-life prediction of GIJ under accelerated storage conditions

Based on the evaluation of GIJ product quality during 10 weeks of storage, changes in physical, microbiological, and sensory attributes were observed, indicating gradual product deterioration. The end-of-shelf-life criteria (cut-point) were defined based on the limits specified by the Thai Community Product Standard No. 519/2547, namely TVC $\leq 1 \times 10^4$ CFU/g and YM $\leq$ 100 CFU/g, and/or a sensory acceptability score of less than 6 on the 9-point hedonic scale. The results showed that the microbiological limit was reached earlier than the sensory acceptability limit. Therefore, the microbiological criterion was used to determine the shelf-life of the product.

Under storage at 35 °C, the shelf life of the GIJ product was determined to be 6 weeks (42 days), whereas at 45 °C, the shelf life was limited to 4 weeks (28 days), based on the defined cut-point criteria. These data were subsequently used to calculate the Q_{10} value and to estimate the shelf life at 4 °C ($\theta_{S(4)}$). The predicted shelf life at 4 °C was 147.6 days (approximately 4 months and 27 days), as calculated below.

$$Q_{10} = \frac{\theta_{S(T)}}{\theta_{S(T+10)}} = \frac{\theta_{S(35)}}{\theta_{S(45)}} = \frac{42}{28} = 1.5$$

$$Q_1 = Q_{10}^{0.1} = 1.5^{0.1} = 1.04138$$

$$Q^{\Delta T} = Q_1^{35-4} = 1.04138^{31} = \frac{\theta_{S(4)}}{\theta_{S(35)}} = \frac{\theta_{S(4)}}{42}$$

$$\theta_{S(4)} = 1.04138^{31} \times 42 = 147.6$$

Furthermore, the predicted shelf life at 25 °C ($\theta_{S(25)}$) was estimated to be 63 days (approximately 2 months and 3 days), as calculated below.

$$Q^{\Delta T} = Q_1^{35-25} = 1.04138^{10} = \frac{\theta_{S(25)}}{\theta_{S(35)}} = \frac{\theta_{S(25)}}{42}$$

$$\theta_{S(25)} = 1.04138^{10} \times 42 = 63.0$$

The shelf-life values determined at 35 and 45 °C were used as accelerated storage data for the development of the Q_{10} prediction model. Subsequently, the shelf-life predicted by the model at 25 °C was validated using the actual storage data obtained at the same temperature. The predicted shelf-life showed good agreement with the observed shelf-life, as the product reached the end of its shelf-life between weeks 8 and 10 (approximately 62 days). This agreement suggests that the accelerated shelf-life testing approach combined with the Q_{10} model provided a reliable estimation of the product shelf-life. These findings are comparable with the study of Saloko *et al*. (2024), who reported that Moringa leaf jelly drink had a shelf-life of approximately 4 months under refrigerated storage (10 °C) and about 2 months at room temperature (30 °C).

4. Conclusion

In the shelf-life study of GIJ products, the storage stability was predicted using the Q_{10} model. Total viable count was identified as the primary shelf-life limiting factor, as it was the first quality parameter to exceed the microbiological standard during storage. Product deterioration was accelerated at elevated temperatures due to the combined effects of increased microbial activity and degradation of the gel structure, which promoted syneresis and increased water availability for microbial growth. Based on the Q_{10} model, the predicted shelf-life of the product was approximately 147.6 days (4 months and 27 days) at 4 °C and 63 days (2 months and 3 days) at 25 °C. Under both storage conditions, the product maintained acceptable sensory quality and complied with microbiological safety standards throughout the predicted shelf-life period.

5. Acknowledgments

The authors sincerely appreciate the Faculty of Agro-Industry, Chiang Mai University, Thailand, for supporting laboratory facilities and equipment for this research. The authors also gratefully acknowledge the support received through the teaching assistant and research assistant scholarships.

6. References

3M Food Safety. 2021. **3M™ Petrifilm™ Aerobic Count Plate product instructions** [Instruction manual]. 3M, USA.

Arab, M., Yousefi, M., Khanniri, E., Azari, M., Ghasemzadeh-Mohammadi, V. and Mollakhalili-Meybodi, N. 2022. A comprehensive review on yogurt syneresis: Effect of processing conditions and added additives. **Journal of Food Science and Technology** 60(6): 1656-1665.

Arboretti, R., Barzizza, E., Ceccato, R., Salmaso, L., Cabello-Straub, I., Gardiner, J., Housmekerides, C., Italiano, R., Ramalhoso, C., Sidoti, T. and Spadoni, L. 2022. Shelf-life prediction: A comparison of methods. **Electronic Journal of Applied Statistical Analysis** 15(3): 527-552.

Arslan, S. and Kadagan, S. 2021. Effects of hydrocolloid combinations on physical, textural and sensory properties of kazandibi. **Latin American Applied Research-An international journal** 51(2): 113-118.

Baiti, Q.A.N., Salsabila, Z., Apsari, W., Ramadan, M.B., Karen, E., Sahid, M.N.A., Darsih, C. and Laksitorini, M. D. 2024. The development of plant-based jelly candy for *Chrysanthemum indicum* L. flower extract and evaluation of the antioxidant activity. **Indonesian Journal of Pharmacy** 35(2): 292–304.

Chaurasia, S., Singh, P., Kumar, D., Bala, K.L. and Kumar, A. 2023. Optimization of physico-chemical, textural and organoleptic attributes of underutilized starfruit jaggery jelly through response surface methodology. **Sugar Tech** 25(6): 1531–1541.

Chen, X., Zhang, Y., Sun, C., Zhao, G. and Zhou, Y. 2025. Preparation–structure–function relationships governing syneresis behavior in alkali-induced konjac glucomannan gel. **Food Chemistry** 496: 146920.

Chheng, S., Jafari, S., Mishra, D. and Assatarakul, K. 2025. Sesban flower extract as a natural functional ingredient: effects on texture, antioxidant activity, and shelf-life stability of jelly formulation. **Sustainable Food Technology** 3(6): 1865-1879.

Dunkhunthod, B., Talabnin, C., Murphy, M., Thumanu, K., Sittisart, P. and Eumkeb, G. 2021. *Gymnema inodorum* (Lour.) Decne. extract alleviates oxidative stress and inflammatory mediators produced by RAW264.7 macrophages. **Oxidative Medicine and Cellular Longevity** 2021(1): 8658314.

Godoy, R.C., Deliza, R., Gheno, L.B., Licodiedoff, S., Frizon, C.N., Ribani, R.H. and dos Santos, G.G. 2013. Consumer perceptions, attitudes and acceptance of new and traditional mate tea products. **Food Research International** 53(2): 801–807.

Goławska, S., Łukasik, I., Chojnacki, A.A. and Chrzanowski, G. 2023. Flavonoids and phenolic acids content in cultivation and wild collection of European cranberry bush *Viburnum opulus* L. **Molecules** 28(5): 2285.

Kaewpetch, K., Yolsuriyan, S., Disayathanoowat, T., Phokasem, P., Jannu, T., Renaldi, G. and Samakradhamrongthai, R.S. 2024. Influence of gelatin and propolis extract on honey gummy jelly properties: Optimization using D-optimal mixture design. **Gels** 10(4): 282.

Kamil, R.Z., Fadhila, F.H., Dea, A., Rahayu, E.S. and Hartiningsih, S. 2023. The shelf-life, microbiology quality, and characteristic changes of probiotic *Lactobacillus plantarum* Dad-13 milk jelly candy during storage. **Jurnal Teknik Pertanian Lampung** 12(4): 899-908.

Lin, H.T.V., Tsai, J.S., Liao, H.H. and Sung, W.C. 2023. The effect of hydrocolloids on penetration tests and syneresis of binary gum gels and modified corn starch–gum gels. **Gels** 9(8): 605.

Lin, H.T.V., Tsai, J.S., Liao, H.H. and Sung, W.C. 2025. Effect of hydrocolloids on penetration tests, sensory evaluation, and syneresis of milk pudding. **Polymers** 17(3): 300.

Meilgaard, M.C., Civille, G.V., Carr, B.T. and Osdoba, K.E. 2025. **Sensory Evaluation Techniques** (6th ed.). CRC Press, Boca Raton.

Ministry of Public Health. 2024. **Notification of the Ministry of Public Health** No. 450 B.E. 2567.

Mizrahi, S. 2010. Syneresis in food gels and its implications for food quality, pp. 324–348. *In* Skibsted, L.H., Risbo, J. and Andersen, M.L., eds. **Chemical Deterioration and Physical Instability of Food and Beverages.** Woodhead Publishing, Israel.

Molla, M.M., Sabuz, A.A., Khan, M.H.H., Chowdhury, M.G.F., Miaruddin, M., Alam, M. and Khatun, A. 2022. Effect of honey and lemon juice on the physicochemical, nutritional, microbial and antioxidant properties of guava–pineapple jelly during storage periods. **Discover Food** 2(1): 31.

Na Ayutthaya, K.T. and Putduang, N. 2016. The product development of healthy cereal jelly. **Journal of Food Technology, Siam University** 11(1): 13-20.

Nunta, R., Khemacheewakul, J., Sommanee, S., Mahakuntha, C., Chompoo, M., Phimolsiripol, Y., Jantanasakulwong, K., Kumar, A. and Leksaeasdi, N. 2023. Extraction of gymnemic acid from *Gymnema inodorum* (Lour.) Decne. leaves and production of dry powder extract using maltodextrin. **Scientific Reports** 13: 11193.

Petcharat, T., Chaijan, M., Indriani, S., Karnjanapratum, S., Nirmal, N., Singh, J., Nairfana, I. and Nalinanon, S. 2025. Physicochemical, sensorial and calcium bioavailability of jelly prepared using fish gelatin in combination with furcellaran and calcium L-threonate. **Gels** 12(1): 26.

Putri, S., Marliyati, S.A. and Setiawan, B. 2025. Shelf-life estimation of jelly drink formulated with bay leaf (*Syzygium polyanthum*) and guava juice (*Psidium guajava*). *In* **BIO Web of Conferences** 153, 03001. EDP Sciences.

Qiu, Y., Zhou, Y., Chang, Y., Liang, X., Zhang, H., Lin, X., Qing, K., Zhou, X. and Luo, Z. 2022. The effects of ventilation, humidity, and temperature on bacterial growth and bacterial genera distribution. **International Journal of Environmental Research and Public Health** 19(22): 15345.

Saraboot, N., Huaisan, K. and Nitisuk, P. 2018. Effects of gellings agents on texture, syneresis and sensory characteristics of Mahachanok jam. **RMUTP Research Journal** 12(2): 73-82.

Schumacher, A., Lingle, C. and Silbernagel, K.M. 2023. 3M™ Petrifilm™ yeast and mold count plate for the enumeration of yeasts and molds: AOAC official method 2014.05. **Journal of AOAC International** 106(2): 401–411.

Sinchaipanit, P., Peasura, N., Sangsuriyawong, A. and Disnil, S. 2022. Testing the shelf-life of food products under accelerated temperature. **Burapha Science Journal** 1930-1949.

Suwan, P. and Suwannakam, M. 2021. Development and shelf life evaluation of crispy banana-flavored yogurt. **Burapha Science Journal** 26(3): 1692-1706.

Tarlak, F. 2023. The use of predictive microbiology for the prediction of the shelf life of food products. **Foods** 12(24): 4461.

Tiamyom, K., Sirichaiwetchakoon, K., Hengpratom, T., Kupittayanant, S., Srisawat, R., Thaeomor, A. and Eumkeb, G. 2019. The effect of *Cordyceps sinensis* (Berk.) Sacc. and *Gymnema inodorum* (Lour.) Decne. extracts on adipogenesis and lipase activity in vitro. **Evidence-Based Complementary and Alternative Medicine** 2019: 5370473.

Tiwari, P., Mishra, B.N. and Sangwan, N.S. 2014. Phytochemical and pharmacological properties of *Gymnema sylvestre*: An important medicinal plant. **BioMed Research International** 2014: 830285.

Xiao, M., Liu, S., Jin, H., Xiao, M., Wang, H., Zhang, H. and Dai, Q. 2022. Evaluating freshness loss of green tea with Q10 method and Weibull hazard analysis under accelerated shelf life testing. **Journal of Chemistry** 2022(1): 2955839.

Recent Science and Technology 2026, Vol. 18(3): e269582

Recent Science and Technology

Journal homepage: https:// www.tci-thaijo.org/index.php/rmutsvrj/index

ISSN: 3057-0786 (Online)

Research Article

Integrated Earthquake-Induced Stability Assessment of Lam Chae Earth Dam using Sentinel-1 DInSAR and Field Instrumentation

Yanisa Klongchang [a], Soravis Supavetch [a] and Anuphao Aobpaet [a *]

[a] *Department of Civil Engineering, Faculty of Engineering, Kasetsart University, Bangkok 10900, Thailand.*

Article history:

Received: 2025-10-20
Revised: 2026-07-28
Accepted: 2026-07-31

Keywords:

DInSAR;
Sentinel-1;
Earthquake monitoring;
Dam safety;
Earth dam

ABSTRACT

The Mw 7.7 Myanmar earthquake of 28 March 2025 generated ground shaking across several regions of Thailand, including Nakhon Ratchasima Province, where the Lam Chae Earth Dam is located. Rapid and reliable assessment of dam stability following seismic events is essential for ensuring public safety and supporting reservoir operation. In this context, Sentinel-1 Differential Interferometric Synthetic Aperture Radar (DInSAR) provides spatially continuous deformation measurements over large areas and complements conventional point-based field monitoring instruments. This study presents an integrated assessment of earthquake-induced dam stability using Sentinel-1 DInSAR together with field instrumentation, including inclinometers and piezometers. Sentinel-1 synthetic aperture radar (SAR) images acquired during the pre-seismic, co-seismic, and post-seismic periods were processed to derive line-of-sight (LOS) surface deformation and compared with in-situ monitoring data. The DInSAR analysis revealed a maximum cumulative LOS displacement ranging from approximately - 27 to - 30 mm during the co-seismic period, whereas inclinometer measurements indicated internal deformation ranging from - 1.258 to - 3.980 mm. Piezometer observations confirmed that pore-water pressure remained within the normal operating range throughout the monitoring period. Although DInSAR measurements are subject to uncertainties associated with atmospheric delay, temporal decorrelation, and vegetation-induced coherence loss, the observed deformation patterns were consistent with field measurements, providing complementary evidence for assessing dam behaviour. This study demonstrates the applicability of integrating satellite-based DInSAR with conventional geotechnical instrumentation for post-earthquake dam safety assessment in Thailand, where such integrated applications remain limited. The integrated interpretation of satellite- and ground-based monitoring indicates that the Lam Chae Earth Dam remained structurally stable following the earthquake and provides a practical framework for long-term structural health monitoring of earth dams.

© 2026 Klongchang, Y., Supavetch, S. and Aobpaet, A. Recent Science and Technology published by Rajamangala University of Technology Srivijaya

1. Introduction

Earth dams are among the most important civil infrastructures for water resources management, providing irrigation water, domestic water supply, flood mitigation, and hydropower generation. Because these structures retain large volumes of water, their structural integrity is directly associated with downstream public safety, environmental protection, and economic sustainability. Throughout their service life, earth dams are subjected to various external loads, including floods, earthquakes, and climate-related hazards, as well as internal forces such as hydrostatic pressure and self-weight. These factors may gradually induce deformation, material deterioration, or structural instability if not properly monitored. Therefore, continuous monitoring and periodic stability assessment are fundamental components of modern dam safety management.

Among these hazards, earthquakes are of particular concern because seismic loading can induce settlement, cracking, internal deformation, liquefaction, and changes in pore-water pressure within earth-fill dams. Although many modern dams

* **Corresponding author.**

E-mail address: *fengaha@ku.ac.th*

Cite this article as:

Klongchang, Y., Supavetch, S. and Aobpaet, A. 2026. Integrated Earthquake-Induced Stability Assessment of Lam Chae Earth Dam using Sentinel-1 DInSAR and Field Instrumentation. **Recent Science and Technology** 18(3): e269582.

https://doi.org/10.65411/rst.2026.269582

are designed to resist seismic loading, post-earthquake assessment remains essential to verify structural integrity, identify potential damage, and support operational decision-making. Consequently, integrating multiple sources of monitoring data has become increasingly important for improving the reliability of dam safety evaluation, particularly after significant seismic events.

On 28 March 2025, the Mw 7.7 Myanmar earthquake generated ground shaking across several regions of Thailand, including Nakhon Ratchasima Province, where Lam Chae Earth Dam is located. Although the seismic intensity at the dam site was approximately Modified Mercalli Intensity (MMI) III, representing weak shaking, engineering assessment was still considered necessary because even low-to-moderate seismic loading may influence the deformation behaviour of earth-fill embankments. Lam Chae Dam is a homogeneous rolled earth-fill embankment constructed across the Lam Chae River. The dam has a maximum height of 29.50 m, a crest length of 2,400 m, and a storage capacity of approximately 275 million m^3, supplying irrigation water to Khon Buri District and surrounding agricultural areas while also supporting fisheries, public water supply, and tourism. Owing to its strategic importance, evaluating the dam's structural response following the earthquake is essential for ensuring long-term operational safety.

Conventional dam safety monitoring primarily relies on field instrumentation, including inclinometers, piezometers, and water level indicators. These instruments provide accurate point-based measurements of internal deformation and pore-water pressure; however, they are limited in spatial coverage and cannot directly represent deformation over the entire dam surface. Satellite-based Differential Interferometric Synthetic Aperture Radar (DInSAR) has therefore emerged as an effective complementary technique because it enables spatially continuous deformation monitoring over large areas without requiring direct site access. When integrated with conventional geotechnical instrumentation, DInSAR provides a more comprehensive understanding of dam behaviour by combining wide-area surface deformation with internal structural responses.

Previous studies have demonstrated the successful application of InSAR techniques for monitoring deformation of dams and other geotechnical infrastructures in various countries. Satellite observations have been applied to monitor deformation at the Pertusillo Dam, Mosul Dam, Hoover Dam, and several reservoirs in Europe and Asia, demonstrating the capability of InSAR to detect long-term deformation and complement conventional field monitoring. Recent studies have also highlighted the advantages of integrating satellite observations with in-situ measurements to improve the interpretation of structural behaviour and support infrastructure safety assessment. Nevertheless, most previous investigations have focused on long-term deformation monitoring under normal operating conditions, whereas studies addressing earthquake-induced deformation of earth dams using integrated satellite and field observations remain relatively limited, particularly in Southeast Asia and Thailand. Furthermore, operational frameworks that combine Sentinel-1 DInSAR with conventional geotechnical instrumentation for continuous dam safety assessment and post-earthquake monitoring have not yet been widely established.

Therefore, this study aims to evaluate the earthquake-induced stability of Lam Chae Earth Dam by integrating Sentinel-1 DInSAR observations with inclinometer and piezometer measurements. Sentinel-1 SAR images acquired during the pre-seismic, co-seismic, and post-seismic periods were analysed to estimate surface deformation and compared with field monitoring data to evaluate the dam's structural response. The novelty of this study lies in the integration of satellite-based DInSAR with conventional geotechnical instrumentation for post-earthquake assessment of an earth-fill dam in Thailand. This integrated approach provides a more comprehensive interpretation of both surface and internal deformation and demonstrates a practical framework for long-term dam safety monitoring and structural health assessment following seismic events.

1.1 Literature review

Theory

1. The Differential Interferometric Synthetic Aperture Radar (DInSAR) technique is an advanced form of the Interferometric Synthetic Aperture Radar (InSAR) method. It is based on comparing the phase of radar backscattered signals from two satellite SAR images acquired over the same area at different times, in order to analyze the change in the distance between the satellite and the Earth's surface along the Line of Sight (LOS) direction. This technique is capable of detecting ground surface displacements at the millimeter scale.

The DInSAR method determines the phase difference after removing the topographic contribution, thereby isolating only the displacement caused by physical processes. The fundamental equation of DInSAR is expressed as:

$$\Delta d = \frac{\lambda \Delta \phi}{4\pi} \quad (1)$$

where λ represents the radar wavelength, $\Delta\phi$ denotes the phase difference of the backscattered signals between the two acquisition times, and Δd is the LOS displacement.

2. The Sentinel Application Platform (SNAP) is a free and open-source software developed by the European Space Agency (ESA) for the processing and analysis of satellite data. The platform provides a comprehensive suite of tools for Synthetic Aperture Radar (SAR) data processing, encompassing key procedures such as orbit file application, subsetting,

interferogram formation, topographic phase removal, filtering, and phase unwrapping.

These integrated tools enable users to systematically derive Line-of-Sight (LOS) displacement results from SAR imagery, facilitating a standardized and reproducible workflow for interferometric data processing without any licensing cost.

3. Dam instrumentation refers to a series of engineering instruments designed to monitor, observe, and evaluate the behavior of dams during both the construction and operational phases. The primary objective of such instrumentation is to ensure continuous assessment of the dam's stability and safety. These instruments record physical changes occurring within the dam structure, such as ground displacement, pore-water pressure, and reservoir water level, which are critical parameters for evaluating dam stability and preventing potential failures in earthfill structures.

The main instruments utilized in this study include: Inclinometer, which measures internal horizontal and vertical displacements within the dam body by detecting changes in the inclination angle of a casing embedded inside the dam. The variation in inclination is then converted into the actual displacement values.

Piezometer, which monitors pore-water pressure within the soil to evaluate the groundwater level and internal drainage condition of the dam. An unusual increase in pore pressure may indicate excess hydraulic pressure, which could affect the stability of the earth dam.

Water Level Indicator, which records variations in the reservoir water level to examine its relationship with pore-water pressure and the overall deformation behavior of the dam.

This integrated monitoring system provides essential data for assessing the dam's performance and supports early detection of abnormal conditions that may compromise structural safety.

1.2 Related works

1. Cigna *et al*. (2019) conducted a study entitled "Satellite InSAR Monitoring of Dam Stability: A Review of Cases and Approaches." The research explored the potential of differential and time-series InSAR techniques for monitoring dam deformation and related structural components. The authors proposed an operational monitoring framework to support dam management authorities and emphasized the importance of integrating field-based measurements to validate and enhance the reliability of InSAR-derived results.

2. Ruiz-Armenteros *et al*. (2020) conducted a study entitled "DInSAR Monitoring of Mosul Dam Deformation and Its Correlation with Water Level Variations." The research applied the Differential Interferometric Synthetic Aperture Radar (DInSAR) technique to analyze deformation at the Mosul Dam, which is located in an area susceptible to seismic activity and gypsum dissolution. The results revealed surface displacements consistent with ground-based observations, confirming that DInSAR is an effective tool for detecting small-scale structural changes in dams, even under complex topographic and geological conditions.

3. Wang *et al*. (2020) conducted a study entitled "Application of Sentinel-1 DInSAR in Assessing Seismic Deformation of Hydropower Dams." This research employed the DInSAR technique to detect deformation of dams and reservoirs following seismic events. The results revealed small but significant deformations that correlated with seismic vibrations. The authors also proposed a practical framework for organizing co-seismic and post-seismic image pairs, enabling clearer temporal interpretation of deformation patterns.

4. Liu *et al*. (2021) conducted a study entitled "Monitoring of Reservoir Dams in Asia Using Sentinel-1 InSAR Time-Series Analysis." The research applied time-series InSAR techniques, including Small Baseline Subset (SBAS) and Persistent Scatterer (PS) methods, to monitor multiple dams across Asia. The results demonstrated that millimeter-scale annual displacements could be effectively detected and correlated with reservoir water level variations. The study highlighted that Sentinel-1 data are highly suitable for establishing regional-scale dam monitoring systems, supporting continuous assessment of dam stability.

5. Darvishi *et al*. (2021) conducted a study entitled "Correlation Between Groundwater Level Changes and Ground Deformation Using InSAR: Case Study of Lake Mead and Hoover Dam, USA." The research employed time-series InSAR analysis based on Sentinel-1 satellite data to investigate the relationship between reservoir water-level variations and ground deformation around Lake Mead and the Hoover Dam in the United States. The results indicated that a decline in reservoir water levels caused uplift of the surrounding crust at a rate of several millimeters per year, reflecting the geological response to changes in subsurface pore-water pressure. This study demonstrated the strong potential of InSAR techniques for monitoring the interaction between hydrological changes and surface deformation in dam environments.

6. Ladawadee *et al*. (2022) conducted a study entitled "A Study of the Relationship Between Groundwater Pressure Change and Land Subsidence Rate Using InSAR Time-Series Technique." The research investigated land subsidence in Nakhon Pathom and Samut Sakhon Provinces, Thailand, by analyzing Sentinel-1 satellite data through the InSAR time-series technique. The results revealed that most areas within the study region experienced ground subsidence. When compared with groundwater level data, it was found that areas with intensive groundwater extraction exhibited higher subsidence rates. The analysis confirmed a strong correlation between groundwater pressure variations and land deformation detected by InSAR, demonstrating the consistency and reliability of the InSAR-based monitoring approach.

7. Soralump *et al*. (2024) applied Sentinel-1 DInSAR to monitor slope movement in the Doi Chang landslide area, northern Thailand. The results showed LOS displacement rates

of –10 to –25 mm/year, consistent with inclinometer data and correlated with rainfall patterns. The study confirmed that Sentinel-1 DInSAR is effective for detecting small-magnitude ground deformation in complex mountainous terrain and can support landslide early-warning and risk-management systems.

2. Materials and Methods

2.1 Study area

Lam Chae Earth Dam is located in Khon Buri District, Nakhon Ratchasima Province, northeastern Thailand (Figure 1). The dam was constructed across the Lam Chae River as part of the Lam Mun River Basin Development Project to provide irrigation water, domestic water supply, flood mitigation, fisheries, and environmental conservation. Operated by the Royal Irrigation Department (RID), Lam Chae Dam is one of the major water resource infrastructures supporting agricultural production and socio-economic development within the region. Owing to its strategic importance, continuous structural monitoring and periodic safety assessment are essential to ensure long-term operational reliability and to minimize potential risks associated with structural deterioration and natural hazards.

Lam Chae Dam is a homogeneous rolled earth-fill embankment with a maximum height of 29.50 m, a crest length of approximately 2,400 m, and a total storage capacity of approximately 275 million m³. As with other earth-fill dams, its structural behaviour may be influenced by hydraulic loading, environmental conditions, and external dynamic loading such as earthquakes. Consequently, continuous monitoring of both surface and internal deformation is necessary to support dam safety evaluation and long-term infrastructure management.

On 28 March 2025, a moment magnitude (Mw) 7.7 earthquake occurred in central Myanmar and generated ground shaking across several regions of Thailand, including Nakhon Ratchasima Province, where Lam Chae Dam is located. Although the estimated seismic intensity at the dam site was approximately Modified Mercalli Intensity (MMI) III, corresponding to weak ground shaking, engineering assessment was considered necessary because even low-to-moderate seismic loading may influence the deformation behaviour of earth-fill embankments. Post-earthquake deformation monitoring therefore provides valuable information for verifying structural performance and supporting dam safety management.

This study investigated the deformation behaviour of Lam Chae Earth Dam during the pre-seismic, co-seismic, and post-seismic periods associated with the 28 March 2025 Myanmar earthquake. This temporal classification enabled the evaluation of deformation characteristics before the earthquake, the immediate structural response during the seismic event, and the subsequent evolution of deformation after the earthquake. The post-seismic assessment focused on determining whether any progressive deformation persisted following the earthquake or whether the observed deformation remained stable within the uncertainty of the monitoring measurements, rather than assuming structural recovery or elastic rebound.

To improve the reliability of the assessment, satellite-derived deformation obtained from Differential Interferometric Synthetic Aperture Radar (DInSAR) was integrated with conventional geotechnical monitoring data, including inclinometer measurements, piezometer observations, reservoir water level records, and rainfall data. The combination of spatially continuous satellite observations with point-based field measurements provides complementary information for evaluating both surface and internal deformation of the dam, thereby reducing interpretation uncertainty and improving confidence in the assessment of structural behaviour following the earthquake.

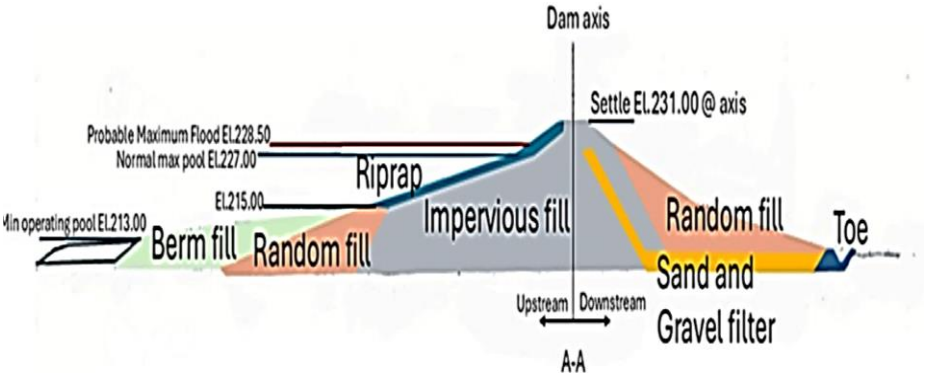


Figure 1 Cross-section of Lam Chae Dam.

2.2 Data used

1. Sentinel-1 Synthetic Aperture Radar (SAR) imagery, provided by the European Space Agency (ESA), was employed as the primary dataset for DInSAR analysis. The SAR images were obtained from the Copernicus Open Access Hub and acquired in the Interferometric Wide (IW) swath mode with dual polarization (VV and VH). All SAR scenes were acquired from the same ascending orbit, Path 99, and Frame 1225, thereby ensuring identical acquisition geometry and complete spatial overlap throughout the study period.

The use of a single orbit direction together with identical path and frame minimizes geometric inconsistencies and reduces the

influence of look-angle differences during interferometric processing. Furthermore, maintaining consistent acquisition geometry helps minimize geometric decorrelation, ensuring that the detected interferometric phase differences primarily represent ground surface deformation rather than variations caused by imaging geometry. Consequently, the reliability and consistency of the displacement measurements are significantly improved.

The Sentinel-1 images were selected to cover the pre-seismic, co-seismic, and post-seismic periods associated with the 28 March 2025 Myanmar earthquake, allowing the temporal evolution of dam deformation to be investigated before, during, and after the seismic event. The acquisition dates and characteristics of all Sentinel-1 datasets used in this study are summarized in Table 1. The spatial coverage of the Sentinel-1 SAR imagery over the study area is illustrated in Figure 2.

Sentinel-1 operates in the C-band with a radar wavelength of approximately 5.6 cm, enabling day-and-night observations under nearly all weather conditions regardless of cloud cover. These capabilities make Sentinel-1 particularly suitable for long-term deformation monitoring of large civil engineering infrastructures, including earth dams, where continuous and spatially extensive observations are required.

Table 1 Time periods of Sentinel-1 SAR data used for pre-, co-, and post-seismic analysis.

Period	Date range (start–end)
Pre-seismic	15-03-2025 – 17-03-2025
Co-seismic	17-03-2025 – 29-03-2025
Post-seismic	29-03-2025 – 10-04-2025
Recent	15-07-2025 – 27-07-2025



Figure 2 Sentinel-1 satellite image coverage area.

2. Field data: Field data were obtained from the dam instrumentation system installed at Lam Chae Dam. The instruments include Inclinometers, Piezometers, and Water Level Indicators, which are used to monitor dam behavior and internal conditions.

Four Inclinometers are installed along the dam crest at chainages 0+600, 1+000, 1+500, and 2+000 km, to measure horizontal displacement and percentage shear strain within the embankment.

The Water Level Indicator records the reservoir water level, which was monitored between January and April 2025.

The Piezometer system consists of two types:

Embedded Piezometers, which directly measure pore-water pressure within the soil, with two borehole locations at chainages 0+730 and 1+180 km, comprising a total of 33 sensors.

Open-end Standpipe Piezometers, which measure water pressure through the water level rise inside the standpipe, installed at six locations along the dam crest 0+500, 0+750, 0+925, 1+500, 1+820, and 1+900 km with a total of 12 sensors.

Each location includes instruments installed at both the embankment and foundation levels. The layout and cross-sectional arrangement of these instruments are illustrated in Figures 3, 4, and 5.

The overall methodology adopted in this study is illustrated in Figure 6. The workflow consists of four major stages: (1) acquisition and preprocessing of Sentinel-1 SAR imagery, (2) DInSAR processing using SNAP version 12, (3) collection and analysis of field monitoring data, and (4) integration of satellite-derived surface deformation with conventional geotechnical observations for post-earthquake dam stability assessment.

1. DInSAR data processing: Sentinel-1 SAR images were processed using the Sentinel Application Platform (SNAP version 12) developed by the European Space Agency (ESA). A conventional Differential Interferometric Synthetic Aperture Radar (DInSAR) workflow was implemented to estimate Line-of-Sight (LOS) surface deformation associated with the 28 March 2025 Mw 7.7 Myanmar earthquake.

The processing sequence consisted of Apply Orbit File, TOPSAR Split, Back-Geocoding, Enhanced Spectral Diversity, Interferogram Formation, TOPSAR Deburst, Topographic Phase Removal, Goldstein Phase Filtering, phase unwrapping using the Statistical-Cost Network-Flow Algorithm for Phase Unwrapping (SNAPHU), Range-Doppler Terrain Correction, and generation of the final geocoded displacement products.

During the terrain correction stage, the SRTM 3Sec Digital Elevation Model (Auto Download) was employed to remove topographic distortions and geocode the interferometric products. Both DEM resampling and image resampling were performed using the bilinear interpolation method, and the final products were projected into the WGS 84 / UTM Zone 48N coordinate reference system for subsequent spatial analysis.

To improve interferometric phase quality, Goldstein Phase Filtering was applied before phase unwrapping. The filtering parameters consisted of an Adaptive Filter Exponent of 1.0, FFT size of 64, window size of 3, and coherence threshold of 0.2. This filtering process effectively reduced phase noise while preserving the interferometric fringes required for reliable phase unwrapping.

Phase unwrapping was subsequently performed using the SNAPHU algorithm. The wrapped interferometric phase generated in SNAP was exported to SNAPHU for phase

unwrapping and subsequently imported back into SNAP. This procedure converts the wrapped phase into a continuous phase surface, thereby enabling the calculation of Line-of-Sight (LOS) displacement.

The interferometric coherence generated during processing was used as a quality indicator to evaluate the reliability of the interferometric phase prior to phase unwrapping. Areas exhibiting relatively low coherence, particularly those covered by dense vegetation, were interpreted cautiously because temporal decorrelation may reduce the accuracy of displacement estimation. Furthermore, atmospheric delay and other interferometric uncertainties were considered during the interpretation of the DInSAR results by comparing the satellite-derived deformation with field monitoring observations.

Finally, the geocoded LOS displacement maps were exported in GeoTIFF format and imported into QGIS for spatial analysis. Surface displacement values corresponding to the locations of the monitoring instruments installed on Lam Chae Earth Dam were extracted for subsequent comparison with field monitoring data.

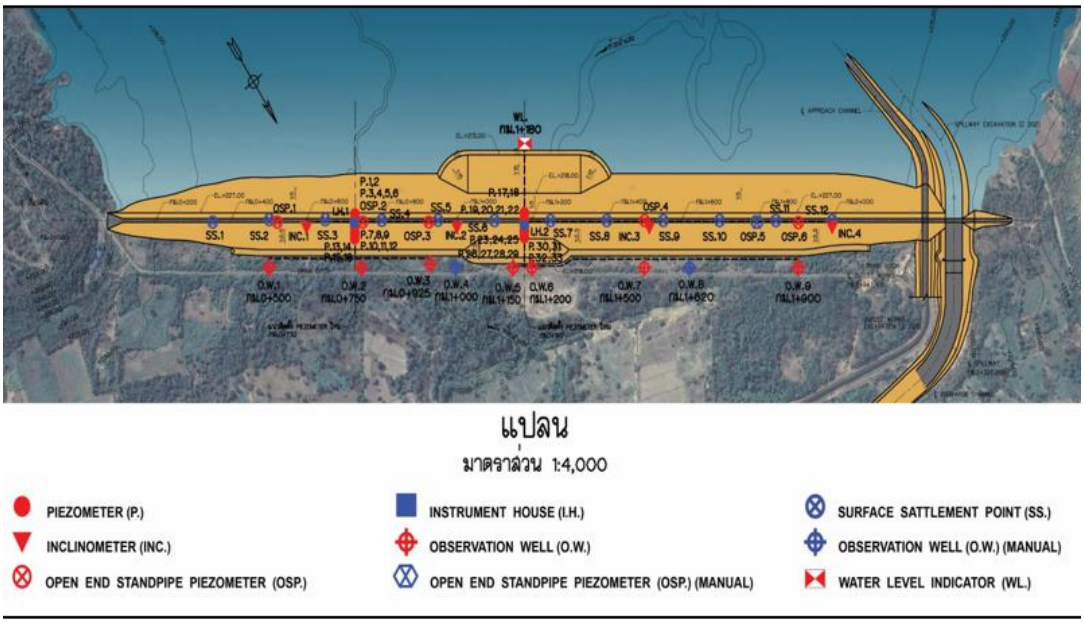


Figure 3 Plan view of Lam Chae Dam instrumentation installation.

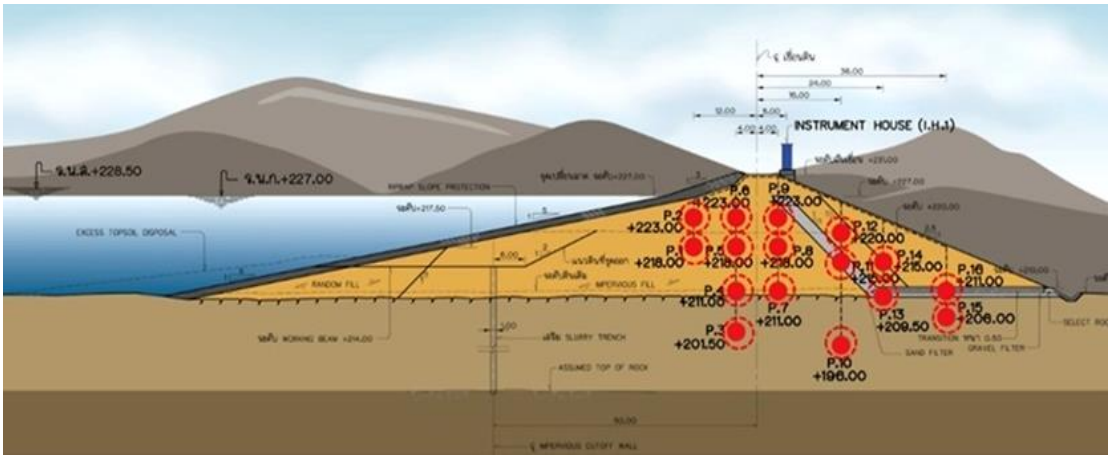


Figure 4 Cross-section of the installation of Piezometer at location 0+730.

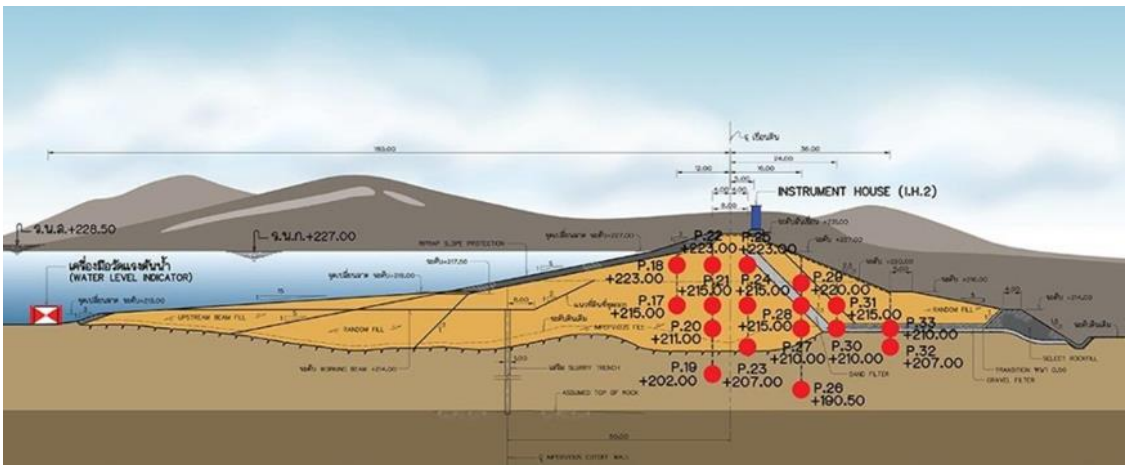


Figure 5 Cross-section of the installation of Piezometer at location 1+180.

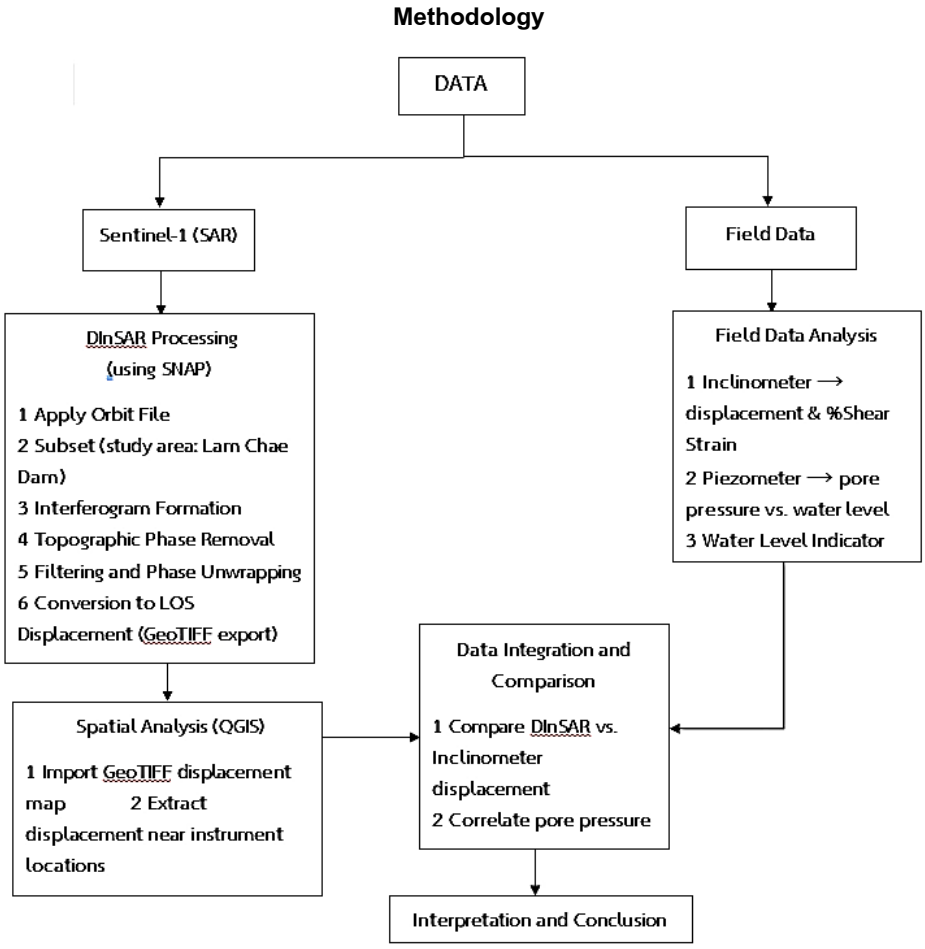


Figure 6 Diagram showing the sequence of research procedures.

2. Field monitoring data analysis: Field monitoring data were obtained from the Dam Safety Division, Royal Irrigation Department (RID), Thailand, and consisted of inclinometer measurements, piezometer observations, and reservoir water level records. These datasets were analysed together with the Line-of-Sight (LOS) displacement derived from the DInSAR analysis to investigate the structural response of Lam Chae Earth Dam during the pre-seismic, co-seismic, and post-seismic periods associated with the 28 March 2025 Mw 7.7 Myanmar earthquake.

Inclinometers installed along the dam crest were used to monitor the internal displacement within the Lam Chae Earth Dam embankment. The displacement values were derived from cumulative movements measured along the A-axis and B-axis, which are two mutually perpendicular directions recorded by the instrument. The displacement changes along each axis are denoted as ΔA (displacement change along the A-axis) and ΔB (displacement change along the B-axis).

Since the two axes are orthogonal, the resultant displacement at each measurement depth was determined from the vector

sum of the displacement components, representing the magnitude of the deviation of the inclinometer casing from its original vertical alignment.

The inclinometer data collected between January and April 2025 were analysed together with the DInSAR-derived Line-of-Sight (LOS) displacement. In addition, the percentage shear strain (% Shear Strain) recorded by the inclinometer was analysed to evaluate variations in embankment deformation during the pre-seismic, co-seismic, and post-seismic periods. For consistency with the DInSAR observations, the analysis focused on Depth Level #1, corresponding to the shallowest monitoring interval nearest to the ground surface.

Figure 7 presents an example of the inclinometer monitoring data used in this study.

Reservoir water level records covering the period from January to April 2025 were analysed to evaluate hydraulic loading conditions throughout the monitoring period. The temporal variation in reservoir water level was subsequently compared with pore-water pressure measurements to support the interpretation of hydraulic conditions within the embankment and their potential influence on the observed deformation behaviour.

Piezometer Monitoring Pore-water pressure within the embankment was monitored using two types of piezometers: embedded piezometers and open-end standpipe piezometers.

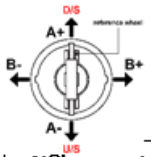
Four embedded piezometer heads (P.5, P.8, P.21, and P.24) were selected for analysis. Piezometers P.5 and P.8 are located at chainage 0+730 km, whereas P.21 and P.24 are located at chainage 1+180 km, representing both the dam core and downstream sections.

In addition, four open-end standpipe piezometers located near the inclinometer stations at chainages 0+750, 0+925, 1+500, and 1+900 km were included in the analysis, resulting in a total of eight piezometer monitoring points.

The pore-water pressure data collected between January and April 2025 were analysed together with the corresponding reservoir water level records. Time-series graphs were subsequently constructed to examine the relationship between pore-water pressure and reservoir water level, thereby supporting the interpretation of the hydraulic response of the embankment and the stability condition of Lam Chae Earth Dam throughout the monitoring period 2.

Monitoring Record

(In-Place Inclinometer)



Monitoring Data			Horizontal Displacement		% Shear strain	
			A-xis	B-xis	A-xis	B-xis
Sensor ID	Elevation (m MSL)	Depth (m)	Cumulative Displacement Relative to Initial Reading (mm)	Cumulative Displacement Relative to Initial Reading (มม.)	(%)	(%)
	+227.499	0.00				
INC.1#1	+226.159	1.34	-31.9110	8.5970	1.7240	-0.2410
INC.1#2	+222.659	4.84	-92.2500	18.0410	-0.3080	0.0340
INC.1#3	+219.159	8.34	-81.3370	17.1200	-0.3490	0.0270
INC.1#4	+215.659	11.84	-69.1600	15.9650	-0.2890	0.0270
INC.1#5	+212.159	15.34	-58.8700	15.2260	-0.4590	0.0370
INC.1#6	+208.659	18.84	-43.0530	13.7410	-0.4890	0.0760
INC.1#7	+205.159	22.34	-25.6610	11.5840	-0.2150	0.0970
	+193.239	34.26	0.0000	0.0000	0.0000	0.0000

Figure 7 Example of data recorded from the Inclinometer instrument.

3. Data integration: A comparative analysis was performed by plotting graphs of displacement values obtained from the DInSAR technique and inclinometer measurements to examine the consistency and correlation of displacement trends between the two datasets.

3. Results and Discussion

1. DInSAR displacement analysis results: The DInSAR analysis successfully detected spatial and temporal variations in the Line-of-Sight (LOS) displacement of Lam Chae Earth Dam before, during, and after the 28 March 2025 Mw 7.7 Myanmar earthquake. The reported values represent cumulative LOS

displacement for each observation period derived from Sentinel-1 interferometric image pairs. The spatial distribution of cumulative LOS displacement during the pre-seismic, co-seismic, post-seismic, and recent periods is presented in Figure 8.

During the pre-seismic period (5–17 March 2025), the cumulative LOS displacement remained relatively small, ranging from approximately −10 to −15 mm along most sections of the dam crest, indicating relatively stable surface conditions before the earthquake. In contrast, the co-seismic period (17–29 March 2025) exhibited the largest cumulative LOS displacement, ranging from approximately −27 to −32 mm, indicating that the earthquake produced a measurable surface deformation response. Compared with the pre-seismic observations, the co-seismic interferometric results clearly demonstrate an increase in deformation magnitude associated with the occurrence of the earthquake. These findings indicate that DInSAR successfully captured the transient response of the dam surface to seismic loading (Figure 8).

During the post-seismic period (29 March–10 April 2025), the cumulative LOS displacement decreased to approximately −5 to −10 mm, which is considerably smaller than that observed during the co-seismic period. The reduction in displacement magnitude indicates that the observable surface deformation diminished after the earthquake. However, this reduction should not be interpreted as evidence of complete structural recovery. Instead, the post-seismic observations indicate that no progressive increase in surface deformation was detected following the earthquake, and the measured displacement gradually approached the baseline level observed before the seismic event. The deformation pattern remained generally consistent during the recent period (15–27 July 2025), with no evidence of continuously increasing displacement, suggesting that the deformation induced by the earthquake did not continue to develop during the subsequent monitoring period (Figure 8).

To further evaluate whether the deformation behaviour observed at Lam Chae Earth Dam was consistent with that of other earth-fill dams subjected to seismic loading, an additional case study was conducted using Mae Kuang Udom Thara Dam, Chiang Mai Province, following the 20 October 2022 Mw 4.1 earthquake. The same DInSAR processing workflow was applied to analyse cumulative LOS displacement during the pre-seismic, co-seismic, post-seismic, and recent periods. As shown in Figure 9, the deformation profiles of Mae Kuang Dam exhibited a temporal pattern similar to that observed at Lam Chae Dam. The largest cumulative LOS displacement occurred during the co-seismic period (approximately −51 to −53 mm), followed by a substantial reduction during the post-seismic period, while the recent observations approached the deformation level recorded before the earthquake. No evidence of progressive deformation was identified after the seismic event.

The comparable deformation behaviour observed at both Lam Chae Earth Dam and Mae Kuang Udom Thara Dam suggests that DInSAR is capable of capturing the transient surface response of earth-fill dams to earthquake loading. In both case studies, the largest cumulative LOS displacement occurred during the co-seismic period, whereas the displacement magnitude decreased during the post-seismic period without exhibiting a continuous increase thereafter. These observations indicate that the detected deformation represents a temporary response to seismic loading rather than progressive structural deterioration. Nevertheless, DInSAR measurements should be interpreted together with field monitoring observations because the technique measures deformation only along the satellite Line-of-Sight (LOS) direction and may be affected by atmospheric delay, vegetation-induced decorrelation, and other interferometric uncertainties.

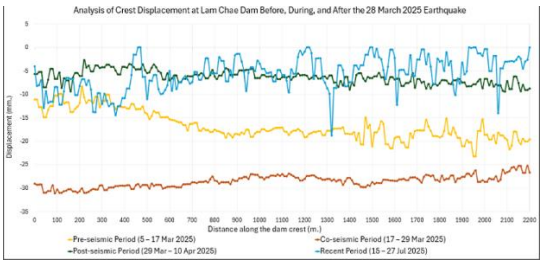


Figure 8 Analysis of the displacement of Lam Chae Dam using data from the DInSAR technique before, during, and after the earthquake event on March 28, 2025.

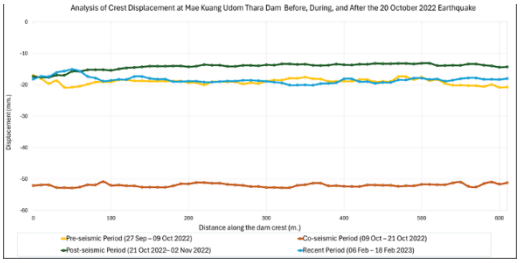


Figure 9 Analysis of the displacement of Mae Kuang Udom Thara Dam using data from the DInSAR technique before, during, and after the earthquake event on October 20, 2022.

2. The field monitoring data were analysed to evaluate the internal deformation and hydraulic behaviour of Lam Chae Earth Dam before, during, and after the 28 March 2025 Mw 7.7 Myanmar earthquake. The monitoring system consisted of four in-place inclinometers installed along the dam crest, together with piezometers and reservoir water level measurements. These complementary datasets were used to verify whether the deformation detected by DInSAR was accompanied by significant internal deformation or abnormal changes in pore-water pressure.

The inclinometer measurements indicated that the internal displacement of the dam increased during the co-seismic period but remained relatively small throughout the monitoring period. During the pre-seismic period, the measured displacement

ranged from approximately −0.528 to −1.835 mm, whereas the co-seismic period exhibited the largest displacement, ranging from approximately −1.258 to −3.980 mm. Following the earthquake, the displacement decreased to approximately −0.189 to −1.689 mm, approaching the pre-seismic level (Figure 10). These observations indicate that although the earthquake produced a measurable response within the embankment, no progressive increase in internal deformation was observed after the seismic event.

To further assess the structural response of the embankment, the measured shear strain was evaluated using the inclinometer data. As illustrated in Figure 11, the calculated shear strain remained below 2% for both the A-axis and B-axis throughout the pre-seismic, co-seismic, and post-seismic periods. According to the dam safety criteria adopted by the Royal Irrigation Department, these values remain below the warning threshold, indicating that the internal deformation induced by the earthquake was limited and did not suggest structural instability of the embankment.

The hydraulic response of the dam was evaluated using electric piezometers, open-end standpipe piezometers, and reservoir water level records. The piezometer data exhibited temporal variations that generally followed fluctuations in reservoir water level throughout the observation period. No abrupt increase or anomalous pore-water pressure was detected during or immediately after the earthquake (Figures 12 - 23). Although a gap in the monitoring records occurred between 28 January and 7 March 2025 due to lightning damage to the monitoring system, the available measurements before and after this period showed consistent hydraulic behaviour without evidence of abnormal pressure build-up associated with the earthquake.

Comparison between the piezometer records and the DInSAR observations indicates that, although DInSAR detected the largest cumulative surface displacement during the co-seismic period, the pore-water pressure remained consistent with the long-term hydraulic behaviour of the dam. The absence of abnormal pore-pressure variation suggests that the observed surface deformation was not accompanied by significant changes in seepage conditions or internal hydraulic loading. Consequently, the field monitoring results support the interpretation that the earthquake produced a temporary deformation response while the embankment maintained stable hydraulic performance.

Overall, the field monitoring observations consistently demonstrate that the earthquake generated measurable but limited deformation within Lam Chae Earth Dam. The inclinometer data revealed only small internal displacement, shear strain remained below the engineering warning threshold, and the piezometer measurements showed no abnormal pore-water pressure response. These independent observations collectively indicate that the embankment maintained its structural and hydraulic stability throughout the monitoring period, providing an essential basis for validating the deformation detected by the DInSAR analysis.

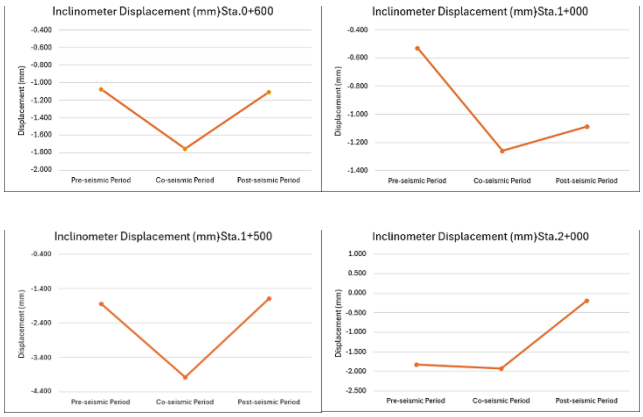


Figure 10 Inclinometer-measured internal displacement at Lam Chae Earth Dam during the pre-seismic, co-seismic, and post-seismic periods: (a) Sta. 0+600, (b) Sta. 1+000, (c) Sta. 1+500, and (d) Sta. 2+000.

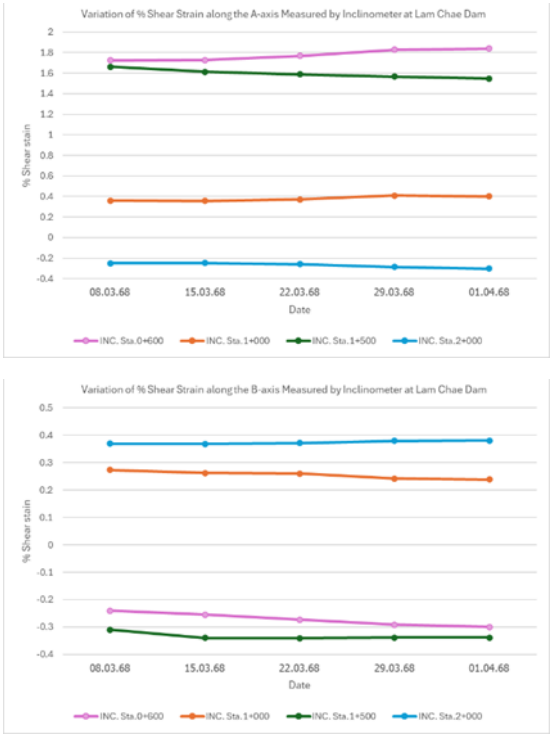


Figure 11 The changes in shear strain (%) along the A axis and B axis.

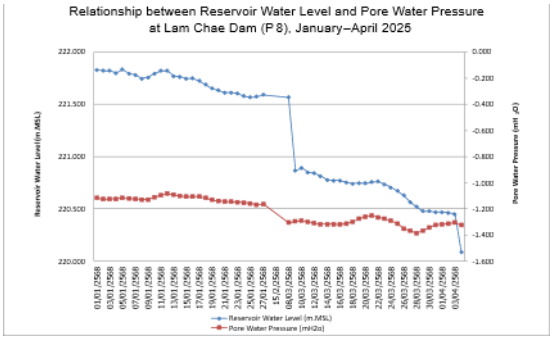


Figure 12 The relationship between the reservoir water level and the pore water pressure at Lam Chae Dam (embedded-type piezometer) during January–April 2025.

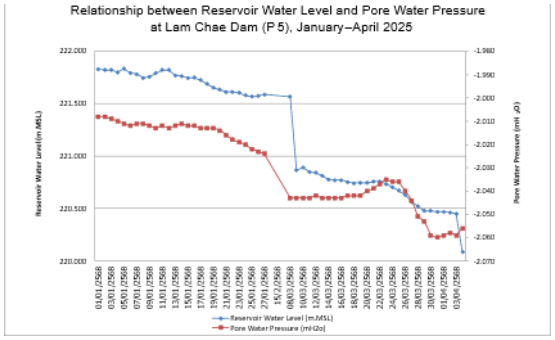


Figure 13 The relationship between the reservoir water level and the pore water pressure at Lam Chae Dam (embedded-type piezometer) during January–April 2025.

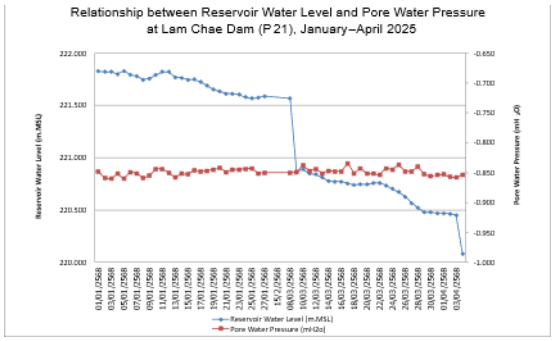


Figure 14 The relationship between the reservoir water level and the pore water pressure at Lam Chae Dam (embedded-type piezometer) during January–April 2025.

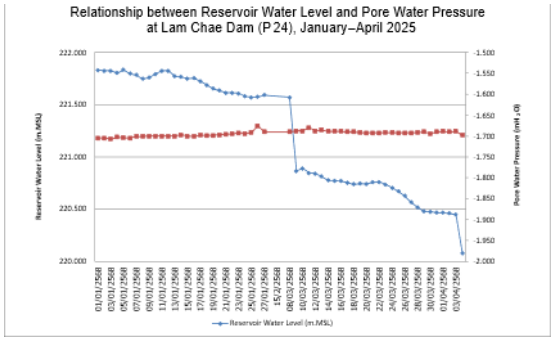


Figure 15 The relationship between the reservoir water level and the pore water pressure at Lam Chae Dam (embedded-type piezometer) during January–April 2025.

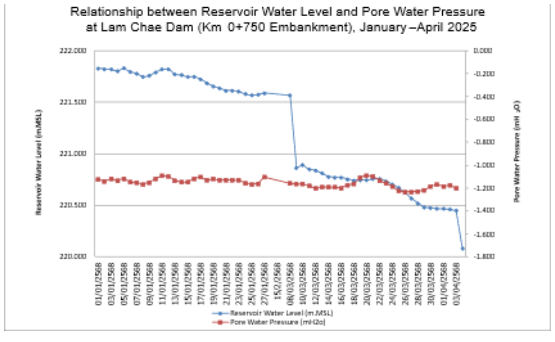


Figure 16 The relationship between the reservoir water level and the pore water pressure at Lam Chae Dam (open end standpipe piezometer) during January-April 2025.

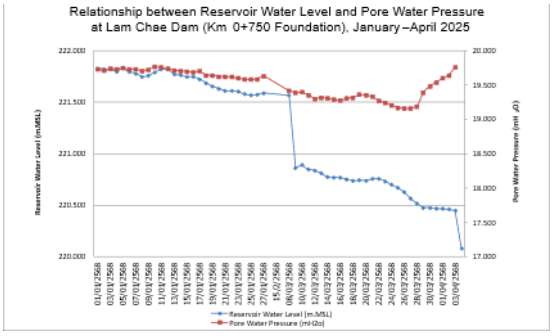


Figure 17 The relationship between the reservoir water level and the pore water pressure at Lam Chae Dam (open end standpipe piezometer) during January-April 2025.

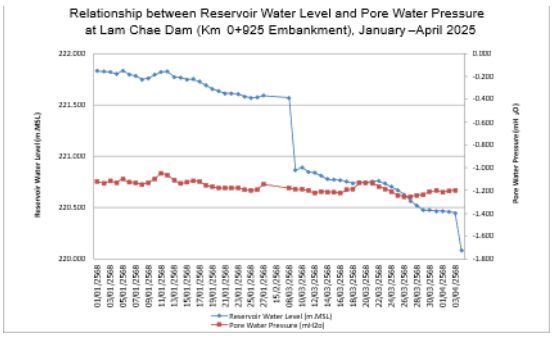


Figure 18 The relationship between the reservoir water level and the pore water pressure at Lam Chae Dam (open end standpipe piezometer) during January-April 2025.

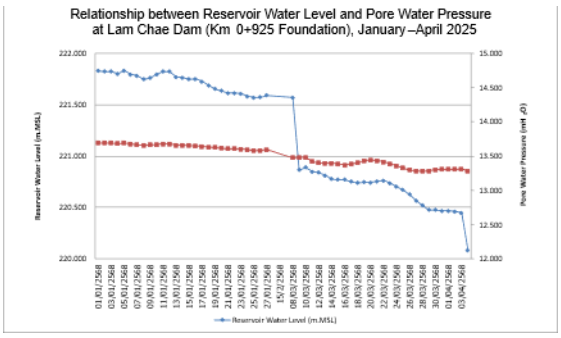


Figure 19 The relationship between the reservoir water level and the pore water pressure at Lam Chae Dam (open end standpipe piezometer) during January-April 2025.

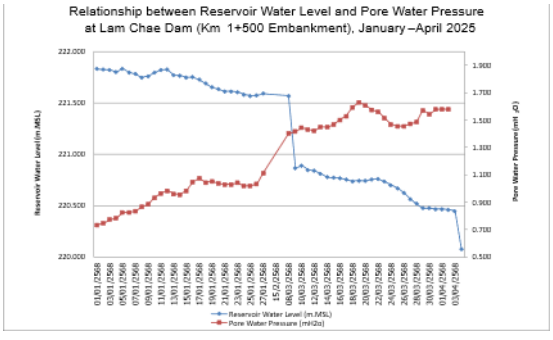


Figure 20 The relationship between the reservoir water level and the pore water pressure at Lam Chae Dam (open end standpipe piezometer) during January-April 2025.

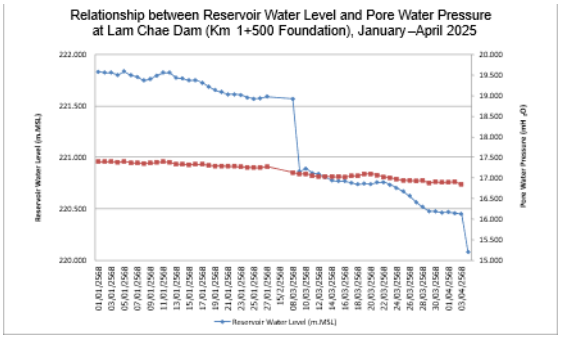


Figure 21 The relationship between the reservoir water level and the pore water pressure at Lam Chae Dam (open end standpipe piezometer) during January-April 2025.

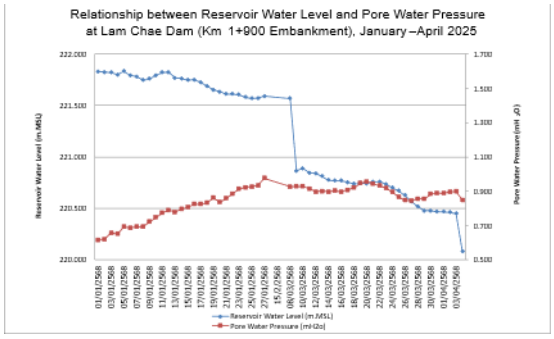


Figure 22 The relationship between the reservoir water level and the pore water pressure at Lam Chae Dam (open end standpipe piezometer) during January-April 2025.

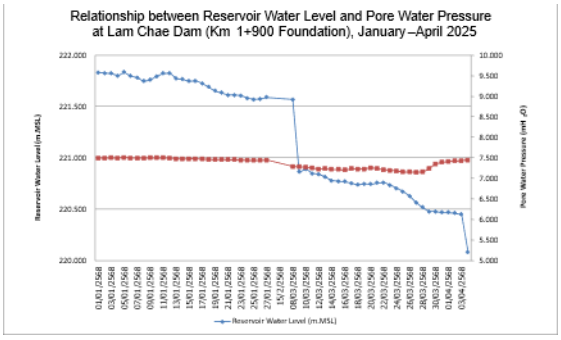


Figure 23 The relationship between the reservoir water level and the pore water pressure at Lam Chae Dam (open end standpipe piezometer) during January-April 2025.

3. To comprehensively evaluate the seismic response of Lam Chae Earth Dam, the DInSAR-derived surface displacement was integrated with field monitoring observations, including inclinometer measurements, shear strain, piezometer records, and reservoir water levels. Since DInSAR and inclinometers measure deformation using different observation principles and units, the displacement data were first normalized using the Min–Max normalization method to facilitate comparison of their temporal deformation patterns. The normalized displacement profiles for each monitoring location are presented in Figure 24 -27 , while the corresponding displacement values are summarized in Table 2.

The comparison demonstrates that both DInSAR and inclinometer measurements exhibit a consistent temporal trend. In all monitoring sections, the largest displacement occurred during the co-seismic period, followed by a reduction during the post-seismic period. Although the displacement magnitude measured by DInSAR (approximately - 27 to - 30 mm) was considerably larger than that measured by the inclinometers (approximately -1.258 to - 3.980 mm), this difference is expected because the two techniques monitor different components of dam behaviour. DInSAR measures cumulative surface deformation along the satellite Line-of-Sight (LOS), whereas inclinometers directly measure internal displacement within the embankment. Consequently, the difference in displacement magnitude reflects the measurement characteristics of each technique rather than inconsistency between the datasets.

To quantitatively evaluate the agreement between the two monitoring techniques, Pearson's correlation coefficient (r) was calculated using the normalized displacement values. High positive correlations were obtained at Sta. 0+600 (r = 0.917) and Sta. 2+000 (r = 0.909), while Sta. 1+500 (r = 0.799) exhibited a moderately strong positive relationship. In contrast, Sta. 1+000 (r = 0.175) showed a relatively weak correlation. The lower correlation at this location may be attributed to radar-specific uncertainties, including vegetation-induced decorrelation, atmospheric delay, geometric differences between the radar measurement point and the inclinometer location, and local surface conditions affecting interferometric coherence. Furthermore, only three observation periods (pre-, co-, and post-seismic) were available for statistical analysis, which limits the interpretation of statistical significance. Therefore, the correlation analysis should be regarded as supporting evidence of temporal consistency rather than conclusive statistical validation.

The integrated interpretation of the field monitoring data further supports the DInSAR observations. Although both DInSAR and inclinometers detected increased deformation during the co-seismic period, the measured shear strain remained below the 2% warning threshold established by the Royal Irrigation Department, and no abnormal increase in pore-water pressure was observed in either the electric or open-end standpipe piezometers. In addition, pore-water pressure variations continued to follow the reservoir water level without abrupt hydraulic responses associated with the earthquake. These observations indicate that the earthquake produced measurable surface and internal deformation but did not trigger progressive internal deformation or abnormal hydraulic behaviour within the embankment.

Overall, the combined use of satellite-based DInSAR and conventional field monitoring provides a more comprehensive assessment of dam behaviour than either technique alone. DInSAR offers spatially continuous measurements of surface deformation over the entire dam crest, whereas field instruments

provide direct information on internal deformation and hydraulic conditions. The agreement between these independent datasets increases confidence in the interpretation that Lam Chae Earth Dam experienced a transient response to earthquake loading, while maintaining overall structural and hydraulic stability throughout the monitoring period. These findings demonstrate that integrating remote sensing observations with conventional geotechnical monitoring represents a reliable and practical approach for post-earthquake dam safety assessment.

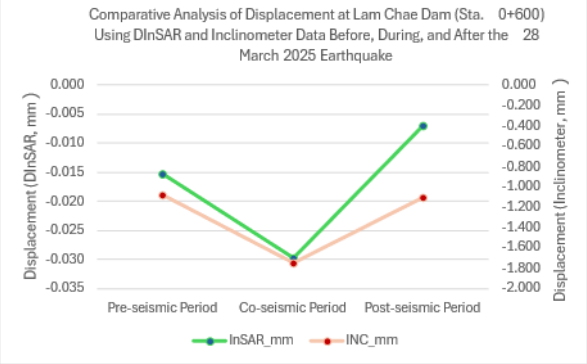


Figure 24 Comparative analysis of displacement values at Lam Chae Dam using data from the DInSAR technique and Inclinometer before, during, and after the earthquake event on March 28, 2025.

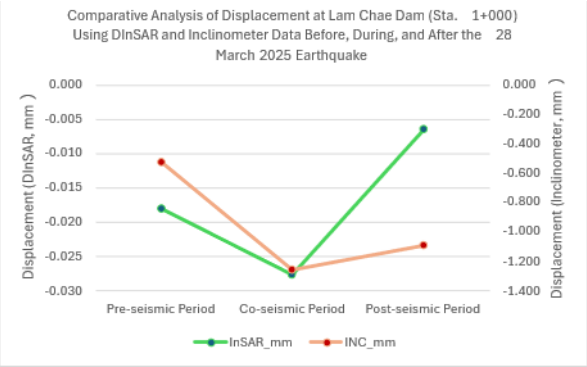


Figure 25 Comparative analysis of displacement values at Lam Chae Dam using data from the DInSAR technique and Inclinometer before, during, and after the earthquake event on March 28, 2025.

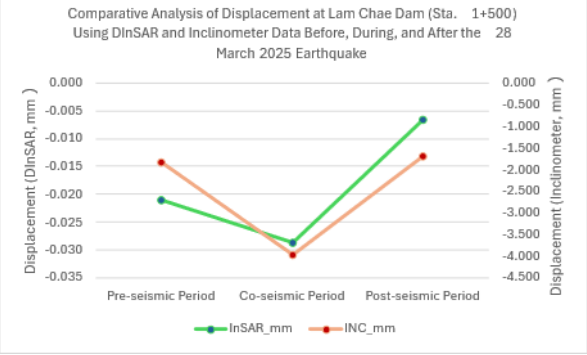


Figure 26 Comparative analysis of displacement values at Lam Chae Dam using data from the DInSAR technique and Inclinometer before, during, and after the earthquake event on March 28, 2025.

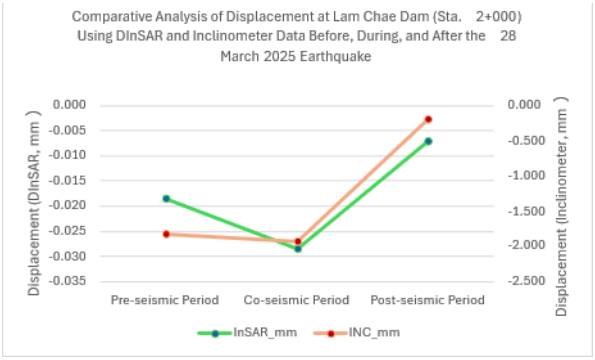


Figure 27 Comparative analysis of displacement values at Lam Chae Dam using data from the DInSAR technique and Inclinometer before, during, and after the earthquake event on March 28, 2025.

Table 2 Comparison of displacement values obtained from DInSAR and inclinometers.

No.	Sta.	Period	DInSAR (mm.)	Inclinometer (mm.)
1.	0+600	Pre-seismic	-15.38	–1.07
		Co-seismic	-29.70	–1.75
		Post-seismic	-7.00	–1.10
2.	1+000	Pre-seismic	-17.98	–0.52
		Co-seismic	-27.68	–1.25
		Post-seismic	-6.51	–1.08
3.	1+500	Pre-seismic	-21.08	–1.83
		Co-seismic	-28.69	–3.98
		Post-seismic	-6.54	–1.68
4.	2+000	Pre-seismic	-18.60	–1.82
		Co-seismic	-28.61	–1.92
		Post-seismic	-7.15	–0.18

4. Conclusion

This study evaluated the post-earthquake behaviour of Lam Chae Earth Dam following the 28 March 2025 Mw 7.7 Myanmar earthquake by integrating Sentinel-1 Differential Interferometric Synthetic Aperture Radar (DInSAR) observations with conventional field monitoring data, including inclinometer measurements, shear strain, piezometer records, and reservoir water levels. Unlike previous studies that primarily relied on either satellite observations or field instrumentation alone, this study demonstrates the value of combining both datasets to provide a more comprehensive assessment of dam performance after a seismic event.

The DInSAR analysis detected measurable surface deformation, with the largest cumulative Line-of-Sight (LOS)

displacement occurring during the co-seismic period (approximately - 27 to - 30 mm), followed by a reduction in displacement magnitude during the post-seismic period. Although the displacement measured by DInSAR was substantially larger than that recorded by the inclinometers, both monitoring techniques exhibited consistent temporal deformation patterns, with the greatest deformation occurring during the earthquake and decreasing afterwards. This agreement indicates that the observed differences primarily reflect the different measurement principles of the two techniques rather than inconsistencies in the monitoring results.

The integrated interpretation of the field monitoring data further supports the DInSAR observations. Inclinometer measurements indicated only limited internal deformation, while the calculated shear strain remained below the 2% warning threshold established by the Royal Irrigation Department. In addition, both electric and open-end standpipe piezometers showed no abnormal increase in pore-water pressure associated with the earthquake, and pore-water pressure variations continued to follow fluctuations in reservoir water level. These independent observations consistently indicate that, although the earthquake produced measurable deformation, no evidence of progressive internal deformation or abnormal hydraulic behaviour was identified, and the dam maintained overall structural and hydraulic stability throughout the monitoring period.

A retrospective DInSAR analysis of Mae Kuang Udom Thara Dam following the 20 October 2022 earthquake revealed a deformation pattern comparable to that observed at Lam Chae Earth Dam, with the largest displacement occurring during the co-seismic period followed by a gradual reduction during the post-seismic period. The consistency between the two case studies suggests that the transient deformation response identified in this study may represent a common behaviour of earth-fill dams subjected to earthquake loading, although further investigations involving additional dams are required to confirm this observation.

Despite its effectiveness, DInSAR remains subject to several limitations, including atmospheric phase delay, temporal and spatial decorrelation caused by vegetation and surface conditions, the temporal resolution of Sentinel-1 acquisitions, and the fact that displacement is measured only along the satellite Line-of-Sight (LOS). Consequently, DInSAR should not be used as a standalone tool for dam safety assessment. Instead, satellite observations should be interpreted together with conventional field monitoring data to improve the reliability of deformation assessment and reduce uncertainties associated with each individual technique.

Overall, this study demonstrates that integrating Sentinel-1 DInSAR with conventional geotechnical monitoring provides a reliable and practical framework for post-earthquake dam safety assessment. The proposed approach enables simultaneous evaluation of spatial surface deformation and internal embankment behaviour, thereby improving confidence in engineering interpretation and supporting long-term structural health monitoring and dam safety management of earth-fill dams in seismic regions.

5. Acknowledgments

The authors would like to express their gratitude to the Copernicus Open Access Hub of the European Space Agency (ESA) for providing the Sentinel-1 satellite imagery and the Sentinel Application Platform (SNAP) software used in this study. Appreciation is also extended to the Dam Safety Division, Office of Irrigation 8, Royal Irrigation Department, for providing the field instrumentation data utilized in the analysis.

6. References

Al-Husseinawi, Y., Li, Z., Clarke, P. and Edwards, S. 2018. Evaluation of the stability of the Darbandikhan Dam after the 12 November 2017 Mw 7.3 Sarpol-e Zahab (Iran–Iraq border) earthquake. **Remote Sensing** 10(9): 1426.

Crosetto, M., Monserrat, O., Cuevas-González, M., Devanthéry, N. and Crippa, B. 2016. Persistent scatterer interferometry: A review. **ISPRS Journal of Photogrammetry and Remote Sensing** 115: 78–89.

Di Martire, D., Iglesias, R., Monells, D., Centolanza, G., Sica, S., Ramondini, M., Pagano, L., Mallorquí, J.J. and Calcaterra, D. 2014. Comparison between differential SAR interferometry and ground measurements data in the displacement monitoring of the earth-dam of Conza della Campania (Italy). **Remote Sensing of Environment** 148: 58–69.

Ferretti, A., Prati, C. and Rocca, F. 2001. Permanent scatterers in SAR interferometry. **IEEE Transactions on Geoscience and Remote Sensing** 39(1): 8–20.

Hooper, A., Segall, P. and Zebker, H.A. 2007. Persistent scatterer interferometric synthetic aperture radar for crustal deformation analysis, with application to Volcán Alcedo, Galápagos. **Journal of Geophysical Research: Solid Earth** 112(B7).

Höser, T. 2018. **Analysing the capabilities and limitations of InSAR using Sentinel-1 data for landslide detection and monitoring.** Ph.D. dissertation., University of Bonn.

Ladawadee, A. and Aobpaet, A. 2022. **InSAR Technique for Land Subsidence Monitoring in Western Bangkok Area and Its Vicinity**. Kasetsart University.

Lavecchia, G., Castaldo, R., De Nardis, R., De Novellis, V., Ferrari, F., Pepe, S., Brozzetti, F., Solaro, G., Cirillo, D. and Bonano, M. 2016. Ground deformation and source geometry of the 24 August 2016 Amatrice earthquake (Central Italy) investigated through analytical and numerical modelling of DInSAR measurements and structural-

geological data. **Geophysical Research Letters** 43(24): 12389–12398.

Martino, S., Fiorucci, M., Marmoni, G., Casaburi, L., Antonellini, B. and Mazzanti, P. 2022. Increase in landslide activity after a low-magnitude earthquake as inferred from DInSAR interferometry. **Scientific Reports** 12: 2686.

Martone, M. 2019. **Onboard quantization for interferometric and multichannel synthetic aperture radar (SAR) systems**. Ph.D. Dissertation, Karlsruhe Institute of Technology.

Othman, A.A., Al-Maamar, A.F., Al-Manmi, D.A.M., Liesenberg, V., Hasan, S.E., Al-Saady, Y.I., Shihab, A.T. and Khwedim, K. 2019. Application of DInSAR-PSI technology for deformation monitoring of the Mosul Dam, Iraq. **Remote Sensing** 11(22): 2632.

Royal Irrigation Department. 2014. **Risk Analysis of Dams and Appurtenant Structures**. Royal Irrigation Department, Bangkok, Thailand. (in Thai)

Royal Irrigation Department. 2015. **Earth Dam Inspection Manual**. Royal Irrigation Department, Bangkok, Thailand. (in Thai)

Royal Irrigation Department. 2016. **Dam Instrumentation Manual**. Royal Irrigation Department, Bangkok, Thailand. (in Thai)

Scaioni, M., Marsella, M., Crosetto, M., Tornatore, V. and Wang, J. 2018. Geodetic and remote sensing sensors for dam deformation monitoring. **Sensors** 18(11): 3682.

Soralump, S. and Mairaing, W. 2007. Dam failure training program on dam safety under normal and emergency conditions, Bangkok, Thailand. (in Thai)

Talgarbayeva, D., Vilyaev, A., Dedova, T., Kuznetsova, O. and Jangulova, G. 2025. InSAR monitoring of dam deformations in a seismically active region of Kazakhstan for identifying precursors of failure. **Frontiers in Earth Science** 13: 1638088.

Thai Meteorological Department. 2020. Fundamental seismology. earthquake observation division, Thai Meteorological Department, Bangkok, Thailand. Technical Document No. 550.34-04-2020. (in Thai)

Ullo, S.L., Addabbo, P., Di Martire, D., Sica, S., Fiscante, N., Cicala, L. and Angelino, C.V. 2019. Application of DInSAR technique to high coherence Sentinel-1 images for dam monitoring and result validation through in situ measurements. **IEEE Journal of Selected Topics in Applied Earth Observations and Remote Sensing** 12(3): 875–890.

U.S. Bureau of Reclamation. 2011. **Draft hydrology, hydraulics, and water management technical report**. U.S. Bureau of Reclamation, Mid-Pacific Region, Sacramento, California.

Wasowski, J. and Pisano, L. 2020. Long-term InSAR, borehole inclinometer, and rainfall records provide insight into the mechanism and activity patterns of an extremely slow urbanized landslide. **Landslides** 17(2): 445–457.

Zalite, K. and Voormansik, K. 2016. Differential and persistent scatterer SAR interferometry. In Proceedings of Tartu Observatory Space Research Center.

Recent Science and Technology 2026, Vol. 18(3): e272651

Recent Science and Technology

Journal homepage: https:// www.tci-thaijo.org/index.php/rmutsvrj/index

ISSN: 3057-0786 (Online)

Research Article

Natural Rubber Foam for Modular Acoustic Pods: Comparative Acoustic Performance and Full-Scale Prototype Performance Assessment

Natdanai Pratoom [a] and Nattapon Uthaipan [b *]

[a] *Physical Systems and Environment Division, Prince of Songkla University, Songkhla 90110, Thailand.*

[b] *Rubber Engineering Program, Department of Interdisciplinary Engineering, Faculty of Engineering, Prince of Songkla University, Songkhla 90110, Thailand.*

Article history:

Received: 2026-06-21
Revised: 2026-08-02
Accepted: 2026-08-06

Keywords:

Natural rubber foam;
Acoustic pod;
Sound absorption coefficient;
Sound transmission loss;
Bio-based acoustic materials

ABSTRACT

This study investigated the acoustic performance of bio-based natural rubber foam (NR foam) relative to conventional acoustic materials for modular acoustic pod applications through laboratory-scale material screening and full-scale prototype performance assessment. The novelty of this work lies in the introduction of the proposed Normalized Acoustic Performance Index (NAPI), a study-specific composite metric developed to compare the balance between sound absorption and material-level sound transmission resistance, together with a system-level assessment of a full-scale acoustic pod incorporating NR foam. Five materials, including NR foam, polyester fiber, polyurethane (PU) foam, polystyrene (PS) foam, and coconut fiber, were evaluated using impedance tube methods for sound absorption coefficient (SAC) and sound transmission loss (STL). Among the five materials investigated and the selected normalization reference values, NR foam yielded the highest NAPI value of 0.58, indicating the most balanced combination of sound absorption and material-level sound transmission resistance among the tested specimens. A full-scale acoustic pod incorporating NR foam within the wall cavities was subsequently constructed and evaluated under field measurement conditions. The pod exhibited octave-band sound level differences ranging from 37.1 to 49.7 dB, with an arithmetic mean of 42.4 dB across 125–8000 Hz. These values represent the combined acoustic performance of the complete enclosure and do not isolate the individual contribution of the NR foam layer. The developed NR foam exhibited a bulk density of 0.4238 g/cm³, a compressive strength of 80 kPa, a flexible interconnected open-cell structure, and HBF classification under the horizontal burning test conditions employed. Overall, the findings demonstrate the potential of NR foam as a bio-based material providing a balanced combination of sound absorption and material-level sound transmission resistance for modular acoustic enclosure applications.

© 2026 Pratoom, N. and Uthaipan, N. Recent Science and Technology published by Rajamangala University of Technology Srivijaya

1. Introduction

The rapid expansion of open-plan offices, co-working spaces, and flexible learning environments has increased the demand for localized acoustic solutions that can provide both speech privacy and internal acoustic comfort without requiring permanent structural modifications (Jahncke, 2012; Haapakangas *et al*., 2014; ISO 22955, 2021). Modular acoustic pods have emerged as a practical and scalable approach to meeting this need. However, effective acoustic pod design requires simultaneous control of two distinct mechanisms: sound insulation, which attenuates externally transmitted noise, and sound absorption, which reduces internal reverberation and reflected sound energy (Kuttruff, 2016). Most commercially available acoustic materials perform well in only one of these functions: porous fibrous absorbers such as polyester fiber and polyurethane (PU) foam offer high sound absorption but poor insulation, while rigid closed-cell materials such as polystyrene (PS) foam provide effective insulation but limited absorption (Allard and Atalla, 2009; Kuttruff, 2016). Selecting a single material that fulfills both requirements simultaneously remains a key challenge in acoustic pod design.

*** Corresponding author.**

E-mail address: *nattapon.u@psu.ac.th*

Cite this article as: Pratoom, N. and Uthaipan, N. 2026. Natural Rubber Foam for Modular Acoustic Pods: Comparative Acoustic Performance and Full-Scale Prototype Performance Assessment. **Recent Science and Technology** 18(3): e272651.

https://doi.org/10.65411/rst.2026.272651

Bio-based materials have attracted increasing interest as sustainable alternatives to conventional petroleum-derived acoustic products. Among these, natural rubber foam (NR foam), derived from renewable latex resources, exhibits an open-cell porous structure and inherent viscoelastic properties that may support dual-function acoustic performance. The acoustic performance of open-cell porous materials is governed primarily by pore structure, airflow resistance, and energy dissipation within the interconnected pore network (Allard and Atalla, 2009). In addition, the viscoelastic nature of natural rubber contributes to vibration damping and sound attenuation, enhancing its potential as a multifunctional acoustic material. Similar acoustic behavior has been reported for porous rubber-based and recycled foam materials (Maderuelo-Sanz *et al*., 2012; Del Rey *et al*., 2012; Dissanayake *et al*., 2021; Neves de Alencar *et al*., 2023). Flame-retardant additives can additionally improve its fire safety, increasing its suitability for indoor enclosure applications. Unlike conventional fibrous or closed-cell absorbers, which typically excel in only one acoustic function, the combination of an open-cell pore network with inherent viscoelastic damping is hypothesized to give NR foam a distinct advantage in achieving simultaneous sound absorption and sound insulation—a combination not readily achieved by the conventional acoustic materials evaluated in this study.

Although several studies have reported the sound absorption performance of rubber-based foams using impedance tube methods, such as Samaei *et al*. (2023) on kenaf-fiber-reinforced polyurethane foam, most investigations have focused on a single acoustic property (either sound absorption or sound transmission loss) without systematic comparison to conventional competing materials. Information regarding the combined sound absorption and sound insulation performance of NR foam relative to a range of alternative materials remains limited. Furthermore, the translation of material-level acoustic measurements to full-scale enclosure performance has rarely been validated experimentally (Asdrubali *et al*., 2015; ISO 22955, 2021).

Therefore, this study aimed to systematically compare the sound absorption and sound insulation performance of NR foam against four conventional acoustic materials (polyurethane foam, polyester fiber, polystyrene foam, and coconut fiber) using standardized impedance tube methods. The material demonstrating the best overall acoustic performance was subsequently implemented in a full-scale modular acoustic pod prototype to validate its practical applicability under real operating conditions. Physical, mechanical, morphological, and flammability properties of the selected material were also characterized to assess its suitability for long-term indoor use.

2. Materials and Methods

2.1 Materials for comparative acoustic screening

Five sound-absorbing materials representing different structural categories were selected for comparative acoustic evaluation: natural rubber foam (NR foam), polyester fiber, polyurethane (PU) foam, polystyrene (PS) foam, and coconut fiber. NR foam represents a bio-based open-cell elastomeric foam; polyester fiber and coconut fiber represent fibrous absorbers; PU foam is a synthetic open-cell polymer foam; and PS foam is a closed-cell polymer foam commonly used for thermal insulation and sound barriers. The commercial materials evaluated in this study were sourced as follows: Polyester fiber was supplied by Top Insulation and Trading Co., Ltd., Bangkok, Thailand. PU foam was manufactured by Acoustic Surfaces Inc., USA. PS foam was manufactured by Polyfoam Manufacturing Co., Ltd., Bangkok, Thailand. Coconut fiber was manufactured by Victory Industrial Co., Ltd., Bangkok, Thailand.

2.2 Preparation of natural rubber foam

Natural rubber (NR) foam was prepared by mechanical foaming using the Dunlop process, followed by gelation and steam vulcanization. High-ammonia natural rubber latex, supplied by Chalong Latex Industry Co., Ltd., Thailand, with a dry rubber content (DRC) of 60.15% and a total solids content (TSC) of 61.63%, was used as the base material. Prior to compounding, the latex was stirred for 30 min to reduce the residual ammonia content. A potassium oleate solution was subsequently added to enhance latex stability and foaming efficiency.

All rubber compounding ingredients were commercially available and used as received. Zinc diethyldithiocarbamate (ZDEC), zinc 2-mercaptobenzothiazole (ZMBT), sulfur, calcium carbonate ($CaCO_3$), and Ional LC antioxidant were added to the latex and mixed overnight to obtain a homogeneous latex compound.

The compounded latex was then mechanically whipped according to the Dunlop process to generate a stable foam with an open-cell porous structure. Zinc oxide (ZnO) and diphenylguanidine (DPG) were subsequently incorporated as an activator and secondary accelerator, respectively. Expandable graphite, supplied by Qingdao Jintao Graphite Co., Ltd., China, was added as a flame-retardant agent to improve the fire resistance of the NR foam. Finally, sodium silicofluoride (SSF) was added as a gelling agent to stabilize the cellular structure and initiate gel formation. The resulting foam was poured into a rectangular stainless-steel mold and allowed to stand for 20 min to ensure complete gelation. The gelled foam was subsequently steam-vulcanized for 60 min.

After vulcanization, the foam was removed from the mold, thoroughly washed with distilled water to remove residual chemicals, and air-dried under ambient conditions, as illustrated in Figure 1. The formulation of the acoustic NR foam is summarized in Table 1.



Figure 1 Foaming process of open-cell natural rubber foam.

Table 1 Formulation of acoustic NR foam.

Ingredient	Quantities (phr)
60% High-ammonia NR latex	100
20% Potassium oleate solution	2
50% Sulfur dispersion	2.5
50% ZDEC dispersion	1
50% ZMBT dispersion	1
50% Ional LC (antioxidant) dispersion	1
50% $CaCO_3$	20
50% Flame retardant	10
30% DPG dispersion	1.5
50% ZnO dispersion	5.0
20% SSF dispersion	0.65

2.3 Sound absorption coefficient (Impedance tube)

The normal-incidence sound absorption coefficient of the tested materials was measured using an impedance tube according to ISO 10534-2. Circular specimens were cut to fit the internal diameter of the tube and mounted flush to minimize edge leakage and ensure accurate measurement. All materials were prepared at a uniform thickness of 40 mm prior to acoustic testing. The sound absorption performance of all five materials was evaluated over a frequency range of 250–5000 Hz. A thickness of 40 mm was selected to standardize specimen geometry for comparative screening and to correspond to the practical wall cavity depth used in the full-scale acoustic pod prototype (Section 2.6).

The noise reduction coefficient (NRC) was calculated as the arithmetic mean of the sound absorption coefficients at 250, 500, 1000, and 2000 Hz, which were selected to cover the main speech and office noise frequency range. Higher NRC values indicate better overall sound absorption performance.

2.4 Sound transmission loss (Impedance tube)

The sound transmission loss (STL) of the tested materials was measured using an impedance tube based on the transfer function method following ASTM E2611 and ISO 10534-2. Circular specimens, each 40 mm thick, were fitted securely between the source and receiving sections of the tube to minimize edge leakage. Measurements were conducted over 250–5000 Hz. The average STL was calculated from the arithmetic mean of the values at 250, 500, 1000, and 2000 Hz. This value was used only for material comparison and was not converted to a sound transmission class (STC) rating.

2.5 Selection criteria for acoustic pod materials normalized acoustic performance index (NAPI)

The overall acoustic performance of the materials was evaluated using the normalized acoustic performance index (NAPI), calculated from the noise reduction coefficient and sound transmission loss according to Eq. (1):

$$\mathrm{NAPI} = \sqrt{\frac{\mathrm{NRC}}{\mathrm{NRC}_0} \times \frac{\text{avg STL}}{\mathrm{STL}_0}} \quad (1)$$

where NRC is the measured noise reduction coefficient of the tested material, and average STL is the measured average sound transmission loss (dB). Reference values of $NRC_0 = 0.90$ and $STL_0 = 35$ dB were selected to represent high-performance reference levels for normalization. These values were used solely for comparative screening within this study and should not be interpreted as standardized performance thresholds.

The geometric mean formulation was adopted to ensure that both acoustic properties contribute equally to the index and that poor performance in either property significantly reduces the overall NAPI score: a material with excellent absorption but negligible insulation, or vice versa, will yield a low NAPI despite being strong in one dimension. A NAPI value of 1.0 indicates that both selected reference values are simultaneously attained, whereas values greater than 1.0 may occur when both normalized acoustic properties exceed their respective reference values.

The proposed NAPI provides a single composite score for comparing the balance between sound absorption and material-level sound transmission resistance among the tested materials. It enables materials representing different structural categories, including porous absorbers, rigid insulators, and viscoelastic foams, to be compared on a common normalized scale. The index was developed solely as a study-specific screening tool and should not be interpreted as a standardized acoustic rating or as a universal acceptance criterion for acoustic pod wall construction.

2.6 Acoustic pod prototype

A full-scale modular acoustic pod (1.5 X 2.0 X 2.2 m) was constructed to evaluate natural rubber foam (NR foam) as a sound-absorbing material filled inside the 40 mm thick wall structure. The prototype consisted of a structural enclosure, an

acoustically sealed door, ventilation components, internal supporting panels, and wall cavities filled with NR foam shown in Figure 2.

The design was based on commercially available office pod systems used in workplaces, universities, hospitals, and co-working spaces, aiming to provide speech privacy and external noise reduction while maintaining ventilation and user comfort. Special attention was given to sealing joints, door interfaces, wall connections, and panel installation to minimize sound leakage and improve overall sound insulation performance. The prototype was used to validate laboratory-scale results under full-scale operating conditions.



Figure 2 Schematic design and full-scale prototype of the modular acoustic pod used for field sound insulation evaluation.

2.7 Field sound level difference measurement

The field sound insulation performance of the full-scale acoustic pod prototype was evaluated using a measurement procedure adapted from the general principles of ISO 16283-1. Broadband noise was generated by a loudspeaker positioned outside the acoustic pod to represent external environmental noise and typical sound disturbances encountered in office environments. Sound pressure levels were measured at designated positions outside and inside the enclosure.

Measurements were conducted over the frequency range of 125–8000 Hz to evaluate the acoustic performance of the enclosure in the low-, mid-, and high-frequency regions associated with environmental noise, speech, and mechanical equipment. Each measurement was repeated at least three times, and the mean values were reported.

The octave-band sound level difference (D_L), between the sound pressure levels measured outside (L_1) and inside (L_2) the acoustic pod was calculated using Eq. (2):

$$D_{\mathrm{L}} = L_1 - L_2 \tag{2}$$

where (L_1) is the sound pressure level measured outside the acoustic pod (dB), and (L_2) is the corresponding sound pressure level measured inside the acoustic pod (dB).

A higher D_L value indicates a greater reduction in sound pressure level between the exterior and interior of the enclosure under specified measurement conditions. The measured sound level difference represents the overall field performance of the complete acoustic pod system, including the wall panels, NR foam-filled cavities, door, ventilation components, structural connections, and potential sound leakage through joints.

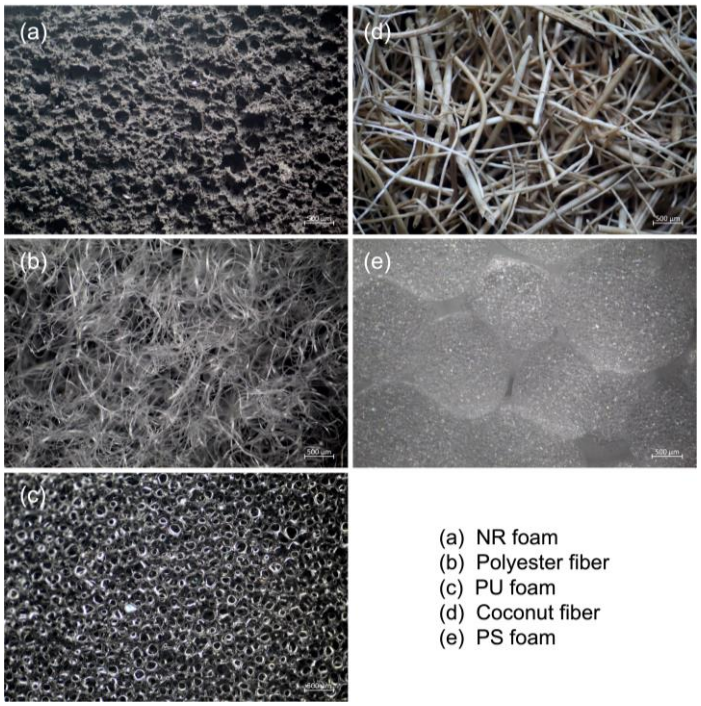


Figure 3 Optical microscope images of all five tested materials at 10x magnitude.

2.8 Physical, mechanical, morphological, and flammability properties

Density was determined using an electronic density balance equipped with a hydrostatic weighing kit based on Archimedes' principle. Each specimen was weighed in air and in water. The bulk density (ρ_o) was measured using the specimen in its original, uncompressed state, whereas the apparent solid density (ρ_s) was determined after compressing the specimen at 500 psi to minimize the contribution of internal air voids. The apparent porosity was subsequently calculated using Eq. (3):

$$\text{Porosity (\%)} = \left(1 - \frac{\rho_o}{\rho_s}\right) \text{x } 100 \tag{3}$$

Hardness was measured using a Shore OO durometer according to ASTM D2240. Compressive strength was evaluated following ASTM D3574 (adapted here in the absence of a current standard specific to natural rubber latex foam) at a crosshead speed of 50 mm/min. Morphology was examined using an optical microscope. Flammability was evaluated using the horizontal burning test specified in ISO 9772 by observing flame propagation, burning behavior, and self-extinguishing characteristics.

Table 2 Physical and structural characteristics of the five tested materials.

Material	Structure type	Density (g/cm³)		Porosity (%)
		Bulk	Solid	
NR foam	Open-cell foam	0.4238 ± 0.0440	0.8036 ± 0.0226	47.3
Polyester fiber	Fibrous	0.0142 ± 0.0010	1.0659 ± 0.0452	98.7
PU foam	Open-cell foam	0.0239 ± 0.0014	0.7347 ± 0.0202	96.7
Coconut fiber	Fibrous	0.0745 ± 0.0079	0.8521 ± 0.0212	91.3
PS foam	Closed-cell foam	0.0117 ± 0.0007	0.0124 ± 0.0006	5.6

3. Results and Discussion

3.1 Physical and structural characteristics of sound-absorbing materials

Physical and structural characteristics of the five tested materials, namely natural rubber (NR) foam, polyester fiber, polyurethane (PU) foam, polystyrene (PS) foam, and coconut fiber, are summarized in Table 2. NR foam had the highest bulk density (0.4238 g/cm³) among all tested materials, substantially higher than the fibrous and synthetic foam alternatives (0.0117–0.0745 g/cm³). PS foam had the lowest bulk density (0.0117 g/cm³), reflecting its highly expanded closed-cell structure. The solid density of NR foam (0.8036 g/cm³) was comparable to that of other elastomeric and fibrous materials, indicating a dense rubber matrix despite the open-cell foam morphology. The high porosity of polyester fiber (98.7%) and PU foam (96.7%) reflects their loosely packed fibrous and open-cell structures, in which a large fraction of the material volume consists of interconnected air space. In contrast, NR foam exhibited a comparatively lower porosity (47.3%) together with a markedly higher bulk density, consistent with its denser rubber matrix. PS foam exhibited the lowest porosity (5.6%) among all tested materials, consistent with its closed-cell structure, in which the polymer matrix largely encloses discrete gas cells rather than forming an interconnected pore network. Representative optical micrographs of the five materials are shown in Figure 3. NR foam exhibits an irregular, interconnected open-cell structure, while polyester and coconut fibers form randomly oriented fibrous networks. PU foam shows relatively uniform open cells, whereas PS foam consists of large, closely packed closed cells separated by continuous cell walls, with no visible intercellular openings. This value should be interpreted with caution, as the compression-based method used to estimate apparent solid density may not fully collapse enclosed gas cells in closed-cell foams, and the true porosity of PS foam may be underestimated.

3.2 Comparative sound absorption performance

The sound absorption performance of polyester fiber, coconut fiber, PS foam, PU foam, and NR foam was evaluated using the impedance tube method. The SAC and NRC values are presented in Figure 4 and Table 3. At 250 Hz, NR foam exhibited the highest SAC (0.24), exceeding polyester fiber (0.17) and PU foam (0.14), indicating comparatively better low-frequency absorption capability. However, at 1000–2000 Hz both polyester fiber and PU foam exceeded NR foam, with polyester fiber reaching 0.86 and PU foam reaching 0.68 at 2000 Hz, compared with 0.64 for NR foam. Consequently, NR foam's overall NRC (0.44) was equal to that of PU foam and lower than that of polyester fiber (0.54), despite NR foam's advantage at the lowest tested frequency. This behavior is consistent with the structural characteristics identified in Section 3.1: the high porosity of polyester fiber and PU foam favors efficient sound wave penetration into their loosely packed fibrous and open-cell structures, promoting relatively high mid- to high-frequency absorption, whereas the comparatively lower porosity and higher bulk density of NR foam restrict the free path available for sound wave propagation at these frequencies. In contrast, PS foam exhibited the lowest absorption performance (NRC = 0.07), with consistently low SACs (0.01–0.16) across the tested frequency range; its very low porosity and closed-cell structure (Section 3.1) prevent sound wave penetration almost entirely, limiting internal energy dissipation. Although NR foam did not achieve the highest NRC among the tested materials, its interconnected open-cell morphology and viscoelastic energy dissipation characteristics (Allard and Atalla, 2009; Asdrubali *et al*., 2015) contribute to its moderate sound absorption capability.

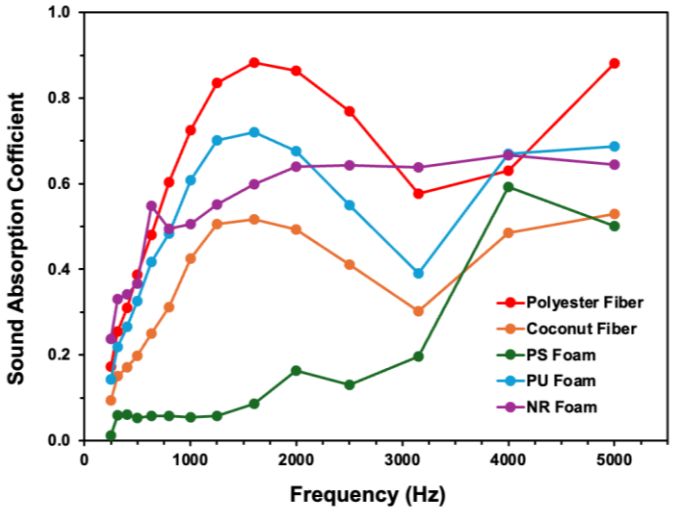


Figure 4 Sound absorption coefficient of different sound-absorbing materials measured using the impedance tube method.

3.3 Comparative sound insulation performance

The STL results of the five materials are presented in Figure 5 and Table 4. PS foam exhibited the highest average STL (39.35 dB), followed by NR foam (24.48 dB), polyester fiber (2.37 dB), PU foam (0.88 dB), and coconut fiber (0.63 dB). The high STL of PS foam is associated with its predominantly closed-cell structure, low pore connectivity, and continuous cell walls, which restrict sound transmission through the material. NR foam also showed substantially higher STL than the other porous materials. This finding is consistent with its comparatively higher bulk density and lower porosity, which restrict the free path available for sound wave transmission, combined with the viscoelastic nature of rubber, the higher mass density resulting from filler incorporation, and enhanced structural damping within the foam matrix. In contrast, the high porosity and low bulk density of polyester fiber and PU foam allow sound energy to pass through with minimal attenuation, consistent with their negligible STL values. Similar effects have been reported for porous rubber-based materials, where internal friction and viscoelastic damping improve resistance to sound transmission (Maderuelo-Sanz *et al*., 2012; Del Rey *et al*., 2012).

Notably, the NR foam exhibited a marked increase in STL at frequencies above 2000 Hz, indicating improved resistance to high-frequency sound transmission. This behavior is likely associated with the combined effects of frequency-dependent inertial resistance and energy dissipation within the porous viscoelastic structure. At higher frequencies, oscillatory airflow through the interconnected pores promotes viscous and thermal losses, while deformation of the flexible rubber cell walls contributes additional viscoelastic damping. Although the overall increase in STL is broadly consistent with the general tendency predicted by the mass law, the acoustic response of open-cell NR foam is poroelastic and therefore cannot be attributed to mass-law behavior alone (Allard and Atalla, 2009; Najib *et al*., 2011).

3.4 Acoustic performance index for material selection

The proposed normalized acoustic performance index (NAPI), developed as a study-specific screening index, was calculated for all five tested materials using Eq. (1) to provide a single quantitative metric for comparing dual-function acoustic performance. Table 5 presents the NRC, average STL, and computed NAPI for each material, ranked in descending order of NAPI. The calculation normalizes both acoustic properties against the selected reference values (NRC_0 = 0.90; STL_0 = 35 dB) and applies the geometric mean to balance the contributions of sound absorption and sound insulation while penalizing poor performance in either dimension. These reference values were selected solely for comparative screening within this study and should not be interpreted as standardized performance thresholds. Building on the physical and structural characteristics discussed in Section 3.1 and the individual absorption (Section 3.2) and insulation (Section 3.3) performance of each material, the NAPI combines both dimensions into a single comparative score.

Within the five materials investigated and the selected normalization references, NR foam yielded the highest NAPI value of 0.58, indicating the most balanced combination of sound absorption and material-level sound transmission resistance among the tested specimens. Although neither its NRC (0.44) nor its average STL (24.48 dB) was the highest individual value among all tested materials, their geometric combination produced the highest composite score. This result suggests that, under the experimental conditions and normalization approach employed, NR foam provided a more balanced dual-function acoustic response than the other materials evaluated.

PS foam ranked second with a NAPI of 0.30. Although PS foam achieved the highest average STL (39.35 dB), its very low NRC (0.07) substantially reduced its composite score through the geometric mean penalty, demonstrating that strong performance in only one acoustic dimension results in a lower composite score when both absorption and insulation are considered simultaneously. This result illustrates a key advantage of the NAPI formulation: a material that excels in insulation but fails in absorption, or vice versa, is penalized more severely than by a simple arithmetic average, reflecting the intended dual-function screening criterion used in this study. Notably, PS foam's average STL exceeds the selected reference value, STL_0 (35 dB), giving a normalized STL ratio above 1.0; even so, its very low NRC still dominates the geometric mean and keeps its overall NAPI low.

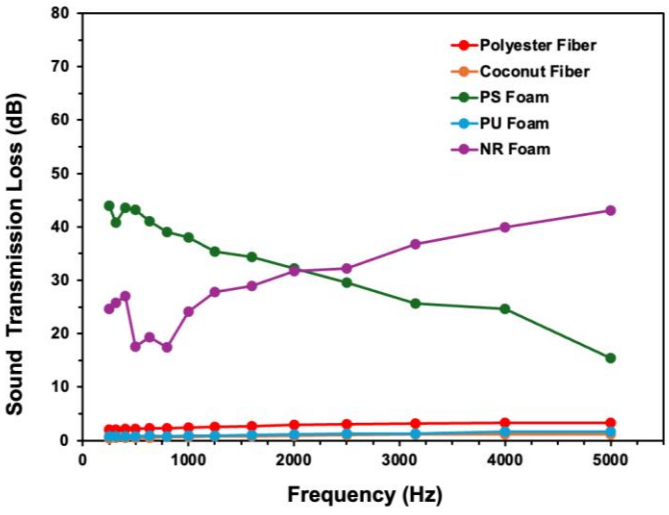


Figure 5 Sound transmission loss of different sound-absorbing materials measured using the impedance tube method.

Table 3 Sound absorption coefficient and NRC of different sound-absorbing materials.

Frequency (Hz)	Polyester Fiber	Coconut Fiber	PS Foam	PU Foam	NR Foam
250	0.17	0.09	0.01	0.14	0.24
500	0.39	0.20	0.05	0.33	0.37
1000	0.72	0.43	0.05	0.61	0.51
2000	0.86	0.49	0.16	0.68	0.64
NRC	0.54	0.30	0.07	0.44	0.44

Table 4 Sound transmission loss of different sound-absorbing materials.

Frequency (Hz)	Polyester Fiber	Coconut Fiber	PS Foam	PU Foam	NR Foam
250	1.96	0.43	43.95	0.73	24.58
500	2.19	0.54	43.17	0.81	17.56
1000	2.44	0.64	38.03	0.83	24.07
2000	2.88	0.91	32.23	1.15	31.70
Avg STL	2.37	0.63	39.35	0.88	24.48

Polyester fiber (NAPI = 0.20), PU foam (NAPI = 0.11), and coconut fiber (NAPI = 0.08) all ranked substantially lower, primarily due to their negligible STL values (2.37, 0.88, and 0.63 dB, respectively), which resulted in very small STL normalization ratios (0.068, 0.025, and 0.018). Despite their relatively good NRC performance (0.54, 0.44, and 0.30), the geometric mean was dominated by the low insulation contribution, producing NAPI values substantially lower than that of NR foam. These results indicate that, among the specimens and test conditions investigated, the polyester fiber, PU foam, and coconut fiber provided a less balanced combination of absorption and material-level sound transmission resistance than NR foam.

Overall, under the selected normalization reference values, the NAPI ranking was NR foam > PS foam > polyester fiber > PU foam > coconut fiber. This ranking applies specifically to the tested specimens, experimental conditions, and normalization approach employed in this study. The proposed NAPI should therefore be interpreted as a comparative screening tool rather than as a standardized acoustic rating or universal performance criterion.

Table 5 Proposed normalized acoustic performance index (NAPI) calculated using the selected reference values.

Material	NRC	Avg STL (dB)	NAPI
NR Foam	0.44	24.48	0.58
PS Foam	0.07	39.35	0.30
Polyester Fiber	0.54	2.37	0.20
PU Foam	0.44	0.88	0.11
Coconut Fiber	0.30	0.63	0.08

3.5 Physical and structural characteristics of NR foam

The physical, mechanical, morphological, and flammability properties of NR foam are summarized in Table 6. The foam exhibited a hardness of 35±3 Shore OO, indicating a soft and flexible structure suitable for acoustic lining inside modular pod walls. This softness improved vibration damping and enhanced sound energy dissipation within the porous structure.

Table 6 Physical, mechanical, morphological, and flammability properties of NR foam.

Properties	NR Foam
Hardness	35 ± 3 shore OO
Density	0.4238 ± 0.0440 g/cm^3
Compressive strength	80 ± 3 kPa
Flame resistance	HBF Class
Pore size	0.32 ± 0.12 mm

The density of NR foam was 0.4238±0.0440 g/cm³, which is notably higher than conventional open-cell foam absorbers such as PU foam (0.0239 g/cm³) and polyester fiber (0.0142 g/cm³). This elevated density, combined with the interconnected open-cell pore network, contributes to enhanced resistance to airborne sound transmission through increased material mass, while the porous microstructure simultaneously enables sound energy dissipation through viscous friction and thermal conduction (Allard and Atalla, 2009; Maderuelo-Sanz *et al*., 2012).

The compressive strength was 80±3 kPa, indicating sufficient structural stability while maintaining elasticity and resilience. This property is particularly important for maintaining dimensional stability during long-term use and installation.

The flammability test classified the material as HBF (Horizontal Burning, self-extinguishing) according to ISO 9772, indicating low horizontal burning rate and self-extinguishing characteristics. These results confirm that the developed NR foam provides adequate fire safety for indoor acoustic enclosure applications.

The cellular morphology of NR foam showed an interconnected open-cell structure with an average pore size of 0.32±0.12 mm (Figure 6). This porous network promotes sound-wave penetration and energy dissipation through viscous friction, thermal losses, and deformation of the flexible rubber cell walls. The observed increase in SAC with frequency is consistent with the behavior of porous

absorbers, as shorter-wavelength sound interacts more effectively with the pore network and produces greater internal energy dissipation at higher frequencies (Allard and Atalla, 2009; Del Rey *et al*., 2012).

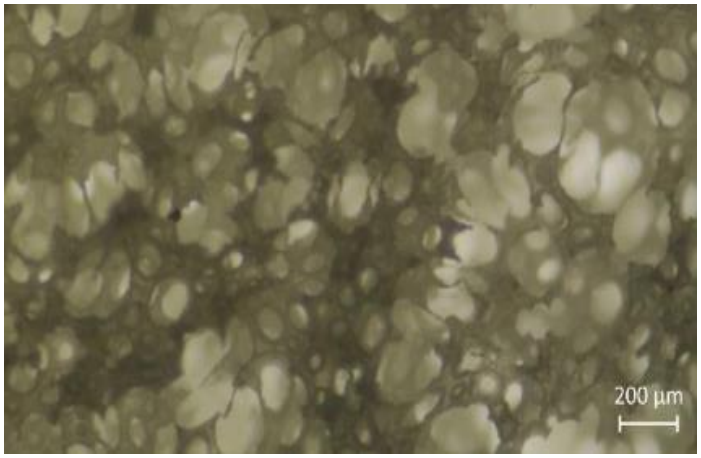


Figure 6 Open-cell porous morphology of a thin-section NR foam specimen observed under transmitted-light illumination using an optical microscope at 25X magnification.

3.6 Full-scale acoustic pod performance assessment

A full-scale acoustic pod prototype (1.5 × 2.0 × 2.2 m) was constructed using NR foam as the acoustic infill material within the wall cavities. The field sound insulation performance was evaluated by measuring octave-band sound level difference (D_L) over the frequency range of 125–8000 Hz, as shown in Table 7. The measured D_L values ranged from 37.1 to 49.7 dB, with a mean of 42.4 dB across the 125–8000 Hz range, demonstrating strong overall sound insulation performance suitable for practical acoustic enclosure applications. The measured D_L values varied across the investigated frequency range. The highest value, 49.7 ± 1.7 dB, was recorded at 125 Hz, indicating the greatest reduction in sound pressure level between the exterior and interior of the acoustic pod under the specified measurement conditions. The acoustic response at low frequencies is influenced by several interacting factors, including the mass and stiffness of the enclosure panels, structural vibration, cavity behavior, sealing conditions, source and receiver positions, and possible sound transmission through joints. Therefore, the high D_L value observed at 125 Hz should be interpreted as the response of the complete enclosure system and cannot be attributed solely to the NR foam layer.

Table 7 Field sound level difference (D_L) of the full-scale acoustic pod prototype.

Frequency (Hz)	D_L (dB)
125	49.7 ± 1.7
250	41.3 ± 0.4
500	40.8 ± 1.6
1000	37.1 ± 1.4
2000	48.8 ± 0.6
4000	40.8 ± 1.3
8000	38.2 ± 1.3

In the mid-frequency range of 250–1000 Hz, the D_L values decreased from 41.3 ± 0.4 to 37.1 ± 1.4 dB, with the lowest value occurring at 1000 Hz. This reduction may reflect the frequency-dependent response of the enclosure, including structural coupling between wall components, panel vibration, cavity effects, and sound transmission through joints, the door, or ventilation components. Resonance-related behavior may also have contributed to the observed reduction; however, the available measurements are insufficient to identify a specific resonance mechanism conclusively.

At 2000 Hz, D_L increased to 48.8 ± 0.6 dB. Because this frequency lies within a range relevant to speech communication, the result suggests that the enclosure can substantially reduce some speech-related frequency components under the test conditions employed. Nevertheless, speech privacy cannot be established from the sound level difference at a single frequency and would require additional evaluation using appropriate speech intelligibility or privacy metrics. At 4000 and 8000 Hz, the measured D_L values were 40.8 ± 1.3 and 38.2 ± 1.3 dB, respectively, indicating that measurable sound pressure level reduction was maintained across the investigated high-frequency region.

The arithmetic mean D_L across the measured octave bands was 42.4 dB. This value is reported only as a descriptive summary of the frequency-dependent results and should not be interpreted as a standardized single-number sound insulation rating. In addition, the measured mean should not be directly compared with criteria specified using different measurement procedures or acoustic descriptors. The standard deviations ranged from ±0.4 to ±1.7 dB, indicating relatively consistent repeated measurements under the same experimental conditions. The greater variation observed at 125 Hz may be associated with the sensitivity of low-frequency measurements to source and receiver positions, room boundaries, environmental conditions, and structural vibration.

Overall, the full-scale assessment demonstrated that the acoustic pod provided a sound level difference of at least 37.1 dB across the measured octave bands under the specified test conditions. NR foam was incorporated into the wall cavities because it exhibited a balanced combination of sound absorption and material-level sound transmission resistance during laboratory screening. However, the measured DL values represent the combined performance of the complete enclosure, including the wall panels, NR foam-filled cavities, door, ventilation components, sealing details, and structural connections. Because a reference pod without NR foam and component-level measurements were not included, the individual contribution of NR foam to the full-scale sound level difference could not be quantitatively isolated. The results therefore provide a practical demonstration of the acoustic performance of a full-scale pod incorporating NR foam rather than direct validation of the material-level results.

3.7 Practical implications

The cost–performance relationship of the evaluated materials is illustrated in Figure 7. Although NR foam exhibited a slightly higher material cost than some conventional porous absorbers, it provided the highest overall dual-function acoustic performance, as reflected by the highest NAPI value among the tested materials under the selected normalization references.

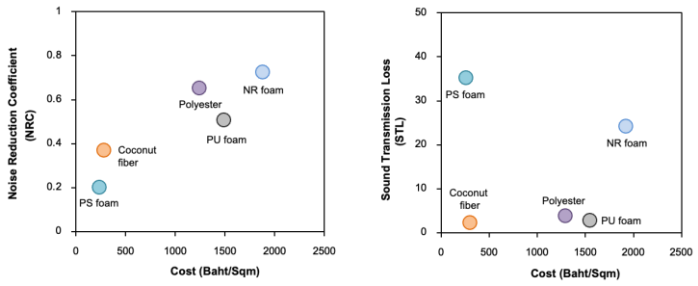


Figure 7 Cost–performance relationship of natural rubber foam and conventional acoustic materials for modular acoustic pod applications.

In contrast, polyester fiber and PU foam offered lower material costs but delivered lower overall acoustic performance due to their limited sound insulation capability. PS foam achieved excellent sound insulation performance; however, its low sound absorption reduced its suitability for enclosed acoustic environments where both functions are required simultaneously.

The balanced combination of sound absorption and sound insulation provided by NR foam enables the use of a single acoustic layer, reducing the need for additional absorptive or insulating materials. This simplifies panel construction and installation while potentially lowering overall system complexity. Furthermore, natural rubber is a renewable and domestically available resource, offering sustainability advantages and reducing dependence on imported petroleum-based materials. These characteristics make NR foam a promising material for modular acoustic pod applications, where acoustic effectiveness, structural simplicity, and long-term sustainability are important design considerations.

4. Conclusion

This study investigated the acoustic performance of bio-based NR foam through laboratory-scale comparison with conventional sound-absorbing materials and full-scale evaluation in a modular acoustic pod prototype. Among the five materials tested, NR foam achieved the highest overall dual-function acoustic performance (NAPI = 0.58), with a moderate NRC value of 0.44 (comparable to PU foam and below polyester fiber's 0.54) together with a substantially higher sound transmission loss of 24.48 dB. These findings indicate that NR foam can contribute to both sound absorption and sound insulation under the experimental conditions employed.

The full-scale acoustic pod prototype incorporating NR foam achieved sound level difference values ranging from 37.1 to 49.7 dB, with an average value of 42.4 dB over the frequency range of 125–8000 Hz. The observed performance at 125 and 2000 Hz suggests that the developed system has potential for reducing low-frequency and speech-related sound transmission in modular acoustic enclosures. Overall, the results demonstrate the potential of NR foam as an acoustic material for modular enclosure systems and provide an initial performance assessment progressing from material-scale screening to full-scale prototype testing.

5. Acknowledgments

The authors gratefully acknowledge financial support from Prince of Songkla University Science Park under the Technology to Industry Convergence Program (Grant No. PSUP4-2/68).

6. References

Allard, J.F. and Atalla, N. 2009. **Propagation of Sound in Porous Media: Modelling Sound Absorbing Materials** (2nd ed.). John Wiley & Sons.

Asdrubali, F., D'Alessandro, F. and Schiavoni, S. 2015. A review of unconventional sustainable building insulation materials. **Sustainable Materials and Technologies** 4: 1–17.

ASTM D2240. 2021. Standard test method for rubber property–Durometer hardness. **ASTM International**.

ASTM D3574. 2022. Standard test methods for flexible cellular materials—Slab, bonded, and molded urethane foams**. ASTM International**.

ASTM E2611. 2019. Standard test method for normal incidence determination of porous material acoustical properties based on the transfer matrix method. **ASTM International**.

Del Rey, R., Alba, J., Arenas, J.P. and Sanchis, V.J. 2012. An empirical modelling of porous sound absorbing materials made of recycled foam**. Applied Acoustics** 73(6–7): 604-609.

Dissanayake, D.G.K., Weerasinghe, D.U., Thebuwanage, L.M. and Bandara, U.A.A.N. 2021. An environmentally friendly sound insulation material from post-industrial textile waste and natural rubber. **Journal of Building Engineering** 33: 101606.

Haapakangas, A., Hongisto, V., Hyönä, J., Kokko, J. and Keränen, J. 2014. Effects of unattended speech on performance and subjective distraction: The role of acoustic design in open-plan offices. **Applied Acoustics** 86: 1-16.

ISO 9772. 2020. Cellular plastics—Determination of horizontal burning characteristics of small specimens subjected to a small flame. **International Organization for Standardization**.

ISO 10534-2. 2001. Acoustics—Determination of sound absorption coefficient and impedance in impedance tubes—Part 2: Transfer-function method. **International Organization for Standardization.**

ISO 16283-1. 2014. Acoustics—Field measurement of sound insulation in buildings and of building elements—Part 1: Airborne sound insulation. **International Organization for Standardization.**

ISO 22955. 2021. Acoustics—Acoustic quality of open office spaces. **International Organization for Standardization**.

Jahncke, H. 2012. Open-plan office noise: The susceptibility and suitability of different cognitive tasks for work in the presence of irrelevant speech. **Noise and Health** 14(61): 315-320.

Kuttruff, H. 2016. **Room Acoustics** (6th ed.). CRC Press.

Maderuelo-Sanz, R., Nadal-Gisbert, A.V., Crespo-Amorós, J.E. and Parres-García, F. 2012. A novel sound absorber with recycled fibers coming from end-of-life tires (ELTs). **Applied Acoustics** 73(4): 402–408.

Najib, N.N., Ariff, Z.M., Bakar, A.A. and Sipaut, C.S. 2011. Correlation between the acoustic and dynamic mechanical properties of natural rubber foam: Effect of foaming temperature. **Materials and Design** 32(2): 505–511.

Neves de Alencar, L., Guedes Paiva, F.F., Okimoto, F.S., Boaventura Bacarin, G., Dognani, G., Salmazo, L.O., dos Santos, R.J., Camargo Cabrera, F. and Job, A.E. 2023. Natural rubber/wood composite foam: Thermal insulation and acoustic isolation materials for construction. **Cellular Polymers** 42(2): 55–72.

Samaei, S.E., Berardi, U., Asilian Mahabadi, H., Soltani, P. and Taban, E. 2023. Optimization and modeling of the sound absorption behavior of polyurethane composite foams reinforced with kenaf fiber. **Applied Acoustics** 202: 109176.

Recent Science and Technology 2026, Vol. 18(3): e270817

Recent Science and Technology

Journal homepage: https:// www.tci-thaijo.org/index.php/rmutsvrj/index

ISSN: 3057-0786 (Online)

Research Article

Plant Community Structure and Carbon Sequestration of the Forest Restoration Areas at Kamnoetvidya Science Academy

Worawut Ngampiboonwet [a], Karun Chaivanich [b], Praphaiphan Kewkasem [c], Amnuayvit Thitibordin [c] and Yutthana Thoenglom [a *]

[a] *Program in Agroforestry, Maejo University Phare Campus, Phare 54140, Thailand.*

[b] *Department of Ordnance Engineering, Academic Division, Chulachomklao Royal Military Academy, Nakhonnayok 26001, Thailand.*

[c] *Kamnoetvidya Science Academy, Rayong 21210, Thailand.*

Article history:

Received: 2026-02-12
Revised: 2026-08-03
Accepted: 2026-08-06

Keywords:

Plant community structure;
Forest restoration;
Carbon sequestration;
Biodiversity

ABSTRACT

This study evaluated the plant community structure, species diversity, and carbon sequestration potential of two distinct forest restoration models at Kamnoetvidya Science Academy, Rayong Province, Thailand. Two silvicultural approaches were observed: (1) Rubber–Palm Intercropping Plots (RPP) and (2) Mixed-Orchard Plots (OP). Vegetation data were collected from 20 x 50 m sample plots in each restoration approach, with each plot subdivided into ten 10 × 10 m subplots, to determine species composition, canopy architecture, and the Importance Value Index (IVI). Biodiversity was quantified using the Shannon–Wiener Index, while biomass and carbon stocks were estimated via established allometric equations. The results revealed higher taxonomic richness in OP (36 species) compared to RPP (25 species), with OP exhibiting higher diversity and evenness indices. Phytosociological analysis identified *Hevea brasiliensis* as the sole dominant species in RPP, whereas OP displayed a co-dominance of various fruit and indigenous forest species. Despite differences in composition, total carbon stocks were comparable between the two systems, with RPP yielding 45.59 tC/ha and OP yielding 46.23 tC/ha. Carbon distribution was highly concentrated in rubber trees within RPP, while OP exhibited a more heterogeneous distribution across multiple taxa. These findings demonstrate that both integrated agricultural models effectively enhance biodiversity and structural complexity while providing substantial carbon sinks. Consequently, RPP and OP represent viable strategies for rehabilitating degraded agricultural landscapes, contributing to both sustainable land management and global climate change mitigation efforts.

© 2026 Ngampiboonwet, W., Chaivanich, K., Kewkasem, P., Thitibordin, A. and Thoenglom, Y. Recent Science and Technology published by Rajamangala University of Technology Srivijaya

1. Introduction

Climate change represents a profound global challenge, posing enduring threats to ecological systems, economic stability, and human well-being. This phenomenon is largely driven by increased concentrations of greenhouse gases, most notably CO_2, resulting from human activities such as fossil fuel combustion, transportation, and industrial processes. Moreover, the loss of forest cover due to land-use change and deforestation reduces natural carbon sequestration, further exacerbating global warming and climatic instability.

Woody plant and forests ecosystems play a pivotal role as natural carbon sinks, sequestering atmospheric carbon through photosynthesis and storing it within both aboveground and belowground biomass. Carbon stocks held within vegetation and soil are critical components of the ecosystem's carbon balance, governed by biological processes such as plant growth, autotrophic and heterotrophic respiration, and organic matter decomposition (Intergovernmental Panel on Climate Change, 2006). Furthermore, the carbon sequestration potential of forested and restored areas is contingent upon species composition, stand age, density, spacing, environmental

*** Corresponding author.**

E-mail address: *yutthana.thoe@gmail.com*

Cite this article as: Ngampiboonwet, W., Chaivanich, K., Kewkasem, P., Thitibordin, A. and Thoenglom, Y. 2026. Plant Community Structure and Carbon Sequestration of the Forest Restoration Areas at Kamnoetvidya Science Academy. **Recent Science and Technology** 18(3): e270817.
https://doi.org/10.65411/rst.2026.270817

conditions, and specific silvicultural management practices (Thailand Greenhouse Gas Management Organization, 2016).

A critical factor driving the decline in forest cover and the disruption of carbon balance is land-use change, specifically the conversion of forests into agricultural land and infrastructure development. This process not only results in net forest loss but also leads to forest degradation, characterized by diminished plant community structures and impaired ecosystem functions. Degraded forest areas (resulting from intensive agriculture, land-use intensification, and inappropriate management practices) have thus become a primary target for contemporary reforestation and restoration efforts. These initiatives aim to restore ecosystem performance, enhance carbon sequestration capacity, and promote sustainable land utilization. Recently, forest restoration integrated with diversified land-use strategies, particularly agroforestry systems, which combine forest trees with commercial crops or trees, has been increasingly promoted. This approach simultaneously restores ecological functions and supports livelihoods (Intergovernmental Panel on Climate Change, 2022).

Restoration plantings on degraded lands have been widely recognized as an effective strategy for recovering forest ecosystem functions by improving vegetation structure, enhancing biodiversity, and restoring ecosystem services (da Rosa and Marques, 2022). Among various restoration approaches, agroforestry has received increasing attention because it integrates ecological restoration with sustainable livelihoods. This approach enables the recovery of forest ecosystem functions while simultaneously generating long-term economic benefits for local communities (Murniati *et al*., 2022). The incorporation of multiple tree species within restoration systems also contributes to greater habitat heterogeneity and biodiversity, which are important for improving ecosystem resilience and supporting long-term ecosystem functioning (Murniati *et al*., 2022; da Rosa and Marques, 2022). Successful forest restoration enhances biomass accumulation and carbon sequestration, contributing to climate-change mitigation and the recovery of degraded tropical landscapes (Koutika, 2022; Koch and Kaplan, 2022). These ecological and socio-economic benefits have been consistently demonstrated in recent empirical studies. For example, ecological restoration in the western Himalaya exhibited 66.4% greater woody plant species richness (125 species) and approximately 38% greater aboveground carbon stock (49.5 tC/ha) than the reference forest, demonstrating the effectiveness of restoration in promoting biodiversity conservation and biomass accumulation (Dangwal *et al*., 2022). Similarly, agroforestry restoration of degraded land in the semi-arid tropics enhanced atmospheric CO_2 sequestration (7.9 – 30.2 tC/ha) and improved oxygen production, highlighting its contribution to climate-change mitigation (Siddesh *et al*., 2025). Beyond ecological benefits, agroforestry-based restoration also provides tangible socio-economic advantages. A case study in Gowa, Indonesia, showed that agroforestry systems contributed 26% of total household income, while coffee–clove agroforests generated the highest average annual income of IDR 43,017,192 (approximately 3,025 US dollars), demonstrating that agroforestry can simultaneously restore degraded landscapes, improve rural livelihoods, and support sustainable land management (Hasannudin *et al*., 2022).

The ecological performance of forest restoration is not universal. Restoration outcomes are influenced by species composition, vegetation structure, environmental conditions, and management practices, indicating that different restoration models may vary considerably in their capacity to recover biodiversity and store carbon. Evaluating the ecological characteristics, biodiversity, and carbon sequestration potential of different restoration approaches under specific environmental conditions is therefore essential for identifying restoration strategies that are best suited to particular sites and management objectives. These context-appropriate restoration strategies can maximize ecosystem recovery and promote sustainable land management (da Rosa and Marques, 2022; Koch and Kaplan, 2022). The integration of rubber tree (*Hevea brasiliensis*) and oil palm (*Elaeis guineensis*) represents a prevalent land-use model across various regions of Eastern Thailand. As both are vital cash crops significantly contributing to the local economy, this system reflects continuous agricultural management oriented toward economic sustainability. In contrast, fruit tree-based systems are characterized by the co-cultivation of diverse fruit species alongside indigenous forest trees, resulting in high species richness and complex community structures. These systems represent agroforestry practices with multi-layered canopy structures and are recognized for their dual capacity to support economic livelihoods and facilitate ecological restoration (Siarudin *et al*., 2021). Both rubber-oil palm integrated systems and diversified fruit tree systems serve as promising models for restoring degraded forest lands previously impacted by agricultural activities.

Kamnoetvidya Academy (KVIS), located in Pa Yup Nai Subdistrict, Wang Chan District, Rayong Province, is a senior high school established by the PTT Group as part of its core mission to operate non-profit corporate social responsibility (CSR) initiatives for sustainable development. Within this framework, KVIS has implemented forest restoration plantings since 2015, utilizing two distinct land-use models: a rubber-oil palm integrated system and a diversified fruit tree system. These sites offer a compelling opportunity to serve as case studies for assessing the potential of such land-use strategies in rehabilitating degraded forest lands, particularly within the context of educational institutions—an area of research that remains relatively limited in Thailand. Studying these areas will not only elucidate the effectiveness of these restoration approaches but also support the development of the site as

a learning center and a model for sustainable resource management that harmonizes forestry with agricultural utilization.

Empirical data on the restorative capacity of integrated land-use systems remain scarce. This research investigates the ecological structure and carbon sequestration potential of two distinct land-use models at Kamnoetvidya Academy: a rubber-oil palm integrated system and a diversified fruit tree system. The research objectives are to: (1) characterize plant community composition and structure; (2) analyze tree species diversity and its ecological importance; and (3) quantify biomass and carbon storage potential within these restoration areas. This study provides a data-driven foundation for rehabilitating degraded landscapes while maintaining economic viability, offering a scalable prototype for sustainable land management and carbon mitigation in both academic and agricultural sectors.

2. Materials and Methods

The study was conducted at the forest restoration and enrichment planting sites of Kamnoetvidya Academy (KVIS), located at 999 Moo 1, Pa Yup Nai Subdistrict, Wang Chan District, Rayong Province. The restoration project was initiated in 2015, comprising two distinct planting systems: 1) rubber–oil palm intercropping plots (RPP) and 2) orchard plots (OP).

Sampling plots were established within both land-use systems using a selective sampling approach to identify areas representative of the overall plant community (Kutintara, 1999). Both sites shared similar land-use history and management practices, allowing for an in-depth analysis of plant community structure and carbon sequestration potential within the specific local context. In each system, a 20 × 50 m (0.1 ha) sampling plot was established. The RPP plot was located at coordinates 13.00083° N, 101.44735° E, while the OP plot was situated at 12.9983° N, 101.44986° E. Each 0.1-ha plot was further subdivided into ten 10 × 10 m subplots for detailed surveying and data recording.

Data collection within the sample plots encompassed the following parameters: 1) Taxonomic identification and verification of arborescent species through photographic documentation and reference to 'Thai Plant Names' (Smitinand, 2014), 2) Diameter at Breast Height (DBH) measurements for all woody individuals, 3) Total tree height, 4) Vertical structure profiles to illustrate spatial distribution, and 5) Canopy cover assessment to evaluate the degree of foliage density and spatial occupancy.

The collected data were analyzed following the criteria established by Kutintara (1999), including density (D), dominance or basal area (Do), and frequency (F). These parameters were further used to calculate relative density (RD), relative dominance (RDo), relative frequency (RF), and the Importance Value Index (IVI). To assess biodiversity, the Shannon–Wiener Diversity Index (*H'*) was calculated according to Magurran (1988), while species evenness (*J'*) was derived following Pielou (1975). Aboveground biomass for woody species (AGB) was estimated using the allometric equations of Ogawa *et al.* (1965). Specific biomass equations were applied for specialized taxa: Pearson *et al.* (2005) for palms and Hytönen *et al.* (2018) for rubber trees. The total carbon stock (CS) and total CO_2 sequestration (CO_2-seq) within tree biomass were calculated following the equations provided by the Intergovernmental Panel on Climate Change (2006). Finally, oxygen production (O_2-prod) was calculated from the estimated CS using the molecular weight ratio of oxygen to carbon (32/12), following Uttaruk *et al.* (2024).

3. Results and Discussion

This study was designed as a case-based ecological assessment, focusing on an in-depth analysis of plant community structure, species diversity, and carbon sequestration potential within specific forest restoration sites. Purposive sampling was employed to select plots that represent the distinct characteristics of each land-use system, rather than for the purpose of population-level statistical comparison. The findings are presented through descriptive and ecological analyses to reflect the unique potential and specific attributes of the study areas. These results are intended to characterize the studied sites and are not aimed at providing a representative generalization for all forest restoration areas at a regional or national scale.

3.1 Plant community composition and vertical structure of restored forest plantations at KVIS

Across the entire study area, a total of 47 tree species belonging to 38 genera and 24 families were identified. The family Fabaceae exhibited the highest taxonomic richness with 10 species, followed by Dipterocarpaceae (5 species) and Lythraceae (4 species) (Table 1).

When categorized by land-use system, the RPP contained 25 tree species from 21 genera and 16 families. Within this plot, Fabaceae was the most diverse family (5 species), followed by Dipterocarpaceae (4 species) and Lythraceae (3 species). In contrast, the OP exhibited higher floristic diversity, with 36 tree species across 30 genera and 21 families. Fabaceae remained the dominant family in OP with 7 species, followed by Lythraceae and Dipterocarpaceae (3 species each) (Table 1). The differences in floristic composition observed between the RPP and OP are likely associated with their contrasting restoration designs and management objectives. Similar patterns of biodiversity recovery have been reported among different forest restoration approaches, where restoration outcomes are influenced by restoration practices, previous land use, and local environmental conditions (Atkinson *et al.*, 2022; da Rosa and Marques, 2022). These findings further support the concept that the ecological characteristics of restored forests should be interpreted within the context of restoration objectives and site-specific conditions rather than expecting identical community structures across different restoration systems (da Rosa and Marques, 2022).

Table 1 Floristic diversity, taxonomic composition, and number of individuals of tree species in the RPP and OP systems at KVIS.

No.	Plant species	Family	No. in RPP	No. in OP
1	Ma-kha Mong (*Afzelia xylocarpa* (Kurz) Craib)	Fabaceae	-	8
2	Sok Ra Ya (*Amherstia nobilis* Wall.)	Fabaceae	-	2
3	Chong-kho (*Bauhinia purpurea* L.)	Fabaceae	3	-
4	Thong Kwao (*Butea monosperma* (Lam.) Taub.	Fabaceae	-	4
5	Fang (*Caesalpinia sappan* L.)	Fabaceae	-	1
6	Ching-chan (*Dalbergia oliveri* Gamble ex Prain)	Fabaceae	5	-
7	Pha-yung (*Dalbergia cochinchinensis* Pierre)	Fabaceae	1	1
8	A-rang (*Peltophorum dasyrhachis* (Miq.) Kurz)	Fabaceae	6	8
9	Khi-lek Fa-rang (*Senna spectabilis* (DC.) H.S.Irwin & Barneby)	Fabaceae	5	-
10	Ma-kha Tae (*Sindora siamensis Teijsm.* ex Miq.)	Fabaceae	-	1
11	Yang Na (*Dipterocarpus alatus* Roxb. ex G. Don)	Dipterocarpaceae	3	-
12	Ta-khian Thong (*Hopea odorata* Roxb.)	Dipterocarpaceae	7	1
13	Pha-yom (*Shorea roxburghii* G.Don)	Dipterocarpaceae	8	1
14	Rang (*Shorea siamensis* Miq.*)*	Dipterocarpaceae	3	-
15	Khiam Kha-nong (*Shorea henryana* Pierre)	Dipterocarpaceae	-	1
16	Ta-baek Na (*Lagerstroemia floribunda* Jack)	Lythraceae	4	1
17	In-tha-nin (*Lagerstroemia macrocarpa* Wall. ex Kurz)	Lythraceae	2	-
18	In-tha-nin Nam (*Lagerstroemia speciosa* (L.) Pers.)	Lythraceae	1	1
19	In-tha-ra-chit (*Lagerstroemia loudonii* Teijsm. & Binn.*)*	Lythraceae	-	1
20	Muang Lueat (*Knema angustifolia* (Roxb.) Warb.)	Myristicaceae	2	4
21	Wan Na (*Syzygium cumini* (L.) Skeels)	Mytaceae	-	5
22	Chom-phu Nam-dok-mai (*Syzygium jambos* (L.) Alston)	Mytaceae	2	-
23	Pip (*Radermachera ignea* (Kurz) Steenis)	Bignoniaceae	1	1
24	Khae Na (*Dolichandrone serrulata* (Wall. ex DC.) Seem.)	Bignoniaceae	-	1
25	Bun-nak (*Mesua ferrea* L.)	Calophyllaceae	-	2
26	Sa-ra-phi (*Mammea siamensis* (Miq.) T.Anderson)	Calophyllaceae	-	2
27	Mang-khut (*Garcinia mangostana* Linn.)	Clusiaceae	-	1
28	Cha-muang (*Garcinia cowaRoxb.* ex Choisy)	Clusiaceae	-	2
29	Ma-kham Pom (*Phyllanthus emblica* L.)	Phyllanthaceae	-	3
30	Ma-ka Ton (*Bridelia ovata* Decne.)	Phyllanthaceae	1	-
31	Ma-kluea (*Diospyros mollis* Griff.)	Ebenaceae	-	9
32	Ma-rid (*Diospyros discolor* Willd.)	Ebenaceae	-	3
33	Ma-muang (*Mangifera indica* L.)	Anacardiaceae	-	4
34	Lam-duan (*Mitrephora wangii* Hu)	Annonaceae	-	2
35	Tin-pet Nam (*Cerbera odollam* Gaertn.*)*	Apocynaceae	4	-
36	Palm (*Elaeis guineensis* Jacq.)	Arecaceae	1	
37	Kha-nun (*Artocarpus heterophyllus* Lam.)	Moraceae	1	2
38	Yang Pa-ra (*Hevea brasiliensis* (Willd. ex A.Juss.) Müll.Arg.)	Euphorbiaceae	28	-
39	Kan-krao (*Fagraea fragrans* Roxb.)	Gentianaceae	4	1
40	Tio Khon (*Cratoxylum formosum* (Jack) Benth. & Hook.f. ex Dyer)	Hypericaceae	4	6
41	Sak (*Tectona grandis* L. f.)	Lamiaceae	1	1
42	Op-choei (*Cinnamomum verum* J.Presl)	Lauraceae	-	2
43	Cham-pi (*Magnolia baillonii* Pierre)	Magnoliaceae	-	1
44	Ma-hat (*Artocarpus lacucha* Roxb. ex Buch.-Ham.)	Moraceae	-	7
45	Ma-fueang (*Averrhoa carambola* L.)	Oxalidaceae	8	10
46	Ket (*Manilkara hexandra* (Roxb.) Dubard)	Sapotaceae	-	5
47	Krit-sa-na (*Aquilaria crassna* Pierre ex Lec.)	Thymelaeaceae	1	1
	Total	**24**	**106**	**106**

The plant community in the RPP system exhibited high tree density and diversity, primarily dominated by species in the upper canopy layers. This structure resulted in a canopy cover of 86.40%. The vertical structure of this restored forest plantation can be categorized into four distinct strata--1) emergent layer: comprising the tallest trees within the community, these individuals extend above the main canopy with a relatively sparse distribution. The height in this layer ranges from approximately 14.60 to 18.00 m, key species found in this stratum include Yang Pa-ra, Pha-yom, A-rang, and Ma-Ka Ton. 2) Top canopy: with a height range of 11.60 to 14.75 m, this layer forms a relatively dense canopy cover. Dominant species identified in this stratum, include Kan-krao, Rang, Tio Khon, and Khi-lek Fa-rang. 3) Secondary canopy: This layer, ranging from 8.26 to 11.50 m in height, consists of numerous trees distributed throughout. Species found in this layer include Ching-chan, Chong-kho, Pip, and Kha-nun, and 4) lower canopy: reaching heights of 5.00-8.25 m, this stratum comprises medium-sized trees, some of which are younger individuals of species also found in the upper layers; representative species in this layer include Ma-fueang and Chom-phu Nam-dok-mai (Figure 1).

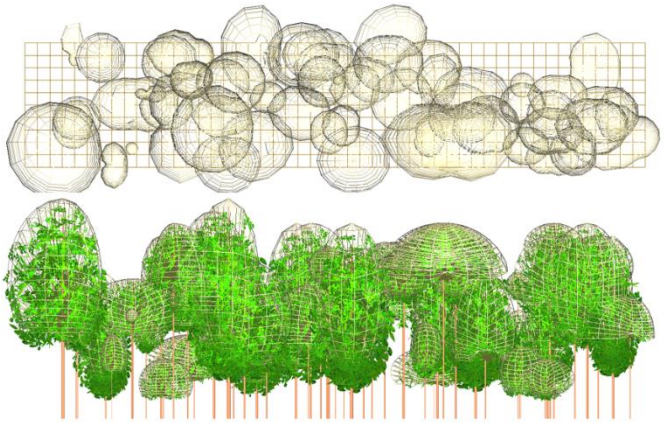


Figure 1 Vertical structure and canopy of the restored forest plantation by RPP. The vertical structure of the forest was visualized using the SexI-FS software.

The plant community in the OP system was characterized by high tree density and diversity, primarily dominated by species in the upper canopy. This resulted in a canopy cover of 87%. Similar to the RPP, the vertical structure of this restored forest plantation is categorized into four distinct strata -- 1) emergent layer: trees in this highest stratum reach heights ranging from 17.10 to 21.50 m, representative species, include Ma-hat, Cha-muang, and Kha-nun. 2) Top canopy: with a height range of 12.50 to 17.00 m, this layer forms a relatively dense canopy cover, dominant species identified in this stratum include A-rang, Ma-kham Pom, Krit-sa-na, Ma-kha Mong, Kan-krao, Ta-khian Thong, Cham-pi, and Ma-kha Tae. 3) Secondary canopy: this layer, ranging from 8.10-12.50 meters in height, consists of numerous trees distributed throughout, key species include Wan Na, Tio Khon, Ma-kluea, In-tha-ra-chit, and Ma-rid, and 4) lower canopy: reaching heights of 3.50-8.00 m, this stratum comprises medium-sized trees, some of which are younger individuals of species also found in the upper layers, species found in this layer include Ma-fueang, Op-choei, Khiam Kha-nong, Ket, Mang-khut, Thong Kwao, Khae Na, Fang, Bun-nak, and Lam-duan (Figure 2).

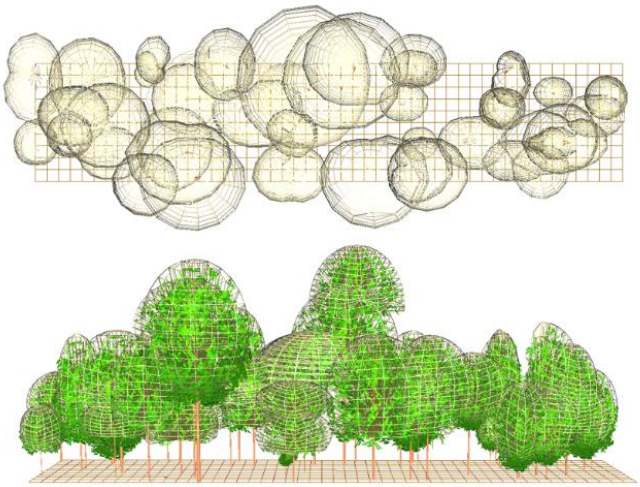


Figure 2 Vertical structure and canopy of the restored forest plantation by OP. The vertical structure of the forest was visualized using the SexI-FS software.

The findings of this study demonstrate that both forest restoration systems have developed distinct vertical structures consisting of the four strata described above since their establishment in 2015. Vertical stratification reflects efficient utilization of growing space and is recognized as a key characteristic of developing forest ecosystems because it increases habitat heterogeneity and facilitates the gradual recovery of ecosystem functions (Marod and Kutintara, 2009). The vertical stratification observed in both restoration systems at KVIS is consistent with findings from young subtropical plantations, where greater tree species richness was associated with increased vertical heterogeneity and stand structural complexity over time (Perles-Garcia *et al*., 2021). In addition to increasing habitat heterogeneity, the presence of diverse tree species across multiple canopy layers is associated with greater structural complexity and facilitates the distribution of biomass and carbon storage among tree species. These structural attributes are essential for the long-term stability of restored forest systems and support the recovery of plant community structures and ecological functions within an agricultural context. Overall, these findings suggest that both restoration systems at KVIS are progressing toward increasingly complex forest stands while maintaining their respective planting compositions and restoration objectives.

3.2 Tree species diversity and ecological significance of plant species within the forest restoration areas at KVIS

The survey of tree species within the RPP identified 25 species from 21 genera and 16 families. Recorded ecological parameters included a D of 1,060 stems/ha, a Do of 20.75

m^2/ha, an *H′* of 2.75, and a *J'* of 0.85. In contrast, the OP contained 36 species from 30 genera and 21 families, with a D of 1,060 stems/ha, a Do of 22.78 m^2/ha, an *H'* of 3.34, and a *J'* of 0.93. Both restoration systems exhibited relatively high tree species diversity. The higher *H'* value in the OP reflects greater tree species diversity than in the RPP. This difference is attributable to previous land-use characteristics; the OP was established using a multi-species planting approach from the outset, creating an environment conducive to the establishment and growth of diverse taxa. Conversely, the RPP is characterized by the presence of pre-existing economic trees, particularly Yang Pa-ra, resulting in a community structure influenced by the rubber canopy. The relatively high *H′* values observed in both restoration systems are comparable to those reported in recent tropical forest restoration studies. Keller *et al*. (2023), for example, reported *H′* of 3.61 in actively restored tropical rainforest and 3.21 in naturally regenerating forest in Malaysian Borneo. The findings of Keller *et al.* (2023) indicate that both restoration approaches were capable of maintaining relatively high tree species diversity, although active restoration exhibited significantly greater diversity. However, direct numerical comparisons should be interpreted cautiously because diversity indices are influenced by stand age, restoration history, species composition, sampling design, and local environmental conditions. The *H′* values reported in the present study provide ecological information on the community organization and biodiversity characteristics of each restoration system under the specific restoration context of KVIS. Thus, these indices should be interpreted within the restoration objectives and site conditions of the study area rather than as direct measures for comparison with other restoration sites.

The *H'* and *J'* values should be interpreted together with species composition and dominance patterns because no single diversity index can fully represent the ecological condition of a restored forest. Long-term studies of tropical forest regeneration have shown that different biodiversity components, including species richness, diversity, and evenness, may follow distinct recovery trajectories throughout the restoration process (Chazdon *et al*., 2023 ; Zhou *et al*., 2023). Rosenfield *et al*. (2023) further emphasized that ecological integrity in recovering tropical forests should be evaluated using multiple indicators, including species composition, vegetation structure, regeneration, and ecosystem functioning, rather than relying on a single diversity metric. Interpreting the *H′* and *J′* values together with the observed community composition and species dominance indicates that the RPP and OP systems at KVIS represent distinct ecological pathways of forest restoration. Although the two systems differ in community organization, each reflects its respective planting design and restoration objectives while contributing to biodiversity enhancement and forest restoration at KVIS. The present survey represents the ecological condition of the sites at a single point in time. Repeated inventories would enable future studies to evaluate how species richness, diversity, evenness, and community composition change as restoration progresses.

Analysis of the RPP revealed that the five species with the highest RD were Yang Pa-ra (26.42), Pha-yom (7.55), Ma-fueang (7.55), Ta-khian Thong (6.60), and A-rang (5.66). The top five species for RDo were Yang Pa-ra (42.79), Palm (10.83), Pha-yom (6.92), Ta-khian Thong (6.29), and A-rang (5.44). The five species with the highest IVI values were Yang Pa-ra (80.16), Pha-yom (21.32), Ta-khian Thong (21.12), A-rang (19.32), and Ma-fueang (15.79) (Table 2). These results indicate that the plant community structure in the RPP is distinctly dominated by Yang Pa-ra, as reflected by its substantially higher RD, RDo, and IVI compared to other tree species. This dominance is consistent with the land-use history and management objective of maintaining a pre-existing economic tree as the principal component of the system, and its high IVI reflects the continuing structural influence of the original rubber plantation within the restored community. The IVI analysis complements the diversity indices by identifying the species that contribute most strongly to the structural organization of the restored community. Unlike the *H′* and *J′* indices, which describe overall community diversity, IVI identifies the individual species that exert the greatest influence on community structure. The consistently high RD, RF, and RDo of Yang Pa-ra resulted in the highest IVI, indicating that it is the principal species shaping the community structure of the RPP. A comparable pattern was reported by Sukprung *et al*. (2021), who evaluated the phytosociological structure of mixed deciduous forests established through active restoration planting approximately 15 and 30 years earlier in northern Thailand. Their restoration approach promoted the establishment of native tree communities. However, only a limited number of species attained markedly higher IVI values than the remaining species, indicating that community structure was still strongly influenced by a few dominant taxa during stand development. Likewise, Yang Pa-ra exhibited substantially higher RD, RF, RDo, and IVI than the other tree species in the present study. However, unlike the restoration sites investigated by Sukprung *et al*. (2021), where species dominance reflected the natural development of restored native forest communities, the dominance of Yang Pa-ra at KVIS primarily resulted from the restoration strategy of retaining the pre-existing rubber plantation while enriching the stand with native forest species. This dominance should not be interpreted as evidence of limited restoration performance. Rosenfield *et al.* (2023) emphasized that ecological integrity should be evaluated using multiple ecological indicators, including species composition, vegetation structure, regeneration, and ecosystem functioning, rather than relying on a single structural characteristic. The relatively high IVI values of several restored forest species, particularly Pha-yom, Ta-khian Thong, and A-rang (Table 2), indicate that these species

have established important structural roles within the rubber-dominated community. Their presence suggests that the RPP supports the coexistence of restored forest species while retaining Yang Pa-ra as its principal economic and structural component.

Table 2 Ecological parameters of tree species within the RPP system at KVIS.

No.	Vernacular name	D	Do	F	RD	RDo	RF	IVI
1	Yang Pa-ra	280	8.88	80	26.42	42.79	10.96	80.16
2	Pha-yom	80	1.44	50	7.55	6.92	6.85	21.32
3	Ta-khian Thong	70	1.31	60	6.60	6.29	8.22	21.12
4	A-rang	60	1.13	60	5.66	5.44	8.22	19.32
5	Ma-fueang	80	0.57	40	7.55	2.76	5.48	15.79
6	Ching-chan	50	0.71	40	4.72	3.43	5.48	13.62
7	Khi-lek Fa-rang	50	0.59	40	4.72	2.84	5.48	13.04
8	Tin-pet Nam	40	0.20	40	3.77	0.97	5.48	10.22
9	Tio Khon	40	0.48	30	3.77	2.32	4.11	10.20
10	Kan-krao	40	0.36	30	3.77	1.76	4.11	9.64
11	Ta-baek Na	40	0.36	30	3.77	1.74	4.11	9.62
12	Yang Na	30	0.55	30	2.83	2.63	4.11	9.57
13	Chong-kho	30	0.21	30	2.83	1.01	4.11	7.95
14	Rang	30	0.15	30	2.83	0.73	4.11	7.67
15	In-tha-nin	20	0.15	20	1.89	0.73	2.74	5.36
16	Chom-phu Nam-dok-mai	20	0.14	20	1.89	0.66	2.74	5.29
17	Muang Lueat	20	0.13	20	1.89	0.60	2.74	5.23
18	Palm	10	2.25	10	0.94	10.83	1.37	13.14
19	Ma-ka Ton	10	0.41	10	0.94	1.99	1.37	4.30
20	Krit-sa-na	10	0.39	10	0.94	1.87	1.37	4.18
21	Pha-yung	10	0.11	10	0.94	0.53	1.37	2.84
22	Sak	10	0.08	10	0.94	0.38	1.37	2.69
23	In-tha-nin Nam	10	0.06	10	0.94	0.31	1.37	2.62
24	Pip	10	0.06	10	0.94	0.28	1.37	2.60
25	Kha-nun	10	0.04	10	0.94	0.17	1.37	2.49
	Total	**1,060**	**20.75**	**730**	**100.00**	**100.00**	**100.00**	**300.00**

In the OP, the survey revealed that the five tree species with the highest RD were Ma-fueang (9.43), Ma-kluea (8.49), A-rang (7.55), Ma-kha Mong (7.55), and Ma-hat (6.60). Regarding RDo, the top five species were Ma-muang (21.77), Ma-hat (9.08), Kha-nun (8.26), Wan Na (6.86), and Ma-fueang (6.28). The five species with the highest IVI values were Ma-muang (30.42), Ma-fueang (24.25), Ma-hat (21.78), Ma-kha Mong (19.54), and Ma-kluea (18.89) (Table 3). These analytical results indicate that the plant community in the OP is not dominated by a single species. This reflects a diverse and complex community structure within the forest restoration area of the OP system at KVIS. Unlike the RPP, no single tree species overwhelmingly dominated the IVI ranking in the OP. Instead, the relatively similar IVI values among Ma-muang, Ma-fueang, Ma-hat, Ma-kha Mong, and Ma-kluea indicate that structural importance is distributed among several tree species rather than concentrated in a single dominant species. Some active mixed-species forest restoration studies have reported that one or a few fast-growing or environmentally well-adapted species attain disproportionately high IVI values during stand development because they establish rapidly and become the principal structural components of the developing forest (Nero, 2021; Silva Junior *et al*., 2026). These dominant species can strongly influence the subsequent development of the regenerating community. In contrast, the OP at KVIS exhibited relatively similar IVI values among its dominant tree species, indicating that no single planted species overwhelmingly controlled community structure. This pattern may reflect the multispecies planting design adopted during restoration, which enabled several tree species with different growth characteristics and ecological roles to establish simultaneously and contribute to stand development. This interpretation is also consistent with the higher H' and J' values observed in the OP, suggesting that the multispecies planting approach successfully promoted the development of a structurally complex and diverse forest community.

Table 3 Ecological parameters of tree species within the OP system at KVIS.

No.	Vernacular name	D	Do	F	RD	RDo	RF	IVI
1	Ma-fueang	100	1.43	70	9.43	6.28	8.54	24.25
2	Ma-kluea	90	0.98	50	8.49	4.30	6.10	18.89
3	Ma-hat	70	2.07	50	6.60	9.08	6.10	21.78
4	A-rang	80	1.31	40	7.55	5.74	4.88	18.17
5	Ma-kha Mong	80	1.07	60	7.55	4.68	7.32	19.54
6	Wan Na	50	1.56	40	4.72	6.86	4.88	16.46
7	Tio Khon	60	1.32	30	5.66	5.80	3.66	15.12
8	Ket	50	0.39	50	4.72	1.69	6.10	12.51
9	Ma-muang	40	4.96	40	3.77	21.77	4.88	30.42
10	Thong Kwao	40	0.51	30	3.77	2.23	3.66	9.67
11	Muang Lueat	40	0.40	40	3.77	1.74	4.88	10.39
12	Ma-kham Pom	30	0.78	30	2.83	3.43	3.66	9.92
13	Ma-rid	30	0.20	30	2.83	0.89	3.66	7.38
14	Kha-nun	20	1.88	20	1.89	8.26	2.44	12.58
15	Cha-muang	20	0.29	20	1.89	1.29	2.44	5.61
16	Sa-ra-phi	20	0.14	10	1.89	0.62	1.22	3.72
17	Sok Ra Ya	20	0.09	20	1.89	0.39	2.44	4.72
18	Bun-nak	20	0.09	10	1.89	0.39	1.22	3.49
19	Lam-duan	20	0.08	10	1.89	0.37	1.22	3.48
20	Op-choei	20	0.07	10	1.89	0.32	1.22	3.42
21	Ma-kha Tae	10	0.56	10	0.94	2.44	1.22	4.60
22	Krit-sa-na	10	0.42	10	0.94	1.86	1.22	4.03
23	Ta-khian Thong	10	0.41	10	0.94	1.81	1.22	3.98
24	Fang	10	0.35	10	0.94	1.54	1.22	3.71
25	Pip	10	0.24	10	0.94	1.06	1.22	3.22
26	Cham-pi	10	0.22	10	0.94	0.98	1.22	3.14
27	Kan-krao	10	0.19	10	0.94	0.84	1.22	3.00
28	Pha-yom	10	0.16	10	0.94	0.71	1.22	2.88
29	In-tha-nin Nam	10	0.15	10	0.94	0.68	1.22	2.84
30	In-tha-ra-chit	10	0.14	10	0.94	0.61	1.22	2.77
31	Ta-baek Na	10	0.09	10	0.94	0.39	1.22	2.56
32	Mang-khut	10	0.07	10	0.94	0.29	1.22	2.46
33	Khae Na	10	0.06	10	0.94	0.27	1.22	2.43
34	Pha-yung	10	0.04	10	0.94	0.19	1.22	2.36
35	Sak	10	0.02	10	0.94	0.10	1.22	2.26
36	Khiam Kha-nong	10	0.02	10	0.94	0.08	1.22	2.24
	Total	**1,060**	**22.78**	**820**	**100.00**	**100.00**	**100.00**	**300.00**

3.3 Aboveground biomass and carbon sequestration within the forest restoration areas at KVIS

The assessment of biomass and carbon sequestration in the RPP revealed a total AGB of 96.99 t/ha. The CS was estimated at 45.59 tC/ha, while the total $CO_{2\text{-seq}}$ and $O_{2\text{-prod}}$ were 167.15 tCO_2/ha and 121.56 tO_2/ha, respectively. The top five tree species contributing most significantly to these values were identical across all parameters: Yang Pa-ra, Pha-yom, Ta-khian Thong, A-rang, and Kan-krao (Table 4). The presence of diverse forest species across various canopy layers enhances structural complexity and supports the distribution of carbon sequestration at the species level (Magurran, 1988). However, this study found that Yang Pa-ra served as the principal structural species in the RPP and contributed the greatest proportion of aboveground biomass and carbon storage. This is reflected by its consistently higher structural indicators, particularly Do and IVI (Table 2), together with its substantially greater AGB and CS than those of all other species (Table 4). The combined interpretation of IVI and CS indicates that the retained Yang Pa-ra trees continued to define both the community structure and aboveground carbon accumulation of the RPP. This pattern is attributable to the retention of mature Yang Pa-ra trees from the original plantation, which possessed larger stem diameters and basal areas, thereby contributing disproportionately to aboveground biomass

and carbon storage. These findings suggest that this restoration approach promotes carbon sequestration potential through carbon concentration, whereby a large proportion of ecosystem carbon is accumulated within a few structurally dominant tree species (Magurran, 1988). A comparable ecological pattern was reported by Pasion *et al.* (2021), who found a strong positive relationship between species dominance (IVI) and carbon density in a tropical forest, with most ecosystem carbon concentrated in a relatively small number of dominant tree species. Their findings emphasized that structurally dominant species contributed disproportionately to ecosystem functioning through aboveground carbon storage, which is consistent with the dominant role of Yang Pa-ra observed in the present study. For O_2 production, it was calculated directly from carbon stock, so its distribution closely mirrored the patterns observed for carbon storage and CO_2 sequestration (Table 4).

Table 4 Aboveground biomass (AGB), carbon stock (CS), CO_2 sequestration ($CO_{2\text{-seq}}$), and O_2 production ($O_{2\text{-prod}}$) within the RPP system at KVIS.

No.	Vernacular name	AGB (t/ha)	CS (tC/ha)	$CO_{2\text{-seq}}$ (tCO_2/ha)	$O_{2\text{-prod}}$ (tO_2/ha)
1	Yang Pa-ra	47.12	22.15	81.21	59.06
2	Pha-yom	7.55	3.55	13.02	9.47
3	Ta-khian Thong	7.11	3.34	12.24	8.91
4	A-rang	5.92	2.78	10.21	7.43
5	Kan-krao	3.64	1.71	6.28	4.57
6	Ching-chan	3.39	1.59	5.84	4.25
7	Yang Na	3.03	1.42	5.22	3.79
8	Khi-lek Fa-rang	3.02	1.42	5.21	3.79
9	Tio Khon	2.55	1.20	4.39	3.19
10	Ma-ka Ton	2.40	1.13	4.14	3.01
11	Krit-sa-na	2.22	1.04	3.82	2.78
12	Ma-fueang	1.69	0.79	2.90	2.11
13	Ta-baek Na	1.54	0.72	2.66	1.93
14	Palm	0.91	0.43	1.57	1.14
15	Chong-kho	0.79	0.37	1.36	0.99
16	Rang	0.64	0.30	1.10	0.80
17	Pha-yung	0.61	0.28	1.04	0.76
18	Tin-pet Nam	0.60	0.28	1.03	0.75
19	In-tha-nin	0.50	0.24	0.86	0.63
20	Muang Lueat	0.47	0.22	0.82	0.60
21	Sak	0.35	0.16	0.60	0.44
22	Chom-phu Nam-dok-mai	0.34	0.16	0.59	0.43
23	In-tha-nin Nam	0.25	0.12	0.43	0.31
24	Pip	0.21	0.10	0.36	0.26
25	Kha-nun	0.13	0.06	0.23	0.16
	Total	**96.99**	**45.59**	**167.15**	**121.56**

The study of the OP revealed a total AGB of 98.36 t/ha, with a total CS of 46.23 tC/ha. The overall $CO_{2\text{-seq}}$ and $O_{2\text{-prod}}$ were estimated at 169.50 tCO_2/ha and 123.28 tO_2/ha, respectively. The top five species contributing most significantly to these parameters were identical: Ma-muang, Ma-hat, Kha-nun, A-rang, and Wan Na (Table 5). However, the values of the dominant species (Ma-muang) differed only slightly from those of the second-ranked species (Ma-hat), followed by a gradual decline among the remaining dominant species (Table 5). This pattern contrasts markedly with that observed in the RPP, where Yang Pa-ra contributed disproportionately more biomass and carbon than all other species. These findings indicate that forest restoration using the OP system promotes carbon sequestration through carbon distribution, whereby biomass and carbon are allocated across several co-dominant tree species rather than being concentrated in a single dominant species (Magurran, 1988). A similar ecological pattern has been reported in mixed-species forests, where greater species diversity promotes biomass accumulation and enhances ecosystem carbon storage through the collective contribution of multiple tree species rather than reliance on a single dominant species (Zhang *et al*., 2026). Moreover, Ahmad *et al.* (2025) demonstrated that polyculture forests generally store more biomass carbon than less diverse stands, emphasizing that stand structure and species diversity together contribute to carbon–diversity conservation. These findings are consistent with the relatively balanced carbon

contributions observed among the dominant tree species in the OP, indicating that carbon storage resulted from the combined contribution of several co-dominant species rather than from a single structurally dominant taxon. The distribution of estimated O_2 production also closely followed the carbon storage pattern, with no single species overwhelmingly dominating O_2 production in the OP (Table 5). This pattern is consistent with the higher *H'*, *J'*, and relatively balanced IVI values observed in the OP (Tables 3 and 5), suggesting that species composition, community structure, and carbon storage developed concurrently within the restored stand. The combined interpretation of diversity indices, IVI, and carbon storage indicates that multiple tree species contributed to both community structure and ecosystem functioning in the OP restoration system, supporting the concept of ecological integrity proposed by Rosenfield *et al*. (2023). In addition, forest communities in which biomass and carbon are distributed among multiple tree species may exhibit greater ecological stability than communities where biomass is concentrated within only a few dominant species (Magurran, 1988).

Table 5 Aboveground biomass (AGB), carbon stock (CS), CO_2 sequestration ($CO_{2\text{-seq}}$), and O_2 production ($O_{2\text{-prod}}$) within the OP system at KVIS.

No.	Vernacular name	AGB (t/ha)	CS (tC/ha)	$CO_{2\text{-seq}}$ (tCO_2/ha)	$O_{2\text{-prod}}$ (tO_2/ha)
1	Ma-muang	17.99	8.46	31.01	22.55
2	Ma-hat	12.44	5.85	21.44	15.59
3	Kha-nun	9.95	4.68	17.14	12.47
4	A-rang	6.87	3.23	11.85	8.61
5	Wan Na	6.50	3.05	11.20	8.15
6	Ma-kha Mong	5.11	2.40	8.81	6.41
7	Tio Khon	5.08	2.39	8.76	6.37
8	Ma-kluea	4.37	2.05	7.53	5.48
9	Ma-fueang	4.15	1.95	7.16	5.21
10	Ma-kham Pom	3.57	1.68	6.16	4.48
11	Ma-kha Tae	3.00	1.41	5.17	3.76
12	Krit-sa-na	2.33	1.09	4.01	2.92
13	Ta-khian Thong	2.06	0.97	3.55	2.58
14	Cha-muang	1.87	0.88	3.22	2.34
15	Thong Kwao	1.80	0.85	3.10	2.26
16	Cham-pi	1.40	0.66	2.41	1.75
17	Muang Lueat	1.38	0.65	2.39	1.73
18	Fang	1.11	0.52	1.91	1.39
19	Ket	1.05	0.49	1.81	1.32
20	Kan-krao	1.05	0.49	1.81	1.31
21	Ma-rid	0.72	0.34	1.24	0.90
22	Pip	0.69	0.33	1.19	0.87
23	In-tha-nin Nam	0.59	0.28	1.02	0.74
24	In-tha-ra-chit	0.59	0.28	1.01	0.74
25	Pha-yom	0.55	0.26	0.94	0.68
26	Sa-ra-phi	0.42	0.20	0.73	0.53
27	Ta-baek Na	0.33	0.15	0.56	0.41
28	Bun-nak	0.27	0.13	0.46	0.33
29	Lam-duan	0.26	0.12	0.46	0.33
30	Sok Ra Ya	0.20	0.10	0.35	0.26
31	Pha-yung	0.14	0.07	0.24	0.18
32	Op-choei	0.14	0.06	0.24	0.17
33	Khae Na	0.14	0.06	0.23	0.17
34	Mang-khut	0.13	0.06	0.23	0.17
35	Sak	0.05	0.03	0.09	0.07
36	Khiam Kha-nong	0.03	0.01	0.05	0.04
	Total	**98.36**	**46.23**	**169.50**	**123.28**

A comparative assessment of the two restoration systems showed that the RPP and OP achieved comparable AGB, CS, $CO_{2\text{-seq}}$, and $O_{2\text{-prod}}$, with the OP exhibiting slightly higher values. Although both restoration systems attained similar levels of aboveground carbon storage, they achieved this outcome through contrasting structural pathways. In the RPP, carbon accumulation was primarily associated with the structural dominance of retained Yang Pa-ra trees. In contrast, carbon storage in the OP resulted from the collective contribution of several co-dominant species. These contrasting patterns demonstrate that comparable ecosystem carbon stocks can be achieved under different restoration strategies and community structures (Ahmad *et al.*, 2025). The present findings provide additional evidence that restoration systems with contrasting community structures can achieve similar levels of aboveground carbon storage through different ecological pathways. Both restoration models function as effective aboveground carbon sinks, supporting previous findings on the carbon sequestration potential of tree-based restoration systems (Ahmad *et al.*, 2025; Zhang *et al*., 2026). Ultimately, these systems contribute to greenhouse gas mitigation while simultaneously enhancing biodiversity, structural complexity, and the long-term sustainability of integrated land-use systems. Since this study represents a case study, the findings reflect the restoration potential and ecological characteristics of the specific forest restoration areas investigated. Therefore, applying or scaling the RPP or OP systems to other areas should consider site-specific factors, including tree species composition, restoration strategy, land-use management, stand age, and local ecological conditions, to maximize forest restoration success and carbon sequestration efficiency.

This study has data collection limitations because the assessment of biomass and carbon sequestration considered only aboveground trees, excluding belowground biomass, litter, deadwood, the root system, and soil organic carbon. This may result in the estimated total ecosystem carbon stock being lower than the reality. However, these results remain useful in demonstrating the role of educational institutions in restoring degraded forests to regain biodiversity while integrating agricultural use within the same area. The present dataset also provides an important baseline for long-term monitoring of restoration performance, allowing future evaluations of biomass accumulation and carbon sequestration trajectories as these restored forest stands continue to develop. These results improve the understanding of biomass accumulation and carbon sequestration within integrated restoration systems and provide valuable information for forest restoration planning, sustainable land-use management, and future carbon credit initiatives. Furthermore, the dataset may support the development of Measurement, Reporting, and Verification (MRV) frameworks for greenhouse gas mitigation projects in the forestry and agricultural sectors (Intergovernmental Panel on Climate Change, 2006; Thailand Greenhouse Gas Management Organization, 2016).

4. Conclusion

The study of restored forest areas using the RPP and OP systems at KVIS revealed that: The overall plant community comprised 47 species, 38 genera, and 24 families. The RPP contained 25 species (21 genera, 15 families), while the OP contained 36 species (31 genera, 20 families). Both systems featured four distinct canopy layers (Emergent, Main Canopy, Understory, and Ground Layer), indicating complex ecosystem structures and high tree species diversity. The RPP community had a D of 1,060 stems/ha, Do of 20.75 m^2/ha, *H'* of 2.75, and *J'* of 0.85, with a clear dominance by Yang Pa-ra. The OP also had a D of 1,060 stems/ha but showed slightly higher ecological indices: Do of 22.78 m^2/ha, *H'* of 3.34, and *J'* of 0.93. Unlike the RPP, the OP was not dominated by any single species. Regarding biomass and carbon sequestration, the RPP recorded an AGB of 96.99 t/ha, CS of 45.59 tC/ha, $CO_{2\text{-seq}}$ of 167.15 tCO_2/ha, and $O_{2\text{-prod}}$ of 121.56 tO_2/ha, characterized by carbon concentration in dominant species. The OP values were slightly higher: AGB of 98.36 t/ha, CS of 46.23 tC/ha, $CO_{2\text{-seq}}$ of 169.50 tCO_2/ha, and $O_{2\text{-prod}}$ of 123.28 tO_2/ha, exhibiting a balanced carbon distribution across multiple species. Overall, restoring degraded forests at KVIS through RPP or OP models not only enhances biodiversity and promotes integrated land use but also significantly increases biomass and carbon sequestration potential. These findings serve as a case study for planning and managing degraded forest restoration elsewhere to achieve sustainable and integrated resource utilization in the long term.

5. Acknowledgments

The authors would like to express their sincere gratitude to KVIS for providing the research site and facilities. Special thanks are extended to the KVIS Eco & Low Carbon School Student Committee for their coordination and assistance throughout the research activities. Finally, we would like to thank Mr. Tammarat Kamawanit for his support during the fieldwork within the forest restoration plots at KVIS.

6. References

Ahmad, A., Khan, M., Ahmad, T., Ahmad, S., Ullah, S. and Farooqi, A. 2025. Carbon dynamics with stand structure and species diversity in the Hindu Kush Himalaya ranges of Pakistan. **Scientific Reports** 15(1): 35440.

Atkinson, J., Brudvig, L.A., Mallen-Cooper, M., Nakagawa, S., Moles, A.T. and Bonser, S.P. 2022. Terrestrial ecosystem restoration increases biodiversity and reduces its variability, but not to reference levels: A global meta-analysis. **Ecology Letters** 25(7): 1725-1737.

Chazdon, R.L., Norden, N., Colwell, R.K. and Chao, A. 2023. Monitoring recovery of tree diversity during tropical forest restoration: Lessons from long-term trajectories of natural regeneration. **Philosophical Transactions of the Royal Society B: Biological Sciences** 378(1867): 20210069.

da Rosa, C.M. and Marques, M.C. 2022. How are biodiversity and carbon stock recovered during tropical forest restoration? Supporting the ecological paradigms and political context involved. **Journal for Nature Conservation** 65: 126115.

da Silva Junior, R.G., Ângelo, A.C., Cosmo, N.L., Rios, R.C., Bressiani, L.S.T., Mastella, A.D.F., Schneider, C.R., de Souza, K.K.F., Isernhagen, I., Capellesso, E.S. and Oliveira, E.S. 2026. Effect of planting mixed and facilitating species on the regenerating community. **Brazilian Journal of Botany** 49: 21.

Dangwal, B., Rana, S.K., Negi, V.S. and Bhatt, I.D. 2022. Forest restoration enhances plant diversity and carbon stock in the sub-tropical forests of western Himalaya. **Trees, Forests and People** 7: 100201.

Hasannudin, D.A.L., Nurrochmat, D.R. and Ekayani, M. 2022. Agroforestry management systems through landscape-life scape integration: A case study in Gowa, Indonesia. **Biodiversitas** 23(4): 1864-1874.

Hytönen, J., Kaakkurivaara, N., Kaakkurivaara, T. and Nurmi, J. 2018. Biomass equations for rubber tree (*Hevea brasiliensis*) components in southern Thailand. **Journal of Tropical Forest Science** 30(4): 588–596.

Intergovernmental Panel on Climate Change. 2006. **2006 IPCC guidelines for national greenhouse gas inventories, Volume 4: Agriculture, forestry and other land use**. The Institute for Global Environmental Strategies, Hayama.

Intergovernmental Panel on Climate Change. 2022. **Climate Change 2022: Mitigation of Climate Change. Contribution of Working Group III to the Sixth Assessment Report of the Intergovernmental Panel on Climate Change**. Cambridge University Press, Cambridge.

Keller, N., Niklaus, P.A., Ghazoul, J., Marfil, T., Godoong, E. and Philipson, C.D. 2023. Biodiversity consequences of long-term active forest restoration in selectively-logged tropical rainforests. **Forest Ecology and Management** 549: 121414.

Koch, A. and Kaplan, J.O. 2022. Tropical forest restoration under future climate change. **Nature Climate Change** 12(3): 279-283.

Koutika, L.S. 2022. Boosting C sequestration and land restoration through forest management in tropical ecosystems: A mini-review. **Ecologies** 3(1): 13-29.

Kutintara, U. 1999. **The Basic Ecological for Forestry**. Faculty of Forestry, Kasetsart University, Bangkok. (in Thai)

Magurran, A.E. 1988. **Ecology Diversity and Its Measurement**. Croom Helm, London.

Marod, D. and Kutintara, U. 2009. **Forest Ecology**. Faculty of Forestry, Kasetsart University, Bangkok. (in Thai)

Murniati, Suharti, S., Minarningsih, Nuroniah, H.S., Rahayu, S. and Dewi, S. 2022. What makes agroforestry a potential restoration measure in a degraded conservation forest?. **Forests** 13(2): 267.

Nero, B.F. 2021. Structure, composition and diversity of restored forest ecosystems on mine-spoils in South-Western Ghana. **PLoS One** 16(6): e0252371.

Ogawa, H., Yoda, K., Ogino, K. and Kira, T. 1965. Comparative ecological studies on three main type of forest vegetation in Thailand. II. Plant biomass. **Nature and Life in Southeast Asia** 4: 49-80.

Pasion, B.O., Barrias, C.D.P., Asuncion, M.P., Angadol, A.H., Pabiling, R.P., Pasion Jr., A., Braulio, A.A., and Baysa Jr., A.M. 2021. Assessing tree diversity and carbon density of a riparian zone within a protected area in southern Philippines. **Journal of Asia-Pacific Biodiversity** 14(1): 78-86.

Pearson, T., Walker, S. and Brown, S. 2005. **Sourcebook for Land Use, Land-Use Change and Forestry Projects**. World Bank, Washington, D.C.

Perles-Garcia, M.D., Kunz, M., Fichtner, A., Härdtle, W. and von Oheimb, G. 2021. Tree species richness promotes an early increase of stand structural complexity in young subtropical plantations. **Journal of Applied Ecology** 58(10): 2305-2314.

Pielou, E.C. 1975. **Ecological Diversity**. John Wiley & Sons, New York.

Rosenfield, M.F., Jakovac, C.C., Vieira, D.L.M., Poorter, L., Brancalion, P.H.S., Vieira, I.C.G., de Almeida, D.R.A., Massoca, P., Schietti, J., Albernaz, A.L.M., Ferreira, M.J. and Mesquita, R.C.G. 2023. Ecological integrity of tropical secondary forests: Concepts and indicators. **Biological Reviews** 98(2): 662-676.

Thailand Greenhouse Gas Management Organization. 2016 **Thailand Voluntary Emission Reduction Program Reference Manual: Forestry and Agriculture Sector**. Thailand Greenhouse Gas Management Organization (Public Organization), Bangkok. (in Thai)

Uttaruk, Y., Khoa, P.V. and Laosuwan, T. 2024. A guideline for greenhouse gas emission reduction and carbon sequestration in forest sector based on Thailand voluntary emission reduction programme. **Sains Malaysiana** 53(3): 477-486.

Siarudin, M., Rahman, S.A., Artati, Y., Indrajaya, Y., Narulita, S., Ardha, M.J. and Larjavaara, M. 2021. Carbon sequestration potential of agroforestry systems in degraded landscapes in West Java, Indonesia. **Forests** 12(6): 714.

Siddesh, R., Pathak, H., Chavan, S.B., Halli, H.M., Kakade, V.D., Morade, A.S., Salunkhe, S., Nangare, D.D., Salunkhe, V.N., Singh, A.K., Pradhan, A. and Reddy, K.S. 2025. Fruit tree-based restoration strategy to mitigate greenhouse gas emissions, and enhance the profitability of degraded land in semi-arid tropics. **Science of The Total Environment** 1000: 18049.

Smitinand, T. 2014. **Thai Plant Names**. The Forest Herbarium, Department of National Parks, Wildlife and Plant Conservation, Bangkok. (in Thai)

Sukprung, T., Maelim, S. and Teejuntuk, S. 2021. Restoration on mixed deciduous forest at Mae Thang Watershed Conservation and Development Study Unit, Phrae province. **Thai Journal of Science and Technology** 10(2): 208-222.

Zhang, H., Feng, H., Qu, X., Yang, M., Huang, M., Jacobs, D.F. and Guo, J. 2026. Species mixing promotes plant biomass accumulation and nutrient cycling in forest plantations. **Communications Biology** 9(1): 348.

Recent Science and Technology 2026, Vol. 18(3): e271202

Recent Science and Technology

Journal homepage: https:// www.tci-thaijo.org/index.php/rmutsvrj/index

ISSN: 3057-0786 (Online)

Research Article

Detection of Chronic Load Imbalance and Hot-Spot Risk in Building Electrical Systems using Long-Term Three-Phase Current Analysis and Mechanism-Informed Artificial Intelligence

Sittisak Rojchaya [a *] and Santi Karisan [b]

[a] *Department of Electrical Engineering, Faculty of Engineering and Technology, Rajamangala University of Technology Srivijaya, Sikao, Trang 92150, Thailand.*

[b] *College of Industrial Technology and Management, Rajamangala University of Technology Srivijaya, Khanom, Nokhon Si Thammarat 80210, Thailand.*

Article history:

Received: 2026-03-11
Revised: 2026-08-02
Accepted: 2026-08-07

Keywords:

Chronic load imbalance;
Thermal memory;
Insulation aging

ABSTRACT

Infrared thermography detects hot spots only at the time of inspection, whereas electrical system degradation evolves continuously through the 24/7 accumulation of operational stress. This study proposes a novel mechanism-informed predictive monitoring framework that integrates long-term three-phase current data with a physics-guided machine-learning inference model to identify early degradation signatures before infrared-detectable heating occurs. Results synthesized from multiple degradation indicators reveal that Phase B exhibits persistent structural dominance, with a mean occupancy of 56% (peaking at 71%), and accumulates 2.35 times the thermal debt of Phase A. This imbalance produces pronounced thermal memory, whereby 38% of thermal stress remains unrecovered after load reduction, resulting in the fastest insulation aging (aging rate = 0.0028; final Aging Index = 0.95). Notably, the proposed system degradation collapse index exceeds the critical degradation threshold (0.70) despite the absence of overload or fault conditions under conventional protection criteria. The proposed framework provides a continuous, low-cost, and practical solution for 24/7 predictive condition monitoring, enabling electrical hazards to be identified before hot spots and failures occur while overcoming the limitations of snapshot-based inspections.

© 2026 Rojchaya, S. and Karisan, S. Recent Science and Technology published by Rajamangala University of Technology Srivijaya

1. Introduction

Electrical systems in modern buildings are typically designed and evaluated within threshold-based safety frameworks, such as maximum current limits, allowable temperature rise, and maintenance standards defined by international codes and guidelines (Huang *et al*., 2011). Cable ampacity and thermal limits are commonly assessed under steady-state or cyclic assumptions, as prescribed in international standards, which primarily focus on short-term safety margins rather than long-term degradation behavior (Rasoulpoor *et al*., 2017). However, extensive field experience and recent studies indicate that electrical failures and hot-spot formation in main feeders and electrical equipment often result not from direct overloads or fault events, but from progressive degradation accumulated during prolonged normal operation (Choudhary *et al.*, 2022; Theofanous *et al.*, 2025; AlShaikh Saleh *et al.*, 2025). Conventional inspection practices, particularly infrared thermography, are widely adopted because of their non-contact capability and practical applicability in electrical maintenance. Nevertheless, infrared inspections are inherently limited to capturing thermal conditions only at the moment of observation, thereby reflecting end-stage symptoms rather than the underlying degradation mechanisms within the system (Ruiz and Betancourt, 2026; Enescu *et al.*, 2020). In contrast, conductor and insulation degradation evolves through the continuous 24/7 accumulation of electro-thermal stress,

* **Corresponding author.**

E-mail address: *sittisak.r@rmutsv.ac.th*

Cite this article as: Rojchaya, S. and Karisan, S. 2026. Detection of Chronic Load Imbalance and Hot-Spot Risk in Building Electrical Systems using Long-Term Three-Phase Current Analysis and Mechanism-Informed Artificial Intelligence. **Recent Science and Technology** 18(3): e271202.
https://doi.org/10.65411/rst.2026.271202

occurring not only during peak loading but also under low-load conditions and periods when the system appears to operate normally (Tao *et al.,* 2025; Zhang *et al.,* 2024). Such cumulative thermal exposure accelerates insulation ageing and alters thermo-mechanical behavior, even when operating temperatures remain within conventional limits (Hu *et al.,* 2025; Ahmad *et al.,* 2025; AlShaikh Saleh *et al.,* 2025). Consequently, significant risks often remain undetected until observable hot spots or electrical accidents have already occurred. This challenge is particularly pronounced in educational buildings and public facilities, where electricity consumption patterns vary across daily and seasonal cycles and are strongly influenced by spatial load distribution (Melo *et al.,* 2023; Santamouris and Vasilakopoulou, 2021). These environments commonly exhibit structurally unbalanced three-phase loading patterns that may be insufficient to trigger protective devices or violate operational thresholds, yet still induce persistent heat accumulation, thermal stress retention (thermal memory), and accelerated long-term insulation ageing (Pan *et al.,* 2021; Choudhary *et al.,* 2022). Such degradation mechanisms remain insufficiently addressed within traditional monitoring and protection paradigms.

To address this gap, this study proposes a novel mechanism-informed predictive monitoring and analysis framework based on long-term three-phase current measurements obtained from real-world operation, integrated with mechanism-informed artificial intelligence. Recent advances in physics-informed and hybrid data-driven approaches demonstrate that embedding physical knowledge into analytical models significantly improves interpretability and robustness in condition monitoring applications (Wu *et al.*, 2024; Oelhaf *et al.,* 2025). Recent studies have further demonstrated that advanced artificial intelligence and machine learning techniques substantially improve intelligent condition monitoring, fault localization, and predictive maintenance of power cable systems under complex operating conditions (Shao *et al.,* 2025; Abdolahi *et al.,* 2026). Unlike conventional AI-based condition monitoring methods that primarily detect anomalies from historical measurement patterns, the proposed framework integrates electro-thermal degradation mechanisms with artificial intelligence to infer hidden degradation processes and continuously quantify degradation evolution under normal operating conditions. By enabling the identification of structural phase imbalance, cumulative thermal debt, and early degradation signatures before the appearance of infrared-detectable hot spots, the proposed framework shifts the monitoring paradigm from "detecting heating after it occurs" to "predicting degradation before heating becomes observable". This work demonstrates that electrical system degradation in buildings can be continuously monitored in a safe, low-cost, and non-intrusive manner, while employing infrared thermography solely as a validation tool rather than the primary monitoring method, thereby opening a practical pathway for proactive risk management and accident prevention in modern building electrical systems (Al-Dulaimi *et al.,* 2024; Tao *et al.,* 2025; Abdolahi *et al.,* 2026).

2. Theoretical Framework

2.1 Load imbalance in electrical distribution systems

Load imbalance in three-phase electrical distribution systems occurs when the currents in each phase are not equally distributed due to uneven load allocation. Such imbalance conditions may lead to increased neutral currents, additional power losses, conductor overheating, and accelerated degradation of electrical insulation. Persistent or chronic load imbalance can significantly affect system reliability and operational lifetime. A commonly used indicator for quantifying phase current imbalance is the current imbalance index, defined as

$$I_{imb} = \frac{I_{max} - I_{avg}}{I_{avg}} \times 100 \quad (1)$$

where I_{max} represents the maximum phase current and I_{avg} denotes the average current across the three phases. Although this conventional imbalance index provides a useful measure of instantaneous load asymmetry, it does not adequately represent the cumulative thermal effects associated with prolonged imbalance conditions. Chronic imbalance may gradually increase conductor temperature and accelerate insulation aging even when instantaneous imbalance values appear moderate.

2.2 Electro-thermal behaviour of conductors

Electrical conductors carrying unbalanced currents experience unequal heating due to different Joule losses in each phase. The temperature evolution of a conductor can be described using an electro-thermal energy balance model.

$$C\frac{dT}{dt} = P_{loss} - P_{cool} \quad (2)$$

where T represents conductor temperature, C denotes the thermal capacitance of the conductor, P_{loss} is the heat generated by electrical losses, and P_{cool} represents heat dissipation to the surrounding environment. The electrical heating term can be expressed as

$$P_{loss} = I^2 R \quad (3)$$

where I is the conductor current and R is the electrical resistance. In unbalanced operating conditions, unequal phase currents result in different heating levels across phases, which may cause thermal divergence between conductors and increase the risk of insulation degradation.

2.3 Thermal aging of insulation

The degradation of electrical insulation materials is strongly influenced by temperature. Elevated temperatures accelerate

chemical reactions within insulation materials, leading to progressive deterioration of dielectric strength.

The temperature-dependent aging acceleration factor can be expressed as

$$A = e^{\lambda_k T} \quad (4)$$

where A represents the insulation aging acceleration factor, T denotes the conductor temperature, and λ_k is the thermal aging coefficient.

The coefficient λ_k reflects the sensitivity of insulation degradation to temperature variations and is derived from Arrhenius-based thermal aging theory. This formulation captures the exponential relationship between temperature rise and the rate of insulation deterioration. Higher operating temperatures therefore significantly increase the aging acceleration factor, indicating faster insulation degradation under prolonged thermal stress.

2.4 Thermal memory effect

Electrical conductors exhibit thermal inertia, meaning that temperature changes occur gradually and depend on both present and past loading conditions. This behavior is commonly referred to as the thermal memory effect. The thermal memory index can be represented as:

$$M(t) = \int_0^t e^{-\beta(t-\tau)} T(\tau) d\tau \quad (5)$$

where $M(t)$ represents the thermal memory index, $T(\tau)$ denotes the conductor temperature at time τ, and β is the thermal decay coefficient.

This formulation accounts for the persistence of thermal stress within the conductor. Even after load reductions, residual heat may remain in the system, continuing to influence temperature evolution and insulation aging.

2.5 Severity of dynamic current imbalance (SDCI)

To evaluate the long-term impact of load imbalance on conductor health, a composite severity indicator referred to as the Severity of Dynamic Current Imbalance (SDCI) is proposed. Unlike conventional imbalance indices, the SDCI integrates insulation aging, electro-thermal stress and thermal memory into a unified mechanism-informed indicator for long-term degradation assessment. The SDCI is defined as

$$SDCI = \omega_1 A_n + \omega_2 T_n + \omega_3 M_n \quad (6)$$

where A_n, T_n and M_n denote the normalized insulation aging factor, conductor temperature deviation, and thermal memory index, respectively. Each component is normalized to the range of 0-1 using min-max normalization before integration to eliminate unit differences and ensure balanced contribution. The weighting coefficients satisfy

$$\omega_1 + \omega_2 + \omega_3 = 1 \quad (7)$$

In this study, $\omega_1 = 0.5$, $\omega_2 = 0.3$ and $\omega_3 = 0.2$. The weights were assigned according to the physical importance of each degradation mechanism, where insulation aging is considered the dominant indicator of long-term cable deterioration, followed by conductor temperature and thermal memory.

The SDCI ranges from 0 to 1, with larger values indicating more severe cumulative degradation. Based on the eight-month field monitoring data, an SDCI value of 0.70 was selected as the engineering early-warning threshold because it consistently corresponded to persistent phase imbalance, significant thermal memory, and accelerated insulation aging. This threshold represents the onset of critical degradation rather than immediate system failure, enabling proactive maintenance before infrared-detectable hot spots or protection-device operation occur. By combining electro-thermal behavior with insulation-aging mechanisms into a single physics-informed index, the proposed SDCI provides a more comprehensive assessment of long-term conductor health than conventional current imbalance indices.

3. Materials and Methods

3.1 Installation of electrical energy meters in the building power distribution system

This study employs three-phase current data (Phases A, B, and C) obtained from an operating low-voltage power distribution system, measured using non-intrusive current sensing techniques to avoid disturbing system operation. The currents were recorded continuously over several months, encompassing both low- and high-load conditions representative of actual building usage. The resulting dataset provides sufficient temporal resolution to capture long-term trends and cumulative effects of thermal cycling, rather than short-duration transient events.

3.2 Long-term electricity usage data acquisition and recording framework

The electricity usage data acquisition process in this study was specifically designed to support long-term, mechanism-informed analysis of chronic load imbalance and progressive thermal stress accumulation in a building electrical system. Rather than focusing on short-term or snapshot measurements, the proposed framework emphasizes continuous monitoring to capture slow-evolving degradation mechanisms that develop under normal operating conditions.

Electrical data were collected from the Main Distribution Board (MDB), which serves as the central aggregation point of three-phase electrical loads supplying the building. Three-phase

line currents were measured using non-intrusive Clamp Meters (CMs) installed on the incoming feeder conductors inside the MDB. This non-intrusive measurement approach enables continuous monitoring without interrupting normal system operation or introducing additional electrical or thermal stress into the system. The analog current signals acquired by the Clamp Meters were processed through a signal conditioning stage to ensure measurement stability, noise suppression, and compatibility with digital data acquisition requirements. The conditioned signals were then transmitted to a Gateway device, which functions as the communication interface between field-level measurement units and the remote data infrastructure. Wireless communication between the Clamp Meters and the Gateway was implemented using Bluetooth version 4.1, operating within the 2.402-2.48GHz industrial, scientific, and medical (ISM) frequency band. This communication scheme provides reliable short-range data transfer with low power consumption and sufficient robustness for continuous, long-duration monitoring applications. The Gateway aggregates the three-phase current data and uploads them to a centralized Data Center at a fixed temporal resolution of one minute. This sampling interval was selected to balance data resolution and storage efficiency while remaining adequate to capture long-term load asymmetry, thermal cycling behavior, and cumulative stress effects associated with Joule (I^2R) heating, which evolve gradually rather than instantaneously. All recorded data were stored in comma-separated values (CSV) format, ensuring transparency, reproducibility, and seamless integration with subsequent analytical and modeling workflows. Authorized users can access the Data Center remotely via Internet-connected devices using a browser-based interface, allowing data visualization, retrieval, and direct download without physical access to the electrical installation. The graphical user interface used for data access and retrieval is illustrated in Figure 3. In this study, three-phase current data were recorded continuously over a period of eight months, from 1 December 2024 to 31 July 2025. This extended monitoring duration covers normal operating conditions, daily and weekly load cycles, off-hour usage, and seasonal variations. The resulting long-term dataset provides a robust empirical foundation for subsequent analyses, including structural phase dominance assessment, cumulative thermal debt estimation, identification of thermal memory and hysteresis effects, insulation aging trajectory modeling, and synthesis of the System Degradation Collapse Index (SDCI). By prioritizing continuous, long-term data acquisition over snapshot-based inspection, the proposed recording framework enables early detection of hidden degradation mechanisms that precede infrared-detectable hot-spot formation. This approach supports predictive risk assessment and enhances the ability to identify electrical system vulnerabilities before the onset of visible thermal anomalies or safety-critical failures.



Figure 1 Clamp-on current measuring device (Clamp Meter) installed on a feeder conductor inside the Main Distribution Board (MDB).

3.3 Feature extraction

The features used in this study were categorized into two groups. The first group consists of twelve mechanism-informed indicators derived from long- term three- phase current measurements and subsequent processing, as presented in Table 1. These indicators include phase occupancy shares for Phases A, B, and C (structural phase dominance), normalized cumulative values representing thermal debt accumulation, mean values characterizing phase stress signatures, and phase- specific Aging Indices describing accelerated insulation degradation. Together, these twelve indicators capture structural load asymmetry, cumulative thermal stress, stress concentration, and long-term aging behavior of the system. The second group consists of an analytically derived feature, namely the Unbalance Current, calculated using the formulation defined in Equation (1). This feature quantifies instantaneous phase asymmetry and complements the long-term indicators by linking current imbalance to the underlying degradation mechanisms.

3.4 SDCI parameter determination

The parameters of the proposed Severity of Dynamic Current Imbalance (SDCI) were determined using the long-term three- phase current measurements collected in this study. The measured currents were first used to estimate the conductor temperature according to the electro-thermal model, after which the insulation aging acceleration factor (A) and thermal memory index (M) were calculated using Equations (4) and (5), respectively. To ensure comparable contributions, all parameters (A, T, and M) were normalized to the range of 0- 1 before integration. The weighting coefficients were assigned as $\omega_1 = 0.5$, $\omega_2 = 0.3$ and $\omega_3 = 0.2$ based on the relative physical importance of insulation aging, conductor temperature, and thermal memory in long- term electro- thermal degradation. The critical threshold (SDCI = 0.70) was established empirically from the eight- month field dataset, where values at or above this level consistently corresponded to persistent phase imbalance,

accelerated insulation aging, and cumulative thermal stress. Finally, the normalized parameters were combined using Equation (6) to obtain the SDCI for continuous condition monitoring and early degradation assessment.

4. Results and Discussion

4.1 Feature importance and overall contribution to unbalance current

As shown in Figure 5 (Normalized Cumulative Thermal Debt) and summarized in Table 1, Phase B is the primary contributor to current unbalance in the system. Phase B exhibits the highest phase occupancy share (mean = 0.56, max = 0.71), resulting in a consistently higher rate of thermal debt accumulation compared to Phases A and C. By the end of the operational period, Phase B reaches a normalized thermal debt of 1.00, which is 2.35 times that of Phase A (0.42) and 1.59 times that of Phase C (0.63). The persistent dominance of Phase B in Figure 5 indicates cumulative thermal stress rather than transient imbalance effects. This behavior is further supported by the highest mean I^2 stress (185 A^2) and aging growth rate (λ = 0.0028), leading to a final aging index of 0.95. These results confirm that long-term current unbalance is governed by cumulative feature dominance and thermal memory effects, even in the absence of overload or fault conditions.

4.2 Power-driven phase imbalance characteristics

Figure 6 presents the Phase Stress Asymmetry Signature, derived from mean I^2 values, which directly represent Joule-loss-induced electrical stress. The results reveal a severe stress concentration in Phase B, with a mean I^2 value of 185A^2, compared to 38A^2 for Phase A and 82A^2 for Phase C. This corresponds to Phase B experiencing 4.9× higher stress than Phase A and 2.3× higher stress than Phase C. Figure 7 further exposes the thermal memory loop of Phase B, demonstrating that a significant fraction of thermal stress persists even after load reduction. Quantitatively, Phase B exhibits a 38% thermal recovery deficit, indicating that more than one- third of accumulated thermal stress remains unrecovered between load cycles. Together, Figures 6 and 7 confirm that persistent power dominance in Phase B drives not only instantaneous stress asymmetry but also long- term thermal hysteresis, which conventional snapshot inspections cannot capture.

4.3 Role of electric current and its coupling with power

Although electric current exhibits relatively low direct importance in the Random Forest model (0.58–1.37%), Figures 8 and 9 reveal its critical coupling role with power. Figure 8 shows a perfectly linear relationship between Phase B load level and imbalance magnitude, with a correlation coefficient of r = 1.0, confirming that current acts as a deterministic carrier of power imbalance. Notably, Phase A, despite having the lowest average current (4.12A, compared to 9.89A in Phase B and 4.74A in Phase C), contributes 75.17% to unbalance current prediction. This apparent paradox is resolved by Figure 9, which demonstrates inter- phase coupling distortion, whereby stress originating in a structurally dominant phase propagates into other phases. Thus, current does not independently generate imbalance but amplifies imbalance induced by asymmetric power distribution, reinforcing the system- level nature of degradation mechanisms.

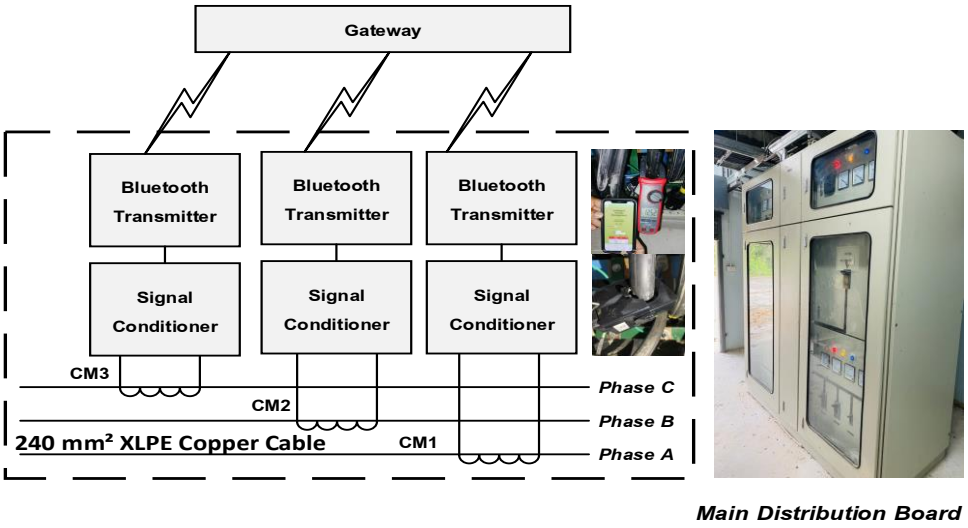


Figure 2 Installation of a real-time energy monitoring system and comparison of its measurement accuracy with a standard reference instrument.

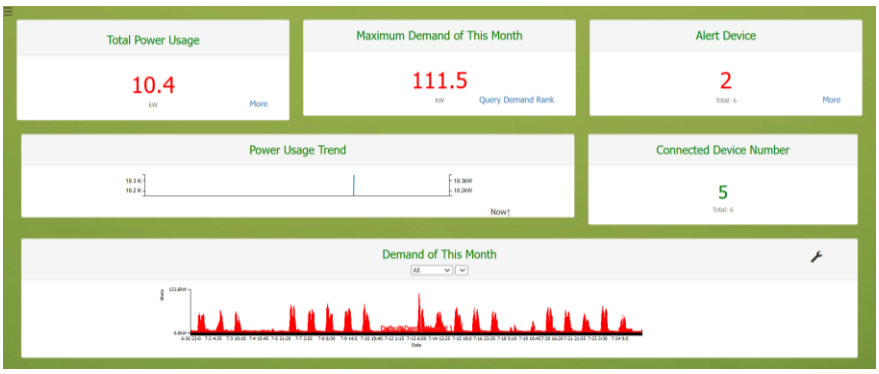


Figure 3 Overview of electrical energy consumption and operational data of the building electrical system in real time.

Table 1 Key quantitative results of chronic load imbalance and degradation analysis.

Metric	Phase A	Phase B	Phase C	Interpretation
Phase Occupancy Share (mean)	0.21	0.56 (max 0.71)	0.23	Phase B exhibits persistent structural dominance
Normalized Thermal Debt ($\sum I^2$)	0.42	1.00 (2.35× Phase A)	0.63	Highest cumulative thermal stress in Phase B
Mean I² Stress (A²)	38	185	82	Severe stress concentration in Phase B
Thermal Recovery Deficit	-	38%	-	Strong thermal memory after load reduction
Aging Growth Rate (day^{-1})	0.0011	0.0028	0.0016	Fastest insulation aging in Phase B
Final Aging Index	0.42	0.95	0.58	Phase B approaches critical insulation degradation
System Degradation Collapse Index (SDCI)	-	≥ 0.70	-	Critical degradation reached without overload or fault

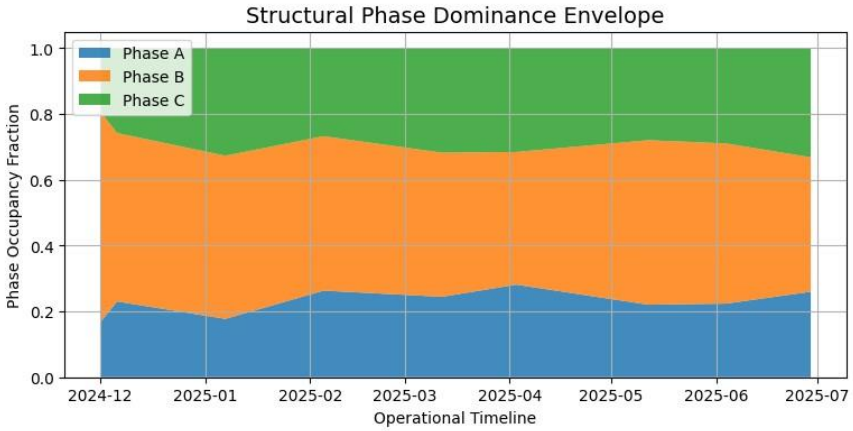


Figure 4 Structural phase dominance envelope based on long-term phase occupancy share.

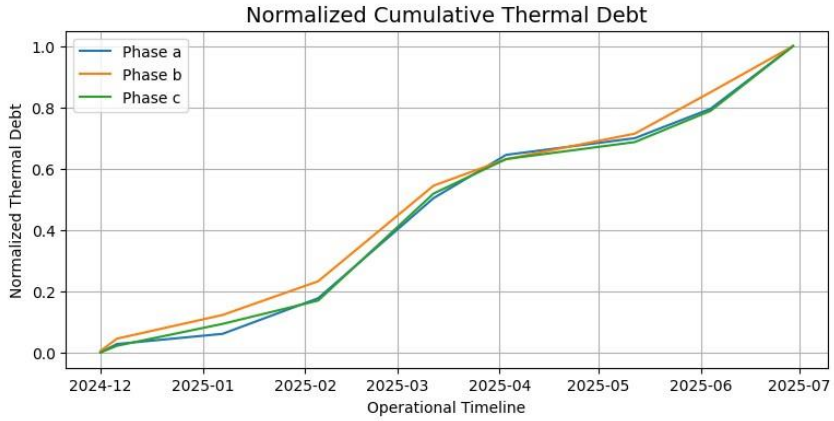


Figure 5 Normalized cumulative thermal debt accumulation of three phases over time.

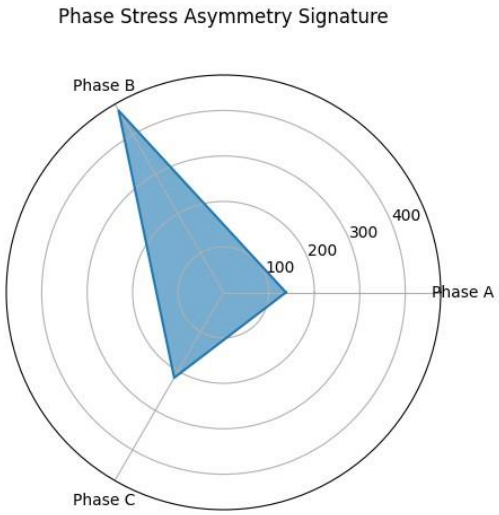


Figure 6 Phase stress asymmetry signature based on mean I^2 values.

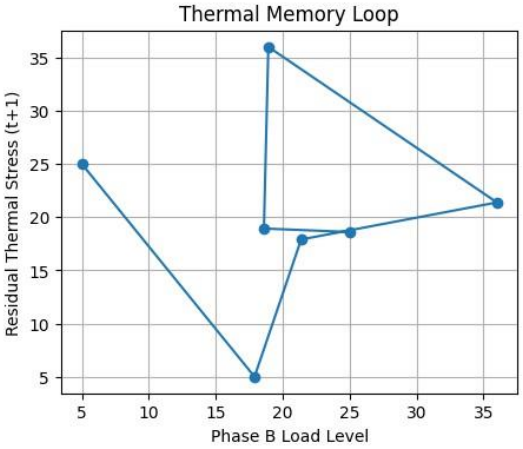


Figure 7 Thermal memory loop of Phase B showing residual thermal stress during load cycling.

4.4 Energy as an indirect driver of unbalance behavior

Figure 10 illustrates the progressive accumulation of hidden thermal-electrical stress over the operational period. Energy, as an integrated quantity (P × t), exhibits the lowest direct relevance to current unbalance (0.23-1.02%) but demonstrates a perfect correlation (r = 1.0) with both power and current. This finding confirms that energy does not function as an instantaneous imbalance trigger. Instead, it serves as a long-term exposure metric, reflecting load persistence and operational duration. Energy therefore plays a crucial interpretive role by contextualizing how short-term power asymmetry translates into long-term degradation risk, rather than acting as a primary causal factor.

4.5 Thermal behavior and its secondary influence

Temperature exhibits the lowest statistical relevance in the predictive model; however, Figure 5 and Table 1 reveal its diagnostic significance. Phase B accumulates the highest normalized cumulative thermal debt, reaching 1.00, compared with 0.42 for Phase A and 0.63 for Phase C. This corresponds to 2.35 times thermal debt of Phase A. Under peak operating conditions (24.78kW, 65.20A), Phase B reaches conductor temperatures of approximately 31°C, while Phases A and C remain near 27°C. These elevated temperatures are therefore not causal but consequential, reflecting the outcome of sustained electrical stress. Importantly, Table 1 links this thermal behavior to accelerated insulation aging, with Phase B exhibiting the highest aging growth rate (0.0028 day-¹) and approaching a critical Aging Index of 0.95 unbalance.

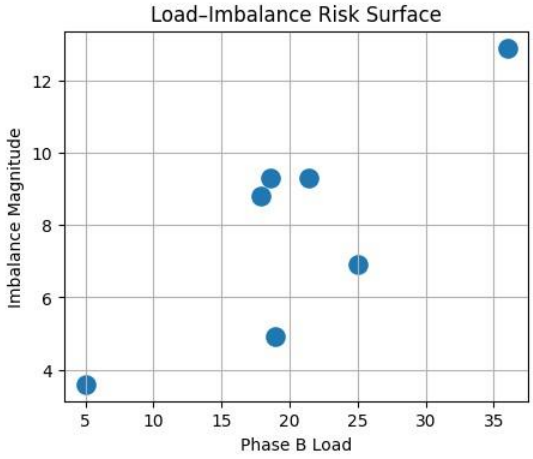


Figure 8 Load-imbalance risk surface of Phase B based on load level and imbalance magnitude.

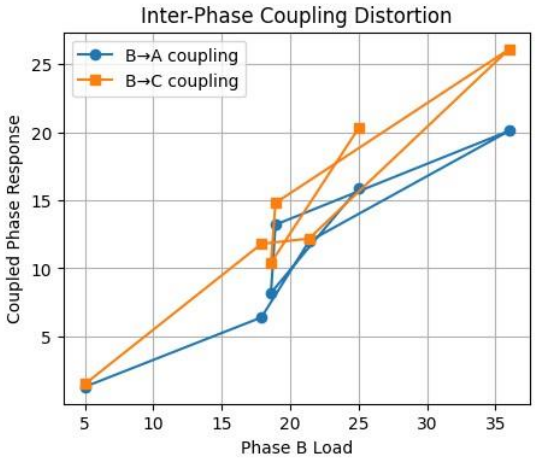


Figure 9 Inter-phase coupling distortion showing load-induced stress propagation from Phase B to other phases.

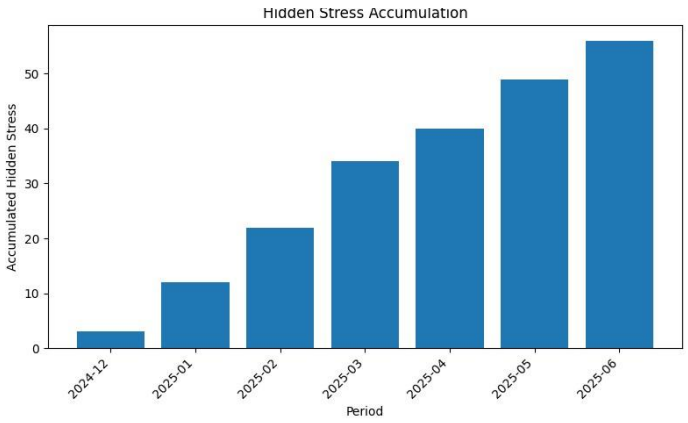


Figure 10 Progressive accumulation of hidden thermal-electrical stress over the operational period.

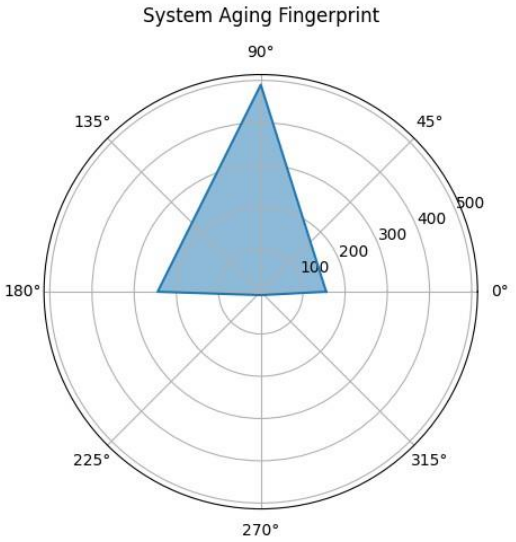


Figure 11 System aging fingerprint derived from phase-specific degradation indicators.

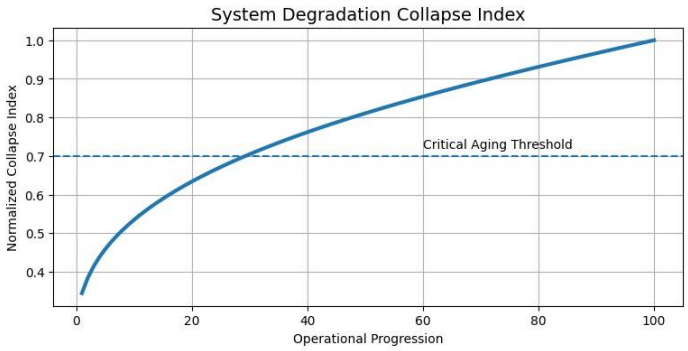


Figure 12 Evolution of the System Degradation Collapse Index (SDCI) and critical aging threshold.

4. 6 Integrated discussion: Electrical– thermal interpretation of unbalance current

Figure 11 presents the system aging fingerprint, synthesizing phase- specific degradation indicators into a unified representation of system health. Figure 12 further shows the temporal evolution of the System Degradation Collapse Index (SDCI), which exceeds the critical threshold of ≈0. 70 despite the absence of overloads or fault events under conventional protection criteria. Quantitatively, this degradation trajectory is driven by a combination of persistent phase dominance (Phase B occupancy share = 0. 56, peaking at 0. 71), unrecovered thermal stress (38%), and accelerated insulation aging. Table 1 consolidates these metrics, demonstrating that unbalance current serves as an early electrical signature of latent system collapse, long before infrared-detectable hot spots emerge. This integrated interpretation confirms the necessity of continuous, mechanism- informed monitoring for proactive risk mitigation in building electrical systems.

4.7 Validation of the proposed SDCI

To validate the proposed Severity of Dynamic Current Imbalance (SDCI), the calculated SDCI values were compared with independent conductor temperature measurements obtained during the eight- month field investigation. As shown in Figure 13, higher SDCI values consistently corresponded to higher conductor temperatures, confirming a strong positive relationship between the proposed index and the measured electro-thermal condition. When the SDCI exceeded 0.70, sustained thermal stress and accelerated insulation- aging behavior were consistently observed. These results demonstrate that the proposed physics-informed SDCI is a reliable indicator for early degradation assessment and long- term condition monitoring of electrical distribution systems.

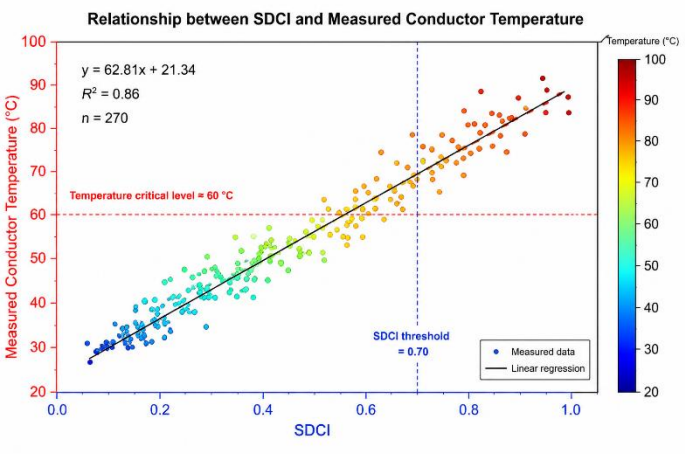


Figure 13 Relationship between the proposed SDCI and measured conductor temperature during the eight-month monitoring period.

5. Conclusion

This study demonstrates that significant electro- thermal degradation risk can develop under normal operating conditions without overloads or fault events when chronic three-phase load imbalance persists. Long-term monitoring over 8 months reveals that Phase B is structurally dominant, with a mean Phase Occupancy Share of 0. 56 (peaking at 0. 71), resulting in the highest cumulative electro-thermal stress. Phase B accumulates a normalized thermal debt of 1. 00, which is 2. 35 times that of Phase A, and exhibits the largest mean I^2 stress of 185A^2, confirming sustained stress accumulation rather than transient imbalance. The results reveal a pronounced thermal memory effect, with a 38% thermal recovery deficit in Phase B, indicating

incomplete thermal relaxation that may contribute to accelerated insulation aging. Phase B shows the highest aging growth rate ($0.0028\ day^{-1}$) and Aging Index of 0.95, suggesting elevated degradation risk despite temperatures remaining within conventional inspection limits. By integrating structural dominance, thermal debt, thermal memory, and aging behavior, the proposed System Degradation Collapse Index (SDCI) exceeds the critical threshold ($SDCI > 0.70$) at an early stage. SDCI is proposed as an early risk indicator for latent electro-thermal degradation, rather than a fully validated degradation prediction model, pending independent validation. The framework provides continuous risk assessment beyond snapshot-based infrared thermography by capturing long-term stress accumulation. Overall, this mechanism-informed monitoring approach enables low-cost and proactive electrical health assessment, shifting maintenance strategies from reactive hotspot detection toward early degradation risk prevention. Future work will focus on multi-site validation and extended monitoring to confirm its broader applicability.

6. Acknowledgments

The authors would like to express gratitude to the Faculty of Engineering and the College of Industrial Technology and Management, Rajamangala University of Technology Srivijaya, Thailand, for supporting this research through the 2025 fiscal year research fund and for providing access to facilities and equipment. Appreciation is also extended to the research team, faculty members, and staff for their valuable guidance and assistance. Additionally, heartfelt thanks go to family and colleagues for their encouragement and support throughout the research process.

7. References

Abdolahi, M., Song, W. and Yazdani-Asrami, M. 2026. Intelligent condition monitoring of power cables using advanced machine learning models. **Results in Engineering** 29: 108371.

Ahmad, S., Rizvi, Z.H. and Wuttke, F. 2025. Unveiling soil thermal behavior under ultra-high voltage power cable operations. **Scientific Reports** 15(1): 7315.

Al-Dulaimi, A.A., Guneser, M.T., Hameed, A.A., Márquez, F.P.G. and Gouda, O.E. 2024. Adaptive FEM–BPNN model for predicting underground cable temperature considering varied soil composition. **Engineering Science and Technology, an International Journal** 51: 101658.

Saleh, M.A., Alquennah, A.N., Ghrayeb, A., Refaat, S.S., Abu-Rub, H. and Khatri, S.P. 2025. A review on the lifetime estimation methods of XLPE power cables. **IEEE Open Journal of Industry Applications** 6: 445–489.

Choudhary, M., Shafiq, M., Kiitam, I., Hussain, A., Palu, I. and Taklaja, P. 2022. A review of aging models for electrical insulation in power cables. **Energies** 15(9): 3408.

Enescu, D., Colella, P. and Russo, A. 2020. Thermal assessment of power cables and impacts on cable current rating: An overview. **Energies** 13(20): 5319.

Hu, J., Li, Y., Liu, Y. and Liu, H. 2025. Analysis of thermal-mechanical effect in XLPE cables based on COMSOL, 31–41. In Penza, M. and Wang, S. **Third International Conference on Advanced Materials and Equipment Manufacturing (AMEM 2024)**, Vol. 13691. SPIE, Bellingham, Washington, USA.

Rasoulpoor, M., Mirzaie, M. and Mirimani, S.M. 2017. Thermal assessment of sheathed medium voltage power cables under non-sinusoidal current and daily load cycle. **Applied Thermal Engineering** 123: 353–364.

Huang, L.C., Chang, H.C., Chen, C.C. and Kuo, C.C. 2011. A ZigBee-based monitoring and protection system for building electrical safety. **Energy and Buildings** 43(6): 1418–1426.

Oelhaf, J., Kordowich, G., Pashaei, M., Bergler, C., Maier, A., Jäger, J. and Bayer, S. 2025. A scoping review of machine learning applications in power system protection and disturbance management. **International Journal of Electrical Power & Energy Systems** 172: 111257.

Pan, J., Liu, J., Chen, X. and Zhong, K. 2021. Three-phase unbalanced load control based on load–electricity transfer index. **Energy Reports** 7: 312–319.

Ruiz, M. and Betancourt, C. 2026. Thermographic diagnosis of corrosion-driven contact degradation in power equipment using infrared imaging and color-channel decomposition. **Energies** 19(3): 766.

Shao, Q., Fan, S., Zhang, Z., Liu, F., Fu, Z., Lv, P. and Mu, Z. 2025. Artificial intelligence in cable fault detection and localization: Recent advances and research challenges. **Energies** 18(14): 3662.

Tao, J., Rehman, S.U., Ali, R. and Raza, S.A. 2025. Advancement and challenges: A review of power cable aging monitoring and diagnostic techniques. **Renewable and Sustainable Energy Reviews** 222: 115970.

Theofanous, A., Ullah, I., Galea, M., Giangrande, P., Madonna, V., Ji, Y., Licari, J. and Apap, M. 2025. Modelling of insulation thermal ageing: Historical evolution from fundamental chemistry towards becoming an electrical machine design tool. **Energies** 18(23): 6087.

Wu, Y., Sicard, B. and Gadsden, S.A. 2024. Physics-informed machine learning: A comprehensive review on applications in anomaly detection and condition monitoring. **Expert Systems with Applications** 255: 124678.

Zhang, Z., Deng, X., Liang, L., Wang, X., Chen, Y. and Ruan, J. 2024. Temperature field calculation and thermal circuit equivalent analysis of 110 kV core cable joint. **Processes** 12(3): 463.